



**HAL**  
open science

# Electrochemical and electromechanical studies on nanostructured electrodes for supercapacitors

Wanli Gao

► **To cite this version:**

Wanli Gao. Electrochemical and electromechanical studies on nanostructured electrodes for supercapacitors. Analytical chemistry. Sorbonne Université / Université Pierre et Marie Curie - Paris VI, 2018. English. NNT: . tel-02304360v1

**HAL Id: tel-02304360**

**<https://theses.hal.science/tel-02304360v1>**

Submitted on 3 Oct 2019 (v1), last revised 10 Nov 2021 (v2)

**HAL** is a multi-disciplinary open access archive for the deposit and dissemination of scientific research documents, whether they are published or not. The documents may come from teaching and research institutions in France or abroad, or from public or private research centers.

L'archive ouverte pluridisciplinaire **HAL**, est destinée au dépôt et à la diffusion de documents scientifiques de niveau recherche, publiés ou non, émanant des établissements d'enseignement et de recherche français ou étrangers, des laboratoires publics ou privés.

# Sorbonne Université

École Doctorale 388 – Chimie Physique et Chimie Analytique de Paris Centre

*Laboratoire Interfaces et Systèmes Electrochimiques, LISE – UMR 8235*

## **Electrochemical and electromechanical studies on nanostructured electrodes for supercapacitors**

Par Wanli GAO

Thèse de doctorat

Dirigée par Dr. Hubert PERROT

Présentée et soutenue publiquement le 12 Octobre 2018

Devant un jury composé de :

Mme. Sabine LUDWIGS	Professeure Université Stuttgart	Rapporteur
Mme. Rezan DEMIR-CAKAN	Professeure Gebze Technical University	Rapporteur
M. Daniel ALVES DALLA CORTE	Ingénieur de Recherche Collège de France	Examineur
Mme. Christel LABERTY	Professeure Sorbonne Université	Examineur
M. Hubert PERROT	Directeur de Recherche CNRS	Directeur de thèse
Mme. Ozlem SEL	Chargé de Recherche CNRS	Co-encadrante de thèse



## Acknowledgements

First of all, I would like to express my sincere thanks to my supervisors Dr Hubert Perrot and Dr Ozlem Sel, who led me into this fantastic field. I highly appreciate the guidance, encouragement and continuous support you have kindly shown to me in my Ph.D. study and research. It is your instructions, suggestions and questions that have helped and inspired every step of my research during last three years.

I would also like to thank my Master's thesis supervisors Prof. Shaoyun Guo and Prof. Jiabin Shen, who brought me into the entrance of the academic career. I would not arrive here today without their guidance.

I also want to thank the jury members Prof. Sabine Ludwigs, Prof. Rezan Demir-Cakan, Dr Daniel Alves Dalla Corte and Prof. Christel Laberty for their efforts devoted to my Ph.D. work.

My heartfelt thanks also go to Dr Catherine Debiemme-Chouvy for XPS measurements and analyses, Dr Laure Fillaud for UV-vis spectroscopy measurements, Dr Alibi Baitukha for FTIR measurements, Ms. Françoise Pillier and Stéphanie Delbrel for FEG-SEM measurements, and Mr. Cyrille Bazin for XRD measurements.

I would like to thank all the lab members for creating a happy work environment. It is my honor to work with you during last three years, which will be an amazing memory in my life. Special thanks are due to Thomas, David, Guillaume, Elise, Antoine, Hajar, Blanca, Lin, Sophie, Gabriel and my previous colleges, Wenchao, Andrew, Pierre, Marie, Simon, Lionel, Ibtissam and Larbi.

Lastly, this thesis is dedicated to my family: my parents, my brother and my girlfriend, Tadeja. At this very moment, I want to express my sincere gratitude to you for everything you have done along this journey. It is never easy to raise a naughty kid to be a Ph.D., so I hope my parents will be proud of me. Dad and Mom, I made it.

# Table of Contents

<b>Chapter I: Introduction</b> .....	1
I.1. Fundamentals of supercapacitors (SCs) .....	1
I.1.1. Electrical double layer capacitors (EDLCs) .....	2
I.1.2. Pseudocapacitors .....	5
I.1.3. SC capacitance, energy and power density.....	7
I.2. Challenges and applications of SCs .....	10
I.3. Electrode materials .....	12
I.3.1. Carbon materials.....	12
I.3.2. Conducting polymers (CPs) .....	16
I.3.3. Transition metal oxides.....	21
I.4. Evaluation tools for SC electrode materials .....	25
I.4.1. Cyclic Voltammetry (CV).....	25
I.4.2. Galvanostatic Charge-Discharge (GCD) .....	27
I.4.3. Electrochemical Impedance Spectroscopy (EIS).....	28
I.4.4. Electrical Quartz crystal microbalance (EQCM).....	29
I.4.5. <i>Ac</i> -electrogravimetry .....	33
I.4.6. Electroacoustic measurements.....	36
I.5. Objectives and outline of the thesis.....	40
<b>Chapter II: Experimental procedures</b> .....	53
II.1. Materials characterization techniques .....	53
II.1.1. Fourier transform infrared (FTIR) spectroscopy.....	53
II.1.2. Ultraviolet-visible (UV-vis) spectroscopy .....	54
II.1.3. Scanning electron microscopy (SEM).....	55
II.1.4. X-ray diffraction (XRD) .....	57
II.1.5. X-ray photoelectron spectroscopy (XPS).....	58
II.2. Electrochemical and electrogravimetric characterization .....	59
II.2.1. Electrochemical quartz crystal microbalance (EQCM).....	60
II.2.2. <i>Ac</i> -electrogravimetry.....	62
II.3. Electroacoustic impedance measurement.....	69
<b>Chapter III: Electrochemical and viscoelastic evolution of dodecyl sulfate-doped polypyrrole films during electrochemical cycling</b> .....	74
III.1. Preamble and Objectives .....	74
III.2. Experimental Methods and Theoretical Background.....	76
III.2.1. Film preparation and characterization .....	76
III.2.2. Electrogravimetric measurements.....	77
III.2.3. Electroacoustic impedance measurements.....	79
III.3. Results and Discussion .....	81
III.3.1. Cyclic electrogravimetric behavior.....	81
III.3.2. <i>Ac</i> -electrogravimetric investigations .....	84
III.3.3. Viscoelastic property changes upon film aging .....	93
III.4. Conclusions .....	97
<b>Chapter IV: Tuning charge storage properties of reduced graphene oxides evidenced by in situ gravimetric</b>	

<b>and viscoelastic explorations</b> .....	101
IV.1. Preamble and Objectives.....	101
IV.2. Experimental Methods and Theoretical Background.....	103
IV.2.1. Synthesis of ERGO electrodes and structural characterization.....	103
IV.2.2. Electroacoustic impedance measurements.....	105
IV.2.3. Electrogravimetric measurements.....	107
IV.3. Results and Discussion.....	108
IV.3.1. Morphology and structure of ERGO electrodes.....	108
IV.3.2. Viscoelasticity of ERGO electrodes and its influence on electrogravimetric performance.....	111
IV.3.3. Cyclic electrogravimetric behavior.....	114
IV.3.4. <i>Ac</i> -electrogravimetric investigations.....	118
IV.4. Conclusions.....	129
<b>Chapter V: Tracking interfacial charge transfer behavior of hydrothermally synthesized ZnO nanostructures via complementary electrogravimetric methods</b> .....	134
V.1. Preamble and Objectives.....	134
V.2. Experimental Methods and Theoretical Background.....	136
V.2.1. Electrode preparation and characterization.....	136
V.2.2. Theoretical considerations for <i>ac</i> -electrogravimetry.....	137
V.3. Results and Discussion.....	138
V.3.1. Cyclic Electrogravimetry (EQCM) and QCM-coupled GCD:.....	139
V.3.2. QCM-coupled to Electrochemical Impedance Spectroscopy ( <i>Ac</i> -electrogravimetry).....	142
V.3.3. Comparison of the EQCM and <i>Ac</i> -electrogravimetry mass responses.....	145
V.4. Conclusions.....	147
<b>Chapter VI: Reduced graphene oxide-sheltered ZnO nanostructures showing enhanced electrochemical performance revealed by an in situ electrogravimetric study</b> .....	150
VI.1. Preamble and Objectives.....	150
VI.2. Experimental Methods and Theoretical Background.....	151
VI.2.1. Synthesis of ZnO seed layer.....	151
VI.2.2. Synthesis of ZnO nanostructures.....	152
VI.2.3. Preparation procedures for ZnO@ERGO electrode.....	152
VI.2.4. Morphological observation of the electrode.....	153
VI.2.5. Complementary electrogravimetric characterizations (EQCM and <i>ac</i> -electrogravimetry).....	153
VI.3. Results and Discussion.....	154
VI.4. Conclusions.....	159
<b>General Conclusions</b> .....	163
<b>Résumé de la Thèse en Français</b> .....	166

# Chapter I: Introduction

## I.1. Fundamentals of supercapacitors (SCs)

Electrochemical capacitors (also called supercapacitors) are a class of electrochemical energy storage devices well suited to the rapid storage and release of energy<sup>1</sup>. SCs first emerged on the market in 1978 as farad-sized devices for backup power of computer memory<sup>2</sup>. The last four decades have seen a tremendous burgeoning of scientific and industrial interest into the potential applications of SCs, mainly due to their high power density and long cycle life<sup>3</sup>. In general, a supercapacitor consists of two electrodes in contact with an electrolyte electrically isolated by a separator. During charge process, the charges can be stored and separated across the two electrode/electrolyte interfaces, which would provide electric energy for the external load upon discharge, as illustrated in **Figure I.1**. According to charge storage mechanism, supercapacitors can be classified into two types: electrical double layer capacitors (EDLCs), which store charges by electrostatic adsorption of electrolyte ions at the electrode-electrolyte interface, typically are based on carbon materials<sup>4-8</sup>; pseudocapacitors, whose energy is stored by fast and reversible redox reactions between the electrolyte and electroactive species on the electrode surface at characteristic potentials, are commonly based on transition metal oxides and conducting polymers (CPs)<sup>9-13</sup>. Though a SC cell usually involves both EDL capacitance and pseudocapacitance in practical applications, it is clearer to discuss them separately.

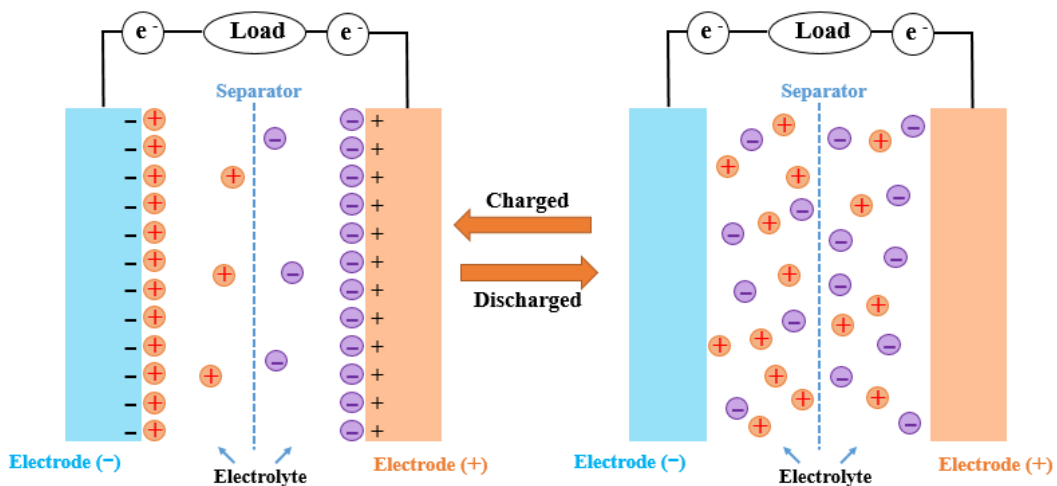


**Figure I.1.** Schematic illustration of a SC in a charged and discharged state.

### I.1.1. Electrical double layer capacitors (EDLCs)

EDLCs store the electrical charge in a physical process without any faradaic reactions on the electrode surface<sup>14</sup>. Only electrons need to be moved to and from the electrode surfaces through an external circuit, and electrolyte ions with counterbalancing charge diffuse in the solution to the charged interfaces to keep electroneutrality. It is thus highly expected that EDLCs have a high degree of recyclability, on the order of  $10^5$ - $10^6$  times, because there is no chemical phase and composition changes during the charging and discharging of EDLCs<sup>1</sup>. For each electrode, the charge separation at the electrode/electrolyte interface upon polarization produces the double layer capacitance ( $C$ ) based on the Helmholtz model<sup>15</sup>, which is shown in **Figure I.2a**<sup>8</sup> and can be defined by **Equation I.1**:

$$C = \varepsilon_0 \cdot \varepsilon_r \cdot \frac{A}{d} \quad (\text{I.1})$$

where  $\varepsilon_0$  (in  $\text{Fm}^{-1}$ ) is the vacuum permittivity,  $\varepsilon_r$  (in  $\text{Fm}^{-1}$ ) is the relative permittivity of the electrolyte,  $A$  (in  $\text{m}^2$ ) is the surface area of the electrode accessible to the electrolyte ions, and  $d$  (in m) is the effective thickness of the electrical double layer (EDL), often approximated as the Debye length<sup>5, 16</sup>. The Helmholtz model describes the charge separation at the electrode/electrolyte interface by an atomic distance. Since this simplified Helmholtz EDL model does not take into consideration the diffusion of ions in the solution and the dipole moment of the solvent and the electrode<sup>5</sup>. To address this issue, a modified Helmholtz EDL model was proposed by Gouy<sup>17</sup> and Chapman<sup>18</sup>, in which a diffuse layer exists from the electrode surface to the fluid bulk (**Figure I.2b**). However, the Gouy-Chapman model is not valid for highly charged electrodes<sup>5, 19</sup> and in 1924, Stern<sup>20</sup> put forward a model combining the Helmholtz model with the Gouy-Chapman model. Two regions of ion distribution were suggested, i.e., the Stern layer and diffuse layer (**Figure I.2c**). Stern layer is an accumulation of ions strongly adsorbed on the electrode surface, which consists of specifically adsorbed ions and non-specifically adsorbed counterions; whereas the diffuse layer refers to a continuous distribution of ionic species in the electrolyte with a hydrodynamic motion, as what the Gouy-Chapman model defines<sup>8</sup>. These two regions are equivalent to two capacitors in series. Therefore, the capacitance of the EDL ( $C_{DL}$ ) can be expressed by **Equation I.2**:

$$\frac{1}{C_{DL}} = \frac{1}{C_H} + \frac{1}{C_D} \quad (\text{I.2})$$

where  $C_H$  and  $C_D$  denote the capacitance from the Stern layer and diffuse layer, respectively.

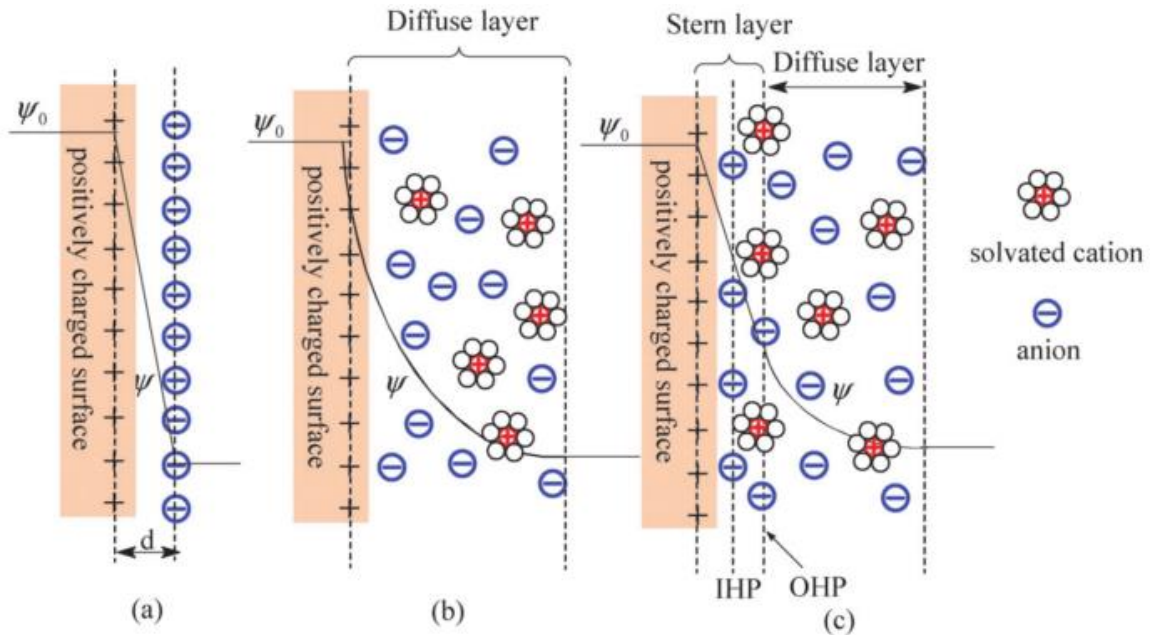


**Figure I.2.** EDL models at a positively charged surface: (a) the Helmholtz model, (b) the Gouy-Chapman model and (c) the Stern model, showing the inner Helmholtz plane (IHP) and outer Helmholtz plane (OHP). The IHP refers to the distance of closest approach of specifically adsorbed ions and OHP refers to that of the non-specifically adsorbed ions<sup>8</sup>.

It has been demonstrated that the correlation between the pore size and ion size plays an important role in maximizing the energy storage characteristics of EDLCs<sup>21-23</sup>. The solvated ions were thought not capable of participating in the formation of EDL owing to their inaccessibility to the micropores, if their size exceeded the pore dimensions. However, the distortion of the solvation shell and even a partial desolvation of hydrated ions were confirmed based on the significant enhancement of the specific capacitance from micropores<sup>6,24</sup>. For example, as shown in **Figure I.3**, the normalized capacitance for the carbons increases at pore size less than 1 nm, which is smaller than the size of solvated ions<sup>6</sup>. These findings further illuminate the relationships between the electrode pore dimensions and ion sizes. It unveils the important contributions of micropores with smaller sizes than solvated ions to increase the capacitance values.

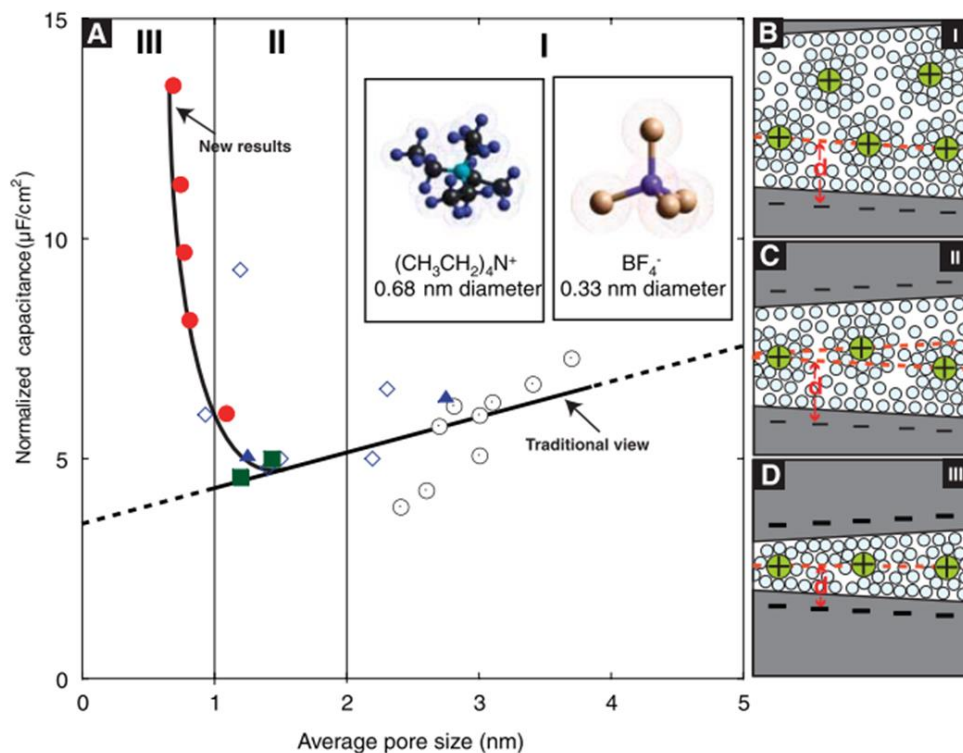


**Figure I.3.** (A) normalized capacitance for the carbons; B to D schematically illustrate the solvated ions in electrode pores with distance between adjacent pore walls (B) greater than 2 nm, (C) between 1 and 2 nm, and (D) less than 1 nm<sup>6</sup>.

Nevertheless, the anomalous increase in carbon capacitance at pore size less than that of solvated ion size cannot be fully interpreted by current EDL charge storage mechanism because of the space confinement for accommodating both Stern layer and diffuse layer. An approach with consideration of pore curvature of carbon-based SC has been suggested to address this issue<sup>25</sup>. For mesoporous carbon electrodes, an electric double-cylinder capacitor (EDCC) model can be applied, as illustrated in **Figure I.4a**, where the pores are sufficiently large so that the effect of pore curvature is not significant. Actually, the EDCC model can be simplified to the classical EDL model shown in **Figure I.2c**. Whereas for microporous carbon electrodes, an electric wire-in-cylinder capacitor (EWCC) model can be proposed, as shown in **Figure I.4b**, where the pores are sufficiently confined and the pore curvature plays an important role in charge storage.

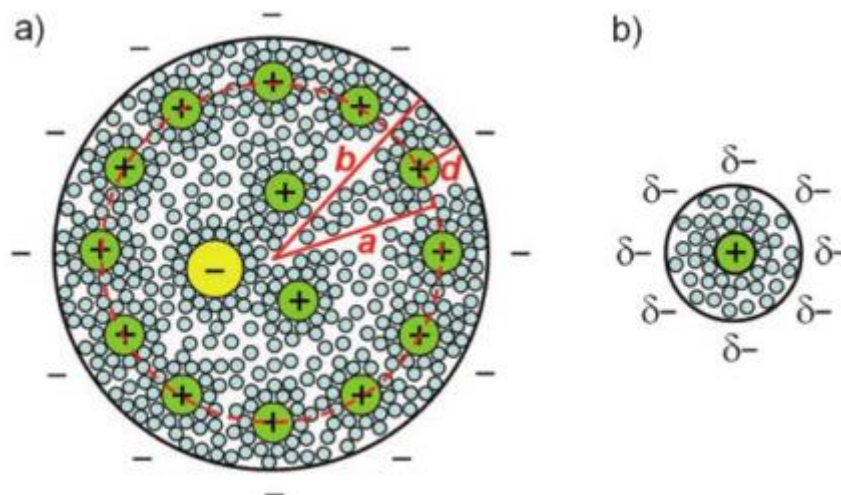


**Figure I.4.** Schematic diagrams (top views) of (a) a negatively charged mesopore with solvated cations approaching the pore wall to form an EDCC and (b) a negatively charged micropore with solvated cations lining up to form an EWCC<sup>25</sup>.

### I.1.2. Pseudocapacitors

By contrast with EDLC, Pseudocapacitors based on conducting polymers (CPs) and transition metal oxides store the electric energy through fast and reversible redox reactions occurring which can provide significantly higher capacitances<sup>26-28</sup>. Conway identified the pseudocapacitance arises from thermodynamic reasons when there is a continuous dependence of a charge ( $q$ ), passed faradaically in oxidation or reduction, upon the electrode potential ( $V$ )<sup>1</sup>. The  $dq/dV$  corresponds to a pseudocapacitance. What differentiates the pseudocapacitance with respect to EDL capacitance lies in the fact that pseudocapacitance is faradic in nature. The most commonly used pseudocapacitive materials involve (i) CPs such as poly(3,4-ethylenedioxythiophene) (PEDOT)<sup>29-30</sup>, polypyrrole (PPy)<sup>31-32</sup>, polyaniline (PANI)<sup>27, 33</sup> and polythiophene (PTh)<sup>34-35</sup>, and (ii) transitional metal oxides such as ruthenium oxide ( $\text{RuO}_2$ )<sup>36</sup>,  $\text{MnO}_2$ <sup>37</sup>,  $\text{ZnO}$ <sup>38</sup> and  $\text{NiO}$ <sup>39</sup>. Although the pseudocapacitance can be much higher than EDL capacitance, it suffers from low power density and poor stability upon cycling.

The pseudocapacitance of CPs relies on ion doping and dedoping (intercalation/deintercalation), which are normally accompanied with volumetric swelling-shrinking during charge/discharge process<sup>40-41</sup>. The ionic fluxes generally accompanied with the free solvent molecules transfer during charging-discharging process may bring about the periodic potential-dependent volumetric

alternations of the conducting polymer electrodes (i.e., swelling and shrinking)<sup>3,35</sup>. These processes are likely to lead to a wide variety of unpredictable mechanical defects (such as polymer electrode fatigue, stress concentration and delamination from current collector) and thus fast capacitance decay of the CP electrodes<sup>27,42</sup>. Furthermore, a stringent potential window is required for CP-based SCs. If the potential is beyond this critical potential, the CP can be degraded (or overoxidized) at more positive potentials<sup>43</sup>; whereas the CP may become insulating (un-doped state) at too negative potential. Therefore, a suitable potential window plays an essential role in the performance of CP-based SCs. **Table I.1** summarizes the operating potentials of the commonly used CP-based electrodes.

**Table I.1.** The electrochemical performance of some CP-based electrode materials

CP-based electrodes	Potential window (V)	Electrolyte	Specific capacitance (F g <sup>-1</sup> )	Reference
PPy/carbon cloth	-0.8-0.5 vs. SCE	5 M LiCl	699 at 1 A g <sup>-1</sup>	44
PPy/graphene	-0.4-0.6 vs. SCE	1 M KCl	237 at 10 mVs <sup>-1</sup>	45
PPy/MnO <sub>2</sub> /CNT	0-0.85 vs. Ag/AgCl	1 M Na <sub>2</sub> SO <sub>4</sub>	461 at 0.2 A g <sup>-1</sup>	46
PANI/CNT	-0.2-0.7 vs. SCE	1 M H <sub>2</sub> SO <sub>4</sub>	1030 at 5.9 A g <sup>-1</sup>	47
PANI	0-0.6	1 M H <sub>2</sub> SO <sub>4</sub>	554 at 1 A g <sup>-1</sup>	43
PANI/CNT	0-0.4	1 M H <sub>2</sub> SO <sub>4</sub>	606 at 1 A g <sup>-1</sup>	43
PTh/CNT	-0.6-0.8 vs. SCE	0.5 M H <sub>2</sub> SO <sub>4</sub>	110 at 1 A g <sup>-1</sup>	48
PTh/CNT	-0.6-1 vs. Ag/AgCl	1 M Na <sub>2</sub> SO <sub>4</sub>	216 at 1 A g <sup>-1</sup>	49

For transition metal oxides, three different types of faradic mechanisms were suggested leading to pseudocapacitance<sup>1, 26, 50</sup>: (1) underpotential deposition (such as Pb on Au), (2) redox pseudocapacitance (such as RuO<sub>2</sub>.nH<sub>2</sub>O), and (3) intercalation pseudocapacitance (such as Nb<sub>2</sub>O<sub>5</sub>), as shown in **Figure I.5**<sup>26</sup>. Underpotential deposition refers to the deposition of a monolayer of metal atoms onto a metal substrate at potentials positive with respect to the reversible Nernst potential<sup>51</sup>. Redox pseudocapacitance originates from the reduction-oxidation reactions of electrode materials with a concomitant faradaic charge-transfer from ions electrochemically adsorbed onto the surface or near the surface of a material. The occurrence of intercalation pseudocapacitance is interpreted as

a result of the intercalation of ions into the tunnels or layers of electrode materials accompanied by a faradaic charge-transfer with no crystallographic phase change<sup>26</sup>. The intercalation mechanism is featured by a capacity that does not vary significantly with charging time, a proportional linearity relationship between currents and the sweep rate and peak potentials that are not sweep-rate dependent<sup>52</sup>.

Pseudocapacitance can be intrinsic or extrinsic to a material<sup>53-55</sup>. Intrinsic pseudocapacitive materials (such as  $\text{RuO}_2 \cdot n\text{H}_2\text{O}$ <sup>56</sup>,  $\text{MnO}_2$ <sup>57</sup> and  $\text{Nb}_2\text{O}_5$ <sup>52</sup>) exhibit the characteristics of capacitive charge storage irrespective of the material's morphology; extrinsic ones (such as  $\text{LiCoO}_2$ <sup>58</sup>,  $\text{MoO}_2$ <sup>59</sup> and  $\text{V}_2\text{O}_5$ <sup>60</sup>) do not display pseudocapacitance in the bulk state due to phase transformations during ion storage<sup>26</sup>. When they are engineered at the nanoscale so that the charge storage sites are on the surface or near-surface region, the pseudocapacitance emerges<sup>53</sup>. Additionally, it should be noted that the oxygen or nitrogen containing functional groups on the carbon materials<sup>61-65</sup>, which are typically served as EDLC materials, can also contribute to pseudocapacitance.

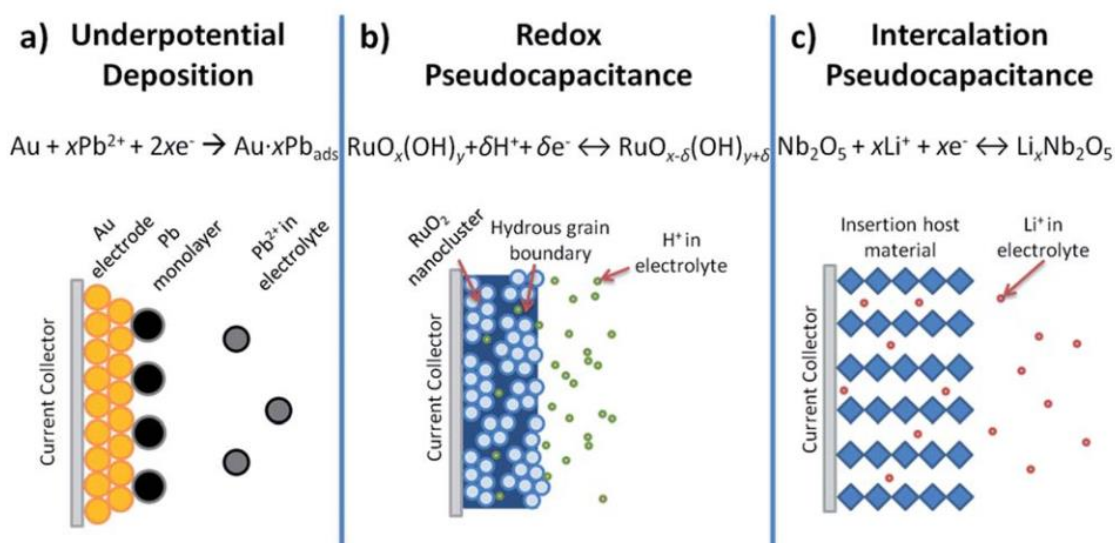


**Figure I.5.** Different types of reversible redox mechanisms that give rise to pseudocapacitance: (a) underpotential deposition, (b) redox pseudocapacitance, and (c) intercalation pseudocapacitance<sup>26</sup>.

### I.1.3. SC capacitance, energy and power density

As shown in **Figure I.1**, the entire SC cell is equivalent to two capacitors in series. The corresponding RC equivalent circuit representation is illustrated in **Figure I.6**. Therefore, the total capacitance of an entire cell ( $C_T$ ) can be described by **Equation I.3**<sup>4</sup>, where  $C_p$  and  $C_n$  are positive

electrode capacitance and negative electrode capacitance, respectively.

$$\frac{1}{C_T} = \frac{1}{C_p} + \frac{1}{C_n} \quad (I.3)$$

Thus, it is obvious that  $C_T$  is mainly dependent on the electrode with smaller capacitance and that a high capacitance of both electrode materials is simultaneously required in order to optimize the  $C_T$  of the SC.

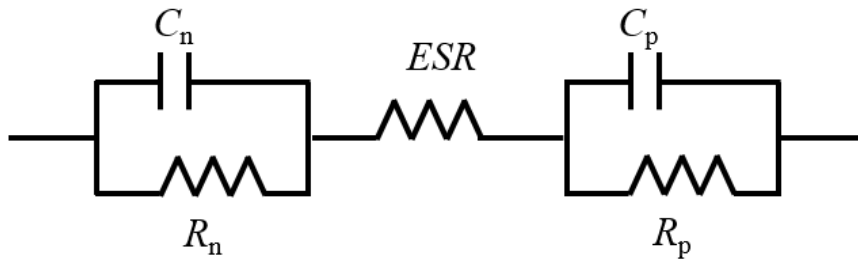


**Figure I.6.** Representation of the equivalent circuit of a symmetric EDL capacitor.  $R_{n/p}$  represents resistors and  $C_{n/p}$  denotes capacitance.

At the packaged cell level, Energy density ( $E$ , in Wh kg<sup>-1</sup>) and power density ( $P$ , in W kg<sup>-1</sup>) are two key parameters to evaluate the practical performance of a SC. These two parameters depend extensively upon package specific parameters such as the mass of dead components and the cell architecture, so the evaluation of energy and power densities should be performed in the condition of a full-sized and well-packaged SC with the consideration of the mass of all cell components<sup>66</sup>. The energy density represents the capacity to perform work, whereas the power density exhibits how fast the energy can be delivered. During charge process, a voltage ( $V$ ) will build up across the two electrodes of the SC. The maximum energy and power densities of the SC are calculated according to **Equations I.4** and **I.5**<sup>8</sup>:

$$E = \frac{1}{2} C_T V^2 \quad (I.4)$$

$$P = \frac{1}{4R_s} V^2 \quad (I.5)$$

in which  $R_s$  denotes the equivalent series resistance (ESR, in  $\Omega$ ) of the system. The capacitance of the cell relies significantly on the electrode materials. The cell operating voltage is restricted by the electrolyte's stability. The ESR corresponds to the sum of various types of the resistances related to

the intrinsic resistivity of the electrodes, the ionic resistance of the electrolyte and the interface resistances between the current collector and the electrode<sup>67</sup>. Based on **Equations I.4** and **I.5**, it can be seen that a large capacitance, high operating potential and minimum ESR are simultaneously required to obtain a superior performance for a SC<sup>8</sup>. Therefore, the development of both electrode materials and electrolytes is highly desirable in terms of optimizing the overall performance of SC devices.

According to the aforementioned discussion, the higher the  $E$  and  $P$  are, the better a SC device should perform. Unfortunately, higher energy densities do not necessarily mean high power densities for supercapacitors<sup>68</sup>. The relationship between energy and power densities is usually illustrated by a Ragone plot, where the specific  $P$  is plotted against the specific  $E$ . The Ragone plot is often used to evaluate the practical performances of electrochemical energy storage devices. **Figure I.7** compares the Ragone plots for various electrochemical energy storage devices<sup>14</sup>. It presents that the SCs possess higher  $P$  and lower  $E$  than batteries. Therefore, how to enhance the energy density becomes a major research focus in the development of SC.

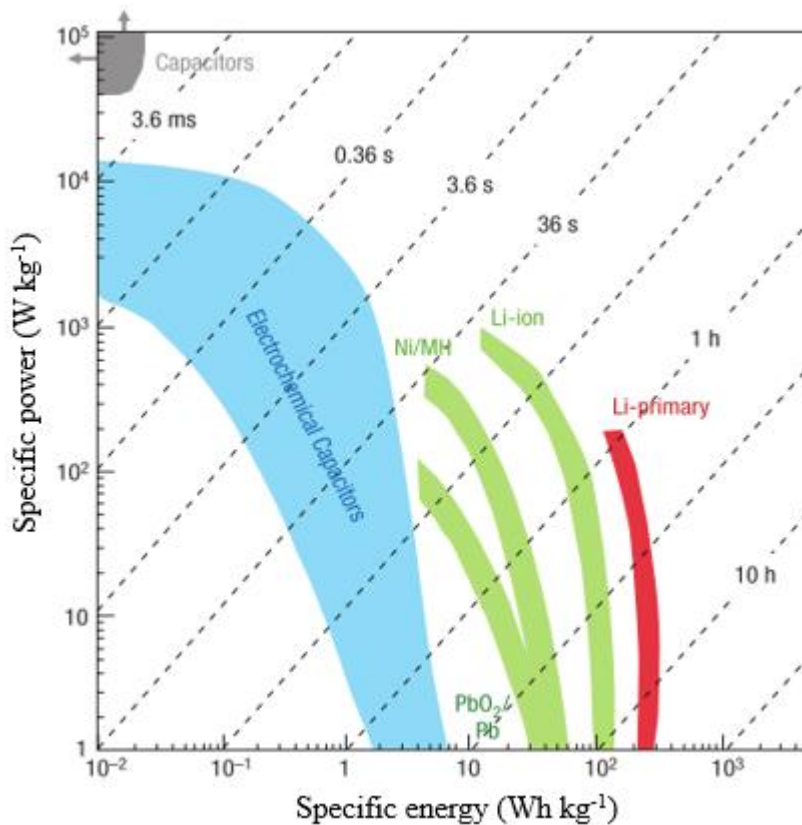


**Figure I.7.** Ragone plot of various electrical energy storage devices<sup>14</sup>.

## I.2. Challenges and applications of SCs

Supercapacitor is featured by high power capability, supreme cyclability and fast dynamics of charge propagation with low maintenance<sup>8, 69-70</sup>. It possesses much higher power density than battery and much larger energy density than conventional capacitors<sup>2, 71-72</sup>. Many advantages though SCs have, they still face some challenges at the contemporary technological stage. **Table I.2**<sup>68</sup> summarizes the advantages and challenges of supercapacitors.

**Table I.2.** Advantages and Challenges of Supercapacitors<sup>68</sup>

Advantages	Challenges
Long life with little degradation over cycling	Low energy density ( $\sim 5\text{Wh kg}^{-1}$ ) compared to batteries ( $> 50\text{ Wh kg}^{-1}$ ) <sup>3</sup>
Low cost per cycle	High self-discharging rate <sup>1, 73</sup>
Superior reversibility	Voltage across supercapacitor drops significantly upon discharge; effective energy storage requires sophisticated electronic control and switching equipment
Very high rates of charge and discharge.	Very low internal resistance allows extremely rapid discharge when shorted, resulting in spark hazard
Extremely low internal resistance (ESR), consequent high cycle efficiency (95% or more), and extremely low heating levels	Raw material costs are significantly high and play important role in pricing of supercapacitor
High output power	Adoption rates increase only gradually as end users realize benefits
High specific power	Power only available for very short duration

New technologies associated with electrochemical energy storage are being widely used in the

form of SCs due to their many advantages. The application of SCs has extended to portable electronics (such as digital cameras and mobile phones), electric vehicles, electric hybrid vehicles, electrical tools, pulse laser techniques, uninterruptible power supplies and storage of energy generated by solar cells. In general, the application of SCs includes:

(1) *Transportation*. Since SC can be charged/discharged in an order of seconds, it can be readily used in dynamic braking of transport systems<sup>19</sup>. The energy can be stored in SC during braking and then released upon accelerating. The most promising market for supercapacitors is in the transportation industry. SCs can be used in automobiles by coupling them with other energy sources such as batteries. They can store energy when an automobile is braking and then releasing the energy when it accelerates, thus enhancing the fuel efficiency. Automobiles powered by coupling fuel cells with SCs are ideal choices for stop-and-go traffic where SCs provide sudden bursts of energy during start-up and fuel cells provide sustained energy<sup>74</sup>.

(2) *Portable electronics*. Supercapacitors are widely used in consumer electronics as back-up energy sources for system memories, microcomputers, system boards and clocks, toys, and mobile phones. They are ideal for devices requiring quick charges. Supercapacitors are cost-effective options because they have extremely long lifetimes and do not need replacement during the lifetimes of the devices they power. For some portable electronic devices with moderate energy demands, SCs may act as rechargeable stand-alone power sources. Currently, batteries are the most convenient power supplies. However, they require long recharge time. SCs can be recharged quickly, and the repeated charging and discharging can proceed without significant losses in efficiency<sup>68</sup>.

(3) *Uninterrupted power supply (UPS) systems*. Supercapacitors can be used for temporary back-up power in UPS systems. They can provide instantaneous supplies of power without delays, helping to prevent malfunctions of mission-critical applications. Supercapacitors quickly bridge the power applications for stationary UPS systems that are augmented with fuel cells. In addition, supercapacitors are best suited to provide power for start-up and during peak load buffering.

(4) *Other applications*. Supercapacitors show promise for critical-load operations such as hospitals, banking centers, airport control towers, and cell phone towers. The critical time between a power outage and the start of a generator can be bridged effectively by supercapacitors because they provide power within milliseconds to a few seconds after an outage.

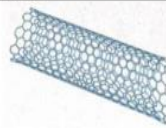
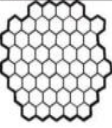
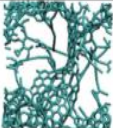
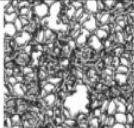
### I.3. Electrode materials

The most important component in SC is electrode material with high surface area and high porosity<sup>3</sup>. Currently, the three major categories of electroactive electrode materials in SC are based on carbon materials<sup>75-76</sup>, conducting polymers<sup>35, 77</sup> and transition metal oxides<sup>78-81</sup>. In this part, these three major electrode materials are reviewed in detail with new trends in the material development of SC electrode. Their advantages/disadvantages and performances as SC electrode materials are also discussed and summarized.

#### I.3.1. Carbon materials

As they exhibit high conductivity, porosity and superior electrochemical stability, carbon materials are widely used as EDLC electrode materials, as described in **Table I.3**<sup>82</sup>. Among them, activated carbon, carbon nanotubes (CNTs) and graphene are the most common ones, which will be separately discussed in detail in this part.

**Table I.3.** Different Carbon Structures Used in EDLCs<sup>82</sup>

Material	Carbon onions	Carbon nanotubes	Graphene	Activated carbon	Carbide derived carbon	Templated carbon
Dimensionality	0-D	1-D	2-D	3-D	3-D	3-D
Conductivity	High	High	High	Low	Moderate	Low
Volumetric Capacitance	Low	Low	Moderate	High	High	Low
Cost	High	High	Moderate	Low	Moderate	High
Structure						

#### (1) Activated carbons (ACs)

ACs are the most widely used electrode materials due to their wide accessibility, low cost and high specific surface area (SSA)<sup>4</sup>, which are generally prepared by creating a three-dimensional porous network in the bulk of carbon materials through a carbonization and subsequent activation process, which involves a controlled oxidation of a very wide selection of natural and synthetic precursors using various activation techniques, such as oxidation in water vapor or KOH<sup>75, 82-83</sup>. Low-cost ACs are generally prepared from natural precursors, including wood, nutshells, fruit pits,

anthracite, coal, petroleum coke, pitch, peat, sucrose, corn grain, leaves, and straw<sup>84-86</sup>. Synthetic precursors (polymers) like polyvinyl chloride (PVC)<sup>87</sup>, polypyrrole (PPy)<sup>88</sup>, polyaniline (PANI)<sup>89</sup> are used for AC synthesis to obtain a more homogeneous microstructure and a better developed porosity.

The carbonization process aims to eliminate non-carbon species of the raw precursors through a thermal decomposition process, whereas activation process is performed to develop the porous structure, which can be generally categorized into two types, i.e., thermal (or physical) and chemical<sup>75, 90</sup>. The thermal activation consists of the pyrolysis of precursor in an inert atmosphere and the following gasification with an oxidizing agent (CO<sub>2</sub>, steam and a mixture of both); the chemical activation involves the reaction of a precursor with a chemical agent, such as KOH<sup>83</sup>, ZnCl<sub>2</sub><sup>91</sup> and H<sub>3</sub>PO<sub>4</sub><sup>92</sup>, and then annealing at elevated temperatures. By contrast with thermal activation, chemical activation is more effective for tuning structure and pore size distribution<sup>93</sup>.

**Figure I.8** is an example of the effect of activation temperature on the AC structure and porosity. **Table I.3** compares the ACs and other typical carbons commonly used in EDLCs. ACs have been widely employed as electrode materials in many types of SCs, due to their high SSA, porous structure as well as low cost and industrial large-scale production<sup>84, 94</sup>. Currently, the decreasing availability of fossil-based carbons has boosted a pursuit of sustainable precursors to synthesize ACs. The utilization of biomass materials<sup>85-86</sup>, such as corn grain<sup>95</sup>, lignocellulosic materials<sup>96</sup> and starch<sup>94</sup>, and recycling of waste products, such as tires<sup>97</sup>, to produce ACs become of interest with consideration of costs, availability and environmental friendliness.

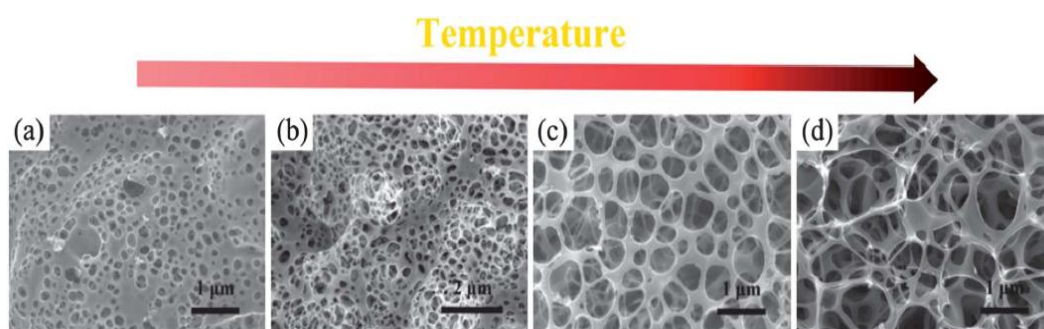


**Figure I.8.** SEM images of the samples obtained by annealing the slurry of PPy and KOH at various temperatures: (a) 500 °C, (b) 600 °C, (c) 700 °C and (d) 750 °C<sup>93</sup>.

## (2) Carbon nanotubes (CNTs)

CNTs are of particular interest for the development of SC electrodes because of their superior electrical conductivity, unique tubular structures and superior mechanical, thermal and chemical stability<sup>8</sup>. CNTs can be categorized into two subgroups based on the number of graphitic layers: single-walled carbon nanotubes (SWCNTs) or multi-walled carbon nanotubes (MWCNTs): SWCNTs consist of a single graphite sheet seamlessly wrapped into a cylindrical tube (**Figure I.9a-c**), whereas MWCNTs comprise an array of such nanotubes that are concentrically nested like rings of a tree trunk<sup>98</sup>. Though sharing a structural similarity with a single sheet of graphite, which is a semiconductor with zero band gap, SWCNTs can be either semiconducting or metallic, depending on the rolling direction of graphite sheet to form a nanotube cylinder<sup>98</sup>. Moreover, the conductivity of perfect MWCNTs is rather comparable to that of perfect SWCNTs because the coupling between nanotubes is weak<sup>98</sup>. CNTs are usually regarded as a promising candidate for high-power electrode material because of the aforementioned properties. Although the surface area of CNTs ( $500 \text{ m}^2 \text{ g}^{-1}$ ) is small as compared to ACs ( $2000\text{-}3000 \text{ m}^2 \text{ g}^{-1}$ )<sup>8, 99</sup>, they can offer a reasonable specific capacitance<sup>100</sup>. It is speculated to stem from their aligned pore structures, which, therefore, contribute to higher ion diffusion kinetics, as illustrated in **Figure I.9d**<sup>101</sup>.

Additionally, CNTs are commonly used as a support for electroactive materials because of their high mechanical resilience and open tubular network, such as CNT/Ni(OH)<sub>2</sub><sup>102</sup>, CNT/PPy<sup>103</sup>, CNT/PPy/MnO<sub>2</sub><sup>104</sup> and CNT/PANI<sup>105</sup>.

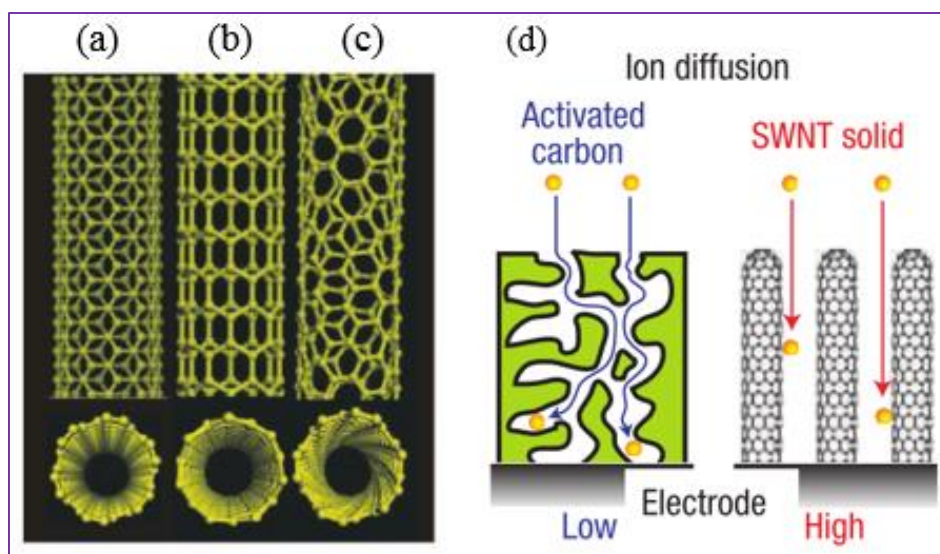


**Figure I.9.** Schematic illustrations of the structures of (a) armchair, (b) zigzag, and (c) chiral

SWCNTs. Projections normal to the tube axis and perspective views along the tube axis are on the top and bottom, respectively<sup>98</sup>. The panel (d) presents a schematic model comparing the ion diffusion for activated carbon and the SWCNT solid material<sup>101</sup>.

### (3) Graphene

Graphene, a  $sp^2$ -bonded carbon monolayer, was believed not to exist in a free state until 2004, when Novoselov and co-workers isolated a single-atom-thick layer of carbon<sup>106</sup>. In recent years, graphene has gained tremendous research attention towards the application of electrochemical energy storage/delivery due to many appealing features, such as high surface area (theoretically as high as  $2630 \text{ m}^2 \cdot \text{g}^{-1}$ ), superior mechanical properties, excellent electronic conductivity and chemical resilience<sup>7, 61, 107-111</sup>. Graphene's properties vary strongly as a function of its production method, which plays an important role in determining the performances of final products<sup>112</sup>. The common methods adopted for graphene production include reduction of graphene oxide (GO)<sup>62, 113</sup>, liquid-phase exfoliation<sup>114</sup>, mechanical exfoliation<sup>106</sup>, synthesis on SiC<sup>115</sup>, bottom-up synthesis<sup>116</sup> and chemical vapour deposition<sup>115</sup>. The comparison among the aforementioned techniques is presented in **Figure I.10**<sup>112</sup>. Although many different methods continue to be explored, the large-scale production of graphene still remains the key challenge before its widespread application<sup>65, 112</sup>.

Reduction of GO is widely employed for the bulk production of graphene because of its low cost, high scalability and competitive yield<sup>112, 117</sup>. GO is usually obtained through oxidation and expansion of graphite, which can be reduced and subsequently exfoliated to form graphene-like materials with similar structure and properties of pristine graphene<sup>118-119</sup>. Reduction of GO leads to the (partial) restoration of the structure and property of graphene by removing the oxygen functionalities on its layers with the recovery of the conjugated system. Different reduction processes result in different structures and properties of reduced GO. Over the past few years, numerous strategies such as thermal, (electro)chemical and even multi-step reduction have been performed to produce reduced graphene oxide (RGO)<sup>120</sup>. The most straightforward goal of GO reduction is to remove functional groups and heal structural defects. Thermal reduction is usually realized at high temperature by thermal, microwave or photo-irradiation, which is accompanied with a sudden deoxygenating reactions of GO films. Contrarily, chemical reduction based on

chemical reactions between chemical reagents (such as hydrazine) and GO is generally carried out at room temperature or by moderate heating. Multi-step reduction is also explored to meet some special purposes. For example, a combination of hydrazine vapour exposure and low-temperature annealing treatment at 200 °C was reported to produce an RGO film with better conductivity than that produced by only thermal annealing at 550 °C<sup>120-121</sup>. Notably, electrochemical reduction is another efficient method to produce reduced GO (ERGO), which relies on electron exchange between GO and electrodes and thus avoids the stringent requirement on high temperature for thermal reduction and the use of chemical reagent for chemical reduction. In this sense, it seems to be a promising protocol for large-scale production of graphene-like materials. This method is adopted in the present thesis and will be discussed in Chapter IV.

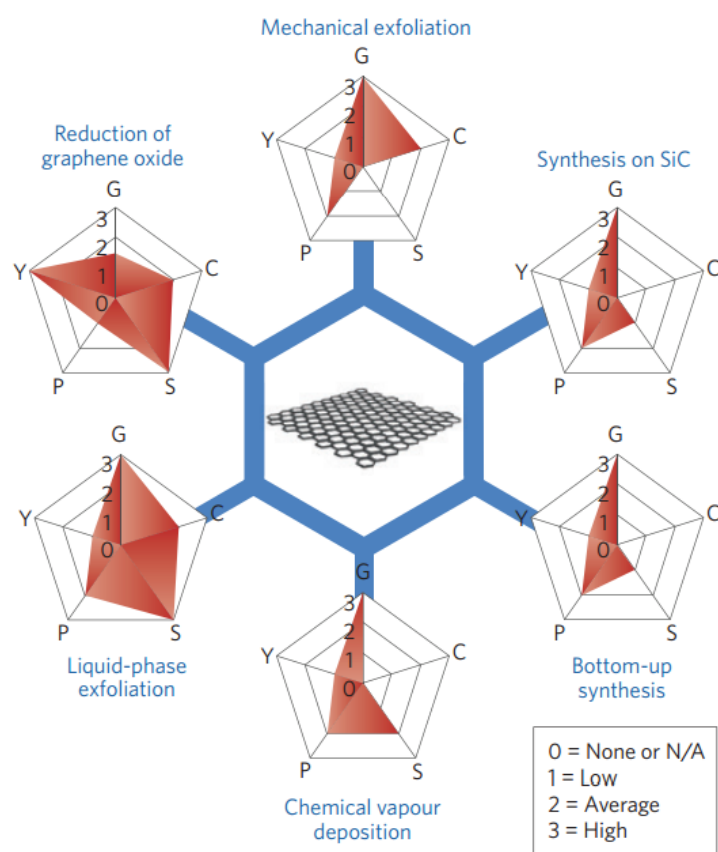
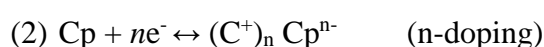
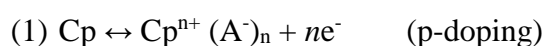


**Figure I.10.** Schematic of the most common graphene production methods. Each method has been evaluated in terms of graphene quality (G), cost aspect (C; a low value corresponds to high cost of production), scalability (S), purity (P) and yield (Y) of the overall production process<sup>112</sup>.

### I.3.2. Conducting polymers (CPs)

CPs are thought to have enticing potential in SC applications because of their high charge capacity, low cost (compared with metal oxides), environmental friendliness, high conductivity in a doped state and relatively wide potential window<sup>3, 122-123</sup>. The conductivity of CPs stems from the conjugated  $\pi$  system along the polymer backbone, which is strongly related to the doping level of counter ions during oxidation process (chemically or electrochemically) of the monomer<sup>35, 124</sup>. CPs can be either p-doped with counter anions upon oxidation or n-doped with counter cations upon reduction. These two charge/discharge processes are expressed as<sup>35</sup>:



The conductivity of these CPs can be tuned in a wide range with different dopants and the doping levels. Due to their redox behavior and superior conductivity, CPs have been readily used as SC electrode materials<sup>125</sup>. However, their poor cyclability is the major obstacle hindering the practical application of CPs in SC. It is caused by continuous swelling/shrinkage of CP-based electrode during charge/discharge process, resulting in a failure of the mechanical integrity and leading to an eventual cyclability fading. Therefore, synthesis of binary or ternary composites such as CPs/metal oxides, CPs/carbon materials and CPs/metal oxides/carbon materials was proposed in order to uprate the performance of CP-based capacitors.

The most commonly studied CPs for SC electrode materials are Polypyrrole (PPy), polyaniline (PANI), polythiophene (PTh) and their derivatives. The structures and specific properties of the three typical CPs are presented in **Figure I.11** and **Table I.4**, respectively. The specific properties of them will be discussed further in the following sections.

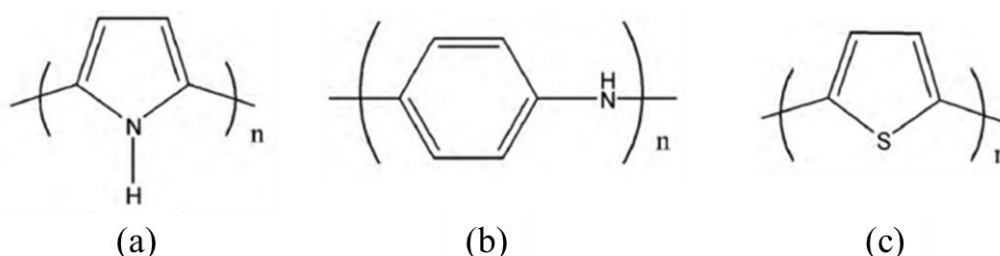


**Figure I.11.** Structures of (a) PPy, (b) PANI and (c) PTh.

**Table I.4.** Properties of different CPs with their theoretical specific capacitance ( $C_{th}$ )<sup>126</sup>

CP	$M$ (g/mol)	Doping level	Potential window (V)	$C_{th}$ (F/g)
PANI	93	0.5	0.7	750
PPy	67	0.33	0.8	620
PTh	84	0.33	0.8	485
PEDOT	142	0.33	1.2	210

$M$  signifies molecular weight per monomer unit.

### (1) Polypyrrole (PPy)

PPy has been exploited in considerable amount of researches, due to its relatively high volumetric capacitance, ease of fabrication, low cost, as well as its particularly supreme flexibility in morphology and structure<sup>127-128</sup>. Additionally, PPy can provide a higher capacitance per unit volume because of its relatively high density, which makes PPy a promising candidate for SC electrode materials used in miniature portable electronics. PPy has been known as an inherent electrically CP due to the conjugated  $\pi$ - $\pi$  system along the polymer backbone. However, undoped PPy has a low electrical conductivity of  $\sim 10^{-6}$  S  $\text{cm}^{-1}$ . It can be significantly enhanced by doping process, where an adequate amount of counter ions, from the solution are incorporated to balance the electrogenerated positive charges (polarons and bipolarons) during the oxidation process<sup>129</sup>.

PPy (as well as PANI, which will be discussed in the following section) can only be p-doped since their n-doping potentials are much lower than the reduction potential of common electrolyte solutions, and thus it has only found use as a cathode material<sup>3, 35</sup>. Single-charged anions such as dodecyl sulfate ( $\text{DS}^-$ ), perchlorate ( $\text{ClO}_4^-$ ) and  $\text{Cl}^-$  are typically used as dopants.

The electrochemical properties of PPy are highly related to the synthesis approaches, involving chemical polymerization and electrochemical polymerization. Chemical polymerization is based on the oxidation of the monomer with all kinds of chemical oxidants, whereas electrochemical polymerization stems from the electrode oxidation of monomers under the applied potential or current<sup>125</sup>. The mass and thickness of the synthesized PPy are more easily controlled in electrochemical polymerization by adjusting the input parameters (such as electrodeposition time, the value of potential and current).

A theoretical capacitance up to 620 F  $\text{g}^{-1}$  can be anticipated in PPy electrodes<sup>126</sup>. However, like

most of CPs, PPy exhibits the poor cycling stability, which fundamentally restricts their practical application as SC electrode materials. To address this limitation, CPs are generally incorporated with other nanostructured materials, such as carbon materials or metal oxides<sup>125</sup>. The introduction of these materials not only improves the charge storage capability of the PPy nanocomposites, but also significantly enhances their cycling performance. For example, CNT embedded PPy nanowires can retain 85 % of initial capacitance after 1000 cycles at  $1 \text{ Ag}^{-1}$  due to the robust support of the CNTs, which enhances the mechanical strength of the composites and prevents the PPy from swelling/shrinking during the long-term cycling<sup>130</sup>. Similarly, PPy/graphene composites can maintain 82% of the original capacitance ( $249$  of  $305 \text{ F g}^{-1}$ ) after 1000 cycles<sup>131</sup>. It is ascribed to the large elastic buffer spaces provided by the mechanically flexible graphene sheet for the swelling/shrinking of PPy. Besides, the intimate  $\pi$ - $\pi$  interaction between PPy and graphene can hinder the re-stacking of graphene layers, which played an important role in superior capacitance and improved cyclability of the electrode. It is also reported that a thin carbonaceous shell deposited onto PPy surface can significantly enhance the cycling stability of PPy electrodes<sup>27</sup>. This carbonaceous shell-coated polypyrrole electrodes achieve remarkable capacitance retentions of  $\sim 85\%$  after 10000 cycles and exhibit comparable specific capacitance and pseudocapacitive behavior as the bare PPy electrodes. It is crucial because the improved cyclability is not at the expense of the electrochemical performance of PPy electrodes.

### (2) Polyaniline (PANI)

PANI, which can be synthesized with aniline monomer via chemical or electrochemical methods, is another promising electrode material for SC due to its relatively facile synthesis, environmental stability and promising electrochemical behaviors<sup>132</sup>. However, it should be noted that proton type electrolytes are required for PANI to be properly charged and discharged, therefore, a protic solvent, an acidic solution or a protic ionic liquid is required<sup>47, 133</sup>.

The electrochemical performance of PANI is intimately related with its morphology, which relies on the synthesis strategies. A better electrochemical behavior can be expected through tuning the PANI morphology during the synthesis process. In general, chemical synthesis can provide a better flexibility for controlling the nucleation and growth during the polymerization, while electrochemical synthesis can generate the PANI directly onto different substrates<sup>132</sup>. Therefore,

chemical synthesis is preferably adopted for preparing a PANI-based nanocomposite and electrochemical counterpart presents its unique advantage for processing binder-free capacitive electrode.

PANI is often composited with other active nanomaterials (especially CNTs) for the practical development of PANI-based SCs. For example, the addition of sulfonated CNTs in PANI (76.4 wt%) exhibited a superior cycling stability, with only 5.4% loss from their initial specific capacitance ( $515.2 \text{ F g}^{-1}$ ) after 1000 cycles. It was attributed to the exceptional mechanical support of CNT and the formation of the charge-transfer complex between the PANI and CNTs<sup>134</sup>. It has also been reported that the combination of a vertically aligned CNT array framework and PANI can provide a hierarchical porous structure, large surface area, and superior conductivity for the composite electrode. This tube-covering-tube nanostructured PANI/CNT composite electrode exhibit a specific capacitance of  $1030 \text{ F g}^{-1}$  and a high stability (5.5% capacity loss after 5000 cycles)<sup>47</sup>.

### (3) Polythiophene (PTh)

PTh and its derivatives are another promising electrode materials for SCs and have raised enormous attractions owing to their flexibility, facile synthesis, favorable cyclability and environmental stability<sup>128, 135</sup>. Unlike PPy and PANI, PTh and its derivatives are both n- and p-dopable. **Table I.5** presents an example of the differences between n- and p-dopable PTh derivatives. It is found that the gravimetric specific capacitance in the n-doped form generally presents a lower value than that in the p-doped one. Additionally, the n-doped PTh-based CP exhibits inferior conductivity, which limits their use in the n-doped form as an anode material. Consequently, they are often employed as the positive electrode (p-doped) in SC with a negative electrode made from another materials such as carbon<sup>35</sup>.

It should be mentioned that poly(3,4-ethylenedioxythiophene) (PEDOT), one of the PTh derivatives has recently gained a lot of research attention. It is highly conductive ( $300\text{-}500 \text{ Scm}^{-1}$ )<sup>126</sup> and has higher potential window (see **Table I.4**). Due to its high surface area coupled with high conductivity, this polymer exhibits high charge mobility, resulting in fast electrochemical kinetics<sup>35</sup>. Additionally, it possesses superior thermal and chemical stability as well as good film-forming properties. However, its large molecular weight leads to a relatively low specific capacitance compared with other CPs (see **Table I.4**).

**Table I.5.** Specific capacitance of p- and n-dopable PTh derivatives<sup>136</sup>.

CP	p-Doping		n-Doping	
	Potential range (V vs. SCE)	Capacitance (F g <sup>-1</sup> )	Potential range (V vs. SCE)	Capacitance (F g <sup>-1</sup> )
PFPT	-0.2/1.0	95	-1.7/-1.0	80
PDTT1	-0.2/1.0	110	-1.5/-0.2	75
PMeT	-0.2/1.15	220	-2.0/-1.0	165

PFPT is poly(3-(4-fluorophenyl)thiophene), PDTT is poly(ditheno(3,4-b:3'4'-d) thiophene) and PMeT is poly(3-methyl thiophene).

### I.3.3. Transition metal oxides

Transition metal oxides have been intensively studied as electrode materials due to their fast and reversible redox reactions occurring at the electrode surface<sup>14</sup>, which can offer additional pseudocapacitances during electrochemical performance. Generally, metal oxides can offer higher energy density than conventional carbon materials and better electrochemical stability than CPs<sup>3</sup>. The metal oxides for SC electrode materials are expected to be sufficiently conductive and to present superior phase stability with intercalation/deintercalation of ions during redox reactions. To date, ruthenium oxide (RuO<sub>2</sub>), manganese dioxide (MnO<sub>2</sub>) and zinc oxide (ZnO) are amongst the most commonly studied metal oxides, which will be discussed in detail in this section.

#### (1) Ruthenium oxide (RuO<sub>2</sub>)

RuO<sub>2</sub> is widely studied because of its excellent electronic conductivity and multiple oxidation states accessible within 1.2 V. Its pseudocapacitive behavior in acidic solutions has been widely studied over the past years and can be described as a fast and reversible electron transfer coupled with an electro-adsorption of protons on the surface of RuO<sub>2</sub> particles, which can be expressed by the following equation<sup>3, 14</sup>:



In RuO<sub>2</sub> electrodes, EDL charging only contributes to ~10% of the accumulated charge, and

parallelly, the redox pseudocapacitance mechanism can occur<sup>3</sup>. Since the pseudocapacitance of RuO<sub>2</sub> originates from the surface redox reactions, where the SSA plays an important role, thus increasing the surface area of the RuO<sub>2</sub> becomes one of the most effective methods to enhance the specific capacitance of RuO<sub>2</sub>-based electrodes. **Figure I.12** offers a strategy to synthesize the high SSA SC electrode materials to increase energy and power densities<sup>14</sup>. The nano-sized RuO<sub>2</sub> pseudocapacitive active materials can be deposited onto the high SSA carbon supports, such as carbon grains and CNTs.

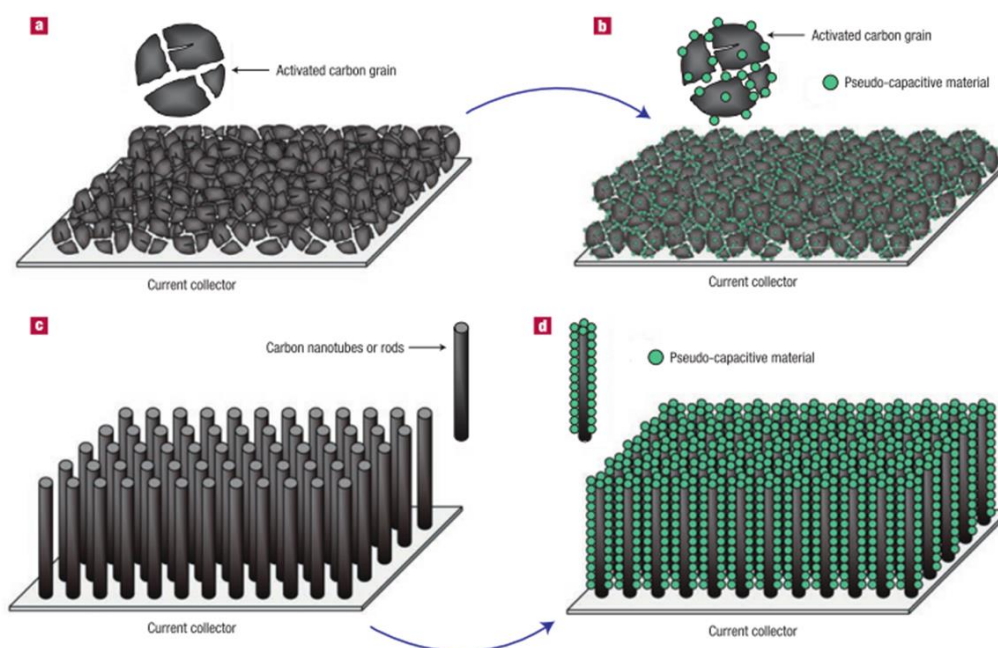


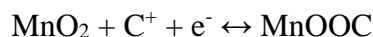
**Figure I.12.** Possible strategies to improve both energy and power densities for SCs<sup>14</sup>.

RuO<sub>2</sub> electrodes, with faradaic nature in charge storage, present an almost rectangular shape as that of EDL in cyclic voltammogram<sup>137-138</sup>. However, it is not a consequence of pure EDL charging, but of a consequence of fast, reversible successive surface redox reactions<sup>74</sup>. Although very high specific capacitance exceeding 700 F g<sup>-1</sup> was reported in hydrated RuO<sub>2</sub> electrodes<sup>26</sup>, the active material itself turned out to be too expensive and environmentally unfriendly, which greatly limits its widespread application. Therefore, other transition metal oxides such as MnO<sub>2</sub> and ZnO have been proposed as alternatives for SC electrode materials.

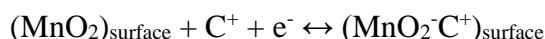
## (2) Manganese dioxide (MnO<sub>2</sub>)

MnO<sub>2</sub> has gained significant attentions as an alternative SC electrode material due to its low

cost, low toxicity, abundant resource, environmental friendliness, as well as high specific capacitance<sup>139-140</sup>. The capacitance of MnO<sub>2</sub> mainly comes from pseudocapacitance. Two charge storage mechanisms have been proposed in MnO<sub>2</sub> electrodes. The first one implies the intercalation of protons (H<sup>+</sup>) or alkali metal cations (C<sup>+</sup>) such as Na<sup>+</sup> in the electrode during reduction and their deintercalation during oxidation<sup>141-144</sup>:



The second mechanism is based on the surface adsorption of cations from electrolyte on the electrode:



It should be noted that, like RuO<sub>2</sub>, MnO<sub>2</sub> can also exhibit a rectangular cyclic voltammetry shape (typically for EDL), though it possesses a redox nature for charge storage<sup>14, 138, 145</sup>.

While MnO<sub>2</sub> is a promising material for pseudocapacitor applications, they suffer from low electrical and ionic conductivities, which are significantly related to its crystallinity and crystal structure. MnO<sub>2</sub> can crystallize into several crystallographic structures, as shown in **Figure I.13**<sup>57</sup>. High crystallinity brings about high conductivity whereas loss of surface area available for electrolyte. Contrarily, although low crystallinity leads to a highly porous microstructure of MnO<sub>2</sub>, the resulting electrical conductivity is low<sup>3</sup>. Therefore, a trade-off between electrical conductivity of MnO<sub>2</sub> and its porous structure for ionic transportation would be reached for specific purposes depending on applications.

Relatively high conductivity of MnO<sub>2</sub> can be obtained by increasing the content of crystallinity and tuning the crystal structure, but its conductivity is still poor (ranging from 10<sup>-7</sup> to 10<sup>-3</sup> S cm<sup>-1</sup> based on different crystal structures) compared with bulk single crystal of RuO<sub>2</sub> (10<sup>4</sup> S cm<sup>-1</sup>)<sup>26</sup>. Consequently, charge storage of MnO<sub>2</sub>-based electrodes confines in a very thin layer of the MnO<sub>2</sub> surface, translating into significantly lower specific capacitance values for thick MnO<sub>2</sub>-based electrodes. Nanostructuring is believed to be a highly effective method for accessing all of the MnO<sub>2</sub> storage sites<sup>26</sup>, which might be a strategy to develop the high-loading MnO<sub>2</sub> electrodes for SCs.

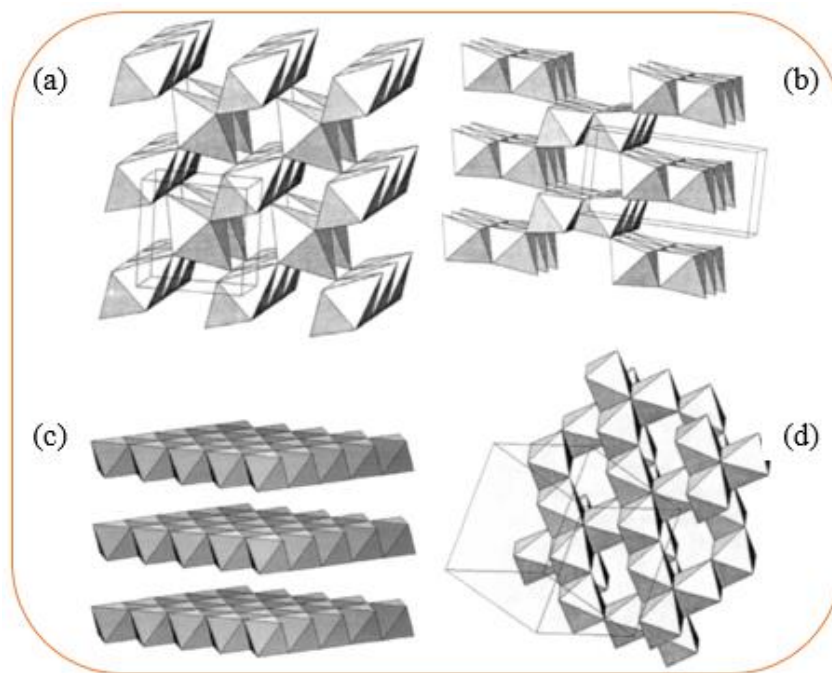


**Figure I.13.** Schematic representation of various crystal structure of  $\text{MnO}_2$ : (a) pyrolusite- $\text{MnO}_2$ , (b) ramsdellite, (c) birnessite  $\delta\text{-MnO}_2$  and (d) spinel  $\lambda\text{-MnO}_2$ <sup>57</sup>.

### (3) Zinc oxide (ZnO)

ZnO is another promising electrode material for SCs due to its low cost, natural abundance, superior electrochemical performance and environmental friendliness<sup>9, 78, 146</sup>. ZnO nanomaterials can be solely deposited on the substrate<sup>38</sup> or composited with other metal oxides<sup>147</sup>, conducting polymers<sup>148</sup> or carbon-based materials<sup>149</sup> to serve as energy storage electrodes. However, its poor electrical conductivity remains a major challenge and limits rate capability for high power performance, thus hindering its wide application in energy storage<sup>150</sup>.

Therefore, one dimensional (1D) ZnO nanostructures have been widely studied because they can provide short diffusion path for ions and efficient mechanical support for other electroactive materials. A high specific capacitance up to  $405 \text{ F g}^{-1}$  at  $10 \text{ mVs}^{-1}$  was achieved by coating a layer of  $\text{MnO}_2$  shell onto the 1D single-crystal ZnO nanorod<sup>147</sup>. Besides, The hybridization of carbon materials with ZnO offers the benefits of both the EDL capacitance of the carbon materials with large SSA and faradaic capacitance of the ZnO, thereby optimizing the electrochemical performance of the ZnO-based SCs. For example, ZnO/reduced graphene oxide/ZnO sandwich-structured composite presented a specific capacitance of  $275 \text{ F g}^{-1}$  at scan rate of  $5 \text{ mVs}^{-1}$  in  $1.0 \text{ M Na}_2\text{SO}_4$  as well as high cycling stability<sup>150</sup>. Similarly, a high specific capacitance of  $314 \text{ F g}^{-1}$  can be delivered

by decorating reduced graphene oxide with ZnO nanoparticles without obvious capacitance decay after 1000 cycles<sup>151</sup>. The electrode composed of 1D ZnO nanostructures sheltered by a thin electrochemically reduced graphene oxide (ERGO) film will be described in Chapter VI.

### I.4. Evaluation tools for SC electrode materials

Cyclic voltammetry (CV), galvanostatic charge-discharge (GCD) and electrochemical impedance spectroscopy (EIS) are the most commonly used techniques to evaluate the electrochemical properties of SCs. Additionally, a coupled electrochemical characterization method, electrical quartz crystal microbalance (EQCM) and a non-conventional method derived from EIS and QCM, the so-called *ac*-electrogravimetry, has been employed to study the electrochemical performances of SCs. Considering the mechanical properties which are also of importance for an efficient and cyclable SC electrode, a method to study the electrode's viscoelasticity, namely electroacoustic impedance has also been introduced.

#### I.4.1. Cyclic Voltammetry (CV)

CV is an effective and basic tool to identify the capacitive behavior of SC electrode materials. The experimental procedure involves potential cycling within a voltage window preselected for a given electrolyte<sup>1</sup>. Specifically, CV test applies a linear change of potential between positive and negative electrodes for two-electrode configurations, and between reference and working electrodes for three-electrode systems<sup>152</sup>. The range of potential change is designated as potential window, and the speed of the potential change is called scan rate. Generally, a plot of the current vs. potential is the output and used to evaluate the electrochemical processes of the electrode<sup>152</sup>.

In a CV experiment, the current response to an applied scan rate will vary depending on whether the electrochemical reaction is diffusion-controlled or surface-controlled (capacitive)<sup>26, 153-155</sup>. The current response stemmed from capacitive process is proportional to the scan rate, while the current limited by semi-infinite diffusion of electrolyte ions varies with the square root of the scan rate. Therefore, the instantaneous current at a certain potential can be expressed as<sup>153</sup>:

$$i(V) = k_1v + k_2v^{1/2} \quad (\text{I.6})$$

$$\text{Or } i(V)/v^{1/2} = k_1v^{1/2} + k_2 \quad (\text{I.7})$$

where  $k_{1\nu}$  is the surface-controlled current and  $k_{2\nu}^{1/2}$  is the diffusion-controlled current. The coefficients  $k_1$  and  $k_2$  can be obtained through the linear fitting of voltammetric currents at each potential. It leads to the calculation of  $k_{1\nu}$  and  $k_{2\nu}^{1/2}$ , which, therefore, allows for the separation of capacitive and diffusion currents<sup>155-157</sup>.

A CV response originated from the EDL generally exhibits a rectangular shape<sup>14</sup>, and the charging and discharging voltammograms are almost mirror images of one another. Contrarily, the pseudocapacitors usually present some redox peaks, leading to a deviation from the rectangular shape in CV curves<sup>125, 158-159</sup>. It should be noted that the fast, reversible successive surface redox reactions may also present a similar shape as that of EDL in CV<sup>14, 137-138</sup>, as shown in **Figure I.14**<sup>14</sup>. The specific capacitance can be calculated by integrating the voltammetric charges from a CV curve based on **Equation I.8**<sup>30, 160</sup>:

$$C_s = \frac{1}{2m\nu(E_2 - E_1)} \int_{E_1}^{E_2} I(E)dE \quad (\text{I.8})$$

where  $m$  is the mass loading of SC electrodes,  $\nu$  is the scan rate,  $E_1$  and  $E_2$  are the low and high end potentials, and  $I(E)$  depicts the response in current.

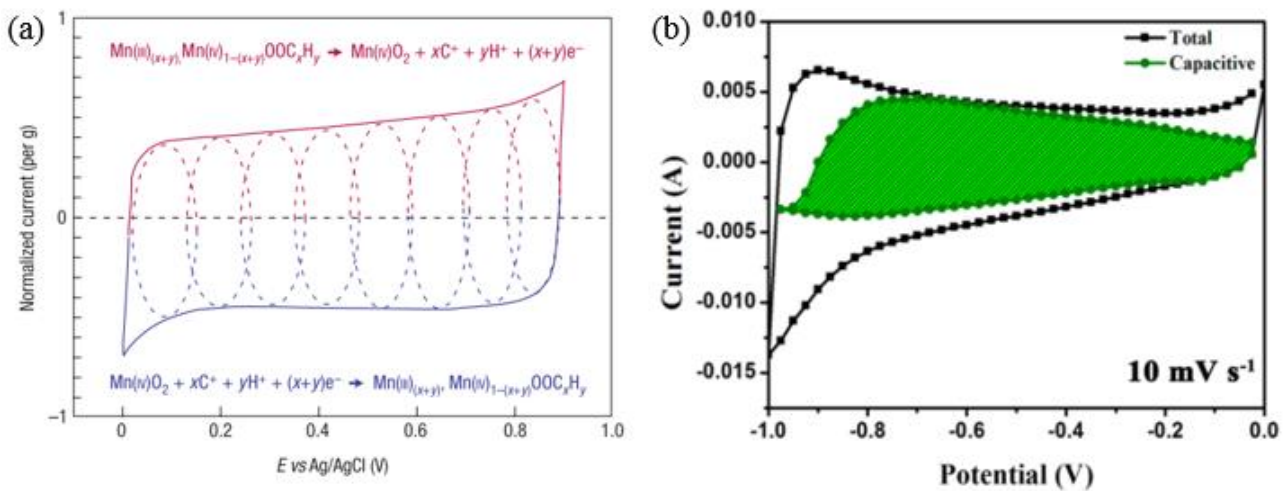


**Figure I.14.** (a) Schematic of CV for a MnO<sub>2</sub> electrode cell in mild aqueous electrolyte (0.1 M K<sub>2</sub>SO<sub>4</sub>) shows the successive multiple surface redox reactions leading to the pseudocapacitive charge storage mechanism<sup>14</sup>. (b) CV of Fe<sub>2</sub>O<sub>3</sub>/nitrogen-doped graphene composite tested in 2 M KOH solution at 10 mV s<sup>-1</sup>, and the shadowed areas represent the capacitive contribution<sup>155</sup>.

### I.4.2. Galvanostatic Charge-Discharge (GCD)

GCD is another widely used technique to characterize the electrochemical performance of SCs under a constant current density<sup>161</sup>. A consecutive charging/discharging of the working electrode is performed at a constant current density with or without a dwelling period (a time period between charging and discharging while the peak voltage  $V_0$  remains constant). A linear response of potential (in V) with respect to charge/discharge time (in s) is anticipated for EDLC, whereas the non-linearity of charge/discharge curves is normally obtained from the pseudocapacitors, which is distinct from the triangular shape from EDLC response<sup>117</sup>, as shown in **Figure I.15**<sup>162</sup>. Generally a plot of the potential ( $E$ ) vs. time ( $t$ ) is the output. Choosing a proper level of the applied constant current is critical to produce consistent and comparable data from a GCD test.

GCD test is regarded as the most versatile and accurate approach in characterizing SC devices. All three core parameters of SC devices, cell (total) capacitance  $C_T$ , operating voltage  $V_0$ , and equivalent series resistance  $R_s$ , can be obtained through this methodology and subsequently used to derive most of the other properties, such as power and energy densities, and leakage and peak current<sup>152</sup>. GCD can also be used to test the cycling performance of SCs. Furthermore, the specific capacitance ( $C_s$ ) can be calculated *via* GCD using the following equation:

$$C_s = \frac{I\Delta t}{m\Delta V} \quad (\text{I.9})$$

where  $I$  is the applied current,  $\Delta t$  is the discharge time,  $m$  is the mass loading of SC electrodes and  $\Delta V$  is the potential drop during discharge<sup>64, 113, 162</sup>.

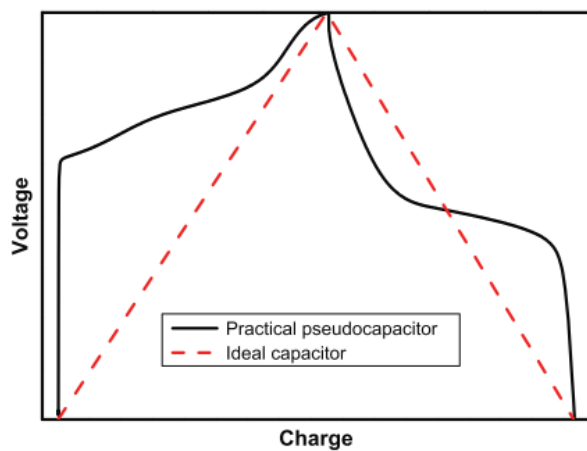


**Figure I.15.** Schematic galvanostatic charge/discharge response of supercapacitor devices: pseudocapacitor and ideal EDLC<sup>162</sup>.

### I.4.3. Electrochemical Impedance Spectroscopy (EIS)

EIS is a powerful diagnostic tool that not only enables the equivalent series resistance and potential-dependent faradaic resistance of the device to be separately evaluated, but also allows the calculation of capacitance of the electrode<sup>1, 68</sup>. More generally, the mechanism of different electrochemical reactions can be discovered by the EIS approach when an appropriate model is used. It is conducted by applying a sinusoidal potential perturbation with a small amplitude (typically 10-20 mV) over a range of frequencies, which must not cause the system to shift from its equilibrium state<sup>1, 68</sup>. The impedance ( $Z$ ) is defined as  $Z = Z' + jZ''$ , where  $Z'$  and  $Z''$  are the real and imaginary part, respectively. The resulting data are usually expressed graphically either in a Bode plot to visualize the dependence of both the absolute value of impedance and phase angle on the frequency, or in a Nyquist plot to show the imaginary and real parts of the electrochemical impedance on a complex plane<sup>66, 163</sup>.

EIS has been widely used to characterize the electrochemical properties of SC electrodes. As presented in **Figure I.16a** and **b**, it is performed to evaluate the effect of carbonaceous coating on the interfacial charge transfer in PANI and PPy nanowires covered by a thin layer of carbonaceous shell of ~5 nm (i.e., PANI@C and PPy@C electrodes)<sup>27</sup>. The  $R_s$  of PANI@C and PPy@C electrodes are higher than the bare polymer electrodes owing to the presence of additional contact resistance between carbonaceous shell and polymer core. Besides, the EIS study of 2D  $Ti_3C_2Tx$  (MXene), a promising material in electrochemical energy storage applications, has also been reported<sup>164</sup>. **Figure I.16c** shows a comparable spectra in the low-frequency domains of the  $Ti_3C_2Tx$  electrode measured in 1 M LiCl and MgCl<sub>2</sub> solutions at -0.2 V vs. Ag/AgCl. However, the high-frequency domain of the electrode spectra in MgCl<sub>2</sub> solution exhibits a depressed semicircle, which is absent in the impedance spectrum measured in LiCl (inset in **Figure I.16c**). This semicircle is believed to stem from the ion transfer across the electrode/electrolyte interface and the Mg<sup>2+</sup> transfer is much slower than the transfer of singly charged Li<sup>+</sup>. Furthermore, the effect of cycling on the capacitive behavior of the electrode is investigated in MgCl<sub>2</sub> solution (**Figure I.16d**), demonstrating that an aging process (100 cycles at a rate of 1 mV s<sup>-1</sup>) can result in a further retardation of the interfacial Mg<sup>2+</sup> ion transfer in the high-frequency domain (inset in **Figure I.16d**).

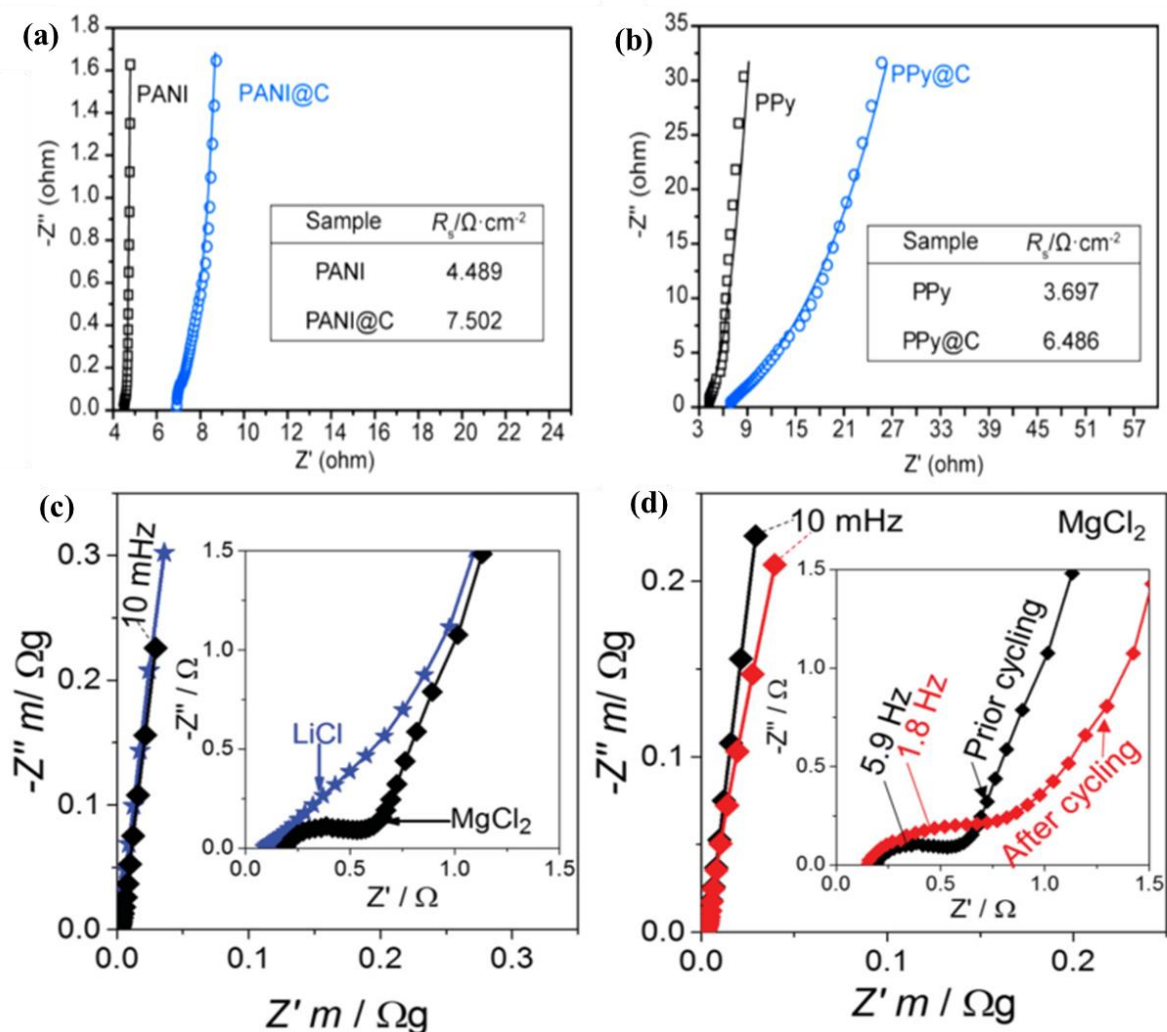


**Figure I.16.** (a, b) Nyquist plots of polymer and carbonaceous shell-coated polymer electrodes measured in 1 M H<sub>2</sub>SO<sub>4</sub> at open circuit potential. Insets show the  $R_s$  values of the electrodes<sup>27</sup>; (c, d) impedance spectra of Ti<sub>3</sub>C<sub>2</sub>T<sub>x</sub> electrode (inset presents enlarged view of high-frequency domain)<sup>164</sup>.

#### I.4.4. Electrical Quartz crystal microbalance (EQCM)

EQCM is based on quartz crystal microbalance (QCM) technology. The QCM comprises a thin piezoelectric quartz crystal sandwiched between two metal electrodes, where an alternating electric field across the crystal is established and causes thickness-shear vibrations of the crystal around its resonant frequency<sup>165-167</sup>. The signal transduction mechanism of the QCM originates from the piezoelectric property of the quartz crystal, which was first discovered in 1880 by Curie brothers<sup>168</sup>. They discovered that the application of a mechanical stress to the surfaces of various crystals, including quartz, rochelle salt (NaKC<sub>4</sub>O<sub>6</sub>·4H<sub>2</sub>O) and tourmaline, produced a corresponding electrical potential across the crystal whose magnitude was proportional to the applied stress. The

name “piezoelectricity” was proposed by Hankel after one year.

Shortly after their initial discovery, the Curie brothers experimentally verified the reverse piezoelectric effect by which the application of an electric field across the crystal afforded a corresponding mechanical strain. As shown in **Figure I.17**<sup>165</sup>, the shear strain is induced through the reorientation of the dipoles in a piezoelectric material by an applied potential. Additionally, the motion of the material is proportional to the applied potential. It should be noted that the reverse piezoelectric effect is the basis of the QCM. The application of an alternating electric field across a quartz crystal produces a vibrational (or oscillatory) motion in the quartz crystal parallel to the surface of the crystal. It leads to the establishment of a transverse acoustic wave that propagates across the crystal thickness ( $d_q$ ). An acoustic standing wave can be formed when the acoustic wave length  $\lambda=2 d_q$ <sup>165</sup>. The quartz oscillator vibrates with minimal energy dissipated at a characteristic resonant frequency, therefore it is deemed as an nearly ideal oscillator<sup>169</sup>.

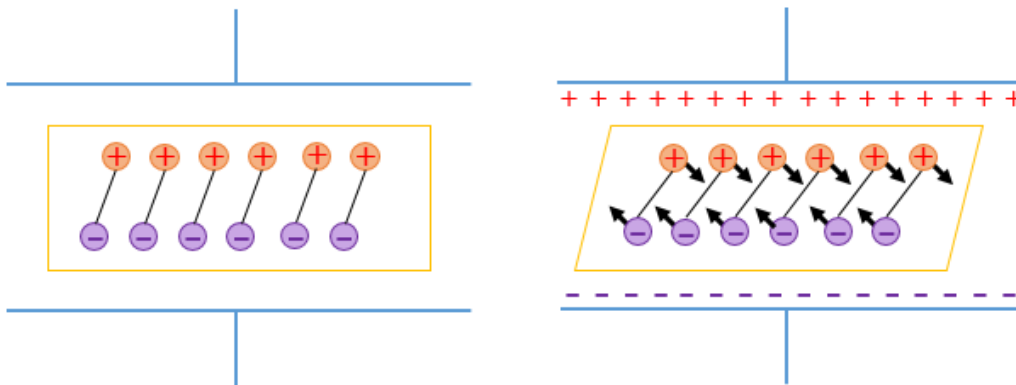


**Figure I.17.** Schematic representation of the converse piezoelectric effect for shear motion. The electric field induces reorientation of the dipoles of the acentric material, resulting in a lattice strain and shear deformation of the material. Direction of shear is dependent upon the applied potential while the extent of shear strain depends on the magnitude of the applied potential<sup>165</sup>.

The nodes of the acoustic wave are positioned in the quartz interior (in the center of the quartz crystal at the fundamental frequency, i.e., at the overtone order,  $n = 1$ ), while the antinodes are located on both surfaces. Correspondingly, when a material is deposited on the surface of the quartz, the acoustic wave will span the quartz/film interface and propagate through the deposited film (**Figure I.18a**). It is implicitly assumed that a continuous displacement (or shear stress) exists across the quartz/film interface, which is referred to as the “no-slip” condition<sup>165</sup>. In other words,

the deposited film could be regarded as an extension the quartz. The film-deposited quartz crystal performs as a composite resonator<sup>165, 170</sup>. It, in turn, can be affected by the electrolyte solution in which it is immersed<sup>170-171</sup>. The thickness increase of this composite resonator due to the deposited film is equivalent to the increase of the wavelength ( $\lambda=2 d_q$ ) and results in a decrease of the quartz fundamental frequency<sup>169</sup>. The composite resonator performs in such a situation that can be modeled by an equivalent electrical circuit, of which the most commonly used is the Butterworth-Van-Dyke (BVD) model (**Figure I.18b**)<sup>170</sup>. This will be discussed later in the description of the electroacoustic impedance measurements (**Section 1.4.6**).

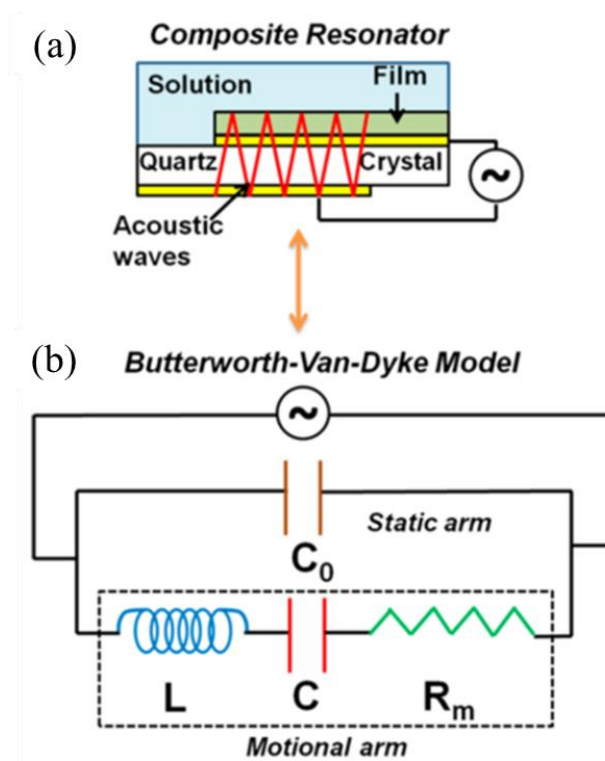


**Figure I.18.** (a) An oscillating mass-loaded quartz crystal immersed in a liquid medium acting as a composite resonator. (b) The corresponding equivalent electrical circuit as per the Butterworth-Van-Dyke Model<sup>170</sup>.

In 1957, Sauerbrey reported a description of the linear relationship between the mass deposited on the quartz surface and the microbalance frequency shift<sup>172</sup>, which can be expressed by **Equation I.10**<sup>165</sup>.

$$\Delta f = \frac{-2f_0^2}{A(\mu_q \rho_q)^{1/2}} \Delta m \quad (\text{I.10})$$

where  $\Delta f$  denotes the measured frequency shift,  $f_0$  is the frequency of the quartz in air prior to the film deposited,  $\Delta m$  is the corresponding mass change,  $A$  is the piezoelectrically active area,  $\mu_q$  is the shear modulus and  $\rho_q$  is the quartz density. When a QCM is used in conjunction with electrochemical measurements, such as CV and GCD, it is frequently referred to as electrochemical quartz crystal microbalance (EQCM).

EQCM has developed into a powerful in situ technique to measure ionic fluxes in different electrochemical systems<sup>167, 173-174</sup>, such as conducting polymers, carbon materials and metal oxides. Here, not only the current response but also the simultaneous mass variation of the electrode is tracked during an electrochemical process.

For example, a mass increase/decrease upon reduction/oxidation was observed in PPy film by EQCM, which is presumably due to the insertion/expulsion of cations (**Figure I.19a**)<sup>175</sup>. Moreover, the mass response, translated from EQCM frequency shift, can separate the ionic fluxes in some basic case for carbon electrode due to adsorption of cations on the negatively charged surface ( $Q < 0$ ) and anions on the positively charged surface ( $Q > 0$ ) (**Figure I.19b**)<sup>176</sup>. Furthermore, EQCM has also been used to study the relationship between the pore sizes of the electrode and ion sizes in the electrolyte. The different ion adsorption behaviors of two carbide-derived carbons with average pore sizes of 1 nm (CDC-1 nm) and 0.65 nm (CDC-0.65 nm) in neat and solvated 1-Ethyl-3-methylimidazolium bis(trifluoromethane-sulfonyl)imide (EMI-TFSI) (2 M EMI-TFSI in acetonitrile) electrolytes have been reported. **Figure I.19c**<sup>167</sup> describes an example for CDC-1 nm electrode, whose pore size is larger than ion size (0.76 and 0.79 nm for the  $\text{EMI}^+$  cation and  $\text{TFSI}^-$  anion). Both (solvated)cations and anions are able to participate in charge balance mainly depending on the potential of zero charge, i.e., cations at  $Q < 0$  and anions at  $Q > 0$ . However, for CDC-0.65 nm electrode, whose pore size is smaller than ion size, no mass change is detected in neat EMI-TFSI electrolyte, and only solvated cation ( $\text{EMI}^+$  hydrated with 1.6 acetonitrile (AN) molecule averagely, i.e.,  $\text{EMI}^+ + 1.6 \text{ AN}$ ) response is observed in solvated electrolyte (2 M EMI-TFSI/AN) when the CDC-0.65 nm electrode is negatively charged. Additionally, the electrochemical behavior of a transition metal oxide,  $\text{MnO}_2$ , has been characterized in 0.5 M  $\text{LiClO}_4$  and  $\text{NaClO}_4$  electrolytes. The current response and the simultaneous mass change are obtained by EQCM measurements (**Figure I.19d**)<sup>177</sup>, from which the mass per mole of electrons (MPE) exchanged between the electrode and the electrolyte can be estimated according to  $MPE = F \Delta m / \Delta q$ .

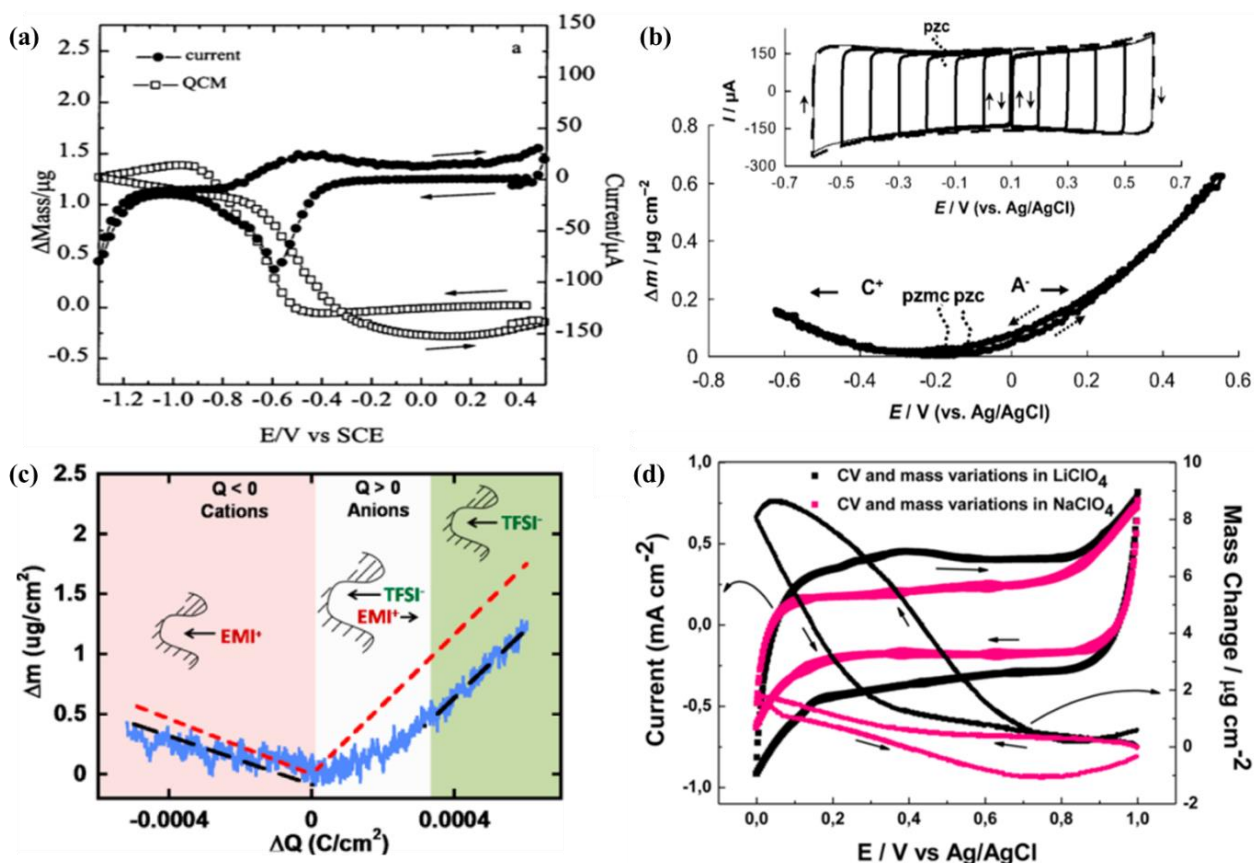


**Figure I.19.** EQCM measurements for a polypyrrole film in 0.1 M  $\text{Na}_2\text{SO}_4$  (a),<sup>175</sup> a carbon electrode in a 0.5 M  $\text{NH}_4\text{Cl}$  aqueous solution at a scan rate of  $20 \text{ mVs}^{-1}$  (b),<sup>176</sup> a carbide-derived carbon with average pore size of 1 nm in neat 1-Ethyl-3-methylimidazolium bis(trifluoromethane-sulfonyl)imide (EMI-TFSI) electrolyte<sup>167</sup> (c) and a film of Li-birnessite type  $\text{MnO}_2$  in 0.5 M  $\text{LiClO}_4$  and 0.5 M  $\text{NaClO}_4$  at a scan rate of  $25 \text{ mVs}^{-1}$  (d).<sup>177</sup>

As discussed above, classical EQCM response allows for insights into the ionic flux exchanged between the electrode and the electrolyte. But it remains challenging for the deconvolution of the global electrogravimetric response into gravimetric and temporal components since the measurements are limited to scan rates or current densities. To overcome these limitations, the *ac*-electrogravimetry is suggested as a complementary tool to the EQCM, where the different scenarios of the charge compensation process in different electrodes can be scrutinized.

#### I.4.5. *Ac*-electrogravimetry

*Ac*-electrogravimetry is based on a QCM used in dynamic regime and coupled with electrochemical impedance spectroscopy, which was proposed in 1988 by Gabrielli<sup>178</sup>. When a

uniform thin layer of a foreign material is added to the surface of the quartz crystal resonator, it can be used as the working electrode (WE) following a classical electrochemical configuration<sup>179</sup>. When a sinusoidal potential perturbation is applied to an electroactive film, it induces concentration variation of the species which results from the species transfer for charge compensation purposes. These concentration or mass variations of species can be tracked thanks to the frequency variation of a specific QCM used under dynamic regime, i.e., under frequency potential modulation of the WE. Through this method, the species transferred, if they intervene with different kinetics in an electrochemical process, can be separated and a clear identification of the species with their molar mass can be achieved<sup>175, 177, 180-184</sup>.

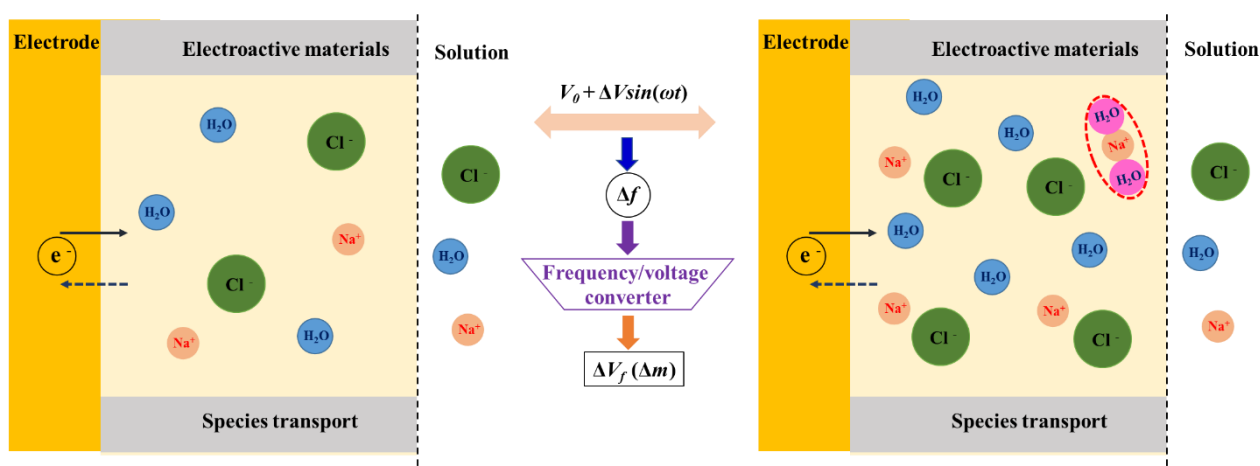


**Figure I.20.** The working mechanism of *ac*-electrogravimetry.

The working mechanism of this technology is schematically described in **Figure I.20**. The QCM working electrode is firstly polarized at  $V_0$  by a potentiostat. Species exchange (not only ionic but also non-charged species like free solvent) occurs at the film/electrolyte interface upon a sinusoidal small amplitude potential perturbation,  $\Delta V \sin(\omega t)$ , superimposed on the stationary potential,  $V_0$ . It can lead to a mass change of the electrode, reflected by a frequency variation of the QCM,  $\Delta f$ . Then the frequency response is translated into a voltage change ( $\Delta V_f$ ) by frequency/voltage converter which is sent to a four-channel Frequency Response Analyzer (FRA), which cannot directly analyze the frequency response. Briefly, the response of the quartz electrode modified with a thin electroactive film to this sinusoidal small amplitude potential perturbation ( $\Delta V$ ) is the current ( $\Delta I$ ) and the mass response (in the form of  $\Delta V_f$ ). Then, thanks to a four-channel FRA,

the following transfer functions ( $\Delta V/\Delta I$ ) and the ( $\Delta V_f/\Delta V$ ) are obtained which are converted to the classical impedance ( $\Delta E/\Delta I$ ) and electrogravimetric or mass/potential ( $\Delta m/\Delta V$ ) transfer function with a mathematical treatment (description of the *ac*-electrogravimetry and the theoretical background will be given in Chapter II).

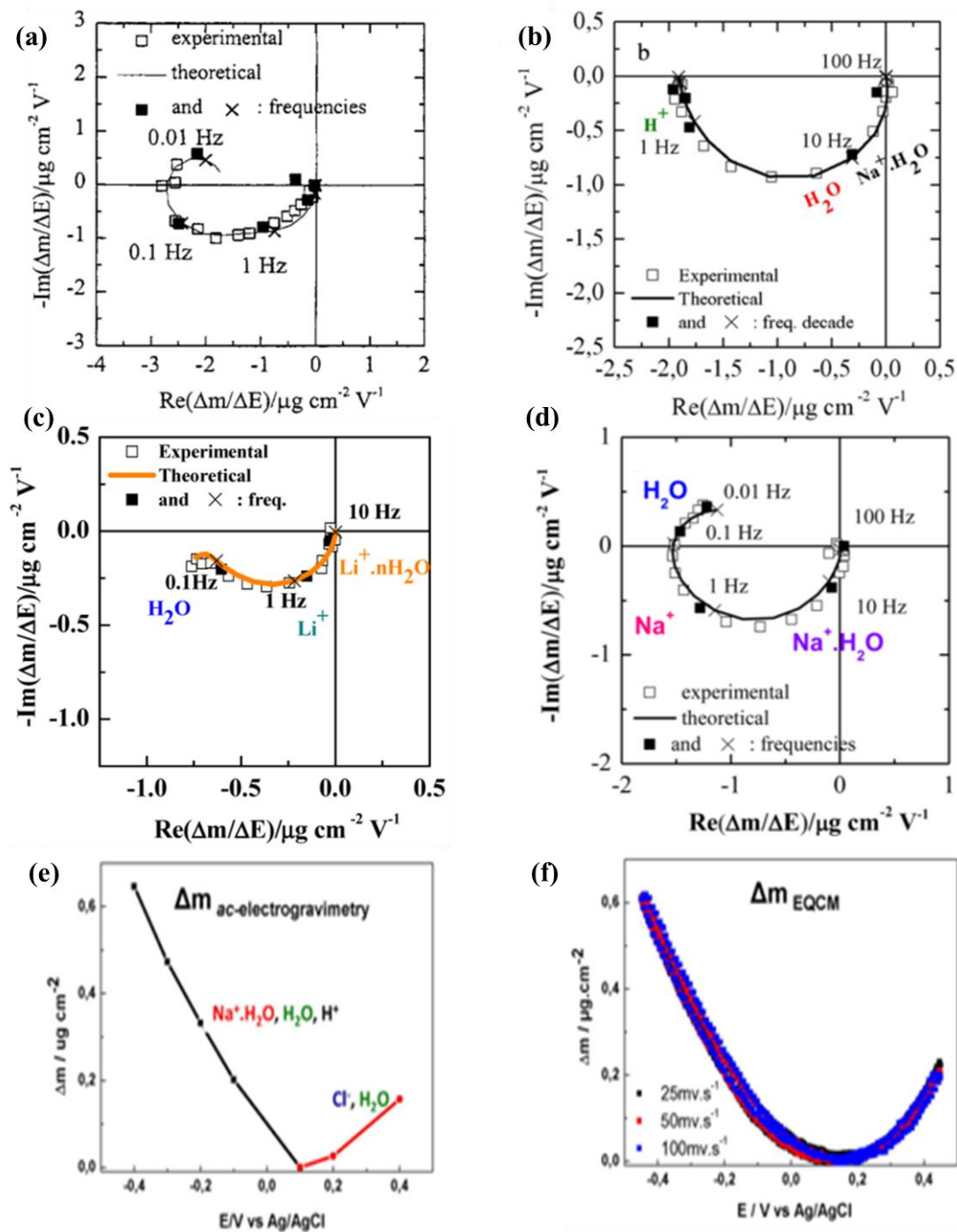


**Figure I.21.** Electrogravimetric TFs for a polypyrrole film in 0.25 M NaCl at -0.55 V vs. SCE (a),<sup>182</sup> a CNT film in 0.5 M NaCl (pH=7) at -0.4 V vs. Ag/AgCl (b),<sup>185</sup> an ERGO film in 0.5 M LiCl

at -0.5 V vs. Ag/AgCl (c)<sup>186</sup> and a film of Li-birnessite type MnO<sub>2</sub> in 0.5 M NaClO<sub>4</sub> at 0.6 V vs. Ag/AgCl (d).<sup>177</sup> (e) and (f) compare the mass variation reconstructed from *ac*-electrogravimetry and obtained from EQCM.<sup>185</sup>

This technique has already been fruitful in differentiating the species contributions in various capacitive and faradaic processes of conducting polymers,<sup>181-182</sup> carbon materials<sup>185-186</sup> and transitional metal oxides.<sup>177</sup> For example, three species with different transfer kinetics are identified in the charge balance of PPy film in 0.25 M NaCl at -0.55 V vs. SCE by *ac*-electrogravimetric measurements, i.e., Na<sup>+</sup> hydrated with two water molecules (Na<sup>+</sup>·2H<sub>2</sub>O), free water molecules and Cl<sup>-</sup> (**Figure I.21a**). The usage of *ac*-electrogravimetry in CNT-based electrode (**Figure I.21b**) reveals that two cations (Na<sup>+</sup>·H<sub>2</sub>O and H<sup>+</sup>) and free water molecules participate in the electroadsorption process when a CNT film is polarized at -0.4 V vs. Ag/AgCl in 0.5 M NaCl (pH=7). **Figure I.21c** shows that hydrated cations (Li<sup>+</sup>·nH<sub>2</sub>O) present a higher transfer kinetics in charge compensation process of ERGO-based electrode than its counterpart (Li<sup>+</sup>) in 0.5 M LiCl at -0.5 V vs. Ag/AgCl. Similar phenomena are observed in a film of Li-birnessite type MnO<sub>2</sub> (**Figure I.21d**), where Na<sup>+</sup>·H<sub>2</sub>O exhibits a higher transfer kinetics than Na<sup>+</sup>. Notably, free water molecules have the same and opposite flux direction with the cationic species in **Figure I.21c** and **d**, respectively. Altogether, *ac*-electrogravimetry contributes to disentangle the subtleties of global charge compensation process involving multiple species, offering a quantitative picture of each participant with their transfer kinetics and identifying them by their molar masses. Besides, it can provide complementary information for EQCM results (**Figure I.21e** and **f**). The complementarity between EQCM and *ac*-electrogravimetry is highly anticipated, limitations of either of which can be compensated by the other to unveil the intricacy of the charge storage mechanisms<sup>185</sup>.

### I.4.6. Electroacoustic measurements

Besides superior electrochemical properties, long-term cycling performances are also of importance for an efficient SC electrode. Upon cycling, periodical ion electroadsorption/electrodesorption and/or insertion/extraction are possibly accompanied with solvent flux which lead to repeated species-transfer-induced deformation as well as viscoelastic changes of the SC electrode. Such viscoelastic changes which are not completely relaxed at the end

of each cycle and tend to gradually accumulate, thereby result in a failure of the mechanical integrity and lead to an eventual cyclability fading. Nevertheless, of practical and fundamental importance but scarcely touched is the correlation between electrode viscoelasticity and its electrochemical performance<sup>164, 187-188</sup>. Electroacoustic impedance technique has been used to estimate the two important parameters for describing the viscoelasticity of the SC electrode, i.e., the storage ( $G'$ ) and loss moduli ( $G''$ )<sup>180, 189-190</sup>.  $G'$  represents the electrode stiffness whereas  $G''$  reflects its viscosity. Here, two models are discussed, BVD (Butterworth-Van Dyke) model and viscoelastic model. BVD model is used for sufficiently thin and rigid film, whereas viscoelastic model for non-rigid or thick films<sup>191-193</sup>.

### (1) BVD (Butterworth-Van Dyke) model

The BVD circuit consists of two parallel branches, as illustrated in **Figure I.22**.  $C_0$  in the static arm refers to the static capacitance of the quartz crystal, which is parallel with a series branch, known as the motional arm. The motional arm consists of an inductance ( $L_1$ ), a capacitance ( $C_1$ ) and a resistance ( $R_1$ ).  $L_1$  is the inertial component related to the displaced mass,  $C_1$  is the compliance of the quartz element presenting the elasticity of the composite resonator and  $R_1$  denotes the energy dissipation during oscillation because of internal friction, mechanical losses in the mounting system as well as acoustical losses to the environment<sup>165</sup>. The relationship between the components of the motional arm and the mechanical properties of the quartz resonator is established. An increase in  $L_1$  and  $R_1$  will result in the corresponding increase in mass loading and dissipated energy, while an increase in  $C_1$  will lead to a decrease in rigidity<sup>165, 170, 194</sup>. The use of the BVD circuit to model the composite resonator is limited to the thin rigid film deposited on the quartz, where the QCM response can be regarded solely from gravimetric contributions. The electromechanical characteristics of the quartz resonators can be reflected by BVD model.

When the surface of the quartz resonator is loaded with some foreign materials, the surface loading can modify the electrical impedance of the unperturbed quartz resonator, which can be expressed by adding an inductance  $L_2$  and a resistance  $R_2$  in the BVD circuit.  $L_2$  Represents the inertial mass of the film and liquid coupled upon oscillation, whereas  $R_2$  represents the energy dissipation in the form of viscoelastic and damping effects of the film and liquid overlayer<sup>194</sup>. The Sauerbrey equation can be directly used to interpret the relationship between frequency shift of the

quartz resonator and loading mass under the condition that the acoustic deformation across the film can be neglected, i.e.,  $R_2$  is  $\sim 0$ <sup>193</sup>.

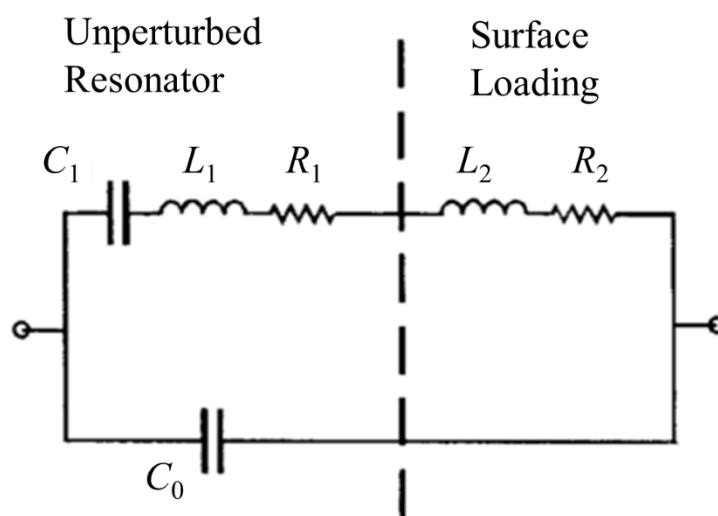


**Figure I.22.** BVD equivalent circuit model for a QCM resonator with a surface loading. The surface loading is resolved into motional inductance  $L_2$  and resistance  $R_2$ <sup>194</sup>.

## (2) Viscoelastic model

It is worth noting that the QCM measures frequency changes instead of mass changes. The interpretation of frequency changes is performed according to the Sauerbrey equation. Therefore, an ideally rigid behavior of deposited film is assumed to meet the criterion of Sauerbrey equation. However, in some cases, the quartz is loaded with non-rigid materials, like polymers, which possess an obvious viscoelastic behaviors and thus, cause a lack of conformance with the Sauerbrey equation. The rheology of these materials should be well defined, because their QCM response is due to both gravimetric and viscoelastic contributions. The latter should be removed in order to get access to the pure gravimetric response. When a viscoelastic film is deposited on the quartz resonator surface (**Figure I.23**)<sup>192</sup>, the shear displacement launched at the inner film/quartz interface propagates across the film, reflecting back into the film at the outer film surface<sup>193</sup>. The breakdown of the BVD approximation with thick films occurs because of the unsynchronized movement of the upper film surface and lower film surface<sup>191</sup>. As shown in **Figure I.24**, for thin and stiff films, a linear Sauerbrey approximation establishes; additionally, the stiffer the film, the higher mass loading it requires to induce deviation from the linear Sauerbrey approximation<sup>191</sup>. It should be

mentioned that, besides viscoelastic effects, other factors, such as high mass loadings, surface roughness, surface stress, interfacial slippage can also cause the failure of Sauerbrey equation<sup>165</sup>.

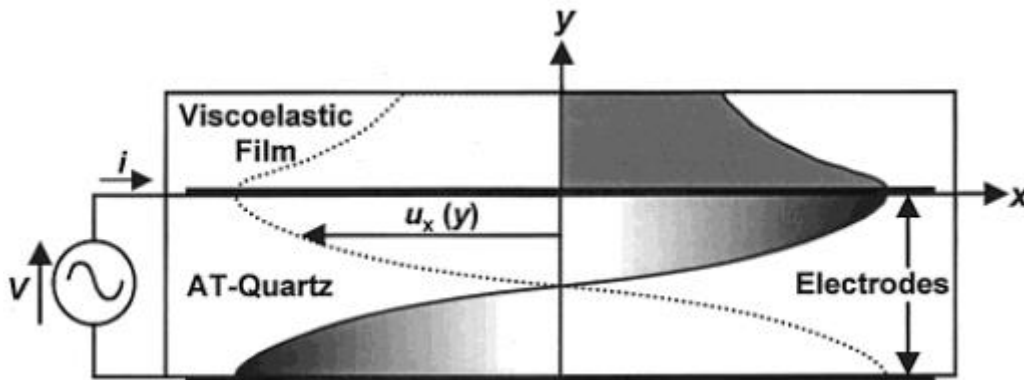


**Figure I.23.** Cross-sectional view of a quartz resonator with a viscoelastic film coating the upper surface. The thickness of the film is exaggerated relative to that of the quartz. The potential,  $V$ , creates the shear deformation in the crystal<sup>192</sup>.

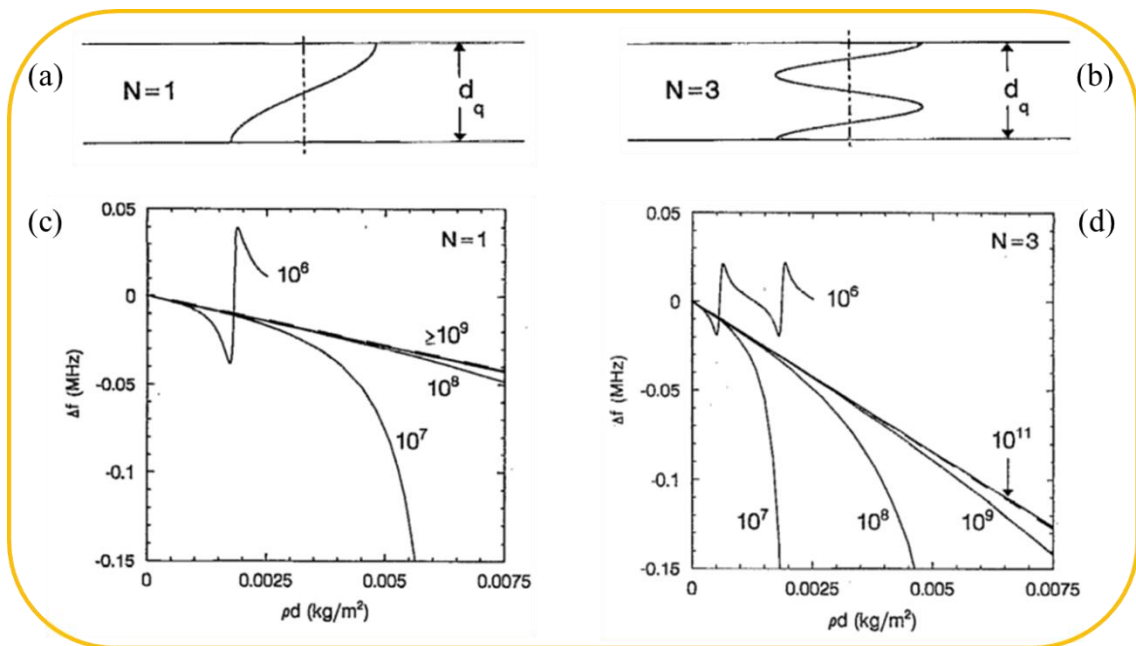


**Figure I.24.** Side cross-sectional view of AT-cut quartz wafer, showing shear displacement profiles for the fundamental (a) and third-harmonic resonances (b). Calculated effect of polymer stiffness for lossless polymers in contact with water at fundamental quartz resonance (c) and third-harmonic quartz resonance (d)<sup>191</sup>.

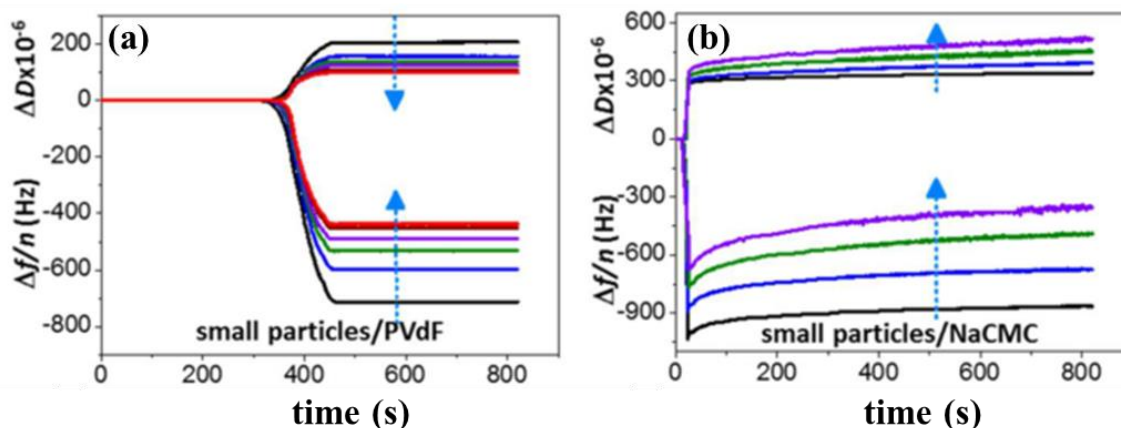


**Figure I.25.** EQCM-D data for composite LFP electrodes with PVdF (a) or NaCMC (b) containing small LFP particles. Dashed arrows show the direction of increasing  $n$ <sup>195</sup>.

Besides, multiharmonic EQCM with dissipation monitoring (EQCM-D) has also been used not only for the electrode structure characterization<sup>174, 196</sup> but also for the investigation of gravimetric and viscoelastic changes of electrodes during charge storage process. It has two output characteristics, i.e., resonant frequency normalized by overtone order ( $f/n$ ) and dissipation factor ( $D$ ), defined as the ratio between the full resonance peak width and the resonance frequency,  $(W/n)/(f/n)$ <sup>195, 197-198</sup>. The raw experimental EQCM-D data collected for the electrodes are fitted by different models depending on the composition of the electrodes in order to retrieve the geometric and mechanical structural characteristics of the probed electrodes. An example of EQCM-D responses for composite  $\text{LiFePO}_4$  (LFP) electrodes ( LFP/PVdF and LFP/NaCMC, with a mass ratio of 90:10) is presented in **Figure I.25**<sup>195</sup>. It shows for the stiff PVdF-containing composite electrode the values of  $\Delta f/n$  and  $\Delta D$  are independent of the time after immersion of the PVdF-containing composite electrode into 0.1 M  $\text{Li}_2\text{SO}_4$  solution. Contrarily, the soft NaCMC-based electrode reveals the  $n$ -dependent changes of  $\Delta f/n$  and  $\Delta D$  with time, which is typical for a progressing material softening.

## I.5. Objectives and outline of the thesis

The primary objectives of the present thesis are to explore the species transfer in the charge storage mechanisms of commonly used supercapacitor electrode materials, i.e., conducting polymers, carbon materials and transitional metal oxides. Additionally, the viscoelastic evolutions

of some specific electrodes are also studied in order to shed light on the correlation between electrochemical and viscoelastic evolutions.

In the present thesis, dodecyl sulfate-doped polypyrrole (PPy-DS) film, electrochemically reduced graphene oxide (ERGO) film and ZnO nanostructures are synthesized as the representative of conducting polymer-, carbon- and metal oxide-based electrode, respectively. To achieve the research goal mentioned above, a combined methodology involving electrochemical quartz-crystal microbalance (EQCM), *ac*-electrogravimetry and electroacoustic impedance measurements is adopted. Specifically, EQCM is used for an in situ capturing of the global transfer of the species at the electrode/electrolyte interface, whereas its complementary counterpart *ac*-electrogravimetry contributes to disentangle the subtleties of global charge compensation process involving multiple species, offering a quantitative picture of each participant with their transfer kinetics and identifying them by their molar masses. Therefore, coupling EQCM with *ac*-electrogravimetry provides a strategy to unveil the charge storage mechanism of the electrode during electrochemical process. Furthermore, its corresponding viscoelastic evolution can be tracked through the electroacoustic impedance measurements. By and large, the usage of this combined methodology may pave the way to understand the charge storage mechanism and the relationship between electrode's electrochemical and mechanical properties, facilitating the fabrication of highly efficient SC electrodes with superior cyclability.

As for conducting polymer-based electrodes, the most critical challenge is the cycling stability. Accordingly, after introducing the general experimental methods in Chapter II, Chapter III describes the correlation between electrochemical and viscoelastic variations of PPy-DS film during cycling. The ionic transfer and viscoelastic properties of PPy-DS film will be investigated after it is progressively cycled. The ion adsorption behavior and viscoelastic changes of ERGO with different content of the oxygen functionalities on its layers are presented in Chapter IV, where (i) the influence of the oxygen functionality contents on the ionic response will be investigated and (ii) the viscoelastic effect of the deposited loading on the QCM will be explored for the validity of Sauerbrey equation. The interfacial charge transfer behaviors of ZnO and its composite ZnO/ERGO are tracked in Chapter V and VI. The complementarity between EQCM and *ac*-electrogravimetry is highlighted in these two chapters. Last but not the least, the general conclusion of this thesis is presented in Chapter VII.

### References

1. Conway, B. E., *Electrochemical Supercapacitors: Scientific Fundamentals and Technological Applications* Kluwer Academic/Plenum, New York **1999**.
2. Miller, J. R.; Simon, P., Electrochemical capacitors for energy management. *Science* **2008**, *321* (5889), 651-652.
3. Wang, G.; Zhang, L.; Zhang, J., A review of electrode materials for electrochemical supercapacitors. *Chem. Soc. Rev.* **2012**, *41* (2), 797-828.
4. Pandolfo, A. G.; Hollenkamp, A. F., Carbon properties and their role in supercapacitors. *J. Power Sources* **2006**, *157* (1), 11-27.
5. Béguin, F.; Presser, V.; Balducci, A.; Frackowiak, E., Carbons and electrolytes for advanced supercapacitors. *Adv. Mater.* **2014**, *26*, 2219-2251.
6. Chmiola, J.; Yushin, G.; Gogotsi, Y.; Portet, C.; Simon, P.; Taberna, P. L., Anomalous increase in carbon capacitance at pore sizes less than 1 nanometer. *Science* **2006**, *313* (5794), 1760-1763.
7. Stoller, M. D.; Park, S. J.; Zhu, Y. W.; An, J. H.; Ruoff, R. S., Graphene-based ultracapacitors. *Nano Lett.* **2008**, *8* (10), 3498-3502.
8. Zhang, L. L.; Zhao, X. S., Carbon-based materials as supercapacitor electrodes. *Chem. Soc. Rev.* **2009**, *38* (9), 2520-2531.
9. Yang, P.; Xiao, X.; Li, Y.; Ding, Y.; Qiang, P.; Tan, X.; Mai, W.; Lin, Z.; Wu, W.; Li, T.; Jin, H.; Liu, P.; Zhou, J.; Wong, C. P.; Wang, Z. L., Hydrogenated ZnO core-shell nanocables for flexible supercapacitors and self-powered systems. *ACS Nano* **2013**, *7* (3), 2617-2626.
10. Conway, B. E., *Electrochemical Supercapacitor: Scientific Fundamentals and Technological Applications*. Kluwer Academic/Plenum Publishers: New York **1999**.
11. Han, L.; Tang, P.; Zhang, L., Hierarchical Co<sub>3</sub>O<sub>4</sub>@PPy@MnO<sub>2</sub> core-shell-shell nanowire arrays for enhanced electrochemical energy storage. *Nano Energy* **2014**, *7*, 42-51.
12. Xia, X.; Chao, D.; Fan, Z.; Guan, C.; Cao, X.; Zhang, H.; Fan, H. J., A new type of porous graphite foams and their integrated composites with oxide/polymer core/shell nanowires for supercapacitors: structural design, fabrication, and full supercapacitor demonstrations. *Nano Lett.* **2014**, *14* (3), 1651-1658.
13. Qu, Q. T.; Zhu, Y. S.; Gao, X. W.; Wu, Y. P., Core-shell structure of polypyrrole grown on V<sub>2</sub>O<sub>5</sub> nanoribbon as high performance anode material for supercapacitors. *Adv. Energy Mater.* **2012**, *2* (8), 950-955.
14. Simon, P.; Gogotsi, Y., Materials for electrochemical capacitors. *Nat. Mater.* **2008**, *7* (11), 845-854.
15. Helmholtz, H., Ueber einige Gesetze der Vertheilung elektrischer Ströme in körperlichen Leitern mit Anwendung auf die thierisch-elektrischen Versuche. *Ann. Phys.* **1853**, *89*, 211-233.
16. Zhang, J.; Zhao, X. S., On the configuration of supercapacitors for maximizing electrochemical performance. *ChemSusChem* **2012**, *5* (5), 818-841.
17. Gouy, M., Sur la constitution de la charge électrique à la surface d'un électrolyte. *Journal de Physique Théorique et Appliquée* **1910**, *9* (1), 457-468.
18. Chapman, D. L., LI. A contribution to the theory of electrocapillarity. *Philos. Mag.* **1913**, *25*, 475-481.
19. Gonzalez, A.; Goikolea, E.; Barrena, J. A.; Mysyk, R., Review on supercapacitors: technologies and materials. *Renewable Sustainable Energy Rev.* **2016**, *58*, 1189-1206.
20. Stern, O., Zur Theorie der Elektrolytischen Doppelschicht. *Z. Elektrochem.* **1924**, *30*, 508-516.
21. L. Eliad; G. Salitra; A. Soffer; Aurbach, D., Ion sieving effects in the electrical double layer of porous carbon electrodes: estimating effective ion size in electrolytic solutions. *J. Phys. Chem. B* **2001**, *105*, 6880-6887.
22. Frackowiak, E., Carbon materials for supercapacitor application. *Phys. Chem. Chem. Phys.* **2007**, *9* (15), 1774-1785.

23. Inagaki, M.; Konno, H.; Tanaïke, O., Carbon materials for electrochemical capacitors. *J. Power Sources* **2010**, *195* (24), 7880-7903.
24. Raymundo-Piñero, E.; Kierzek, K.; Machnikowski, J.; Béguin, F., Relationship between the nanoporous texture of activated carbons and their capacitance properties in different electrolytes. *Carbon* **2006**, *44* (12), 2498-2507.
25. Huang, J.; Sumpster, B. G.; Meunier, V., A universal model for nanoporous carbon supercapacitors applicable to diverse pore regimes, carbon materials, and electrolytes. *Chem. Eur. J.* **2008**, *14* (22), 6614-6626.
26. Augustyn, V.; Simon, P.; Dunn, B., Pseudocapacitive oxide materials for high-rate electrochemical energy storage. *Energy Environ. Sci.* **2014**, *7* (5), 1597.
27. Liu, T.; Finn, L.; Yu, M.; Wang, H.; Zhai, T.; Lu, X.; Tong, Y.; Li, Y., Polyaniline and polypyrrole pseudocapacitor electrodes with excellent cycling stability. *Nano Lett.* **2014**, *14* (5), 2522-2527.
28. Lu, X. H.; Yu, M. H.; Wang, G. M.; Tong, Y. X.; Li, Y., Flexible solid-state supercapacitors: design, fabrication and applications. *Energy Environ. Sci.* **2014**, *7* (7), 2160-2181.
29. Zhan, L. Z.; Song, Z. P.; Zhang, J. Y.; Tang, J.; Zhan, H.; Zhou, Y. H.; Zhan, C. M., PEDOT: Cathode active material with high specific capacity in novel electrolyte system. *Electrochim. Acta* **2008**, *53* (28), 8319-8323.
30. Mo, D. Z.; Zhou, W. Q.; Ma, X. M.; Xu, J. K.; Zhu, D. H.; Lu, B. Y., Electrochemical synthesis and capacitance properties of a novel poly(3,4-ethylenedioxythiophene bis-substituted bithiophene) electrode material. *Electrochim. Acta* **2014**, *132*, 67-74.
31. Feng, H. X.; Wang, B.; Tan, L.; Chen, N. L.; Wang, N. X.; Chen, B. Y., Polypyrrole/hexadecylpyridinium chloride-modified graphite oxide composites: Fabrication, characterization, and application in supercapacitors. *J. Power Sources* **2014**, *246*, 621-628.
32. Tang, H.; Wang, J.; Yin, H.; Zhao, H.; Wang, D.; Tang, Z., Growth of polypyrrole ultrathin films on MoS<sub>2</sub> monolayers as high-performance supercapacitor electrodes. *Adv. Mater.* **2015**, *27* (6), 1117-1123.
33. Wang, L.; Feng, X.; Ren, L.; Piao, Q.; Zhong, J.; Wang, Y.; Li, H.; Chen, Y.; Wang, B., Flexible solid-state supercapacitor based on a metal-organic framework interwoven by electrochemically-deposited PANI. *J. Am. Chem. Soc.* **2015**, *137* (15), 4920-4923.
34. Ambade, R. B.; Ambade, S. B.; Shrestha, N. K.; Nah, Y. C.; Han, S. H.; Lee, W.; Lee, S. H., Polythiophene infiltrated TiO<sub>2</sub> nanotubes as high-performance supercapacitor electrodes. *Chem. Commun.* **2013**, *49* (23), 2308-2310.
35. Snook, G. A.; Kao, P.; Best, A. S., Conducting-polymer-based supercapacitor devices and electrodes. *J. Power Sources* **2011**, *196* (1), 1-12.
36. Shen, J. F.; Li, T.; Huang, W. S.; Long, Y.; Li, N.; Ye, M. X., One-pot polyelectrolyte assisted hydrothermal synthesis of RuO<sub>2</sub>-reduced graphene oxide nanocomposite. *Electrochim. Acta* **2013**, *95*, 155-161.
37. Long, X.; Zeng, Z. G.; Guo, E. J.; Shi, X. B.; Zhou, H. J.; Wang, X. H., Facile fabrication of all-solid-state flexible interdigitated MnO<sub>2</sub> supercapacitor via in-situ catalytic solution route. *J. Power Sources* **2016**, *325*, 264-272.
38. Bae, J.; Song, M. K.; Park, Y. J.; Kim, J. M.; Liu, M.; Wang, Z. L., Fiber supercapacitors made of nanowire-fiber hybrid structures for wearable/flexible energy storage. *Angew. Chem. Int. Ed.* **2011**, *50* (7), 1683-1687.
39. Wang, D.-W.; Li, F.; Cheng, H.-M., Hierarchical porous nickel oxide and carbon as electrode materials for asymmetric supercapacitor. *J. Power Sources* **2008**, *185* (2), 1563-1568.
40. Zhao, Y.; Liu, B. R.; Pan, L. J.; Yu, G. H., 3D nanostructured conductive polymer hydrogels for high-performance electrochemical devices. *Energy Environ. Sci.* **2013**, *6* (10), 2856-2870.
41. Meng, C.; Liu, C.; Chen, L.; Hu, C.; Fan, S., Highly flexible and all-solid-state paperlike polymer supercapacitors. *Nano Lett.* **2010**, *10* (10), 4025-4031.
42. GAO, W.; Sel, O.; Perrot, H., Electrochemical and viscoelastic evolution of dodecyl sulfate-doped polypyrrole films during electrochemical cycling. *Electrochim. Acta* **2017**, *233*, 262-273.
43. Sivakkumar, S. R.; Kim, W. J.; Choi, J. A.; MacFarlane, D. R.; Forsyth, M.; Kim, D. W., Electrochemical

- performance of polyaniline nanofibres and polyaniline/multi-walled carbon nanotube composite as an electrode material for aqueous redox supercapacitors. *J. Power Sources* **2007**, *171* (2), 1062-1068.
44. Huang, Z. H.; Song, Y.; Xu, X. X.; Liu, X. X., Ordered polypyrrole nanowire arrays grown on a carbon cloth substrate for a high-performance pseudocapacitor electrode. *ACS Appl. Mater. Interfaces* **2015**, *7* (45), 25506-25513.
45. Davies, A.; Audette, P.; Farrow, B.; Hassan, F.; Chen, Z. W.; Choi, J. Y.; Yu, A. P., Graphene-based flexible supercapacitors: pulse-electropolymerization of polypyrrole on free-standing graphene films. *J. Phys. Chem. C* **2011**, *115* (35), 17612-17620.
46. Yun, T. G.; Hwang, B.; Kim, D.; Hyun, S.; Han, S. M., Polypyrrole-MnO<sub>2</sub>-coated textile-based flexible-stretchable supercapacitor with high electrochemical and mechanical reliability. *ACS Appl. Mater. Interfaces* **2015**, *7* (17), 9228-9234.
47. Zhang, H.; Cao, G. P.; Wang, Z. Y.; Yang, Y. S.; Shi, Z. J.; Gu, Z. N., Tube-covering-tube nanostructured polyaniline/carbon nanotube array composite electrode with high capacitance and superior rate performance as well as good cycling stability. *Electrochem. Commun.* **2008**, *10* (7), 1056-1059.
48. Fu, C. P.; Zhou, H. H.; Liu, R.; Huang, Z. Y.; Chen, J. H.; Kuang, Y. F., Supercapacitor based on electropolymerized polythiophene and multi-walled carbon nanotubes composites. *Mater Chem Phys* **2012**, *132*, 596-600.
49. Zhang, H.; Hu, Z.; Li, M.; Hu, L.; Jiao, S., A high-performance supercapacitor based on a polythiophene/multiwalled carbon nanotube composite by electropolymerization in an ionic liquid microemulsion. *J. Mater. Chem. A* **2014**, *2* (40), 17024-17030.
50. B.E. Conway; V. Birss; Wojtowicz, J., The role and utilization of pseudocapacitance for energy storage by supercapacitors. *J. Power Sources* **1997**, *66*, 1-14.
51. Kolb, D. M.; Przasnyski, M.; Gerischer, H., Underpotential deposition of metals and work function differences. *J. Electroanal. Chem. Interfacial Electrochem.* **1974**, *54*, 25-38.
52. Augustyn, V.; Come, J.; Lowe, M. A.; Kim, J. W.; Taberna, P. L.; Tolbert, S. H.; Abruña, H. D.; Simon, P.; Dunn, B., High-rate electrochemical energy storage through Li<sup>+</sup> intercalation pseudocapacitance. *Nat. Mater.* **2013**, *12* (6), 518-522.
53. Simon, P.; Gogotsi, Y.; Dunn, B., Where do batteries end and supercapacitors begin? *Science* **2014**, *343*, 1210-1211.
54. Brousse, T.; Bédanger, D.; Long, J. W., To be or not to be pseudocapacitive? *J. Electrochem. Soc.* **2015**, *162* (5), A5185-A5189.
55. Chao, D.; Zhu, C.; Yang, P.; Xia, X.; Liu, J.; Wang, J.; Fan, X.; Savilov, S. V.; Lin, J.; Fan, H. J.; Shen, Z. X., Array of nanosheets render ultrafast and high-capacity Na-ion storage by tunable pseudocapacitance. *Nat. Commun.* **2016**, *7*, 12122.
56. J. P. Zheng; P. J. Cygan; Jow, T. R., Hydrous ruthenium oxide as an electrode material for electrochemical capacitors. *J. Electrochem. Soc.* **1995**, *142*, 2699-2703.
57. Brousse, T.; Toupin, M.; Dugas, R.; Athouël, L.; Crosnier, O.; Bélanger, D., Crystalline MnO<sub>2</sub> as possible alternatives to amorphous compounds in electrochemical supercapacitors. *J. Electrochem. Soc.* **2006**, *153* (12), A2171-A2180.
58. Okubo, M.; Hosono, E.; Kim, J.; Enomoto, M.; Kojima, N.; Kudo, T.; Zhou, H. S.; Honma, I., Nanosize effect on high-rate Li-ion intercalation in LiCoO<sub>2</sub> electrode. *J. Am. Chem. Soc.* **2007**, *129*, 7444-7452.
59. Kim, H. S.; Cook, J. B.; Tolbert, S. H.; Dunn, B., The development of pseudocapacitive properties in nanosized-MoO<sub>2</sub>. *J. Electrochem. Soc.* **2015**, *162*, A5083-A5090.
60. Sathiyaraj, M.; Prakash, A. S.; Ramesha, K.; Tarascon, J. M.; Shukla, A. K., V<sub>2</sub>O<sub>5</sub>-anchored carbon nanotubes for enhanced electrochemical energy storage. *J. Am. Chem. Soc.* **2011**, *133* (40), 16291-16299.

61. Zhai, Y.; Dou, Y.; Zhao, D.; Fulvio, P. F.; Mayes, R. T.; Dai, S., Carbon materials for chemical capacitive energy storage. *Adv. Mater.* **2011**, *23* (42), 4828-4850.
62. Xu, B.; Yue, S.; Sui, Z.; Zhang, X.; Hou, S.; Cao, G.; Yang, Y., What is the choice for supercapacitors: graphene or graphene oxide? *Energy Environ. Sci.* **2011**, *4* (8), 2826-2830.
63. Raymundo-Piñero, E.; Cadek, M.; Béguin, F., Tuning carbon materials for supercapacitors by direct pyrolysis of seaweeds. *Adv. Funct. Mater.* **2009**, *19* (7), 1032-1039.
64. Du, Q.; Zheng, M.; Zhang, L.; Wang, Y.; Chen, J.; Xue, L.; Dai, W.; Ji, G.; Cao, J., Preparation of functionalized graphene sheets by a low-temperature thermal exfoliation approach and their electrochemical supercapacitive behaviors. *Electrochim. Acta* **2010**, *55* (12), 3897-3903.
65. Yan, J.; Wang, Q.; Wei, T.; Fan, Z. J., Recent advances in design and fabrication of electrochemical supercapacitors with high energy densities. *Adv. Energy Mater.* **2014**, *4* (4), 1300816.
66. Stoller, M. D.; Ruoff, R. S., Best practice methods for determining an electrode material's performance for ultracapacitors. *Energy Environ. Sci.* **2010**, *3* (9), 1294-1301.
67. K. H. An; W. S. Kim; Y. S. Park; J.-M. Moon; D. J. Bae; S. C. Lim; Lee, Y. S.; Lee, Y. H., Electrochemical properties of high-Power supercapacitors using single-walled carbon nanotube electrodes. *Adv. Funct. Mater.* **2001**, *11*, 387-392.
68. A. Yu; Chabot, V.; Zhang, J., *Electrochemical Supercapacitors for Energy Storage and Delivery: Fundamentals and Applications*. CRC Press, Taylor & Francis, Boca Raton, FL **2013**.
69. Winter, M.; Brodd, R. J., What are batteries, fuel cells, and supercapacitors? *Chem. Rev.* **2004**, *104* (10), 4245-4269.
70. Zhang, L. L.; Zhou, R.; Zhao, X. S., Graphene-based materials as supercapacitor electrodes. *J. Mater. Chem.* **2010**, *20* (29), 5983-5992.
71. Deng, M.-J.; Wang, C.-C.; Ho, P.-J.; Lin, C.-M.; Chen, J.-M.; Lu, K.-T., Facile electrochemical synthesis of 3D nano-architected CuO electrodes for high-performance supercapacitors. *J. Mater. Chem. A* **2014**, *2* (32), 12857-12865.
72. Rakhi, R. B.; Chen, W.; Hedhili, M. N.; Cha, D.; Alshareef, H. N., Enhanced rate performance of mesoporous Co<sub>3</sub>O<sub>4</sub> nanosheet supercapacitor electrodes by hydrous RuO<sub>2</sub> nanoparticle decoration. *ACS Appl. Mater. Interfaces* **2014**, *6* (6), 4196-4206.
73. Chen, H.; Cong, T. N.; Yang, W.; Tan, C.; Li, Y.; Ding, Y., Progress in electrical energy storage system: A critical review. *Prog. Nat. Sci.* **2009**, *19* (3), 291-312.
74. Kütz, R.; Carlen, M., Principles and applications of electrochemical capacitors. *Electrochim. Acta* **2000**, *45*, 2483-2498.
75. Gu, W.; Yushin, G., Review of nanostructured carbon materials for electrochemical capacitor applications: advantages and limitations of activated carbon, carbide-derived carbon, zeolite-templated carbon, carbon aerogels, carbon nanotubes, onion-like carbon, and graphene. *Wiley Interdiscip. Rev.: Energy Environ.* **2014**, *3* (5), 424-473.
76. Gogotsi, Y.; Simon, P., True performance metrics in electrochemical energy storage. *Science* **2011**, *334* (6058), 917-918.
77. Guo, Y.; Li, W.; Yu, H.; Perepichka, D. F.; Meng, H., Flexible asymmetric supercapacitors via spray coating of a new electrochromic donor-acceptor polymer. *Adv. Energy Mater.* **2017**, *7* (2), 1601623.
78. Sankapal, B. R.; Gajare, H. B.; Karade, S. S.; Salunkhe, R. R.; Dubal, D. P., Zinc oxide encapsulated carbon nanotube thin films for energy storage applications. *Electrochim. Acta* **2016**, *192*, 377-384.
79. Cai, D.; Huang, H.; Wang, D.; Liu, B.; Wang, L.; Liu, Y.; Li, Q.; Wang, T., High-performance supercapacitor electrode based on the unique ZnO@Co<sub>3</sub>O<sub>4</sub> core/shell heterostructures on nickel foam. *ACS Appl. Mater. Interfaces* **2014**, *6* (18), 15905-15912.

80. Ellis, B. L.; Knauth, P.; Djenizian, T., Three-dimensional self-supported metal oxides for advanced energy storage. *Adv. Mater.* **2014**, *26* (21), 3368-3397.
81. Liao, Q. Y.; Li, N.; Jin, S. X.; Yang, G. W.; Wang, C. X., All-solid-state symmetric supercapacitor based on Co<sub>3</sub>O<sub>4</sub> nanoparticles on vertically aligned graphene. *ACS Nano* **2015**, *9* (5), 5310-5317.
82. Simon, P.; Gogotsi, Y., Capacitive energy storage in nanostructured carbon-electrolyte systems. *Acc. Chem. Res.* **2013**, *46*, 1094-1103.
83. Sevilla, M.; Fuertes, A. B.; Mokaya, R., High density hydrogen storage in superactivated carbons from hydrothermally carbonized renewable organic materials. *Energy Environ. Sci.* **2011**, *4* (4), 1400-1410.
84. Wei, L.; Yushin, G., Nanostructured activated carbons from natural precursors for electrical double layer capacitors. *Nano Energy* **2012**, *1* (4), 552-565.
85. Titirici, M. M.; White, R. J.; Falco, C.; Sevilla, M., Black perspectives for a green future: hydrothermal carbons for environment protection and energy storage. *Energy Environ. Sci.* **2012**, *5* (5), 6796-6822.
86. Wang, R.; Wang, P.; Yan, X.; Lang, J.; Peng, C.; Xue, Q., Promising porous carbon derived from celtuce leaves with outstanding supercapacitance and CO<sub>2</sub> capture performance. *ACS Appl. Mater. Interfaces* **2012**, *4* (11), 5800-5806.
87. Eliad, L.; Pollak, E.; Levy, N.; Salitra, G.; Soffer, A.; Aurbach, D., Assessing optimal pore-to-ion size relations in the design of porous poly(vinylidene chloride) carbons for EDL capacitors. *Appl. Phys. A* **2005**, *82* (4), 607-613.
88. Wei, L.; Sevilla, M.; Fuertes, A. B.; Mokaya, R.; Yushin, G., Polypyrrole-derived activated carbons for high-performance electrical double-layer capacitors with ionic liquid electrolyte. *Adv. Funct. Mater.* **2012**, *22* (4), 827-834.
89. Yan, J.; Wei, T.; Qiao, W. M.; Fan, Z. J.; Zhang, L. J.; Li, T. Y.; Zhao, Q. K., A high-performance carbon derived from polyaniline for supercapacitors. *Electrochem. Commun.* **2010**, *12* (10), 1279-1282.
90. Ioannidou, O.; Zabaniotou, A., Agricultural residues as precursors for activated carbon production—A review. *Renewable Sustainable Energy Rev.* **2007**, *11* (9), 1966-2005.
91. Xiang, X.; Liu, E.; Huang, Z.; Shen, H.; Tian, Y.; Xiao, C.; Yang, J.; Mao, Z., Preparation of activated carbon from polyaniline by zinc chloride activation as supercapacitor electrodes. *J. Solid State Electrochem.* **2010**, *15* (11-12), 2667-2674.
92. Hulicova-Jurcakova, D.; Puziy, A. M.; Poddubnaya, O. I.; Suarez-Garcia, F.; Tascon, J. M.; Lu, G. Q., Highly stable performance of supercapacitors from phosphorus-enriched carbons. *J. Am. Chem. Soc.* **2009**, *131* (14), 5026-5027.
93. Qie, L.; Chen, W. M.; Xu, H. H.; Xiong, X. Q.; Jiang, Y.; Zou, F.; Hu, X. L.; Xin, Y.; Zhang, Z. L.; Huang, Y. H., Synthesis of functionalized 3D hierarchical porous carbon for high-performance supercapacitors. *Energy Environ. Sci.* **2013**, *6* (8), 2497-2504.
94. Wei, L.; Sevilla, M.; Fuertes, A. B.; Mokaya, R.; Yushin, G., Hydrothermal carbonization of abundant renewable natural organic chemicals for high-performance supercapacitor electrodes. *Adv. Energy Mater.* **2011**, *1* (3), 356-361.
95. Balathanigaimani, M. S.; Shim, W. G.; Lee, M. J.; Kim, C.; Lee, J. W.; Moon, H., Highly porous electrodes from novel corn grains-based activated carbons for electrical double layer capacitors. *Electrochem. Commun.* **2008**, *10* (6), 868-871.
96. Wu, F. C.; Tseng, R. L.; Hu, C. C.; Wang, C. C., Physical and electrochemical characterization of activated carbons prepared from firwoods for supercapacitors. *J. Power Sources* **2004**, *138* (1-2), 351-359.
97. Zhi, M. J.; Yang, F.; Meng, F. K.; Li, M. Q.; Manivannan, A.; Wu, N. Q., Effects of pore structure on performance of an activated-carbon supercapacitor electrode recycled from scrap waste tires. *ACS Sustainable Chem. Eng.* **2014**, *2* (7), 1592-1598.
98. Baughman, R. H.; Zakhidov, A. A.; de Heer, W. A., Carbon nanotubes-the route toward applications. *Science* **2002**, *297* (5582), 787-792.

99. Davies, A.; Yu, A. P., Material Advancements in Supercapacitors: From Activated Carbon to Carbon Nanotube and Graphene. *Can. J. Chem. Eng.* **2011**, *89* (6), 1342-1357.
100. An, K. H.; Kim, W. S.; Park, Y. S.; Jeong, H. J.; Choi, Y. C.; Moon, J.-M.; Bae, D. J.; Lim, S. C.; Lee, Y. H., Supercapacitors using singlewalled carbon nanotube electrodes. *AIP Conference Proceedings* **2001**, *590*, 241-244.
101. Futaba, D. N.; Hata, K.; Yamada, T.; Hiraoka, T.; Hayamizu, Y.; Kakudate, Y.; Tanaike, O.; Hatori, H.; Yumura, M.; Iijima, S., Shape-engineerable and highly densely packed single-walled carbon nanotubes and their application as super-capacitor electrodes. *Nat. Mater.* **2006**, *5* (12), 987-994.
102. Tang, Z.; Tang, C. H.; Gong, H., A high energy density asymmetric supercapacitor from nano-architected Ni(OH)<sub>2</sub>/carbon nanotube electrodes. *Adv. Funct. Mater.* **2012**, *22* (6), 1272-1278.
103. Chen, Y. L.; Du, L. H.; Yang, P. H.; Sun, P.; Yu, X.; Mai, W. J., Significantly enhanced robustness and electrochemical performance of flexible carbon nanotube-based supercapacitors by electrodepositing polypyrrole. *J. Power Sources* **2015**, *287*, 68-74.
104. Li, P.; Yang, Y.; Shi, E.; Shen, Q.; Shang, Y.; Wu, S.; Wei, J.; Wang, K.; Zhu, H.; Yuan, Q.; Cao, A.; Wu, D., Core-double-shell, carbon nanotube@polypyrrole@MnO<sub>2</sub> sponge as freestanding, compressible supercapacitor electrode. *ACS Appl. Mater. Interfaces* **2014**, *6* (7), 5228-5234.
105. Zeng, S.; Chen, H. Y.; Cai, F.; Kang, Y. R.; Chen, M. H.; Li, Q. W., Electrochemical fabrication of carbon nanotube/polyaniline hydrogel film for all-solid-state flexible supercapacitor with high areal capacitance. *J. Mater. Chem. A* **2015**, *3* (47), 23864-23870.
106. Novoselov, K. S.; Geim, A. K.; Morozov, S. V.; Jiang, D.; Zhang, Y.; Dubonos, S. V.; I.V.Grigorieva; Firsov, A. A., Electric field effect in atomically thin carbon films. *Science* **2004**, *306*, 666-669.
107. El-Kady, M. F.; Strong, V.; Dubin, S.; Kaner, R. B., Laser scribing of high-performance and flexible graphene-based electrochemical capacitors. *Science* **2012**, *335* (6074), 1326-1330.
108. Wang, M.; Duong le, D.; Mai, N. T.; Kim, S.; Kim, Y.; Seo, H.; Kim, Y. C.; Jang, W.; Lee, Y.; Suhr, J.; Nam, J. D., All-solid-state reduced graphene oxide supercapacitor with large volumetric capacitance and ultralong stability prepared by electrophoretic deposition method. *ACS Appl. Mater. Interfaces* **2015**, *7* (2), 1348-1354.
109. Wang, S.; Liu, N.; Su, J.; Li, L.; Long, F.; Zou, Z.; Jiang, X.; Gao, Y., Highly stretchable and self-healable supercapacitor with reduced graphene oxide based fiber springs. *ACS Nano* **2017**, *11* (2), 2066-2074.
110. Xu, J.; Tan, Z.; Zeng, W.; Chen, G.; Wu, S.; Zhao, Y.; Ni, K.; Tao, Z.; Ikram, M.; Ji, H.; Zhu, Y., A hierarchical carbon derived from sponge-templated activation of graphene oxide for high-performance supercapacitor electrodes. *Adv. Mater.* **2016**, *28* (26), 5222-5228.
111. Yang, X.; Zhu, J.; Qiu, L.; Li, D., Bioinspired effective prevention of restacking in multilayered graphene films: towards the next generation of high-performance supercapacitors. *Adv. Mater.* **2011**, *23* (25), 2833-2838.
112. Raccichini, R.; Varzi, A.; Passerini, S.; Scrosati, B., The role of graphene for electrochemical energy storage. *Nat. Mater.* **2015**, *14* (3), 271-279.
113. Chen, Y.; Zhang, X.; Zhang, D.; Yu, P.; Ma, Y., High performance supercapacitors based on reduced graphene oxide in aqueous and ionic liquid electrolytes. *Carbon* **2011**, *49* (2), 573-580.
114. Cai, M.; Thorpe, D.; Adamson, D. H.; Schniepp, H. C., Methods of graphite exfoliation. *J. Mater. Chem.* **2012**, *22* (48), 24992.
115. Novoselov, K. S.; Fal'ko, V. I.; Colombo, L.; Gellert, P. R.; Schwab, M. G.; Kim, K., A roadmap for graphene. *Nature* **2012**, *490* (7419), 192-200.
116. Cai, J.; Ruffieux, P.; Jaafar, R.; Bieri, M.; Braun, T.; Blankenburg, S.; Muoth, M.; Seitsonen, A. P.; Saleh, M.; Feng, X.; Mullen, K.; Fasel, R., Atomically precise bottom-up fabrication of graphene nanoribbons. *Nature* **2010**, *466* (7305), 470-473.
117. X-Y Peng; Liu, X.-X.; Diamond, D.; Lau, K. T., Synthesis of electrochemically-reduced graphene oxide film with

- controllable size and thickness and its use in supercapacitor. *Carbon* **2011**, *49*, 3488-3496.
118. Yang, D. F.; Bock, C., Laser reduced graphene for supercapacitor applications. *J. Power Sources* **2017**, *337*, 73-81.
119. Hou, J.; Shao, Y.; Ellis, M. W.; Moore, R. B.; Yi, B., Graphene-based electrochemical energy conversion and storage: fuel cells, supercapacitors and lithium ion batteries. *Phys. Chem. Chem. Phys.* **2011**, *13* (34), 15384-15402.
120. Pei, S. F.; Cheng, H. M., The reduction of graphene oxide. *Carbon* **2012**, *50* (9), 3210-3228.
121. Eda, G.; Fanchini, G.; Chhowalla, M., Large-area ultrathin films of reduced graphene oxide as a transparent and flexible electronic material. *Nat. Nanotechnol.* **2008**, *3* (5), 270-274.
122. Ryu, K. S.; Kim, K. M.; Park, N. G.; Park, Y. J.; Chang, S. H., Symmetric redox supercapacitor with conducting polyaniline electrodes. *J. Power Sources* **2002**, *103* (2), 305-309.
123. Wang, K.; Wu, H.; Meng, Y.; Wei, Z., Conducting polymer nanowire arrays for high performance supercapacitors. *Small* **2014**, *10* (1), 14-31.
124. Heeger, A. H., Semiconducting and metallic polymers: the fourth generation of polymeric materials (Nobel lecture). *Angew. Chem. Int. Ed.* **2001**, *40* (14), 2591-2611.
125. Huang, Y.; Li, H. F.; Wang, Z. F.; Zhu, M. S.; Pei, Z. X.; Xue, Q.; Huang, Y.; Zhi, C. Y., Nanostructured polypyrrole as a flexible electrode material of supercapacitor. *Nano Energy* **2016**, *22*, 422-438.
126. Lota, K.; Khomenko, V.; Frackowiak, E., Capacitance properties of poly(3,4-ethylenedioxythiophene)/carbon nanotubes composites. *J. Phys. Chem. Solids* **2004**, *65* (2-3), 295-301.
127. Zhou, C.; Zhang, Y.; Li, Y.; Liu, J., Construction of high-capacitance 3D CoO@polypyrrole nanowire array electrode for aqueous asymmetric supercapacitor. *Nano Lett.* **2013**, *13* (5), 2078-2085.
128. Meng, Q.; Cai, K.; Chen, Y.; Chen, L., Research progress on conducting polymer based supercapacitor electrode materials. *Nano Energy* **2017**, *36*, 268-285.
129. Wang, G. X.; Yang, L.; Chen, Y.; Wang, J. Z.; Bewlay, S.; Liu, H. K., An investigation of polypyrrole-LiFePO<sub>4</sub> composite cathode materials for lithium-ion batteries. *Electrochim. Acta* **2005**, *50* (24), 4649-4654.
130. Fu, H.; Du, Z. J.; Zou, W.; Li, H. Q.; Zhang, C., Carbon nanotube reinforced polypyrrole nanowire network as a high-performance supercapacitor electrode. *J. Mater. Chem. A* **2013**, *1* (47), 14943-14950.
131. Song, Y.; Xu, J. L.; Liu, X. X., Electrochemical anchoring of dual doping polypyrrole on graphene sheets partially exfoliated from graphite foil for high-performance supercapacitor electrode. *J. Power Sources* **2014**, *249*, 48-58.
132. Eftekhari, A.; Li, L.; Yang, Y., Polyaniline supercapacitors. *J. Power Sources* **2017**, *347*, 86-107.
133. Wu, M. Q.; Snook, G. A.; Gupta, V.; Shaffer, M.; Fray, D. J.; Chen, G. Z., Electrochemical fabrication and capacitance of composite films of carbon nanotubes and polyaniline. *J. Mater. Chem.* **2005**, *15* (23), 2297-2303.
134. Zhu, Z. Z.; Wang, G. C.; Sun, M. Q.; Li, X. W.; Li, C. Z., Fabrication and electrochemical characterization of polyaniline nanorods modified with sulfonated carbon nanotubes for supercapacitor applications. *Electrochim. Acta* **2011**, *56* (3), 1366-1372.
135. Nyholm, L.; Nystrom, G.; Mihranyan, A.; Stromme, M., Toward flexible polymer and paper-based energy storage devices. *Adv. Mater.* **2011**, *23* (33), 3751-3769.
136. Mastragostino, M.; Arbizzani, C.; Soavi, F., Conducting polymers as electrode materials in supercapacitors. *Solid State Ionics* **2002**, *148*, 493-498.
137. Kim, C. H.; Kim, B.-H., Zinc oxide/activated carbon nanofiber composites for high-performance supercapacitor electrodes. *J. Power Sources* **2015**, *274*, 512-520.
138. Lee, H. Y.; Goodenough, J. B., Supercapacitor behavior with KCl electrolyte. *J. Solid State Chem.* **1999**, *144*, 220-223.
139. Wei, W.; Cui, X.; Chen, W.; Ivey, D. G., Manganese oxide-based materials as electrochemical supercapacitor electrodes. *Chem. Soc. Rev.* **2011**, *40* (3), 1697-1721.
140. Lu, X. H.; Zheng, D. Z.; Zhai, T.; Liu, Z. Q.; Huang, Y. Y.; Xie, S. L.; Tong, Y. X., Facile synthesis of large-area

- manganese oxide nanorod arrays as a high-performance electrochemical supercapacitor. *Energy Environ. Sci.* **2011**, *4* (8), 2915-2921.
141. Yan, J.; Fan, Z.; Wei, T.; Qian, W.; Zhang, M.; Wei, F., Fast and reversible surface redox reaction of graphene-MnO<sub>2</sub> composites as supercapacitor electrodes. *Carbon* **2010**, *48* (13), 3825-3833.
142. Subramanian, V.; Zhu, H.; Wei, B., Nanostructured MnO<sub>2</sub>: Hydrothermal synthesis and electrochemical properties as a supercapacitor electrode material. *J. Power Sources* **2006**, *159* (1), 361-364.
143. Pang, S. C.; Anderson, M. A.; Chapman, T. W., Novel electrode materials for thin-film ultracapacitors: Comparison of electrochemical properties of sol-gel-derived and electrodeposited manganese dioxide. *J. Electrochem. Soc.* **2000**, *147* (2), 444-450.
144. Toupin, M.; Brousse, T.; Belanger, D., Charge storage mechanism of MnO<sub>2</sub> electrode used in aqueous electrochemical capacitor. *Chem. Mater.* **2004**, *16* (16), 3184-3190.
145. Xu, M. W.; Jia, W.; Bao, S. J.; Su, Z.; Dong, B., Novel mesoporous MnO<sub>2</sub> for high-rate electrochemical capacitive energy storage. *Electrochim. Acta* **2010**, *55* (18), 5117-5122.
146. Faraji, S.; Ani, F. N., Microwave-assisted synthesis of metal oxide/hydroxide composite electrodes for high power supercapacitors – A review. *J. Power Sources* **2014**, *263*, 338-360.
147. He, Y. B.; Li, G. R.; Wang, Z. L.; Su, C. Y.; Tong, Y. X., Single-crystal ZnO nanorod/amorphous and nanoporous metal oxide shell composites: Controllable electrochemical synthesis and enhanced supercapacitor performances. *Energy Environ. Sci.* **2011**, *4* (4), 1288-1292.
148. Pruna, A.; Shao, Q.; Kamruzzaman, M.; Zapien, J. A.; Ruotolo, A., Enhanced electrochemical performance of ZnO nanorod core/polypyrrole shell arrays by graphene oxide. *Electrochim. Acta* **2016**, *187*, 517-524.
149. Chen, Y. L.; Hu, Z. A.; Chang, Y. Q.; Wang, H. W.; Zhang, Z. Y.; Yang, Y. Y.; Wu, H. Y., Zinc oxide/reduced graphene oxide composites and electrochemical capacitance enhanced by homogeneous incorporation of reduced graphene oxide sheets in zinc oxide matrix. *J. Phys. Chem. C* **2011**, *115* (5), 2563-2571.
150. Li, Z.; Liu, P.; Yun, G.; Shi, K.; Lv, X.; Li, K.; Xing, J.; Yang, B., 3D (Three-dimensional) sandwich-structured of ZnO (zinc oxide)/rGO (reduced graphene oxide)/ZnO for high performance supercapacitors. *Energy* **2014**, *69*, 266-271.
151. Haldorai, Y.; Voit, W.; Shim, J.-J., Nano ZnO@reduced graphene oxide composite for high performance supercapacitor: Green synthesis in supercritical fluid. *Electrochim. Acta* **2014**, *120*, 65-72.
152. Zhang, S. L.; Pan, N., Supercapacitors performance evaluation. *Adv. Energy Mater.* **2015**, *5* (6), 1401401.
153. T.-C. Liu; W. G. Pell; Conway, B. E.; Roberson, S. L., Behavior of molybdenum nitrides as materials for electrochemical capacitors - Comparison with ruthenium oxide. *J. Electrochem. Soc.* **1998**, *145*, 1882-1888.
154. Chen, Z.; Weng, D.; Wang, X.; Cheng, Y.; Wang, G.; Lu, Y., Ready fabrication of thin-film electrodes from building nanocrystals for micro-supercapacitors. *Chem. Commun.* **2012**, *48* (31), 3736-3738.
155. Liu, L.; Lang, J.; Zhang, P.; Hu, B.; Yan, X., Facile synthesis of Fe<sub>2</sub>O<sub>3</sub> nano-dots@nitrogen-doped graphene for supercapacitor electrode with ultralong cycle life in KOH electrolyte. *ACS Appl. Mater. Interfaces* **2016**, *8* (14), 9335-9344.
156. Yan, W. B.; Kim, J. Y.; Xing, W. D.; Donovan, K. C.; Ayyazian, T.; Penner, R. M., Lithographically patterned gold/manganese dioxide core/shell nanowires for high capacity, high rate, and high cyclability hybrid electrical energy storage. *Chem. Mater.* **2012**, *24* (12), 2382-2390.
157. Li, R. Z.; Liu, J. P., Mechanistic investigation of the charge storage process of pseudocapacitive Fe<sub>3</sub>O<sub>4</sub> nanorod film. *Electrochim. Acta* **2014**, *120*, 52-56.
158. Fan, L. Z.; Maier, J., High-performance polypyrrole electrode materials for redox supercapacitors. *Electrochem. Commun.* **2006**, *8* (6), 937-940.
159. Vonlanthen, D.; Lazarev, P.; See, K. A.; Wudl, F.; Heeger, A. J., A stable polyaniline-benzoquinone-hydroquinone supercapacitor. *Adv. Mater.* **2014**, *26* (30), 5095-5100.

160. Nam, K.-W.; Kim, K.-B., A study of the preparation of NiO<sub>x</sub> electrode via electrochemical route for supercapacitor applications and their charge storage mechanism. *J. Electrochem. Soc.* **2002**, *149* (3), A346.
161. Burke, A.; Miller, M., Testing of electrochemical capacitors: Capacitance, resistance, energy density, and power capability. *Electrochim. Acta* **2010**, *55* (25), 7538-7548.
162. Chen, K.; Xue, D., Water-soluble inorganic salt with ultrahigh specific capacitance: Ce(NO<sub>3</sub>)<sub>3</sub> can be designed as excellent pseudocapacitor electrode. *J. Colloid. Interface Sci.* **2014**, *416*, 172-176.
163. Ballester, S. C. S., Synthesis and characterization of new polymer electrolytes to use in fuel cells fed with bio-alcohols. *Ph.D. thesis. Universitat Politècnica de València* **2017**.
164. Levi, M. D.; Lukatskaya, M. R.; Sigalov, S.; Beidaghi, M.; Shpigel, N.; Daikhin, L.; Aurbach, D.; Barsoum, M. W.; Gogotsi, Y., Solving the capacitive paradox of 2D MXene using electrochemical quartz-crystal admittance and in situ electronic conductance measurements. *Adv. Energy Mater.* **2015**, *5* (1), 1400815.
165. Buttry, D. A.; Ward, M. D., Measurement of interfacial processes at electrode surfaces with the electrochemical quartz crystal microbalance. *Chem. Rev.* **1992**, *92*, 1355-1379.
166. Dragoman, M.; Muller, A.; Neculoiu, D.; Vasilache, D.; Konstantinidis, G.; Grenier, K.; Dubuc, D.; Bary, L.; Plana, R.; Flahaut, E., High performance thin film bulk acoustic resonator covered with carbon nanotubes. *Appl. Phys. Lett.* **2006**, *89* (14), 143122.
167. Tsai, W. Y.; Taberna, P. L.; Simon, P., Electrochemical quartz crystal microbalance (EQCM) study of ion dynamics in nanoporous carbons. *J. Am. Chem. Soc.* **2014**, *136* (24), 8722-8728.
168. Curie, P.; Curie, J., Développement par pression de l'électricité polaire dans les cristaux hémihédres à faces inclinées. *Comput. Rend. Acad. Sci.* **1880**, *91*, 294-295.
169. Ward, M. D.; Buttey, D. A., In situ interfacial mass detection with piezoelectric transducers. *Science* **1990**, *249*, 1000-1007.
170. John, J.; Hugar, K. M.; Rivera-Melendez, J.; Kostalik, H. A. t.; Rus, E. D.; Wang, H.; Coates, G. W.; Abruna, H. D., An electrochemical quartz crystal microbalance study of a prospective alkaline anion exchange membrane material for fuel cells: anion exchange dynamics and membrane swelling. *J. Am. Chem. Soc.* **2014**, *136* (14), 5309-5322.
171. Rodriguez-Pardo, L.; Fariña, J.; Gabrielli, C.; Perrot, H.; Brendel, R., Resolution in quartz crystal oscillator circuits for high sensitivity microbalance sensors in damping media. *Sens. Actuators B: Chem.* **2004**, *103* (1-2), 318-324.
172. Sauerbrey, G., Use of quartz vibrator for weighing thin films on a microbalance. *Z. Phys.* **1959**, *155*, 206-210.
173. Levi, M. D.; Salitra, G.; Levy, N.; Aurbach, D.; Maier, J., Application of a quartz-crystal microbalance to measure ionic fluxes in microporous carbons for energy storage. *Nat. Mater.* **2009**, *8* (11), 872-875.
174. Levi, M. D.; Daikhin, L.; Aurbach, D.; Presser, V., Quartz crystal microbalance with dissipation monitoring (EQCM-D) for in-situ studies of electrodes for supercapacitors and batteries: A mini-review. *Electrochem. Commun.* **2016**, *67*, 16-21.
175. Gabrielli, C.; Garcia-Jareño, J. J.; Perrot, H., Charge compensation process in polypyrrole studied by ac electrogravimetry. *Electrochim. Acta* **2001**, *46* (26), 4095-4103.
176. Levi, M. D.; Sigalov, S.; Salitra, G.; Aurbach, D.; Maier, J., The effect of specific adsorption of cations and their size on the charge-compensation mechanism in carbon micropores: The role of anion desorption. *Chemphyschem* **2011**, *12* (4), 854-862.
177. Arias, C. R.; Debiemme-Chouvy, C.; Gabrielli, C.; Laberty-Robert, C.; Pailleret, A.; Perrot, H.; Sel, O., New insights into pseudocapacitive charge-storage mechanisms in Li-Birnessite type MnO<sub>2</sub> monitored by fast quartz crystal microbalance methods. *J. Phys. Chem. C* **2014**, *118* (46), 26551-26559.
178. Bourkane, S.; Gabrielli, C.; Keddam, M., Kinetic study of electrode processes by ac quartz electrogravimetry. *J. Electroanal. Chem.* **1988**, *256*, 471-475.

179. Torres, R.; Arnau, A.; Perrot, H.; García, J.; Gabrielli, C., Analogue–digital phase-locked loop for alternating current quartz electrogravimetry. *Electron. Lett.* **2006**, *42* (22), 1272.
180. García-Jareño, J. J.; Gabrielli, C.; Perrot, H., Validation of the mass response of a quartz crystal microbalance coated with Prussian Blue film for ac electrogravimetry. *Electrochem. Commun.* **2000**, *2* (3), 195-200.
181. Gabrielli, C.; Keddad, M.; Nadi, N.; Perrot, H., Ions and solvent transport across conducting polymers investigated by ac electrogravimetry. Application to polyaniline. *J. Electroanal. Chem.* **2000**, *485*, 101-113.
182. Gabrielli, C.; Garcia-Jareno, J. J.; Keddad, M.; Perrot, H.; Vicente, F., Ac-electrogravimetry study of electroactive thin films. II. Application to polypyrrole. *J. Phys. Chem. B* **2002**, *106*, 3192-3201.
183. To Thi Kim, L.; Sel, O.; Debiemme-Chouvy, C.; Gabrielli, C.; Laberty-Robert, C.; Perrot, H.; Sanchez, C., Proton transport properties in hybrid membranes investigated by ac-electrogravimetry. *Electrochem. Commun.* **2010**, *12* (8), 1136-1139.
184. Agrisuelas, J.; Delgado, C.; Gabrielli, C.; García-Jareño, J. J.; Perrot, H.; Sel, O.; Vicente, F., The role of  $\text{NH}_4^+$  cations on the electrochemistry of prussian blue studied by electrochemical, mass, and color impedance spectroscopy. *J. Solid State Electrochem.* **2015**, *19* (9), 2555-2564.
185. Escobar-Teran, F.; Arnau, A.; Garcia, J. V.; Jiménez, Y.; Perrot, H.; Sel, O., Gravimetric and dynamic deconvolution of global EQCM response of carbon nanotube based electrodes by Ac-electrogravimetry. *Electrochem. Commun.* **2016**, *70*, 73-77.
186. Goubaa, H.; Escobar-Teran, F.; Ressam, I.; Gao, W.; El Kadib, A.; Lucas, I. T.; Raihane, M.; Lahcini, M.; Perrot, H.; Sel, O., Dynamic resolution of ion transfer in electrochemically reduced graphene oxides revealed by electrogravimetric impedance. *J. Phys. Chem. C* **2017**, *121* (17), 9370-9380.
187. Levi, M. D.; Shpigel, N.; Sigalov, S.; Dargel, V.; Daikhin, L.; Aurbach, D., In situ porous structure characterization of electrodes for energy storage and conversion by EQCM-D: a review. *Electrochim. Acta* **2017**, *232*, 271-284.
188. Shpigel, N.; Lukatskaya, M. R.; Sigalov, S.; Ren, C. E.; Nayak, P.; Levi, M. D.; Daikhin, L.; Aurbach, D.; Gogotsi, Y., In situ monitoring of gravimetric and viscoelastic changes in 2D intercalation electrodes. *ACS Energy Lett.* **2017**, *2* (6), 1407-1415.
189. Hillman, A. R.; Efimov, I.; Skompska, M., Dynamics of regioregular conducting polymer electrodes in response to electrochemical stimuli. *Faraday Discuss.* **2002**, *121*, 423-439.
190. Koehler, S.; Bund, A.; Efimov, I., Shear moduli of anion and cation exchanging polypyrrole films. *J. Electroanal. Chem.* **2006**, *589* (1), 82-86.
191. Granstaff, V. E.; Martin, S. J., Characterization of a thickness-shear mode quartz resonator with multiple nonpiezoelectric layers. *J. Appl. Phys.* **1994**, *75* (3), 1319-1329.
192. Martin, S. J.; Bandey, H. L.; Cernosek, R. W.; Hillman, A. R.; J., B. M., Equivalent-circuit model for the thickness-shear mode resonator with a viscoelastic film near film resonance. *Anal. Chem.* **2000**, *72*, 141-149.
193. Hillman, A. R.; Jackson, A.; Martin, S. J., The problem of uniqueness of fit for viscoelastic films on thickness-shear mode resonator surfaces. *Anal. Chem.* **2001**, *73*, 540-549.
194. Sabot, A.; Krause, S., Simultaneous quartz crystal microbalance impedance and electrochemical impedance measurements. Investigation into the degradation of thin polymer films. *Anal. Chem.* **2002**, *74*, 3304-3311.
195. Dargel, V.; Jackel, N.; Shpigel, N.; Sigalov, S.; Levi, M. D.; Daikhin, L.; Presser, V.; Aurbach, D., In situ multilength-scale tracking of dimensional and viscoelastic changes in composite battery electrodes. *ACS Appl. Mater. Interfaces* **2017**, *9* (33), 27664-27675.
196. Shpigel, N.; Levi, M. D.; Sigalov, S.; Girshevitz, O.; Aurbach, D.; Daikhin, L.; Pikma, P.; Marandi, M.; Janes, A.; Lust, E.; Jackel, N.; Presser, V., In situ hydrodynamic spectroscopy for structure characterization of porous energy storage electrodes. *Nat. Mater.* **2016**, *15* (5), 570-575.
197. Shpigel, N.; Levi, M. D.; Sigalov, S.; Mathis, T. S.; Gogotsi, Y.; Aurbach, D., Direct assessment of nanoconfined

water in 2D  $\text{Ti}_3\text{C}_2$  electrode interspaces by a surface acoustic technique. *J. Am. Chem. Soc.* **2018**, *140* (28), 8910-8917.

198. Shpigel, N.; Levi, M. D.; Sigalov, S.; Daikhin, L.; Aurbach, D., In situ real-time mechanical and morphological characterization of electrodes for electrochemical energy storage and conversion by electrochemical quartz crystal microbalance with dissipation monitoring. *Acc. Chem. Res.* **2018**, *51* (1), 69-79.

Chapter II: Experimental procedures

## II.1. Materials characterization techniques

This section summarizes the techniques for structural and morphological characterizations of the materials used in the present thesis, involving their operation principles, instrument type as well as specific sample preparations.

### II.1.1. Fourier transform infrared (FTIR) spectroscopy

FTIR is an analytical spectroscopy technique for the identification of materials and molecules based on their specific infrared absorption, which utilizes the infrared light spectrum to probe sample interactions<sup>1-3</sup>. In principle, when a beam of infrared (IR) light passes through a sample, some of the IR light is absorbed by the material and some is transmitted through it. The absorbed photons can excite molecules into a higher vibrational energy state. The energy absorbed corresponds to the vibrational frequency of the sample molecules' functional groups and thus permits its identification<sup>2</sup>.

At the heart of every FTIR is an optical device named an interferometer. The oldest and perhaps the most common type of interferometer in use today is the Michelson interferometer, which consists of four arms (**Figure II.1a**)<sup>1</sup>. The top arm comprises an infrared source and a collimating mirror, which is used to collect the light from the source and parallelize its rays; a fixed mirror is contained in the bottom arm, which is contrary to the moving mirror capable of moving left and right (right arm); the sample and the detector are located in the left arm. In the center of the interferometer is an optical device called a beam splitter, which can transmit and reflect some of the light incident upon it. The light transmitted and reflected by the beam splitter travels towards the fixed mirror and moving mirror, respectively. Then, the light will be reflected from these two mirrors and travel back to the beam splitter, where they are recombined into a single light beam that leaves the interferometer, interacts with the sample, and strikes the detector<sup>1</sup>.

An interferogram is the fundamental measurement obtained by an FTIR, which is Fourier transformed to yield a spectrum giving information about the infrared energy corresponding to the sample absorption<sup>1, 4</sup>. As shown in **Figure II.1b**, a FTIR spectrum is a plot of the infrared intensity

versus the wavenumber (in  $\text{cm}^{-1}$ ) obtained after a FT of the interferogram.

The FTIR spectra were recorded on VERTEX 70 spectrometer (BRUKER Co., USA) from 2000 to  $650\text{ cm}^{-1}$  using the Attenuated Total Reflectance (ATR) mode with a  $4\text{ cm}^{-1}$  resolution. Before each measurement, background spectra were collected in order to eliminate the interference from the environment. The films used for FTIR spectroscopy measurements were prepared on ITO coated glass slides and cycled under the same conditions as those on gold electrode of the quartz resonators.

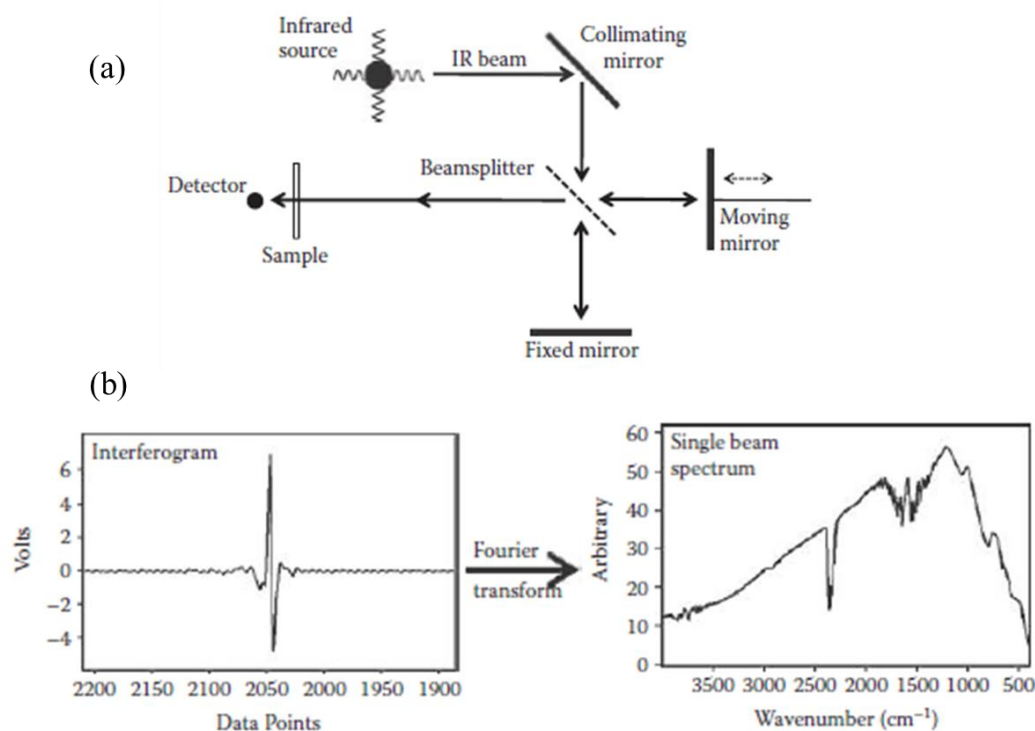


**Figure II.1.** (a) The optical diagram of a Michelson interferometer and (b) the Fourier transformation of an interferogram to a single beam spectrum<sup>1</sup>.

### II.1.2. Ultraviolet-visible (UV-vis) spectroscopy

UV-vis spectroscopy is an analytical technique routinely used for the quantitative determination of a large number of analytes, including inorganic, organic and biological species<sup>5</sup>. Spectroscopy in the UV-vis spectral region of the electromagnetic spectrum is often called electronic spectroscopy because electrons are transferred from low-energy to high-energy molecular orbitals when the material is irradiated with light<sup>6-7</sup>.

In principle, energetically favored electronic transitions in the molecule are from the highest occupied molecular orbital (HOMO) to the lowest unoccupied molecular orbital (LUMO).

Absorption of light in the UV-vis range promotes the electrons in a lone pair (n) or bonding ( $\sigma$  or  $\pi$ ) orbital to an antibonding ( $\sigma^*$  or  $\pi^*$ ) orbital. The wavelength of light absorbed depends on the energy gap between the ground state (lower energy state) and the excited state (higher energy level) of molecular orbitals. If the energy gap is large, photons with higher energy are absorbed, corresponding to the short wavelength. When the energy gap in the molecule becomes smaller, the wavelength absorbed moves towards the low energy range of UV-vis spectral region, leading to a red shift<sup>8</sup>.

As described in **Figure II.2a**, a longer conjugated  $\pi$  system results in a smaller HOMO-LUMO gap, leading to a longer wavelength of the light absorbed<sup>8</sup>. Therefore, it is a useful tool to track the electrochemical activity loss of conducting polymers upon cycling. An example of UV-vis spectra of dodecylsulfate-doped polypyrrole (PPy-DS) film during electrochemical cycling process is presented in **Figure II.2b**.

UV-vis spectra were used in this PhD work to determine the change of band energies of PPy during cycling, reflecting the evolution of its conjugation length. UV-vis spectra were collected with a Hitachi U-4001 spectrophotometer. The films used for UV-vis spectroscopy measurements were prepared on ITO coated glass slides and cycled under the same conditions as those on gold electrode of the quartz resonators.

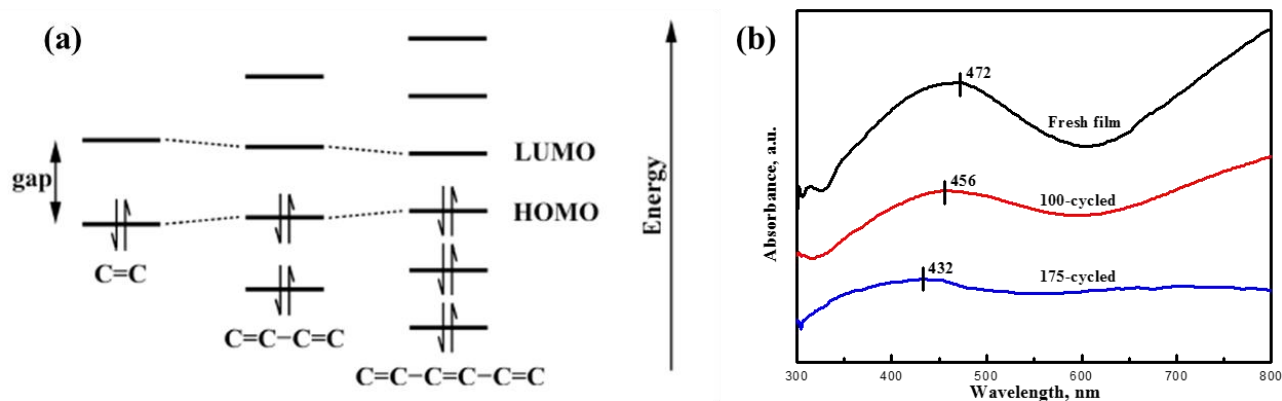


**Figure II.2.** (a) The relationship between the conjugated length in the molecule and the corresponding HOMO-LUMO gap<sup>8</sup>. (b) UV-vis spectra of fresh, 100- and 175-cycled PPy-DS film<sup>9</sup>.

### II.1.3. Scanning electron microscopy (SEM)

SEM is one of the most versatile techniques available for the examination and analysis of the morphology of materials.

The SEM technique uses a focused electron beam to scan the surface of the sample, as shown in **Figure II.3**<sup>2</sup>. SEM is performed under high vacuum in order to exclude the obstruction of the electron beam through the microscope by small particles, gas molecules or air, which could deflect the electrons and thus modify the obtained results<sup>4</sup>. Samples must be electronically conductive, at least on the surface, to prevent the accumulation of electrostatic charges that can blur the image quality at higher resolutions. Therefore, nonconductive samples are usually sputtered with an ultrathin coating of electrically conducting materials, such as gold or platinum<sup>10-11</sup>, to provide a nanometer-thick conductive layer.

The sample is irradiated by a focused electron beam, which is typically generated from an electron gun fitted with a tungsten filament cathode. Instead of bouncing off immediately, the incident electrons penetrate for some distance before they collide with surface atoms of the sample and a region of primary excitation, where signals such as secondary electrons, backscattered electrons, Auger electrons and characteristic X-rays are produced, is created<sup>2</sup>. Secondary electrons and backscattered electrons are commonly used for imaging. The secondary electrons are low energy electrons, which can reach the detector in great number depending on the incidence angle and generate topographic information of the sample surface with good edge details; whereas the backscattered electrons are electrons with higher energy deflected elastically or scattered back to the detector. They produce images of different brightness based on the sample composition: heavier elements present brighter images compared with lighter elements due to greater backscattering intensity. Therefore, the surface composition can be obtained through the images generated from the backscattered electrons<sup>2,4</sup>.

The SEM analyses of the materials in this present thesis were performed under vacuum conditions using a field emission gun scanning electron microscope (FEG-SEM, Zeiss, Supra 55).

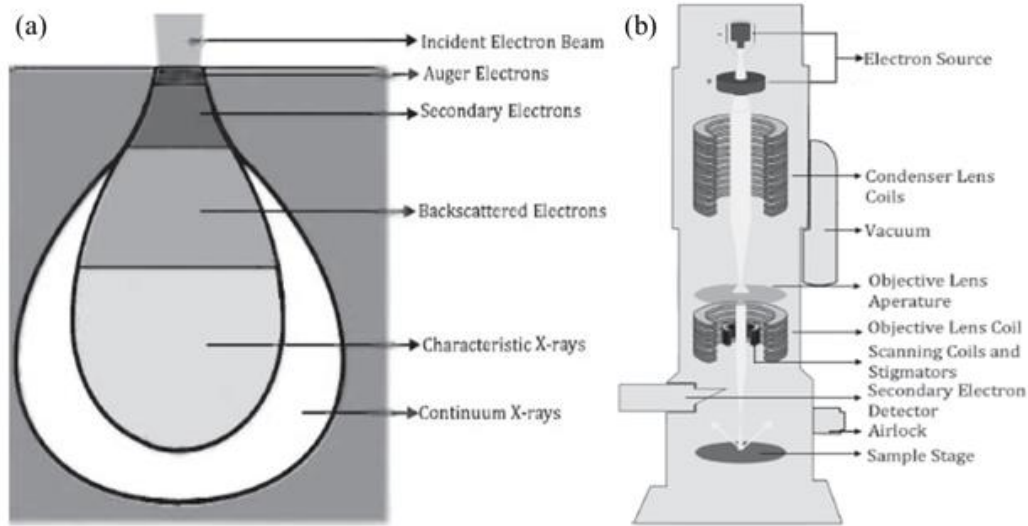


**Figure II.3.** (a) Signals generated by interaction of electron beam and specimen and regions from which each signal type can be detected. (b) Scanning electron microscope<sup>2</sup>.

#### II.1.4. X-ray diffraction (XRD)

X-rays are high-energy electromagnetic radiations. They have energies ranging from about 200 eV to 1 MeV, locating between  $\gamma$ -rays and ultraviolet (UV) radiation in the electromagnetic spectrum<sup>12</sup>. XRD is a nondestructive analytical technique where a sample is bombarded with an x-ray beam to analyze the transmitted and diffracted beams<sup>2</sup>, which can be used for characterizing and identifying crystalline structures. As shown in **Figure II.4a**<sup>12</sup>, X-rays are generated in an x-ray tube consisting of two electrodes enclosed in a vacuum chamber. The cathode (usually a tungsten filament) is heated to produce the electron emission. They are accelerated by a high potential towards the anode (usually a copper), which is grounded. The electrons with high velocity can collide with the anode and thus induce the emission of x-ray radiations<sup>12</sup>.

Each quantum of electromagnetic radiation, or photon, has an energy,  $E$ , which is proportional to its frequency,  $\nu$ :

$$E = h\nu \quad (\text{II.1})$$

The wavelength ( $\lambda$ ) of X-rays related to its frequency is characteristic of the anode material and can be expressed by:

$$\lambda = \frac{hc}{E} \quad (\text{II.2})$$

where  $h$  is the Planck's constant and  $c$  is the speed of light.

XRD can be effectively used to characterize and identify the crystal structures of materials. It is possible to determine the average spacings between layers or rows of atoms, where Bragg's law plays a fundamental role<sup>13</sup>:

$$n\lambda = 2d \sin \theta \quad (\text{II.3})$$

where  $d$  presents the interplanar spacing (the difference in path length for the ray scattered from the top plane and the ray scattered from the bottom plane),  $\theta$  is the scattering angle and  $n$  is an integer representing the order of the diffraction peak, shown in **Figure II.4 (b)**<sup>4</sup>. It demonstrates that the constructive wave interference (strong diffraction) occurs when the difference in path length for the top and bottom rays is equal to an integer multiple of the wavelength.

The XRD measurements were performed at ambient conditions using Phillips PANalytical X'Pert Pro diffractometer with Cu  $K\alpha$  radiation ( $\lambda = 1.54184 \text{ \AA}$ ).

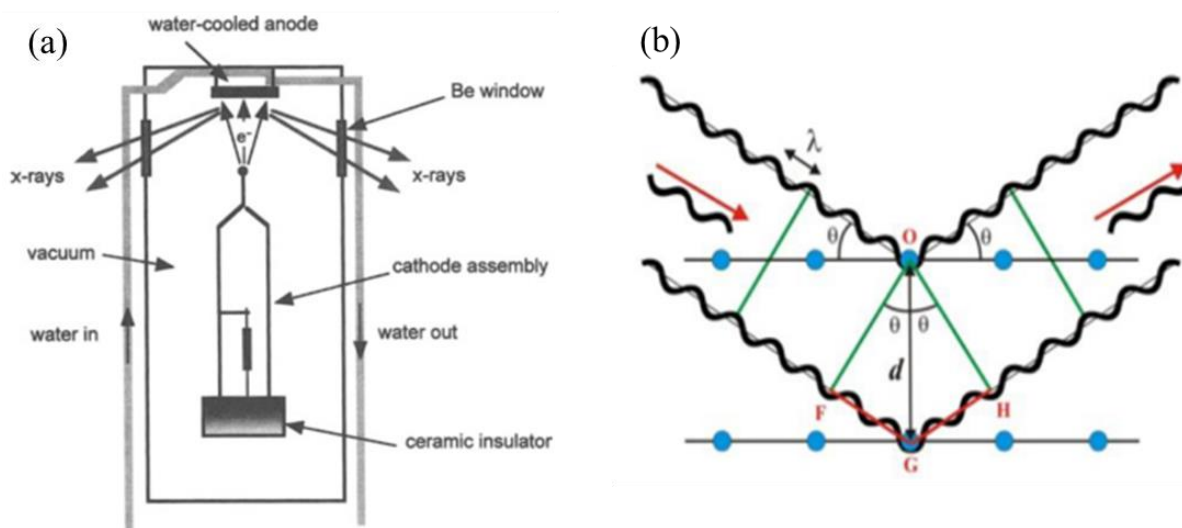


**Figure II.4.** (a) Schematic showing the essential components of a modern x-ray tube<sup>12</sup> and (b) illustration for the Bragg's law<sup>4</sup>.

### II.1.5. X-ray photoelectron spectroscopy (XPS)

XPS is one of the most powerful and common chemical analysis techniques to analyze the surface of a sample, i.e., the elements constituting the sample, surface composition and its chemical bonding state by irradiating the sample surface with photons of characteristic energy (usually  $MgK\alpha$  radiation,  $h\nu = 1253.6 \text{ eV}$ , linewidth  $0.70 \text{ eV}$ ; and  $AlK\alpha$  radiation,  $h\nu = 1486.6 \text{ eV}$ , linewidth  $0.85 \text{ eV}$ )<sup>14-16</sup>. These photons directly interact with core electrons of the sample atoms. As a result, ionized states are

created, and photoelectrons are emitted<sup>15</sup>.

Based on the photoelectric effect, the binding energy ( $E_B$ ) of a core-level electron is overcome by the energy ( $h\nu$ ) of the incident X-ray photon, resulting in the core-level electron excited and ejected from the sample. The kinetic energies ( $E_K$ ) of the ejected photoelectrons are measured by an electron spectrometer whose work function is  $\phi$ . Therefore, the ( $E_B$ ) of each emitted electron can be described by the following relationship<sup>17</sup>:

$$E_B = h\nu - E_K - \phi \quad (\text{II.4})$$

In practice, a sample is illuminated with a monochromatic single wavelength x-ray beam, causing core electrons of the sample surface to overcome their binding energy and thus escape from the sample surface where they are detected<sup>2</sup>. The binding energy of the photoelectron is characteristic of the orbital from which the photoelectron originates<sup>17</sup>. It provides detailed information about the surface elements and composition.

XPS spectra are usually plotted by intensity (counts per second) as a function of the  $E_B$  of the electrons detected, which quantify both peak intensity and peak position. The former measures how much of a material is at the sample surface, while the latter indicate the elemental and chemical composition<sup>4, 15</sup>.

In the present thesis, XPS measurements were performed using a Thermo Scientific K-Alpha X-ray photoelectron spectrometer with monochromatized Al K $\alpha$  excitation. Survey and high-resolution spectra were acquired with a pass energy of 100 eV and 20 eV, respectively. The experimental data were analyzed using the Avantage software. The sample elemental composition was determined by measuring the photopeak area after a Shirley background subtraction.

## II.2. Electrochemical and electrogravimetric characterization

The electrochemical and electrogravimetric characterizations were performed based on quartz crystal microbalance (QCM). In the present PhD work, the global electrochemical behaviors of different SC electrodes were tracked by coupling the QCM with cyclic voltammetry (CV) and galvanostatic charge/discharge (GCD) techniques, namely, electrochemical quartz crystal microbalance (EQCM). A method coupling QCM with electrochemical impedance spectroscopy (EIS), i.e., *ac*-electrogravimetry, was employed to disentangle the subtleties of global charge

compensation process, offering a quantitative picture of each participant with their transfer kinetics and identifying them by their molar masses.

### II.2.1. Electrochemical quartz crystal microbalance (EQCM)

EQCM, also called cyclic electrogravimetry, is a technique coupling Quartz Crystal Microbalance (QCM) and electrochemical measurements, which cannot only track the current response but also the simultaneous mass change occurring in the working electrode during an electrochemical process<sup>18-20</sup>.

The gravimetric measurements were performed based on quartz crystal microbalance (QCM) with piezoelectric effect. **Figure II.5** schematically illustrates the piezoelectric effect through the generating of an electric charge as the result of a force exerted on the piezoelectric material<sup>21</sup>. The gravity centers of the negative and positive charges of each molecule coincide before the material subjected to the external force (**Figure II.5a**), resulting in the reciprocal cancellation of the external effects from negative and positive charges; upon an external force, dipoles can be formed because of the separation of the positive and negative gravity centers of the molecules (**Figure II.5b**); Then, an electric field appears in the material (**Figure II.5c**). Contrarily, when a voltage is applied on a piezoelectric material, a corresponding mechanical deformation would be produced, which is called reverse piezoelectric effect and serves as the fundamental principle for the microbalance operation.

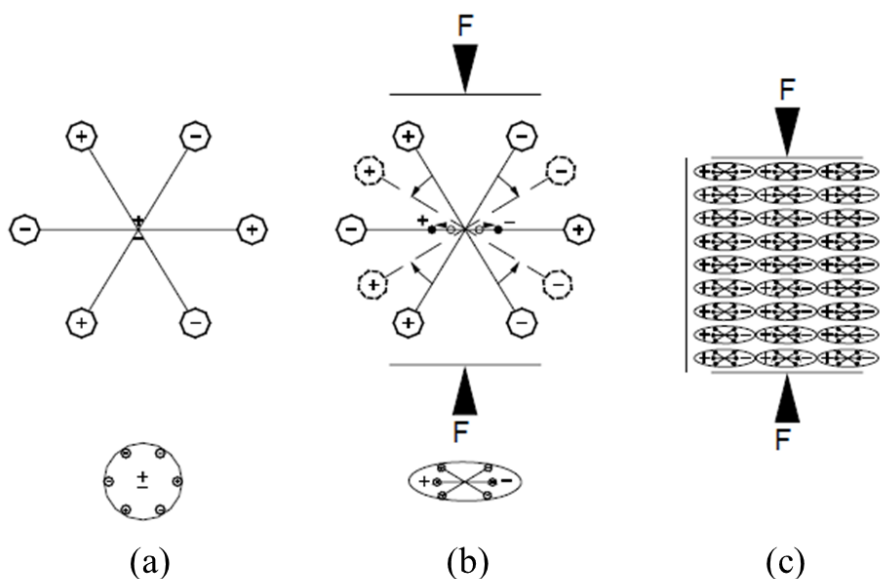


**Figure II.5.** Simple molecular model for explaining the piezoelectric effect: (a) unperturbed molecule; (b) molecule subjected to an external force, and (c) polarizing effect on the material surfaces<sup>21</sup>.

In the present work, the gold (0.2 cm<sup>2</sup>) coated quartz resonator with a diameter of 14 mm (9 MHz-AWS, Valencia, Spain) is used. The electrochemical performances of different electroactive materials-loaded quartz resonator were characterized by CV and GCD. The QCM was coupled with both measurements to track the simultaneous frequency shift ( $\Delta f$ ) of the quartz resonator electrode during electrochemical process, which can be converted into mass response ( $\Delta m$ ) according to Sauerbrey equation<sup>22</sup>:

$$\Delta f = -C_f \times \Delta m \quad (\text{II.5})$$

where  $C_f$  is the sensitivity factor of the quartz crystal resonator and can be checked by the electroacoustic measurements<sup>23</sup> and  $\Delta m$  presents the film mass change per unit area. It should be noted that electroacoustic measurements are necessary for the correction of sensitivity factor of the quartz resonator since Sauerbrey equation is only valid for sufficiently thin and rigid film.

The EQCM measurements were performed employing a standard three-electrode electrochemical cell (**Figure II.6a**), which consisted of electroactive materials-loaded quartz resonator (9 MHz-AWS, Valencia, Spain) as the working electrode, a saturated calomel electrode (SCE) or Ag/AgCl (3 M KCl saturated with AgCl) as the reference electrode, and platinum grid as the counter electrode. The cell is connected to a Yokogawa frequency counter and a potentiostat (Biologic SP200 or Autolab PGSTAT 100). **Figure II.6b** presented an example of EQCM result from quartz resonator loaded by electrochemically reduced graphene oxide (ERGO) with the different content of oxygen functionalities on its basal planes in 1 M NaCl at a scan rate of 10mV/s, which will be discussed in detail in Chapter IV.

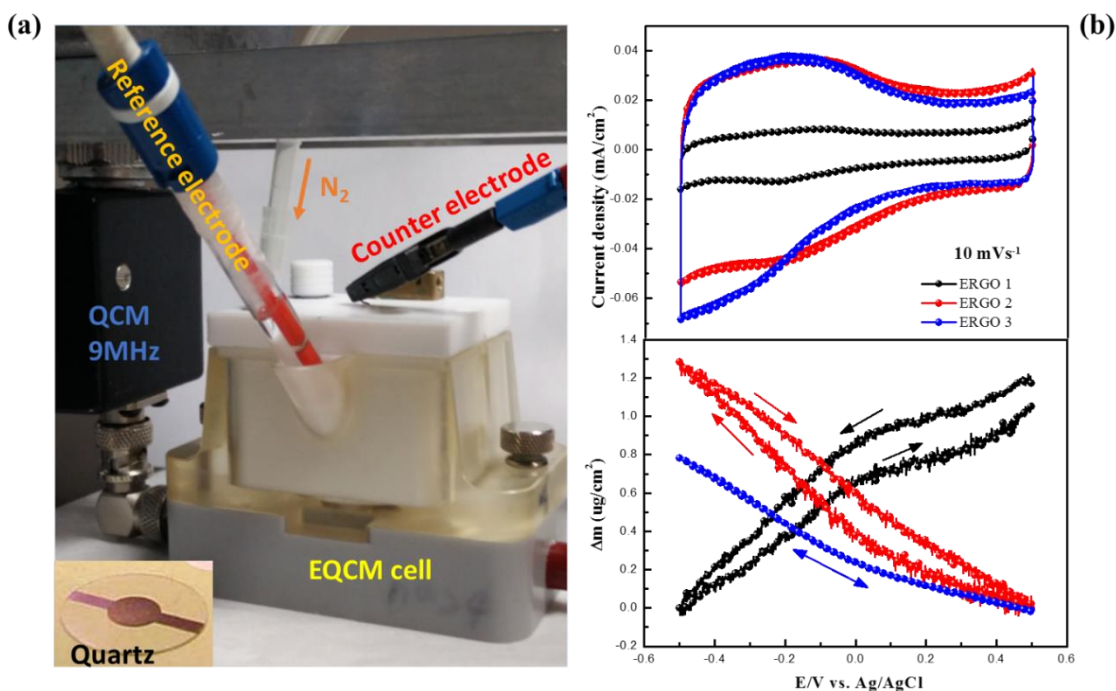


**Figure II.6.** (a) A lab-made EQCM cell and (b) EQCM results of ERGO electrodes with the different content of oxygen functionalities. The inset in (a) is the picture of quartz resonator used in the present work. The upper curve in (b) is the current response whereas the lower curve is the corresponding mass vs. potential profile during cycling.

### II.2.2. *Ac*-electrogravimetry

*Ac*-electrogravimetry is a pertinent method to study the mechanism of transfer of different species directly or indirectly involved in the charge compensation process associated to an electrochemical process. In this approach, these transferred species at different kinetics can be separated and their identification can also be clearly achieved<sup>24-25</sup>.

In *ac*-electrogravimetry, one of the most important components of the experimental set-up is the frequency/voltage (F/V) converter, where the analog processing was obtained by means of a phase lock loop circuit, as described in **Figure II.7**<sup>26</sup>. More precisely, the microbalance frequency signal is translated into the voltage signal in frequency/voltage converter and sent to the Frequency Response Analyzer (FRA, SOLARTRON 1254), as shown in **Figure II.8**. The electrogravimetric transfer function (TF),  $\frac{\Delta m}{\Delta E}(\omega)$  can be simultaneously obtained with the electrochemical impedance,  $\frac{\Delta E}{\Delta I}(\omega)$ . It should be noted that these two TFs are not directly obtained. The raw TFs,  $\frac{\Delta V_f}{\Delta V}(\omega)$

and  $\frac{\Delta V}{\Delta I}(\omega)$  are directly measured by the FRA from which the  $\frac{\Delta m}{\Delta E}(\omega)$  and  $\frac{\Delta E}{\Delta I}(\omega)$  are obtained after a numerical treatment in Mathcad software.

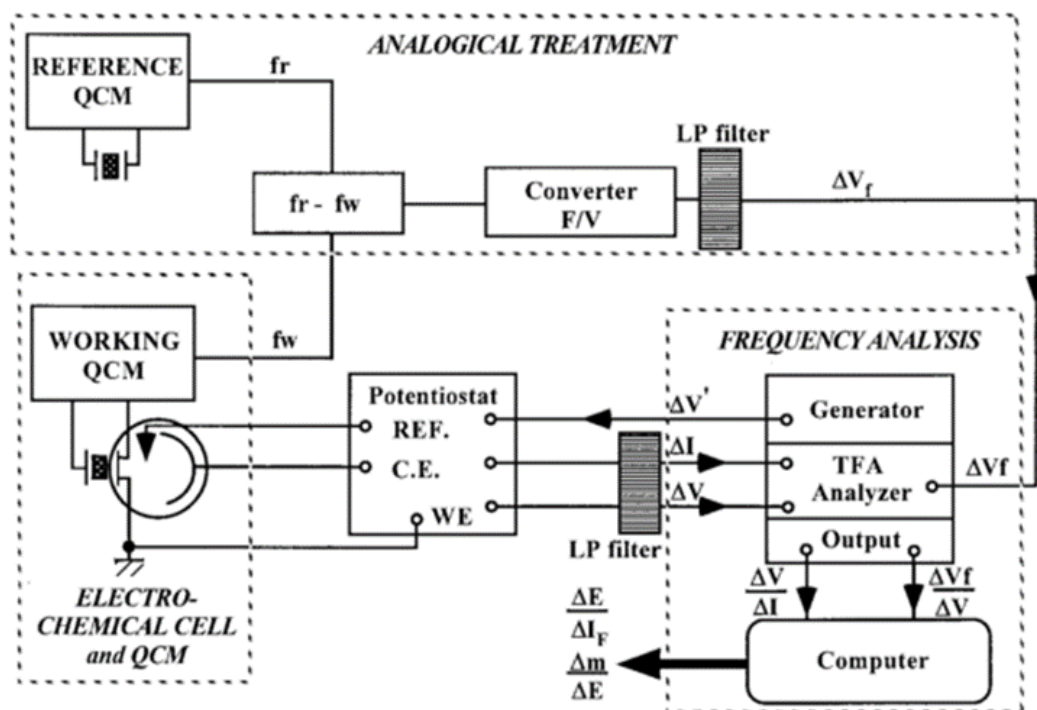


Figure II.7. Block diagram of the experimental set-up.<sup>26</sup>

Although the electrochemical impedance and the electrogravimetric TF are simultaneously measured, the frequency range of measurement for impedance is from ~65 KHz to ~10 mHz but only from ~1 KHz to ~10 mHz for the electrogravimetric TF, which is ascribed to a distortion of working frequency signal (phase shift and modulus attenuation) occurring in the detection device (F/V converter).<sup>26</sup> The F/V converter sensitivity in the linear part is around  $29\text{mVHz}^{-1}$ .<sup>27-28</sup>

Compared to  $\frac{\Delta E}{\Delta I}(\omega)$  TF, only considering the ionic species transfer, the  $\frac{\Delta m}{\Delta E}(\omega)$  TF also takes the free solvent contribution into account. It should be noted that the microbalance frequency change,  $\Delta f_m$ , is generally around tens of hertz while the carrier frequency,  $f_m$ , is around 9 MHz. In order to have a higher level of performance of the F/V converter, the carrier frequency is reduced to a few hundred hertz (generally ~ 400 Hz). Herein, a reference frequency synthesizer (Agilent 33250A) is used to obtain a frequency difference of ~ 400 Hz between the microbalance quartz frequency (shown on the frequency counter) and that from the reference synthesizer. Finally, the raw TF  $\frac{\Delta V_f}{\Delta V}(\omega)$  and

$\frac{\Delta V}{\Delta I}(\omega)$  were measured by the FRA, which leads to the electrogravimetric TF ( $\frac{\Delta m}{\Delta E}(\omega)$ ) and the electrical TF ( $\frac{\Delta E}{\Delta I}(\omega)$ ) to be obtained simultaneously at a given potential and frequency modulation,  $f$  (pulsation  $\omega=2\pi f$ ).

Based on the electrochemical impedance ( $\frac{\Delta E}{\Delta I}(\omega)$ ), the experimental charge/potential  $\frac{\Delta q}{\Delta E}(\omega)$  TF can be calculated in order to have a clearer view on the ionic species involved in the electrochemical process:

$$\left. \frac{\Delta q}{\Delta E}(\omega) \right|_{\text{exp}} = \frac{1}{j\omega} \left. \frac{\Delta I}{\Delta E}(\omega) \right|_{\text{exp}} \quad (\text{II.6})$$

Correspondingly, from the experimental electrogravimetric TF,  $\frac{\Delta m}{\Delta E}(\omega)$ , several partial mass/potential transfer functions can also be calculated by removing one of the participants in the charge compensation process. For example, if four species are involved in the electrochemical process: cation 1 ( $c_1$ ) with valence  $Z_{c_1}$ , cation 2 ( $c_2$ ) with valence  $Z_{c_2}$ , anion ( $a$ ) with valence  $Z_a$  and solvent ( $s$ ), the different experimental partial mass/potential TFs can be estimated by extracting contributions from anion, cation 1 and cation 2, respectively, which can be expressed as following equations:

$$\left. \frac{\Delta m}{\Delta E}(\omega) \right|_{\text{exp}}^{c_1 c_2 s} = \left. \frac{\Delta m}{\Delta E}(\omega) \right|_{\text{exp}} - \frac{M_a}{FZ_a} \left. \frac{\Delta q}{\Delta E}(\omega) \right|_{\text{exp}} \quad (\text{II.7})$$

$$\left. \frac{\Delta m}{\Delta E}(\omega) \right|_{\text{exp}}^{c_2 a s} = \left. \frac{\Delta m}{\Delta E}(\omega) \right|_{\text{exp}} + \frac{M_{c_1}}{FZ_{c_1}} \left. \frac{\Delta q}{\Delta E}(\omega) \right|_{\text{exp}} \quad (\text{II.8})$$

$$\left. \frac{\Delta m}{\Delta E}(\omega) \right|_{\text{exp}}^{c_1 a s} = \left. \frac{\Delta m}{\Delta E}(\omega) \right|_{\text{exp}} + \frac{M_{c_2}}{FZ_{c_2}} \left. \frac{\Delta q}{\Delta E}(\omega) \right|_{\text{exp}} \quad (\text{II.9})$$

From a theoretical point of view, the concentration variation of each species,  $\Delta C_i$ , under a sinusoidal potential perturbation,  $\Delta E$ , at the film/electrolyte interface can be described as<sup>25, 29</sup>:

$$\left. \frac{\Delta C_i}{\Delta E}(\omega) \right|_{\text{th}} = \frac{-G_i}{j\omega d_f + K_i} \quad (\text{II.10})$$

where  $K_i$  and  $G_i$  are the partial derivatives of the flux ( $J_i$ ) with respect to the concentration and the potential, respectively and  $d_f$  is the film thickness.

$K_i$  represents the transfer kinetics of each species related to the characteristic frequency of one species

(*f*) while  $G_i$  is the reciprocal of the transfer resistance ( $Rt_i = \frac{1}{FG_i}$ ). It represents the ease or difficulty of the species transfer at the film/electrolyte interface. Similarly, four species are considered in the electrochemical process, cation 1 ( $c_1$ ) with valence  $Z_{c_1}$ , cation 2 ( $c_2$ ) with valence  $Z_{c_2}$ , anion ( $a$ ) with valence  $Z_a$  and solvent ( $s$ ), the faradic impedance,  $Z_F(\omega)$  can be expressed as:

$$Z_F(\omega)\Big|_{th} = \frac{\Delta E}{\Delta I_F}(\omega)\Big|_{th} = \left[ j\omega F d_f \left( -Z_{c_1} \frac{\Delta C_{c_1}}{\Delta E}(\omega) - Z_{c_2} \frac{\Delta C_{c_2}}{\Delta E}(\omega) + Z_a \frac{\Delta C_a}{\Delta E}(\omega) \right) \right]^{-1} \quad (\text{II.11})$$

where  $\Delta C_{c_1}$ ,  $\Delta C_{c_2}$  and  $\Delta C_a$  are the concentration changes for cation 1, 2 and anion,  $F$  is the Faraday constant and  $\omega$  is the pulsation.

Then, the global electrochemical impedance,  $\frac{\Delta E}{\Delta I}(\omega)$  can be defined as:

$$\frac{\Delta E}{\Delta I}(\omega)\Big|_{th} = \left[ j\omega C_{dl} + j\omega F d_f \left( Z_{c_1} \frac{G_{c_1}}{j\omega d_f + K_{c_1}} + Z_{c_2} \frac{G_{c_2}}{j\omega d_f + K_{c_2}} - Z_a \frac{G_a}{j\omega d_f + K_a} \right) \right]^{-1} + R_{el} \quad (\text{II.12})$$

where  $C_{dl}$  and  $R_{el}$  are the interfacial capacitance and electrolyte resistance, respectively.

Parallely, the electrogravimetric transfer function,  $\frac{\Delta m}{\Delta E}(\omega)$  can be expressed as **Equation II.13**,

where  $M_i$  ( $i = c_1, c_2, a$  and  $s$ ) is the molar mass for each participant.

$$\frac{\Delta m}{\Delta E}(\omega)\Big|_{th} = -d_f \left( M_{c_1} \frac{G_{c_1}}{j\omega d_f + K_{c_1}} + M_{c_2} \frac{G_{c_2}}{j\omega d_f + K_{c_2}} + M_a \frac{G_a}{j\omega d_f + K_a} + M_s \frac{G_s}{j\omega d_f + K_s} \right) \quad (\text{II.13})$$

Charge/potential transfer function,  $\frac{\Delta q}{\Delta E}(\omega)$  only takes into consideration ionic species transfer

and it can be defined as:

$$\frac{\Delta q}{\Delta E}(\omega)\Big|_{th} = \frac{1}{j\omega} \frac{\Delta I_F}{\Delta E}(\omega) = F d_f \left( Z_{c_1} \frac{G_{c_1}}{j\omega d_f + K_{c_1}} + Z_{c_2} \frac{G_{c_2}}{j\omega d_f + K_{c_2}} - Z_a \frac{G_a}{j\omega d_f + K_a} \right) \quad (\text{II.14})$$

Additionally, the partial TFs are used to provide a crosscheck for validation of hypothesis involving a multiple species transfer. For example, the partial TF,  $\frac{\Delta m}{\Delta E}(\omega)\Big|_{th}^{c_1 c_2 s}$  can be obtained by

removing the anion contribution:

$$\frac{\Delta m}{\Delta E}(\omega)\Big|_{th}^{c_1 c_2 s} = \frac{\Delta m}{\Delta E}(\omega) - M_a \left( -\frac{\Delta C_{c_1}}{\Delta E}(\omega) - \frac{\Delta C_{c_2}}{\Delta E}(\omega) + \frac{\Delta C_a}{\Delta E}(\omega) \right)$$

$$= -d_f \left( (M_{c_1} + M_a) \frac{G_{c_1}}{j\omega d_f + K_{c_1}} + (M_{c_2} + M_a) \frac{G_{c_2}}{j\omega d_f + K_{c_2}} + M_s \frac{G_s}{j\omega d_f + K_s} \right) \quad (\text{II.15})$$

Similarly, removing the contribution from cation 1 or 2 leads to the partial TF  $\left. \frac{\Delta m}{\Delta E}(\omega) \right|_{th}^{c_2as}$  and

$\left. \frac{\Delta m}{\Delta E}(\omega) \right|_{th}^{c_1as}$ , respectively:

$$\begin{aligned} \left. \frac{\Delta m}{\Delta E}(\omega) \right|_{th}^{c_2as} &= \frac{\Delta m}{\Delta E}(\omega) + M_{c_1} \left( -\frac{\Delta C_{c_1}}{\Delta E}(\omega) - \frac{\Delta C_{c_2}}{\Delta E}(\omega) + \frac{\Delta C_a}{\Delta E}(\omega) \right) \\ &= -d_f \left( (M_{c_2} - M_{c_1}) \frac{G_{c_2}}{j\omega d_f + K_{c_2}} + (M_a + M_{c_1}) \frac{G_a}{j\omega d_f + K_a} + M_s \frac{G_s}{j\omega d_f + K_s} \right) \end{aligned} \quad (\text{II.16})$$

$$\begin{aligned} \left. \frac{\Delta m}{\Delta E}(\omega) \right|_{th}^{c_1as} &= \frac{\Delta m}{\Delta E}(\omega) + M_{c_2} \left( -\frac{\Delta C_{c_1}}{\Delta E}(\omega) - \frac{\Delta C_{c_2}}{\Delta E}(\omega) + \frac{\Delta C_a}{\Delta E}(\omega) \right) \\ &= -d_f \left( (M_{c_1} - M_{c_2}) \frac{G_{c_1}}{j\omega d_f + K_{c_1}} + (M_a + M_{c_2}) \frac{G_a}{j\omega d_f + K_a} + M_s \frac{G_s}{j\omega d_f + K_s} \right) \end{aligned} \quad (\text{II.17})$$

To illustrate what the experimental *ac*-electrogravimetry data may look like, the  $\frac{\Delta E}{\Delta I}(\omega)$ ,

$\frac{\Delta q}{\Delta E}(\omega)$  and  $\frac{\Delta m}{\Delta E}(\omega)$  TFs are shown schematically in **Figure II.8**. For a single ion transfer at the

electrode/electrolyte interface, a typical cation and anion contribution appear characteristically on the

III and the I quadrant (Cartesian system) of the  $\frac{\Delta m}{\Delta E}(\omega)$  TF (**Figure II.8c**), respectively. It is

important to note that the  $\frac{\Delta m}{\Delta E}(\omega)$  is the only TF that can discriminate between the cations or anions

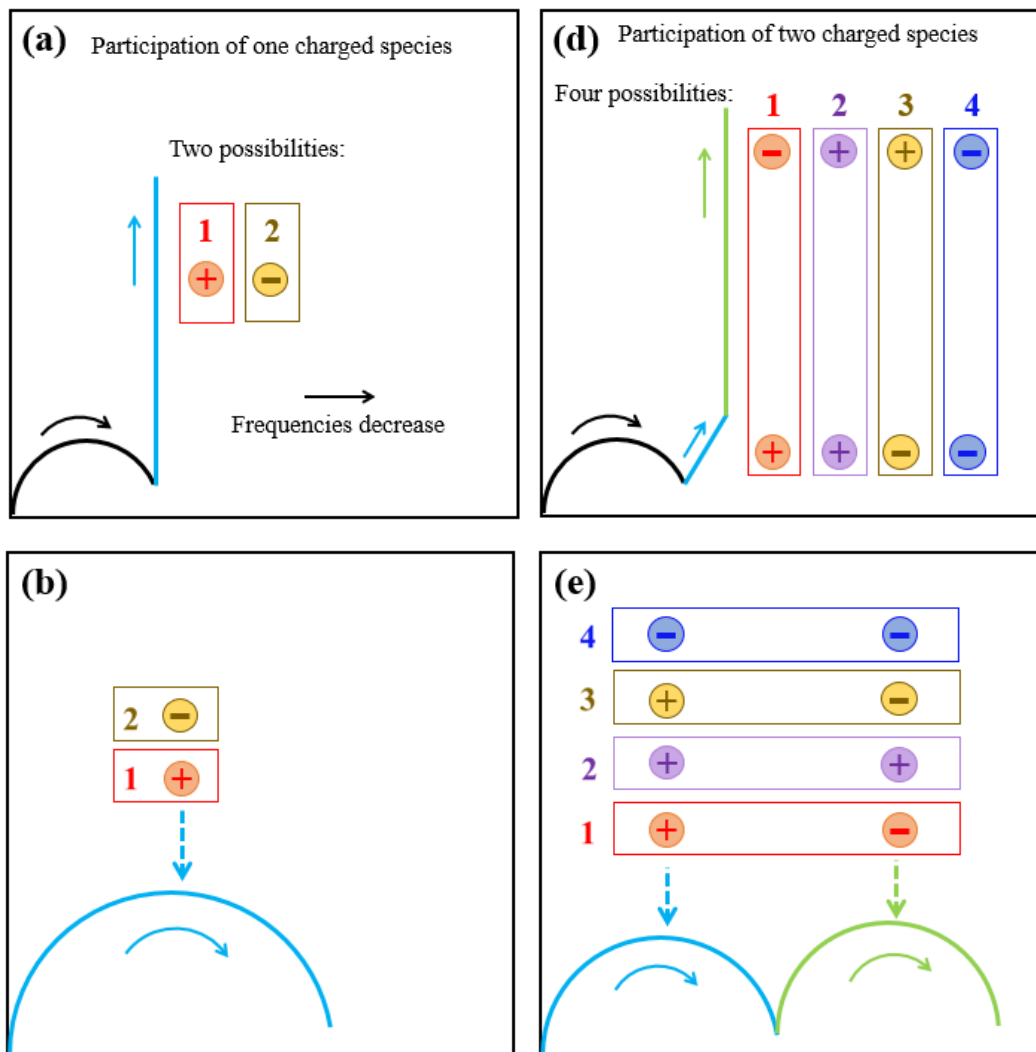
and identify them by their molar mass. In a more complex electrochemical process, where a multi-ion transfer occurs, the above mentioned TFs may look like as shown in **Figure II.8d-f**. The low

frequency response of the  $\frac{\Delta E}{\Delta I}(\omega)$  (**Figure II.8d**) may translate into two separate loops if the

respective time constants of the participating ions are different enough. However, it is noted that the

four different configurations given in **Figure II.8e** result in the same response in terms of  $\frac{\Delta q}{\Delta E}(\omega)$

TF. The utility and the power of the  $\frac{\Delta m}{\Delta E}(\omega)$  TF is more evident in **Figure II.8f**, where 4 possibilities of ionic transfers (two cations, two anions, a cation/anion and an anion/cation) can be distinguished, with further kinetic resolution depending on the dynamics of interfacial transfer (i.e., the configuration 1 shows the case where the cation transfer is faster than that of anion and the configuration 3 presents the case which is the *vice versa*. Configurations 2 and 4 show two other different cases). For the sake of clarity, the H<sub>2</sub>O contribution was not taken into account, which can participate in charge compensation (i) in the free form with the same direction of a cation or an anion flux or (ii) in the hydration shell of a cation or an anion.



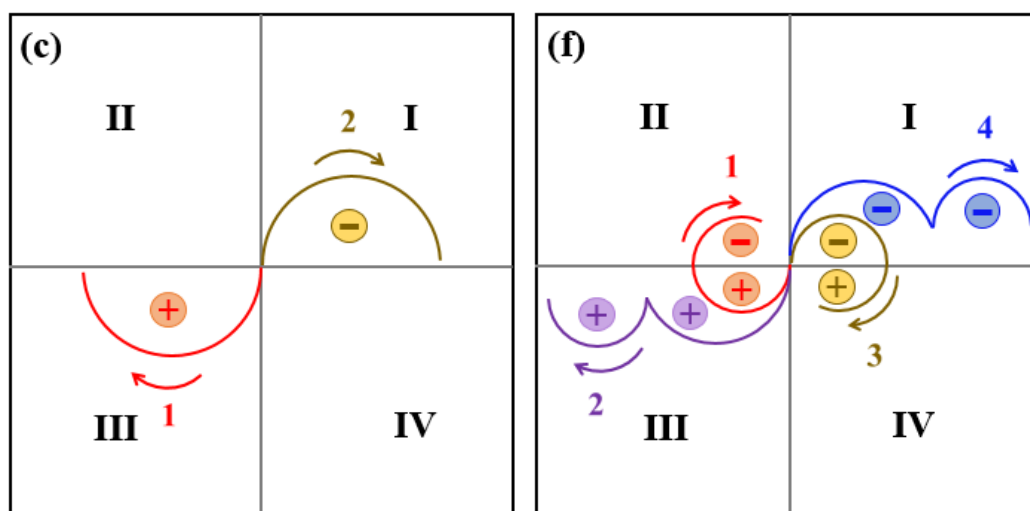


**Figure II.8.** Representation of the some of the possible experimental Transfer Functions (TFs) for  $\Delta E/\Delta I(\omega)$  (a, d),  $\Delta q/\Delta E(\omega)$  (b, e) and  $\Delta m/\Delta E(\omega)$  (c, f). The response of one and two charged species was depicted in (a, b, c) and (d, e, f), respectively. Note:  $H_2O$  contribution was not taken into account, which can participate in charge compensation either in the free form with the same direction of a cation/anion flux or in the hydration shell of cation/anion. In these representations, the time constants of ionic species are different enough so that they are seen as separate contributions.

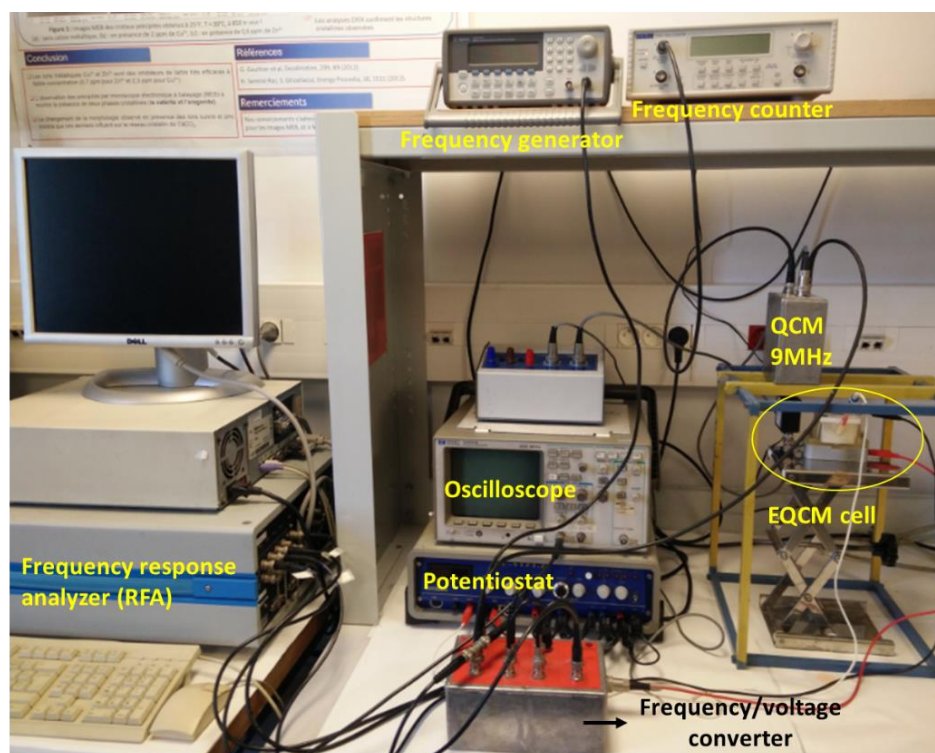


**Figure II.9.** Ac-electrogravimetry setup.

*Ac*-electrogravimetry measurements were performed in the same three-electrode cell as described in EQCM measurements (**Figure II.9**). The QCM was performed under dynamic regime, and the modified working electrode was polarized at selected potentials to which a sinusoidal small amplitude potential perturbation (80 mV rms) was superimposed.

### II.3. Electroacoustic impedance measurement

Electroacoustic impedance/admittance measurement is an effective technique to investigate the viscoelastic properties of thin films. It can be used to study the viscoelastic effect of the deposited film on the QCM and if necessary, to correct the gravimetric sensitivity coefficient given by the Sauerbrey equation<sup>23</sup>. Due to the piezoelectric nature of the quartz crystal, the film's viscoelastic properties are reflected in the electrical response of the film-loaded quartz resonator, as measured in an electroacoustic impedance experiment<sup>30</sup>. The surface mechanical impedance ( $Z_m^V$ ) at the quartz resonator surface determining the electrical response of the film-loaded quartz resonator, can be expressed by the following equation<sup>23, 30-31</sup>:

$$Z_m^V(\omega) = \frac{h_q^2}{4 \times e_q^2 \times A} \times Z_f \times \frac{Z_s + Z_f \times \tanh(\theta_f \times h_f)}{Z_f + Z_s \times \tanh(\theta_f \times h_f)} \quad (\text{II.18})$$

where  $h_q$  is the quartz thickness,  $e_q$  is the quartz piezoelectric constant,  $A$  is the active mass area,  $Z_f$  is the acoustic impedance of the film,  $Z_s$  is the acoustic impedance of the liquid,  $\theta_f$  is the complex propagation constant of the film and  $h_f$  is its thickness. Moreover,  $Z_f$  and  $\theta_f$  can be described as:

$$Z_f = \sqrt{\rho_f \times G_f} \quad (\text{II.19})$$

$$\theta_f = \sqrt{\frac{\rho_f}{G_f}} \quad (\text{II.20})$$

where  $\rho_f$  is the film density and  $G_f$  is the shear thickness modulus of the film, which can be written as a complex number with a real and imaginary part,  $G_f = G + jG''$ , where  $j^2 = -1$ .

Two methods were proposed to obtain a mass sensitivity coefficient of the Sauerbrey equation,

which eliminates the viscoelastic contribution of the loaded film<sup>23</sup>. The first is based on the assumption that the thickness of the loaded film is constant:

$$C_f^{h_f} = \frac{f_s^V(\rho_f^{\max}, h_f, G_1, G_2) - f_s^V(\rho_f^{\min}, h_f, G_1, G_2)}{(\rho_f^{\max} - \rho_f^{\min}) \times h_f} \quad (\text{II.21})$$

And the second is based on a constant film density:

$$C_f^{\rho_f} = \frac{f_s^V(\rho_f, h_f^{\max}, G_1, G_2) - f_s^V(\rho_f, h_f^{\min}, G_1, G_2)}{(h_f^{\max} - h_f^{\min}) \times \rho_f} \quad (\text{II.22})$$

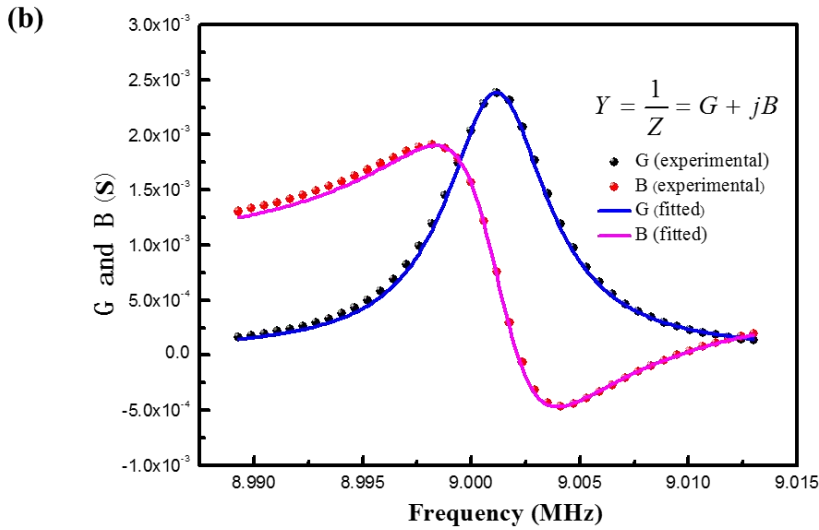
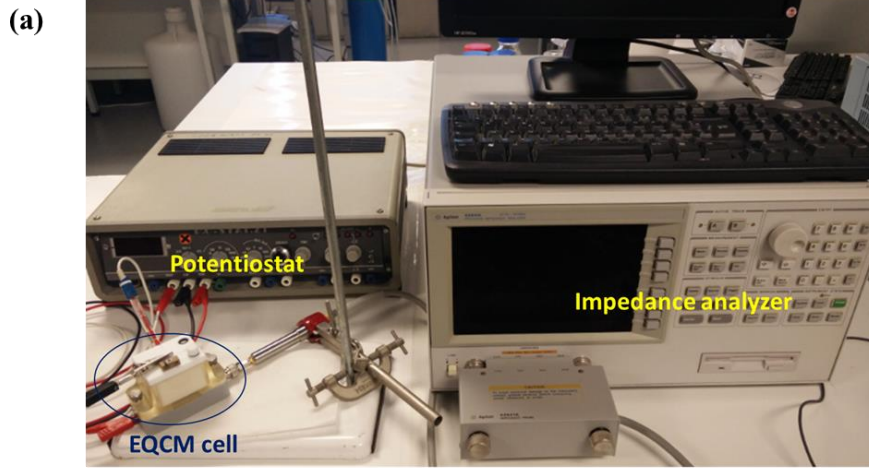


**Figure II.10.** (a) Electroacoustic impedance set-up and (b) an example for the fitting of the experimental response for ERGO-1 at -0.2 V. Fitting parameters:  $G' = 6.29 \times 10^5 \text{ N.m}^{-2}$ ,  $G'' = 0.84 \times 10^5 \text{ N.m}^{-2}$ ,  $d_f = 146 \text{ nm}$  and  $\rho_f = 2 \text{ g.cm}^{-3}$ .

In the present thesis, an Agilent 4294A impedance analyzer coupled with a lab-made potentiostat

(SOTELEM-PGSTAT), as shown in **Figure II.10a**, was used to perform the electroacoustic admittance measurements under polarization. The electroacoustic impedance measurements of neat quartz resonator in air and in solution were firstly conducted. Then, the film was (electro)deposited on the same quartz resonator, namely, a film-loaded quartz resonator. Similarly, the electroacoustic impedance measurements of the film-loaded quartz resonator were also carried out in air and in solution, respectively. In the end, the electroacoustic measurements were performed at different polarization values.

A software developed in our laboratory (Simad) was used for fitting the experimental data of quartz resonator in air and in solution to get its characteristic parameters, which can be used for extracting the storage moduli ( $G'$ ) and the loss moduli ( $G''$ ) of the film. **Figure II.10b** shows an example for the fitting of the experimental response of ERGO-1 at -0.2 V, which takes into consideration four parameters of the film, i.e., film thickness ( $d_f$ ), film density ( $\rho_f$ ),  $G'$  and  $G''$ . These results will be discussed in details in Chapter IV.

### References

1. Smith, B. C., Fundamentals of Fourier transform infrared spectroscopy. *2nd ed. CRC Press, Boca Raton* **2011**.
2. A. Yu; Chabot, V.; Zhang, J., Electrochemical Supercapacitors for Energy Storage and Delivery: Fundamentals and Applications. *CRC Press, Taylor & Francis, Boca Raton, FL* **2013**.
3. Bagheri, S.; Weber, K.; Gissibl, T.; Weiss, T.; Neubrech, F.; Giessen, H., Fabrication of Square-Centimeter Plasmonic Nanoantenna Arrays by Femtosecond Direct Laser Writing Lithography: Effects of Collective Excitations on SEIRA Enhancement. *ACS Photonics* **2015**, *2* (6), 779-786.
4. Ballester, S. C. S., Synthesis and characterization of new polymer electrolytes to use in fuel cells fed with bio-alcohols. *Ph.D. thesis. Universitat Politècnica de València* **2017**.
5. Skoog, D. A.; Holler, F. J.; Crouch, S. R., Principles of instrumental analysis (6th ed.). *Thomson-Brooks/Cole, Belmont, USA* **2007**.
6. Weckhuysen, B. M., in-situ spectroscopy of catalysts. *American scientific publishers: Stevenson Ranch, CA*. **2004**.
7. Weckhuysen, B. M.; Van Der Voort, P.; Catana, G., Spectroscopy of transition metal ions on surfaces. *Leuven University Press, Belgium* **2000**.
8. Jacobsen, N. E., NMR data interpretation explained: understanding 1D and 2D NMR spectra of organic compounds and natural products. *John Wiley & Sons, Inc., Hoboken, New Jersey* **2017**.
9. GAO, W.; Sel, O.; Perrot, H., Electrochemical and viscoelastic evolution of dodecyl sulfate-doped polypyrrole films during electrochemical cycling. *Electrochim. Acta* **2017**, *233*, 262-273.
10. Zhou, W.; Apkarian, R. P.; Wang, Z. L.; Joy, D., Scanning electron microscopy (SEM). In: Zhou, W. and Wang, Z.L., Eds., Scanning microscopy for nanotechnology: techniques and applications. Springer, New York. **2006**.
11. Reimer, L., Scanning electron microscopy: physics of image formation and microanalysis, 2nd ed. Springer, Berlin. **1998**.
12. Suryanarayana, C.; Norton, M. G., X-ray diffraction. Springer, New York. **1998**.
13. Fultz, B.; Howe, J., Transmission electron microscopy and diffractometry of materials. *Springer, 2013* **2013**.
14. Chen, M.; Wang, X.; Yu, Y. H.; Pei, Z. L.; Bai, X. D.; Sun, C.; Huang, R. F.; Wen, L. S., X-ray photoelectron spectroscopy and auger electron spectroscopy studies of Al-doped ZnO films. *Appl. Surf. Sci.* **2000**, *158*, 134-140.
15. Hofmann, S., Auger- and X-ray photoelectron spectroscopy in materials science. *Springer Verlag, Berlin* **2013**.
16. Alford, T. L.; Feldman, L. C.; Mayer, J. W., Fundamentals of nanoscale film analysis. *Springer, New York* **2007**.
17. Vij, D. R., Handbook of applied solid state spectroscopy. *Springer, New York* **2006**.
18. Tsai, W. Y.; Taberna, P. L.; Simon, P., Electrochemical quartz crystal microbalance (EQCM) study of ion dynamics in nanoporous carbons. *J. Am. Chem. Soc.* **2014**, *136* (24), 8722-8.
19. Inzelt, G.; Kertesz, V.; Nyback, A.-S., Electrochemical quartz crystal microbalance study of ion transport accompanying charging-discharging of poly(pyrrole) films. *J. Solid State Electrochem.* **1999**, *3*, 251-257.
20. Levi, M. D.; Salitra, G.; Levy, N.; Aurbach, D.; Maier, J., Application of a quartz-crystal microbalance to measure ionic fluxes in microporous carbons for energy storage. *Nat. Mater.* **2009**, *8* (11), 872-5.
21. Vives, A. A., Piezoelectric Transducers and Applications *Springer-Verlag, Berlin Heidelberg* **2008**.
22. Sauerbrey, G., The use of a quartz crystal oscillator for weighing thin layers and microweighing applications. *Z. Phys.* **1959**, *155*, 206-222.
23. García-Jareño, J. J.; Gabrielli, C.; Perrot, H., Validation of the mass response of a quartz crystal microbalance coated with Prussian Blue film for ac electrogravimetry. *Electrochem. Commun.* **2000**, *2* (3), 195-200.
24. Gabrielli, C.; Garcia-Jareno, J. J.; Keddam, M.; Perrot, H.; Vicente, F., Ac-electrogravimetry study of electroactive thin films. II. Application to polypyrrole. *J. Phys. Chem. B* **2002**, *106*, 3192-3201.
25. Gabrielli, C.; Garcia-Jareño, J. J.; Perrot, H., Charge compensation process in polypyrrole studied by ac

## Chapter II: Experimental procedures

---

electrogravimetry. *Electrochim. Acta* **2001**, *46* (26), 4095-4103.

26. Gabrielli, C.; Keddam, M.; Perrot, H.; Pham, M. C.; Torresi, R., Separation of ionic and solvent transport during charge compensation processes in electroactive polymers by a.c. electrogravimetry. *Electrochim. Acta* **1999**, *44*, 4217-4225.

27. Kim, L. T. T., Etude de films électroactifs par couplage de techniques électrochimique et gravimétrique. Application à la caractérisation de membranes à conduction protonique. *Ph.D. thesis. Université Pierre et Marie Curie* **2009**.

28. Teran, F. E., A new approach towards understanding the ion transfer dynamics in nanostructured carbon-based thin films for energy storage applications. *Ph.D. thesis. Université Pierre et Marie Curie* **2016**.

29. Gabrielli, C.; Perrot, H., Ac-electrogravimetry investigation in electroactive thin films. *Mod. Aspects Electrochem.* **2009**, *44*, 151-238.

30. Hillman, A. R.; Jackson, A.; Martin, S. J., The problem of uniqueness of fit for viscoelastic films on thickness-shear mode resonator surfaces. *Anal. Chem.* **2001**, *73*, 540-549.

31. Granstaff, V. E.; Martin, S. J., Characterization of a thickness-shear mode quartz resonator with multiple nonpiezoelectric layers. *J. Appl. Phys.* **1994**, *75* (3), 1319-1329.

## Chapter III: Electrochemical and viscoelastic evolution of dodecyl sulfate-doped polypyrrole films during electrochemical cycling

In this chapter, the correlation between electrochemical and viscoelastic properties of electrodeposited dodecylsulfate-doped polypyrrole (PPy-DS) during electrochemical cycling process was described through combining electrochemical quartz crystal microbalance (EQCM), *ac*-electrogravimetric characterizations and electroacoustic measurements. As the PPy-DS electrode evolves during the course of consecutive cycling in aqueous NaCl electrolyte, the film exhibits (i) an obvious ion-selective transition from cations to anions in the charge compensation process; (ii) an inferior electrochemical performance accompanied with increased stiffness (increased storage moduli,  $G'$ ); and (iii) depleted capability of ionic exchange through film/electrolyte interface. PPy-DS conducting polymer electrodes (CPEs) are of interest in energy storage and the relationship between electrochemical and viscoelastic properties during electrochemical cycling process is essential for promoting the performance of these devices. In this perspective, *ac*-electrogravimetry combined with electroacoustic measurements can be suggested as an alternative method to synchronously probe the electrochemical and mechanical evolution and has the potential to offer a generalized route to study aging mechanism of CPEs.

### III.1. Preamble and Objectives

Species transfer in conducting polymer electrodes (CPEs) plays a key role in numerous applications, such as electrochemical sensors<sup>1-2</sup>, batteries<sup>3-4</sup>, supercapacitors<sup>5-6</sup>. Up to date, significant attention has been drawn to enhance the ionic transfer/transport and cycling stability of CPEs to devise electronics with effective energy storage capability<sup>7-10</sup>, thereby demanding a thorough understanding of the ion transfer behavior at the CPEs/electrolyte interface. Another issue is that the CPEs experience inevitable structural changes in practical applications primarily due to the electrochemical aging of the polymer. The latter may aggravate the mechanical properties of CPEs which can be reflected in the viscoelastic variations of polymer electrodes during electrochemical cycling<sup>11-13</sup>. Many CPEs have been studied for their appealing electrochemical properties<sup>14</sup>, such as poly(3,4-ethylenedioxythiophene) (PEDOT)<sup>15-16</sup>, polypyrrole (PPy)<sup>17-19</sup>,

polyaniline (PANI)<sup>8, 20</sup> and polythiophene (PHT)<sup>21-22</sup>. PPy has been exploited in considerable amount of researches, due to its relatively higher pseudocapacitance and lower cost, as well as its particularly supreme flexibility in morphology and structure<sup>23</sup>. However, inferior cycle stability caused by significant dimensional changes during charge-discharge process greatly hinders their applications. Therefore, the relationship between internal structure and film properties has been scrutinized with the purpose of promoting the performance of CPEs in applications (i.e., energy storage).

Electrochemical quartz crystal microbalance (EQCM) and its coupling with electrochemical impedance spectroscopy (the so-called *ac*-electrogravimetry) have proved themselves as baseline analytical tools to probe electrochemical processes, with tremendous benefits in *in situ* capturing ionic fluxes in various electrodes, including carbon based electrodes<sup>24-26</sup> and CPEs<sup>27-28</sup>. Considerable amount of work have focused on the exploration of electrochemical properties of CPEs, which has been regarded as a prerequisite for improving performances of electrochemical devices<sup>29-30</sup>. However, their physical or viscoelastic properties are of equal importance especially for the electrode cycling stability and should not be neglected. The ionic fluxes accompanied the free solvent molecules transfer during charging-discharging process may bring about the periodic potential-dependent volumetric changes of the electrodes (*i.e.*, swelling and shrinking)<sup>14, 22</sup>. These processes are likely to result in a wide variety of unpredictable mechanical defects, i.e. polymer electrode fatigue, stress concentration and delamination from current collector. Thus, a measurement methodology capable of capturing the ionic transfer as well as viscoelastic evolution of the CPEs synchronously is highly desirable.

The viscoelastic properties of CPEs have been extensively investigated through the electroacoustic impedance method<sup>31-33</sup>, by which the storage ( $G'$ ) and loss moduli ( $G''$ ) of the polymer film can be determined. As the film ages, the viscoelastic changes may occur inside the film due to polymer chain rearrangements and species transfer through film/electrolyte interface<sup>32</sup>. Hillman and co-workers have reported an increase in the stiffness of PANI films due to insertion of anions and the expulsion of the solvent molecules<sup>12, 34</sup>. Bund et al. observed that the influx of anions may increase the stiffness of PEDOT film and the variations of  $G'$  and  $G''$  were correlated with concentrations of charged species within film<sup>35-36</sup>. It is considered that such viscoelastic changes are somewhat associated with the electrochemical performance of the film, as the flux of ions and solvent during the charge-discharge process can modify the intermolecular interactions between

polymer chains, which in turn substantially affect the film viscoelasticity. Herein, a methodology which combines the EQCM, *ac*-electrogravimetry and electroacoustic measurements was proposed to get a broader view of the physico-chemical interactions inside the CPEs over the course of electrochemical aging. The particularity of this methodology stems from the utility of EQCM together with *ac*-electrogravimetry and electroacoustic impedance for electrogravimetric evaluation and for viscoelastic tests, respectively.

With the aim of synchronous description of the relationship between electrochemical properties and viscoelastic evolution during PPy electrode electrochemical aging, the combined methodology (involving EQCM, *ac*-electrogravimetry and electroacoustic impedance measurements) was applied to characterize PPy film doped with DS<sup>-</sup> anions (PPy-DS) after every 25 charge/discharge cycles in aqueous electrolytes until 175<sup>th</sup> cycle was reached. Due to the nanometric film thickness, film/electrolyte configuration can be considered as a zoom of a real macroscopic electrode/electrolyte interface. During the limited number of cycles, various phenomena might be amplified which can permit to predict an eventual degradation of CPEs. This systematic study is expected to provide insights into the relationship between the internal structure of the CPE film and the ability to maintain its electrochemical and mechanical performance. To the best of our knowledge, such systematic study has not yet been reported. In previous works of our group<sup>11, 27</sup>, either materials and dopants or the methods for exploration in mechanical properties were different. The influences of aging degree and applied potential on the species transfer (charged or uncharged), hydration/dehydration of ions and free solvents motion and intimately related viscoelastic changes of PPy-DS electrode were investigated during film aging upon cycling and a model was proposed to illustrate the electrochemical cycling process.

## **III.2. Experimental Methods and Theoretical Background**

### **III.2.1. Film preparation and characterization**

Pyrrrole solution (Py), sodium dodecyl sulphate (NaDS) and NaCl salts were purchased from Sigma Aldrich. The Py monomer was distilled before use and kept at -20 °C. All the solutions were prepared with bi-distilled water.

Polypyrrole films doped with DS<sup>-</sup> anions were electrodeposited on the gold electrode (0.2 cm<sup>2</sup>) of a quartz crystal resonator (9 MHz-AWS, Valencia, Spain) where a platinum grid and a saturated calomel electrode (SCE) are used as counter and reference electrode, respectively. The PPy-DS

films were electrodeposited by cyclic voltammetry (2 cycles from the higher potential to the lower potential) from 0.675 V to 0 V *vs.* SCE at 10 mV·s<sup>-1</sup> in a solution of 0.1 M pyrrole and 0.05 M NaDS<sup>27, 37</sup>. The average film thickness of the electrogenerated PPy-DS film and 175-cycled film was analyzed using a field emission gun scanning electron microscope (FEG-SEM, Zeiss, Supra 55). Fourier transform infrared (FTIR) spectra were recorded on VERTEX 70 spectrometer (BRUKER Co., USA) from 2000 to 650 cm<sup>-1</sup> with a 4 cm<sup>-1</sup> resolution. Ultraviolet-visible (UV-vis) spectra were recorded with a U-4001 spectrophotometer. The films used for FTIR and UV-vis were prepared on ITO coated glass slides and cycled under the same conditions as those on gold electrode of the quartz resonators.

### III.2.2. Electrogravimetric measurements

All of the electrochemical experiments were carried out using an Autolab potentiostat-galvanostat electrochemical workstation (PGSTAT302). After the PPy-DS film electrogeneration, the *ac*-electrogravimetry cannot be conducted immediately because the film composition is not under equilibrium. Thus, it was stabilized by 15 scan cycles from -1.3 V to 0.5 V *vs.* SCE at 50 mV·s<sup>-1</sup> in 0.25 M NaCl aqueous electrolyte. This stabilized film was deemed as fresh film. Subsequently, *ac*-electrogravimetric investigation of fresh PPy film was performed at two different potentials -0.6 V and -0.2 V *vs.* SCE, respectively. The *ac*-electrogravimetric measurements of the film were tracked after each 25 CV cycles up until 175 cycles were reached, where the electrogravimetric response is too weak to be analyzed. The procedure is illustrated schematically in **Figure III.1a**. Two key potentials were selected: (i) -0.6 V, located between the reduction (-0.68 V) and oxidation (-0.5 V) peak for fresh film and thus, can be regarded to be a representative potential of the Faradaic process. (ii) -0.2 V, approximately a constant current response was observed for fresh film in the vicinity of this potential, therefore, it can be considered to be indicative of a non-Faradaic process. In order to have a coherent comparison, it is decided to keep monitoring the changes at these two potentials, even slight shifts may occur during the electrochemical cycling.

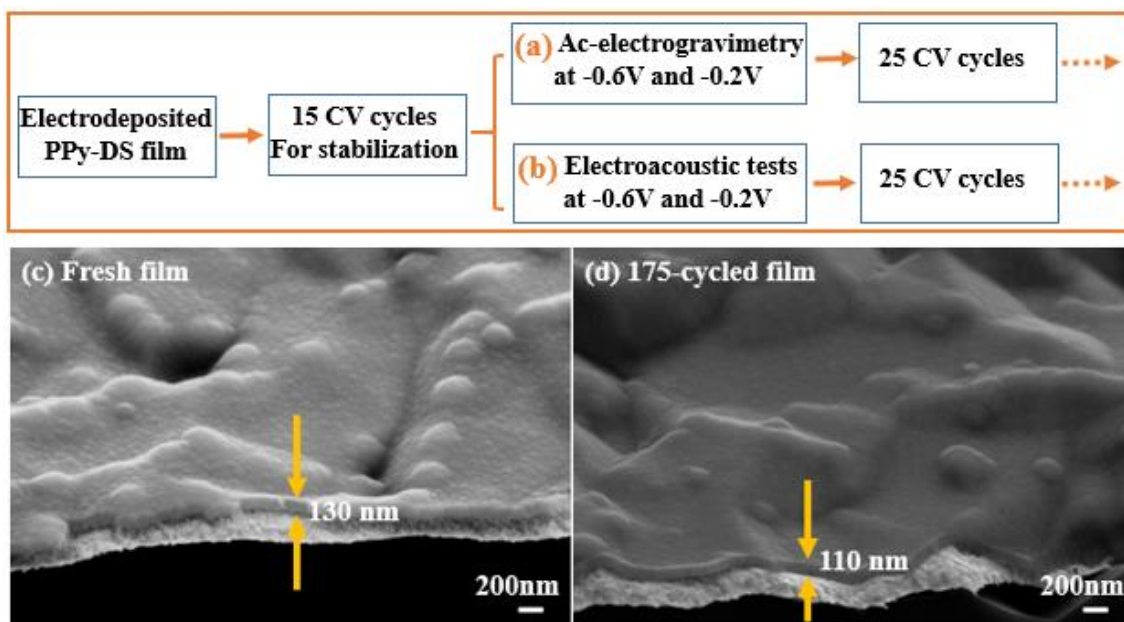


**Figure III.1.** Schematic illustration of the measurement procedures for (a) *ac*-electrogravimetry and (b) electroacoustic tests during film electrochemical cycling. The panels (c) and (d) are the morphological observations of electrodeposited fresh and 175-cycled PPy-DS film by FEG-SEM, respectively.

For *ac*-electrogravimetry, a four-channel frequency response analyser (FRA, Solartron 1254) and a lab-made potentiostat (SOTELEM-PGSTAT) were used. The QCM was used under dynamic regime, the working electrode (WE) was polarized at previously selected potentials, and sinusoidal small amplitude potential perturbation (80 mV rms) was superimposed. The microbalance frequency change ( $\Delta f_m$ ) related with the mass response ( $\Delta m$ ) of the modified working electrode was measured simultaneously with the charge response ( $\Delta q$ ) of the electrochemical system. The resulting signals were sent to the four-channel FRA, which allowed the electrogravimetric transfer function ( $\frac{\Delta m}{\Delta E}(\omega)$ ) and the charge/potential transfer function ( $\frac{\Delta q}{\Delta E}(\omega)$ ) to be obtained simultaneously at the given potential and frequency modulation,  $f$  (pulsation  $\omega=2\pi f$ ). The charge/potential transfer function ( $\frac{\Delta q}{\Delta E}(\omega)$ ) and mass/potential transfer function ( $\frac{\Delta m}{\Delta E}(\omega)$ ) can be theoretically calculated by using the **Equations III.1, III.2 and III.3**, where  $\Delta c_i$  presents the change of the concentration of each species (ions and free solvent) in the film,  $\omega$  the pulsation,  $d_f$  the film thickness (here 200 nm estimated through QCM measurements),  $K_i$  and  $G_i$  are the partial

derivatives of the flux ( $J_i$ ) with respect to the concentration and the potential, respectively.  $K_i$  describes the kinetics of transfer.  $G_i$  is the reciprocal of the transfer resistance ( $Rt_i$ ), exhibiting the ease or difficulty in the transfer at the film/electrolyte interface for respective species (more details about *ac*-electrogravimetry are given in Chapter II).

$$\frac{\Delta c_i}{\Delta E}(\omega) = \frac{G_i}{(j\omega d_f) + K_i} \quad (\text{III.1})$$

$$\frac{\Delta q}{\Delta E}(\omega) = Fd_f \sum_i \frac{G_i}{(j\omega d_f) + K_i} \quad (i: \text{ ions}) \quad (\text{III.2})$$

$$\frac{\Delta m}{\Delta E}(\omega) = -d_f \sum_i M_i \frac{G_i}{(j\omega d_f) + K_i} \quad (i: \text{ ions and non-charged species}) \quad (\text{III.3})$$

On the basis of the above parameters, the characteristic frequency of transfer ( $f_i$ ), the transfer resistance ( $Rt_i$ ) and the instantaneous capacitance ( $C_i$ ) of each species are further considered and calculated using **Equations III.4 to III.6**.

$$f_i = \frac{K_i}{2\pi d_f} \quad (\text{III.4})$$

$$Rt_i = \frac{1}{FG_i} \quad (\text{III.5})$$

$$C_i = \frac{-Fd_f G_i}{K_i} \quad (\text{III.6})$$

After the *ac*-electrogravimetry measurements, the experimental data obtained from fresh film, 100 and 175 times-cycled films were fitted with the theoretical functions given in **Equations III.2** and **III.3** by using the Mathcad software.

### III. 2. 3. Electroacoustic impedance measurements

The viscoelastic properties of the PPy-DS film during electrochemical aging were explored through the electroacoustic admittance method. To track the viscoelastic variation of our films and to corroborate with the *ac*-electrogravimetry results, electroacoustic measurements were performed at the same stationary potentials (-0.6 V and -0.2 V) after each 25 cycles up to the 175<sup>th</sup> cycle was reached (**Figure III.1b**). To perform the electroacoustic admittance measurements under polarization, an Agilent 4294A impedance analyzer associated to a lab-made potentiostat (SOTELEM-PGSTAT) was used.

A software developed in our laboratory (Simad) was used for fitting the experimental data for

extracting the storage moduli ( $G'$ ) and loss moduli ( $G''$ ) of the film. The real component ( $G'$ ) describes the energy storage capability of the polymer chains and the imaginary part ( $G''$ ) is associated with the energy dissipation of the film due to irreversible deformation of polymer chains<sup>38</sup>.

The complete theoretical electrical admittance,  $Y_{th}^V(\omega)$ , of the loaded quartz resonator is:

$$Y_{th}^V(\omega) = \frac{1}{Z_{th}^V(\omega)} = i \times \omega \times C_p + \frac{1}{Z_m^V(\omega)} \quad (III.7)$$

where  $\omega = 2 \times \pi \times f$ ,  $C_p$  is the parasitic capacitance and  $Z_m^V$  is the motional impedance of the loaded quartz resonator calculated with a viscoelastic model.

The motional impedance,  $Z_m^V$ , can be completely modelled according to the work of Martin *etal.*<sup>39</sup> If the characteristics of the quartz and of the liquid are considered as constants, the motional electrical impedance,  $Z_m^V$  of the coated resonator is:

$$Z_m^V(\omega) = \frac{h_q^2}{4 \times e_q^2 \times A} \times Z_f \times \frac{Z_s + Z_f \times \tanh(\theta_f \times h_f)}{Z_f + Z_s \times \tanh(\theta_f \times h_f)} \quad (III.8)$$

where  $h_q$  is the quartz thickness,  $e_q$  is the quartz piezoelectric constant,  $A$  is the active mass area,  $Z_f$  is the acoustic impedance of the film,  $Z_s$  is the acoustic impedance of the liquid,  $\theta_f$  is the complex propagation constant of the film and  $h_f$  is its thickness. Moreover,  $Z_f$  and  $\theta_f$  can be described as:

$$Z_f = \sqrt{\rho_f \times G_f} \quad (III.9)$$

$$\theta_f = \sqrt{\frac{\rho_f}{G_f}} \quad (III.10)$$

where  $\rho_f$  is the film density and  $G_f$  is the shear thickness modulus of the film, which can be written as a complex number with a real and imaginary part,  $G_f = G' + jG''$ , where  $j^2 = -1$ .

The acoustic impedance of the solution,  $Z_s$ , is defined as **Equation III.9** except that  $G'$  becomes negligible and for a Newtonian liquid,  $G'' = 2\pi f \eta_s$ , where  $f$  is the frequency and  $\eta_s$  the liquid viscosity.

### III.3. Results and Discussion

#### III.3.1. Cyclic electrogravimetric behavior

The cross-sectional morphology of electrodeposited PPy-DS films were observed by FEG-SEM (Figure III.1c and d). The average film thickness is ~130 nm and ~110 nm for the fresh and 175-cycled film, respectively. These values correspond to the shrunken state of the film under the vacuum conditions of the measurements. Parallely, the Sauerbrey equation was used to convert the microbalance frequency shift, ( $\Delta f$ ) to mass change ( $\Delta m$ ) during the PPy-DS electrodeposition<sup>40</sup>:  $\Delta f = -C_f \times \Delta m$ , where  $C_f$  is the sensitivity factor of the quartz crystal resonator ( $C_f = 16.3 \times 10^7 \text{ Hz.g}^{-1}.\text{cm}^2$ ) and  $\Delta m$  presents the film mass change per unit area. The estimated film thickness from the Sauerbrey equation is around 216 nm and 184 nm for the fresh and 175 times cycled films, respectively. An average film thickness of 200 nm is used for the fitting of the *ac*-electrogravimetric and electroacoustic data.

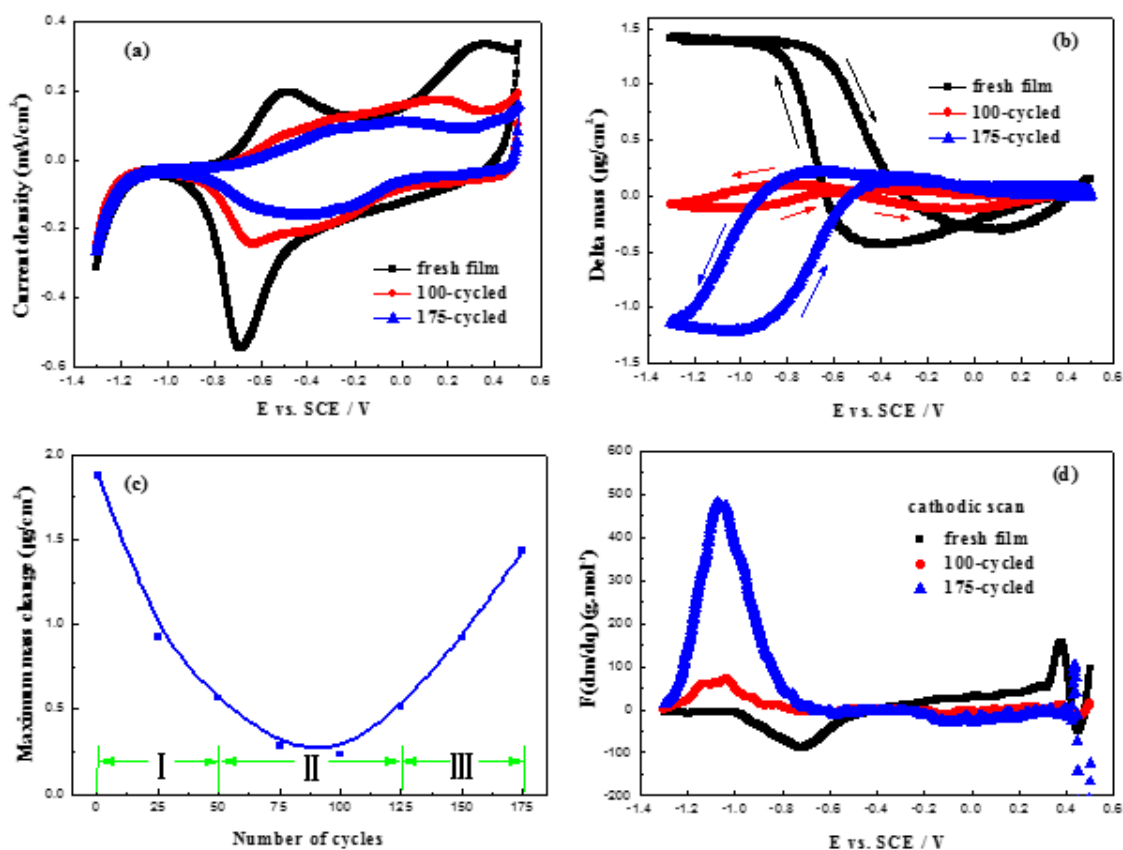


**Figure III.2.** Cyclic voltammetry (a), mass change ( $\Delta m$ ) (b), the maximum mass change (c) and  $F(dm/dq)$  function calculated from the reduction branch (d) of PPy-DS film in 0.25 M NaCl aqueous solution between -1.3 V and 0.5 V vs. SCE at a scan rate of  $50 \text{ mV}\cdot\text{s}^{-1}$ .

First of all, to explore the effect of electrochemical cycling on the electrochemical responses of the PPy-DS film, cyclic electrogravimetry (EQCM) was exploited to follow the current and the simultaneous mass responses as a function of the electrochemical aging in aqueous 0.25 M NaCl. The two anodic peaks of fresh film in **Figure III.2a** are likely to be related to creation of the polarons and bipolarons in agreement with the previous works<sup>41-42</sup> without any clear attribution of each peak to either of them. Alternately, reference 27 and 42 has reported indications that the first oxidation peak I at -0.5 V and the second oxidation peak II at 0.3 V are related to cations and anions' transfer, respectively<sup>27</sup>. As shown in **Figure III.2a**, the redox peaks progressively disappear and the shape of CV curves tends to become quasi rectangular. This observation indicates the fading of the pseudocapacitive capability and/or an increase in the contribution of capacitive response to the charge compensation process. In spite of the fairly clear CV responses, the evolution of the mass response (**Figure III.2b**) during cycling is rather complex. For a fresh film, a mass increase and a decrease were observed during the reduction and the oxidation process, respectively. After 100 cycles, the global mass response has been significantly decreased suggesting the presence of either smaller mass changes of the film or different flux directions of the species participating in the charge compensation process. After the film was cycled 175 times, the mass response displayed an opposite behavior relative to that of fresh film, *i.e.*, mass decrease during reduction and mass ingress during oxidation. Therefore, from a global point of view, it can be suggested that the fresh film experiences cation insertion and expulsion during reduction and oxidation, respectively, whereas the 175 times-cycled film undergoes anion expulsion during reduction and insertion during oxidation. Concerning the 100 times-cycled film, both cations and anions can participate in the charge compensation and they may play an equal part in the electrochemical response without consideration of solvent exchange. Thus, the mass contribution from cations and anions may offset which leads to this almost “no mass response” for 100-cycled film, which is illustrated in **Figure III.2c-zone II**.

The maximum mass change ( $M_{max}$ ) during a redox cycle was tracked after every 25 scan cycles, as depicted in **Figure III.2c**. The  $M_{max}$  value of the film decreases and reaches to a minimum after 100 cycles, *i.e.*  $0.23 \mu\text{g}\cdot\text{cm}^{-2}$ , which is approximately 7 times less than that of a fresh film. After that,  $M_{max}$  values gradually increase to  $1.4 \mu\text{g}\cdot\text{cm}^{-2}$  for 175-cycled film. This “quasi-U” shape describes an obvious transition where the predominance of cation participation is gradually replaced by anion participation in the charge compensation process as the film is electrochemically cycled.

The above discussion considers the ionic species as the major contribution but the free solvent contributions cannot be excluded. It has been widely reported that the ion exchanges during redox reactions are commonly accompanied with flux of solvent<sup>43-44</sup>. To get insights into the nature of the ionic species and possible free solvent molecules' contribution, the EQCM results are further analyzed. The molar mass,  $M_i$ , of each species involved in the charge compensation process can provide a better understanding of the species transfer as a function of the number of cycles.

To do this, the  $F \frac{\Delta m}{\Delta q}$  function was calculated as a function of applied potential using the current and the mass response of the film (**Figure III.2a and b**), as follows:

$$M_i = F \frac{dm}{dq} = F \left( \frac{dm}{dt} \right) \cdot \frac{1}{i} \quad (\text{III.11})$$

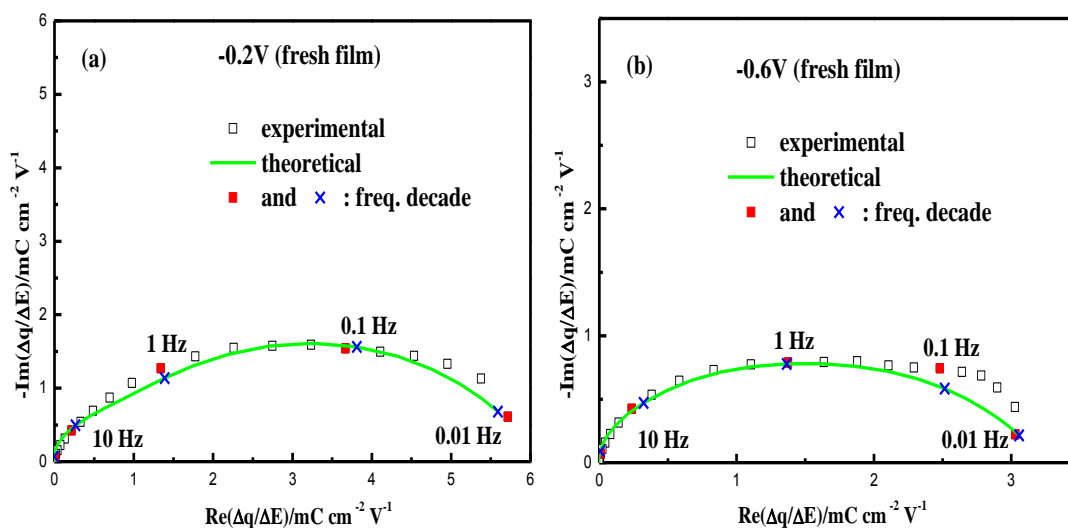
This function provides a global estimation of the molar mass of the species ( $M_i$ ) that may participate in the charge compensation process. The  $F \frac{\Delta m}{\Delta q}$  function was calculated from the reduction branch of the EQCM data and **Figure III.2d** compares  $M_i$  of the species involved in the reduction process as the film is electrochemically cycled. It is evident that  $M_i$  presents a potential and cycling dependence. For fresh film,  $M_i$  exhibits a negative value reaching  $-88 \text{ g}\cdot\text{mol}^{-1}$  at  $-0.7 \text{ V}$  without an evident plateau in the reduction sweep regime. It should be kept in mind that the ions present in the electrolyte are only sodium cations ( $\text{Na}^+$ ,  $23 \text{ g}\cdot\text{mol}^{-1}$ ) and chloride anions ( $\text{Cl}^-$ ,  $35.5 \text{ g}\cdot\text{mol}^{-1}$ ). In the  $F \frac{\Delta m}{\Delta q}$  function, negative and positive values are characteristic of cations and anions, respectively<sup>28, 43</sup>. The values higher than expected molar mass of the cations suggest that cations are inserted into the fresh film accompanied with water in either free form with the same flux direction or in the hydration shell of  $\text{Na}^+$ . After the film is 100 times-cycled, the potential corresponding to the max  $M_i$  value is moved to more cathodic potential (from  $-0.7 \text{ V}$  to  $-1.05 \text{ V}$ ). When the film is further cycled up to 175 cycles, the peak intensity dramatically increases approximately 5 times up to  $479 \text{ g}\cdot\text{mol}^{-1}$  compared to that observed after 100 times cycling. This indicates that the nature of the species involved in the charge compensation are dependent on the film cycling state. The film exhibits unexpected behavior: the cations dominate charge balance when the film is fresh, while anion's contribution increases as the film is electrochemically cycled and predominates in charge balance in the end. Since the estimated molar mass values are much higher than the theoretical ones ( $\text{Na}^+$ ,  $23 \text{ g}\cdot\text{mol}^{-1}$  and  $\text{Cl}^-$ ,  $35.5 \text{ g}\cdot\text{mol}^{-1}$ ), the water molecules are

speculated to play a significant role in the electrochemical process.

However, it is not straightforward to separate each species contribution and the possible synergistic effect among them. Indeed, the deconvolution of the global cyclic electrogravimetry response into gravimetric and dynamic components is quite challenging since the measurements are done at a certain scan rate. Therefore, coupling of the QCM with electrochemical impedance spectroscopy (*ac*-electrogravimetry) was suggested<sup>27</sup>. To shed light on the subtleties of the charge compensation process during electrochemical aging, an *ac*-electrogravimetric study was performed to understand the relationship between film cycling and charge compensation process.

### III.3.2. *Ac*-electrogravimetric investigations

To gain insights into the dynamic behavior of the species transfer at the film/electrolyte interface at the temporal scale, *ac*-electrogravimetry was performed to probe the influence of film cycling on the transfer of charged and non-charged species. **Figure III.3** compares the charge/potential transfer function  $\frac{\Delta q}{\Delta E}(\omega)$  TF, obtained at -0.6V and -0.2V at different cycling state of the film, respectively.



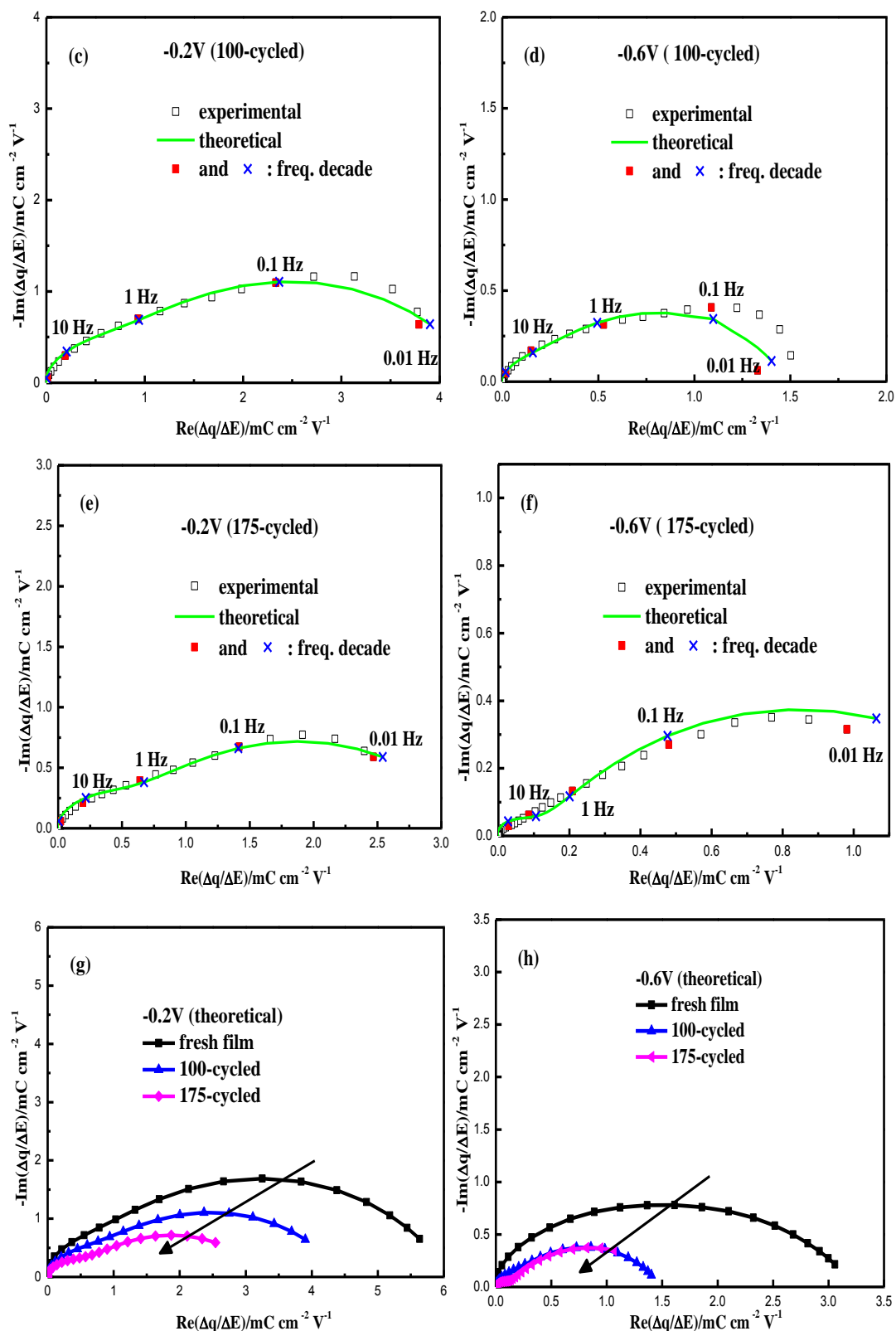


**Figure III.3.** Experimental and theoretical  $\frac{\Delta q}{\Delta E}(\omega)$  transfer functions for PPy film at different cycled state: (a), (c) and (e) were measured for fresh film, 100- and 175-cycled film at -0.2V, while

(b), (d) and (f) at -0.6V, respectively. Panels (g) and (h) are theoretical TFs of  $\frac{\Delta q}{\Delta E}(\omega)$  as film cycled at -0.2V and -0.6V.

Theoretically, the  $\frac{\Delta q}{\Delta E}(\omega)$  TF in **Figure III.3** appears as a single loop if there is only one charged species transferred. In this study, the  $\frac{\Delta q}{\Delta E}(\omega)$  TF shows mainly one suppressed loop (a composition of several loops) at both potentials at different cycled state of the film, suggesting the presence of more than one species participating in the charge compensation. It is also likely that their time constants are not significantly different to have them appear as separate loops. The experiment data were fitted using theoretical **Equation III.2** and two ionic species were involved. Their corresponding values of  $K_i$  and  $G_i$ , obtained through the fitting process are given in **Table III.1**. As the film ages, the diameter of the global loop gets smaller, which may indicate that the population of the ions involved in the charge compensation is reduced as clearly indicated in **Figure III.3g** and **h** for both potentials. This result is coherent with the decrease of the current values observed in **Figure III.2a**.

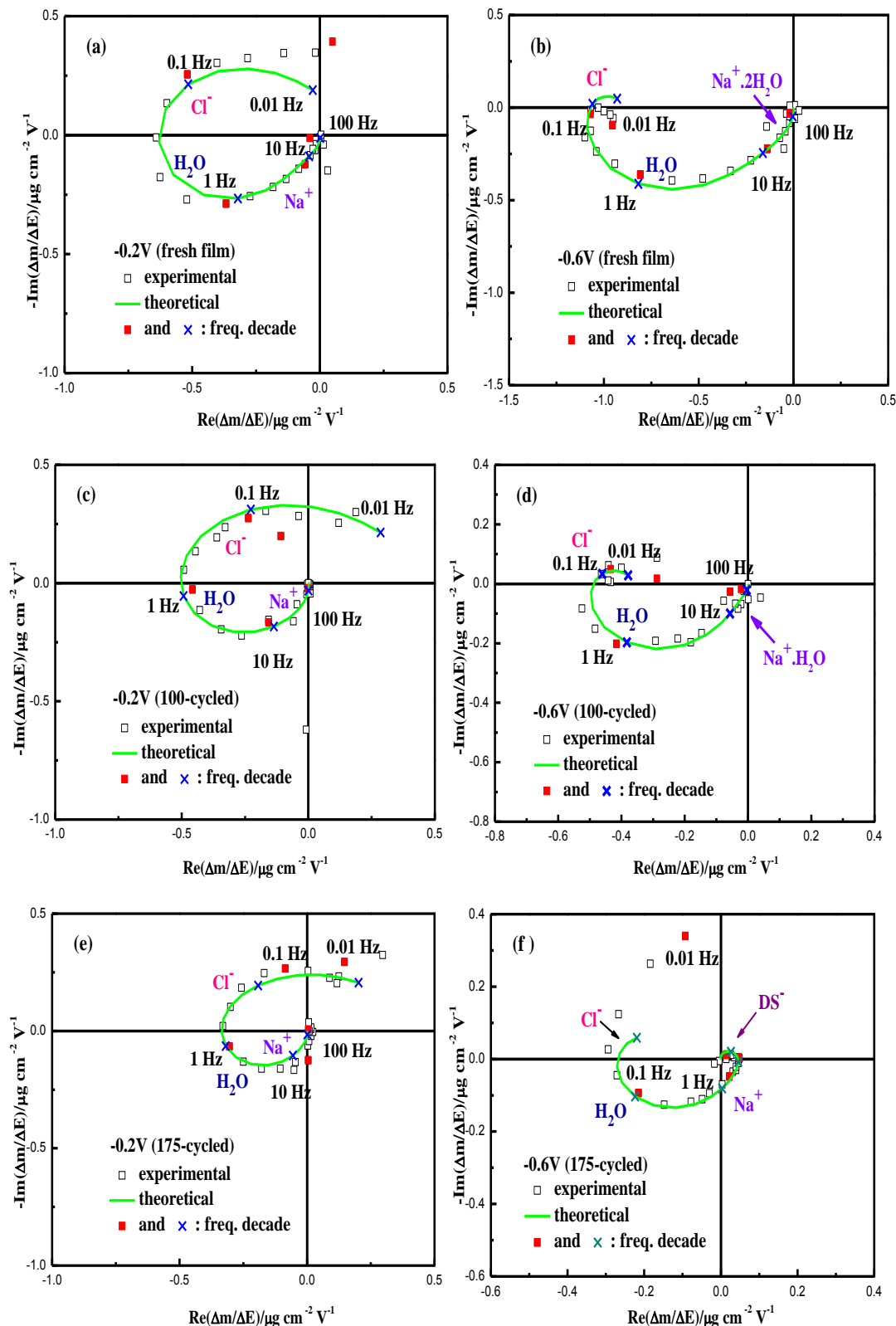
**Table III.1.** Fitting parameters,  $K_i$  and  $G_i$ , obtained from *ac*-electrogravimetry.

		$K_c (\times 10^{-4})$	$G_c (\times 10^{-8})$	$K_a (\times 10^{-6})$	$G_a (\times 10^{-9})$	$K_s (\times 10^{-5})$	$G_s (\times 10^{-8})$
-0.2V	fresh film	6.518	26.17	25.51	-47.19	8.796	24.63
	100-cycle	3.826	11.86	17.59	-23.75	25.95	33.73
	175-cycle	3.607	7.934	11.61	-11.61	31.67	23.75
-0.6V	fresh film	7.213	28.85	40.46	-32.37	15.83	31.67
	100-cycle	8.005	7.204	39.58	-18.21	17.59	24.63
	175-cycle	5.278	1.847	9.676	-4.645	2.815	3.659

Note:  $\text{cm}\cdot\text{s}^{-1}$  and  $\text{mol}\cdot\text{s}^{-1}\cdot\text{cm}^{-2}\cdot\text{V}^{-1}$  are for the units of  $K_i$  and  $G_i$  parameters, respectively. Cation, anion and solvent in the Table III.1 refer to  $\text{Na}^+$  or hydrated  $\text{Na}^+$ ,  $\text{Cl}^-$  and free  $\text{H}_2\text{O}$ . For 175-cycle film at -0.6 V, the fitting parameters for  $\text{DS}^-$  are  $K=2.815\times 10^{-3} \text{ cm}\cdot\text{s}^{-1}$  and  $G=-2.815\times 10^{-8}$

$\text{mol}\cdot\text{s}^{-1}\cdot\text{cm}^{-2}\cdot\text{V}^{-1}$ .

Apart from the charge/potential TF, the electrogravimetric response,  $\frac{\Delta m}{\Delta E}(\omega)$ , which can provide information on both the charged and non-charged species transfer, was simultaneously obtained (**Figure III.4**). For all  $\frac{\Delta m}{\Delta E}(\omega)$  fittings (except **Figure III.4f**), three species,  $\text{Na}^+$  (hydrated or not), free water molecules and  $\text{Cl}^-$  were identified, which led to a good agreement between the experimental and theoretical curves. Our data presented in **Figure III.4** indicate that the cations appear at high frequencies, followed by free water molecules at intermediate frequencies and anions at low frequencies, independently of the cycling degree of the film at both potentials. At -0.6 V, a fairly good agreement between the experimental and theoretical  $\frac{\Delta m}{\Delta E}(\omega)$  data was obtained by considering the molar mass of hydrated cations ( $\text{Na}^+\cdot 2\text{H}_2\text{O}$ ) for fresh film (**Figure III.4a**). It seems that the solvation shell of the  $\text{Na}^+$  is gradually removed at -0.6 V as the film is electrochemically cycled (**Figure III.4 c and e**). At -0.2 V, the electrogravimetric response is rather constant and only desolvated sodium at high frequencies, free water contribution at intermediate frequencies and chloride at low frequencies were detected (**Figure III.4b, d and f**). It is interesting to note that a small loop appears in the first quadrant at very high frequencies for the 175-cycled film (**Figure III.4f**). It is supposed that some of the  $\text{DS}^-$  anions anchored on the polymer chains are removed and start to participate in the charge compensation process, as the molar mass of  $\text{DS}^-$  was determined. This is probably related to the periodic swelling-shrinking process of the film cycling which modifies the film structure and permits the exchange of  $\text{DS}^-$ . It will be further explored in the electroacoustic part (III.3.3).



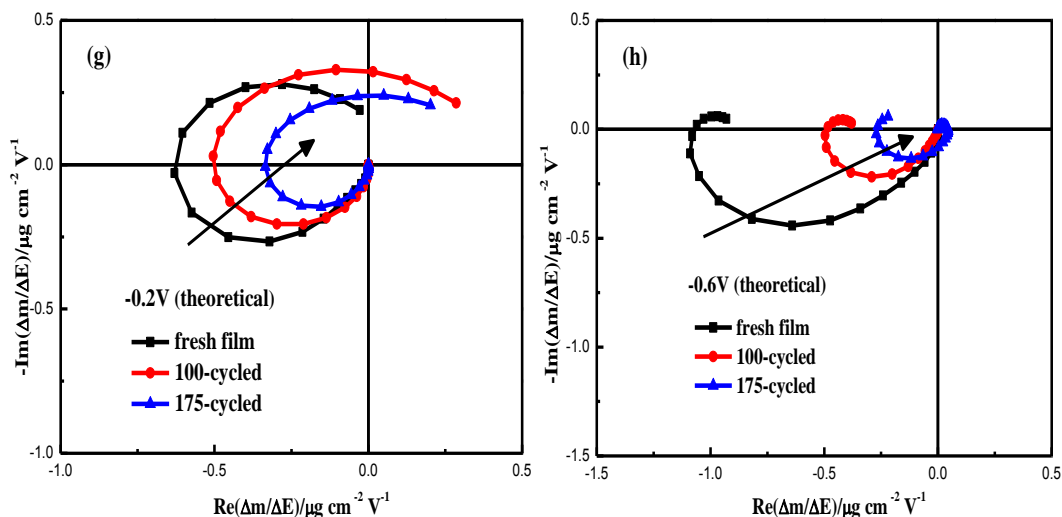


**Figure III.4.** Evolution of transfer function of  $\frac{\Delta m}{\Delta E}(\omega)$  with film cycling: (a), (c) and (e) were measured for fresh film, 100-cycled and 175-cycled film at -0.2 V, (b), (d) and (f) at -0.6 V, (g) and (h) theoretical TFs of  $\frac{\Delta m}{\Delta E}(\omega)$  as film is cycled at -0.2 V and -0.6 V, respectively.

The  $\frac{\Delta m}{\Delta E}(\omega)$  TFs at both potentials for all cycled films (**Figure III.4g** and **h**) present one big loop in the third quadrant at high and intermediate frequencies (HF and IF), and another one in the fourth quadrant at lower frequencies (LF). It is worth mentioning here that the loops in the third quadrant are characteristic of contributions originated from cations and/or free solvent with the same flux direction as cations<sup>27</sup>. These loops in the third quadrant are reduced in diameter as the film is electrochemically cycled (**Figure III.4a-e**) which indicates either a decrease of the cation/free solvent contributions or a decrease of the molar mass of the cations by losing their solvation shell.

The characteristic frequencies,  $f_i$ , in **Figure III.5a** and **b** display that cations (hydrated or not) have the highest kinetics of transfer at the electrode/electrolyte interfaces, followed subsequently by H<sub>2</sub>O molecules and Cl<sup>-</sup> anions ( $f_c > f_s > f_a$ ) at both potentials as the film is electrochemically cycled. Additionally, it is noted that only for the 175-cycled film at -0.6 V, the DS<sup>-</sup> anions are observed in the charge compensation process where they possess the highest kinetics of transfer (DS<sup>-</sup> anions were not taken into account in **Figure III.5b, d** and **f** as they are only detected for 175-cycled film at -0.6 V).

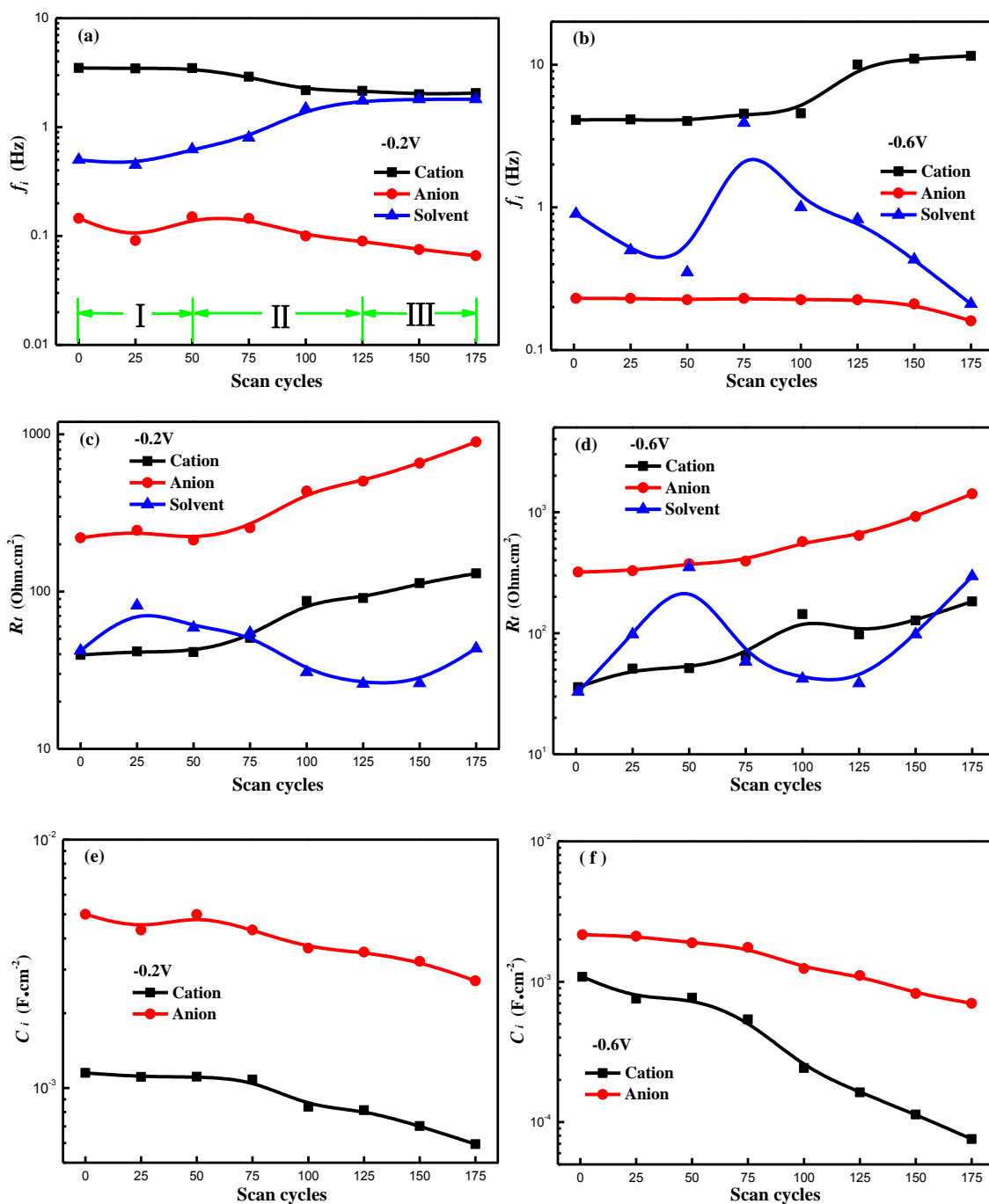


**Figure III.5.** (a), (b) Evolution of characteristic frequency ( $f_i$ ). (c), (d) transfer resistance ( $R_t$ ) and (e), (f) instantaneous capacitance ( $C_i$ ) for each species at two different potentials as the film is electrochemically cycled. Herein, anion only refers to  $\text{Cl}^-$ .

At -0.2 V (**Figure III.5a**), the  $f_i$  of  $\text{H}_2\text{O}$  molecules is enhanced nearly 3 times up to 1.75 Hz in the region II, accompanied with a decrease in cation transfer kinetics (from 3.45 Hz to 2.15 Hz). When the film is electrochemically cycled up to region III, the  $f_i$  value of the cation and solvent molecules approaches and they eventually exhibit equivalent transfer kinetics. The transfer of

anions remain as the slowest contribution at both potentials over the course of film cycling, which is in agreement with the higher  $R_t$  value of anions compared to that of cations and water molecules, as shown in **Figure III.5c**.

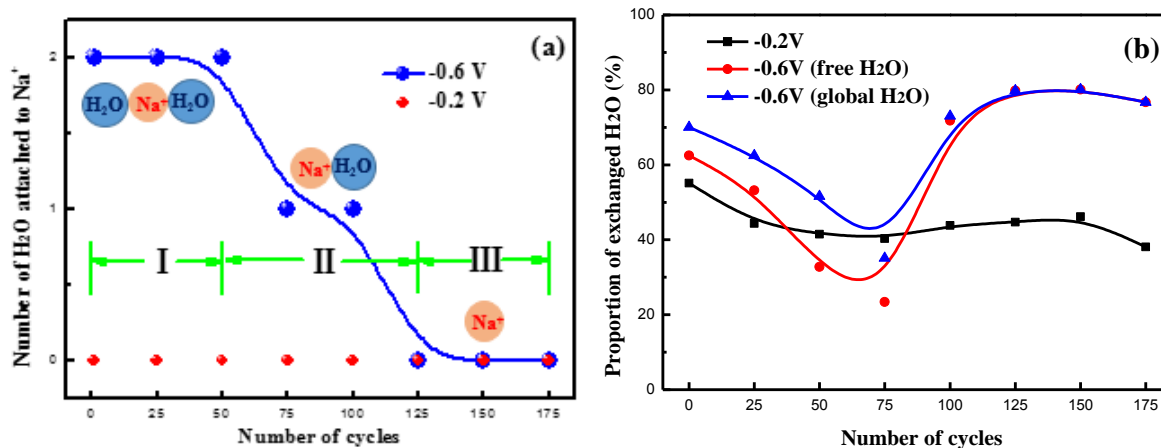


**Figure III.6.** (a) Dehydration process for hydrated cations ( $\text{Na}\cdot 2\text{H}_2\text{O}$ ) transferred at the film/solution interface at  $-0.6\text{ V}$  as the film is electrochemically cycled, and (b) proportion of exchanged  $\text{H}_2\text{O}$  (calculated using **Equations III.12** and **III.13**) participating in charge compensation at both potentials. Global  $\text{H}_2\text{O}$  represents the sum of free  $\text{H}_2\text{O}$  and the  $\text{H}_2\text{O}$  molecules within the hydration shell of cations.

On the contrary, the cation transfer kinetics become faster in the end of region II at  $-0.6\text{ V}$  (**Figure III.5b**), which can be attributed to the dehydration process of hydrated cations ( $\text{Na}^+\cdot 2\text{H}_2\text{O}$ ) on the course of film cycling as depicted in **Figure III.6a**. Meanwhile, it also demonstrates higher transfer capability of dehydrated  $\text{Na}^+$  relative to the hydrated counterparts due to its smaller size.

An interesting phenomenon is observed in the transfer of  $\text{H}_2\text{O}$  molecules at  $-0.6\text{ V}$  (**Figure III.5b**) as follows. The  $f_i$  of  $\text{H}_2\text{O}$  molecules experience a slight decrease (from  $0.90\text{ Hz}$  to  $0.35\text{ Hz}$ ) in region I, followed by a surge up to  $3.9\text{ Hz}$  at the beginning of region II. Afterwards, it progressively decreases to  $0.21\text{ Hz}$  at the end of region III. Correspondingly, the  $R_t$  of  $\text{H}_2\text{O}$  molecules (**Figure III.5d**) shows an approximate mirror symmetry, except that the peak value of  $f_i$  is reached after 75 cycles whereas the minimum value of  $R_t$  appears after 125 cycles (i.e.  $\sim 50$  cycles lag between the  $f_i$  and  $R_t$ ). In fact, this is not contradictory because the  $f_i$  is related with the transfer kinetics of the species, while the  $R_t$  is correlated to the ease/difficulty of their transfer. As the film is 75 times-cycled, the hydration shell of cations becomes smaller (one  $\text{H}_2\text{O}$  molecule removed), and the cation motion is somewhat released from the restriction of  $\text{H}_2\text{O}$  shell, resulting in an increase of  $f_c$ .

Meanwhile, much more steric spaces inside the film would become accessible for free H<sub>2</sub>O molecules due to the smaller size of cations. This can lead to an ease in the solvent transfer which is translated into a decrease of  $R_t$  (H<sub>2</sub>O) values. After that, the cations completely remove their hydration shell towards the 125 times-cycled state (the end of region II), *i.e.* bare cations (**Figure III.6a**). Due to the relatively smaller size of bare cations, free H<sub>2</sub>O molecules inside the film may be better accommodated leading to a minimum of  $R_t$  (H<sub>2</sub>O) value observed at around 125 cycles (**Figure III.5d**). In this case, H<sub>2</sub>O molecules possess the greatest potential to be transferred at the film/electrolyte interface, which can be further confirmed in **Figure III.6b**. For the measurements at -0.6 V, the proportion of free H<sub>2</sub>O transferred through the film/electrolyte interface (calculated using **Equations III.12** and **III.13**) reaches maximum at the end of region II, *i.e.* 80% after 125 cycles (**Figure III.6b**). This observation can be discussed by consideration of an increased amount of space available inside the film provided by the dehydration process of the cations in region II. This results in a minimum value of the  $R_{t_s}$  lagging behind ~50 cycles to the peak of  $f_s$  (**Figure III.5b** and **d**). Additionally, the film at -0.6 V undergoes more H<sub>2</sub>O exchange than that at -0.2 V for the major portions of the cycling period (**Figure III.6b**). This finding may indicate a relatively higher swollen state and porosity of the film when polarized at -0.6 V. It can facilitate the transfer of bigger ions and may be the reason for (i) the transfer of hydrated cations (Na<sup>+</sup>·2H<sub>2</sub>O) at -0.6 V rather than at -0.2 V as the film is electrochemically cycled in region I, and (ii) the transfer of bigger anions (DS<sup>-</sup>) after the film is cycled ~ 175 times.

$$H_2O(\text{free}) = \frac{\left| \frac{-G_{H_2O}}{K_{H_2O}} \right|}{\left| \frac{-G_{H_2O}}{K_{H_2O}} \right| + \left| \frac{-G_{Na^+}}{K_{Na^+}} \right| + \left| \frac{-G_{Na^+ + xH_2O}}{K_{Na^+ + xH_2O}} \right| + \left| \frac{-G_{Cl^-}}{K_{Cl^-}} \right|} \quad (\text{III.12})$$

$$H_2O(\text{global}) = \frac{\left| \frac{-G_{H_2O}}{K_{H_2O}} \right| + x \left| \frac{-G_{Na^+ + xH_2O}}{K_{Na^+ + xH_2O}} \right|}{\left| \frac{-G_{H_2O}}{K_{H_2O}} \right| + \left| \frac{-G_{Na^+}}{K_{Na^+}} \right| + \left| \frac{-G_{Na^+ + xH_2O}}{K_{Na^+ + xH_2O}} \right| + \left| \frac{-G_{Cl^-}}{K_{Cl^-}} \right|} \quad (\text{III.13})$$

The  $R_{t_i}$  and  $C_i$  (instantaneous capacitance) of cations and anions (Cl<sup>-</sup>, without consideration of DS<sup>-</sup>) possess a similar dependence on the electrochemical cycling (**Figure III.5c-f**). When the data obtained at -0.2 V is taken as an example, the  $R_{t_i}$  of ions shows a progressive increase with electrochemical cycling, indicating that the more the film is cycled, the more difficult the ionic transfer becomes. Accordingly, the ionic capacitance,  $C_i$  decreases for both cations and anions. This

observation may indicate that transfer process of ions progressively degrades. Hence, it can be suggested that the periodic charging-discharging process can weaken the capability of CPEs to exchange ions at the film/electrolyte interface as a function of cycle number.

### III.3.3. Viscoelastic property changes upon film aging

Numerous studies have reported that the viscoelastic properties of the electroactive polymer play a crucial role in the electrogravimetric response if the film is not sufficiently thin or rigid<sup>45</sup>. More importantly, the viscoelastic change with electrochemical cycling is supposed to have a great influence on the electrochemical performance of the film primarily because volumetric changes during the redox process (insertion or expulsion of charged and non-charged species) are strongly associated with the viscoelastic properties of the polymer chains. Thus, the variation of the viscoelastic properties of the film during electrochemical cycling process was examined and the correlation between electrochemical and viscoelastic properties was further considered with regard to long term performance of CPEs.

**Figure III.7a** displays a similar change of  $G'$  and  $G''$  at the two selected potentials. Taking the film measured at -0.6 V for example, the storage modulus ( $G'$ ) is increased by approximately 200% as the film is electrochemically cycled. However,  $G''$  shows an entirely opposite tendency with film cycling, decreasing from  $0.77 \times 10^5 \text{ N.m}^{-2}$  to  $0.19 \times 10^5 \text{ N.m}^{-2}$  at -0.6 V. It has been revealed that the  $G'$  is correlated with the film stiffness, while  $G''$  is a measure of the film viscosity<sup>12, 38</sup>. The progressively increased  $G'$  and decreased  $G''$  suggest that the periodical cycling renders the PPy-DS film stiffer and less viscous. Nevertheless, this should not be attributed to the overoxidation of PPy because it starts at potentials greater than 0.7 V vs. SCE<sup>46-47</sup>. Additionally, FTIR spectra of the fresh and cycled PPy-DS films (**Figure III.8a**) exhibit the characteristic vibrational bands associated with the doped polypyrrole structure. The spectra of the fresh, 100- and 175-cycled film do not show remarkable differences which suggests the absence of polymer crosslinking phenomena upon electrochemical cycling. The absence of a band at  $\sim 1700 \text{ cm}^{-1}$  (corresponding to C=O functions) further indicates that there is no overoxidation of the polymer film<sup>48</sup>.

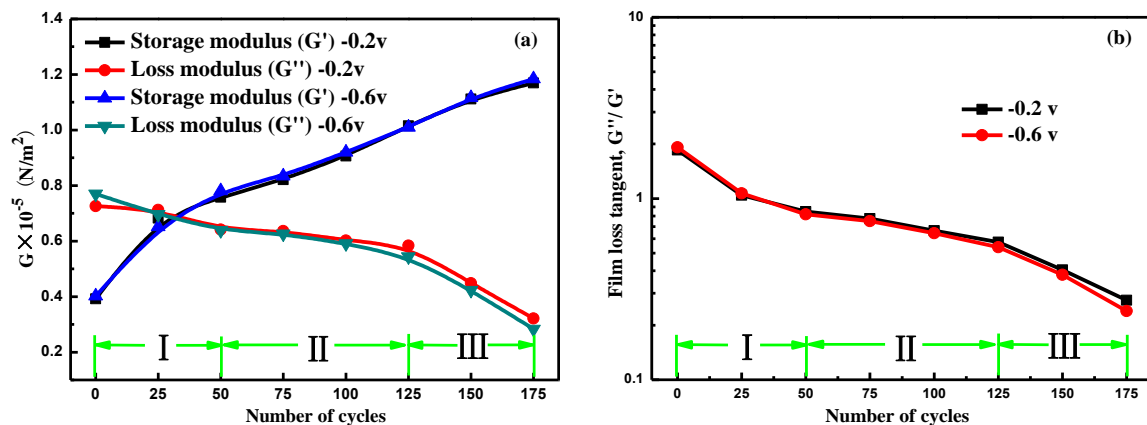


**Figure III.7.** (a) Evolution of real and imaginary components of complex shear modulus and (b) film loss tangent,  $G''/G'$ , during cycling at -0.2 V and -0.6 V, respectively.

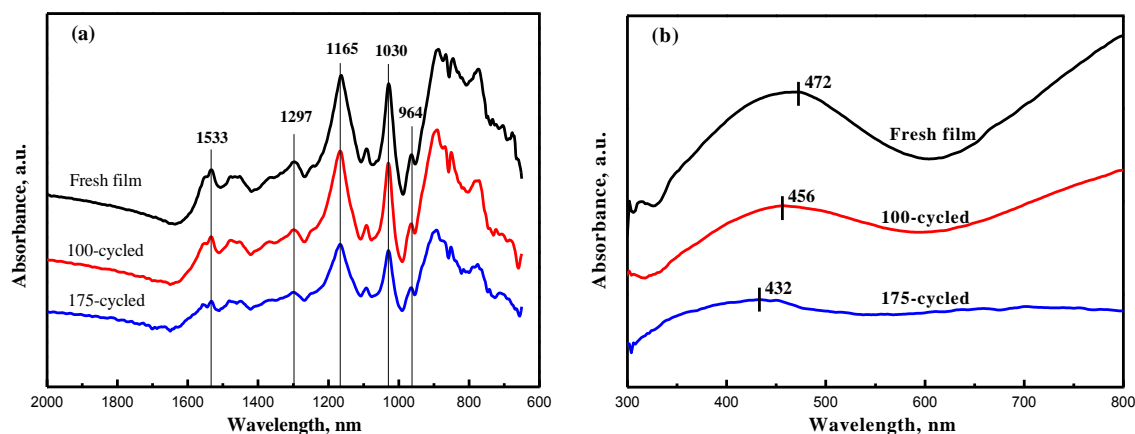


**Figure III.8.** (a) FTIR and (b) UV-vis spectra of fresh, 100- and 175-cycled PPy-DS film. The peak in (a) at  $1533\text{ cm}^{-1}$  corresponds to the C=C stretching of PPy; the peak at  $1297\text{ cm}^{-1}$  corresponds to the C-H in-plane deformation; two doping-induced bands at  $1165\text{ cm}^{-1}$  and  $964\text{ cm}^{-1}$  correspond to C-N stretching vibration and C-H out-of-plane vibration, respectively; the band at  $1030\text{ cm}^{-1}$  corresponds to C-H in-plane stretching vibration<sup>49-50</sup>.

In this work, we hold that the reformation of the polymer chains resulted from cycling process endows the film more rigid (increased  $G'$ ) and less viscous (decreased  $G''$ ). It has been reported that the requirement of co-planarity of  $\pi$  orbitals for long conjugation leads to the stiffness of poly (3-alkylthiophene)s through the reconfiguration and rearrangements of polymer chains<sup>32</sup>. Briefly, redox process of PPy-DS films involves a sequence of events: (i) electrons transferred between the film and the working electrode, (ii) exchange of cations and/or anions between the film and electrolyte to satisfy electroneutrality which is often coupled with free solvent transfer to meet the volumetric confinement of the viscoelastic film and lastly, (iii) reformation of polymer chains to be compatible with such new spatial architecture of the film. In a redox process, PPy

chain's reformation takes place to keep sufficient  $\pi$  orbital overlaps for conduction structure, where a co-planarity of  $\pi$  orbitals is required within  $40^\circ$ .<sup>51</sup> Therefore, upon electrochemical aging process, the structure of the polymer chains can be progressively altered due to such conformational changes. Specifically, for fresh PPy-DS film, pyrrole rings possess a coplanar conformation<sup>47</sup>, and the movement of  $DS^-$  ions is greatly restricted by strong interactions from large conjugated  $\pi$  systems. During film aging process, the coplanar conformation of PPy is gradually forced to approach a non-coplanar one by means of PPy chain's motions, giving rise to a progressive deterioration of long conjugated systems and consequently loss of electroactive sites or electronic conductivity, as it is approved by the fading electrical response of cyclic voltammetry in **Figure III.2a** or charge/potential TF in **Figure III.3g** and **h**. When the film is further electrochemically cycled (175 cycles), the  $DS^-$  ions are released out of the film and embark on the charge compensation process, as supported by **Figure III.4f**. Altogether, the electrochemical cycling process causes the reformation of the polymer chains, which brings about the stiffness of the film with fading electronic conductivity.

The film loss tangent,  $G''/G'$  was further used for describing the viscoelastic evolution of the film upon cycling process. As depicted in **Figure III.7b**, the film loss tangent shows a comparable decrease upon cycling at the two different potentials. It indicates that the cycling process confers increasing stiffness on the film. Namely, region I can be generally regarded as viscous region, region II becomes viscoelastic while region III is fairly elastic in the film electrochemical cycling evolution.

The stiffness of the film can restrict the volumetric changes and make it more difficult for ionic species not only to be transferred at the film/electrolyte interface but transported in the film bulk as well, which is in agreement with results obtained from the present cyclic electrogravimetric and *ac*-electrogravimetric studies, *i.e.*, *i*) fading of the pseudocapacitive capability *ii*) increase of the ionic transfer resistance,  $Rt_i$  and *iii*) decrease of the instantaneous capacitance,  $C_i$ , of each charged species.

As a matter of fact, the volume of the PPy-DS film can be varied from cathodic to anodic potentials within one cycle (**Figure III.9**-Route I) and also at the same potential after many cycles (**Figure III.9**-Route II). As **Figure III.9**-Route I shows, the PPy-DS film undergoes successive swelling and shrinking cycles during the redox process. In addition, a dehydration process of cations for freshly prepared films has been reported during anodic potential sweep due to the lower porosity of PPy-DS film in a relatively shrunken state<sup>38</sup>. As for route II which is explored in this

work, the volumetric change capability of the film can become poorer upon cycling, and the solvation shell of cation at -0.6 V is removed during the cycling process. **Figure III.9** elucidates the two different ways which can stiffen the PPy-DS film, i.e. anodic sweep and film cycling. Both can prohibit the transfer of hydrated  $\text{Na}^+$ . On the course of electrochemical cycling, the film would hardly experience volumetric change any more, which is accompanied with a fading of the electrochemical performance as seen in CV responses (**Figure III.2a**) and charge/potential response (**Figure III.3g** and **h**). The electrochemical activity loss upon cycling is further investigated by UV-vis spectroscopy. **Figure III.8b** indicates the presence of a distinct band appearing below  $\sim 480$  nm which is due to  $\pi$ - $\pi^*$  transitions<sup>52</sup>. When the PPy-DS films are cycled for 100 and 175 times, a decrease of the intensity and a shift to lower wavelength values of this characteristic band are observed. A blue shift and a decrease in the intensity of this band indicate an increase in the band gap of the PPy-DS films and a decrease in the conjugation length of the conducting polymer upon electrochemical cycling. This observation is in agreement with (i) the cyclic voltammetry investigations showing a considerable electrochemical activity loss and (ii) with the viscoelastic property investigations indicating a stiffening of the polymer which is likely to render the charge transfer more difficult. To the best of our knowledge, it is the first time that the correlation between electrochemical and viscoelastic properties in an electrochemical cycling process has been systematically investigated<sup>53</sup>.

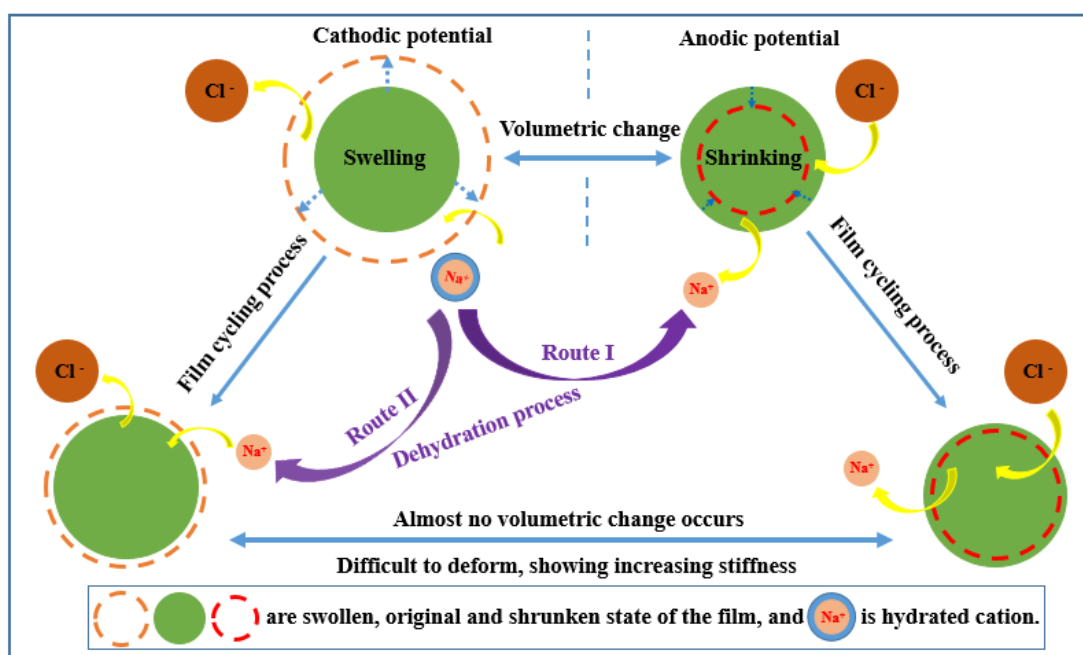


**Figure III.9.** Schematic of volumetric evolution of PPy electrode during film cycling, without considering the exchange of free  $\text{H}_2\text{O}$  molecules.

### III.4. Conclusions

The combination of EQCM, *ac*-electrogravimetry and electroacoustic measurements was proposed to track the electrochemical and viscoelastic evolution during the electrochemical cycling of PPy-DS films. An obvious ion-selective transition from cations to anions for charge compensation is observed during film cycling process. A predominant role is played by cations for fresh and slightly cycled films, whereas anions dominate the charge balance in relatively long-time cycled films.

The electrochemical performance was investigated at two different potentials. At -0.6 V, the film presents a relatively more swollen state than that at -0.2 V due to the higher amount of H<sub>2</sub>O molecules insertion, facilitating the transfer of bigger ions, *i.e.*, Na<sup>+</sup> with two H<sub>2</sub>O molecules in the hydration shell and DS<sup>-</sup> anions. Kinetics of H<sub>2</sub>O molecule in region II (50-125<sup>th</sup> cycle in **Figure III.5b**) show a complex and cycling-dependent property due to the competitive relationship between availability for accommodation inside the film provided by cation's dehydration process (favoring H<sub>2</sub>O transfer) and polymer chain's increasing stiffness during film cycling (increased  $G'$ ; prohibiting H<sub>2</sub>O transfer). At -0.2 V, desolvated Na<sup>+</sup> is the only form of cations participating in the charge compensation. The cation is the fastest species (except the DS<sup>-</sup> at -0.6 V for 175-times-cycled film) transferred at the film/electrolyte interface followed by free H<sub>2</sub>O molecules at intermediate frequencies and anions are the slowest species at both potentials irrespective of cycling degree of the film.

For PPy-DS electrodes, the ionic transfer becomes more difficult upon electrochemical cycling process followed in the present work. It should be noted that this modification can also be influenced by the film thickness, the nature and the concentration of electrolytes, and the scan rate. The observed ionic transfer change is not only due to the loss of electroactive sites inside the film but also due to the increasing stiffness of the polymer chains. It is attributed to the reformation of the PPy chains which consequently result in the deterioration of the conjugated  $\pi$  systems. This study presents an example showing the utility of complementary electrochemical methods to investigate the correlation between electrochemical performance and viscoelastic variations of PPy-DS electrodes upon cycling. The suggested diagnostic strategy can be applied to other CPEs and may help to develop new synthetic strategies for designing highly efficient electrodes in energy devices with improved performance.

## References

1. Knopfmacher, O.; Hammock, M. L.; Appleton, A. L.; Schwartz, G.; Mei, J.; Lei, T.; Pei, J.; Bao, Z., Highly stable organic polymer field-effect transistor sensor for selective detection in the marine environment. *Nat. Commun.* **2014**, *5*, 2954.
2. Ramanavičius, A.; Ramanavičienė, A.; Malinauskas, A., Electrochemical sensors based on conducting polymer—polypyrrole. *Electrochim. Acta* **2006**, *51* (27), 6025-6037.
3. Gracia, R.; Mecerreyes, D., Polymers with redox properties: materials for batteries, biosensors and more. *Polym. Chem.* **2013**, *4* (7), 2206.
4. Li, F. S.; Wu, Y. S.; Chou, J.; Winter, M.; Wu, N. L., A mechanically robust and highly ion-conductive polymer-blend coating for high-power and long-life lithium-ion battery anodes. *Adv. Mater.* **2015**, *27* (1), 130-137.
5. Wang, K.; Wu, H.; Meng, Y.; Wei, Z., Conducting polymer nanowire arrays for high performance supercapacitors. *Small* **2014**, *10* (1), 14-31.
6. Ghenaatian, H. R.; Mousavi, M. F.; Rahmanifar, M. S., High performance hybrid supercapacitor based on two nanostructured conducting polymers: Self-doped polyaniline and polypyrrole nanofibers. *Electrochim. Acta* **2012**, *78*, 212-222.
7. Han, L.; Tang, P.; Zhang, L., Hierarchical Co<sub>3</sub>O<sub>4</sub>@PPy@MnO<sub>2</sub> core-shell-shell nanowire arrays for enhanced electrochemical energy storage. *Nano Energy* **2014**, *7*, 42-51.
8. Liu, T.; Finn, L.; Yu, M.; Wang, H.; Zhai, T.; Lu, X.; Tong, Y.; Li, Y., Polyaniline and polypyrrole pseudocapacitor electrodes with excellent cycling stability. *Nano Lett.* **2014**, *14* (5), 2522-2527.
9. Holze, R.; Wu, Y. P., Intrinsically conducting polymers in electrochemical energy technology: Trends and progress. *Electrochim. Acta* **2014**, *122*, 93-107.
10. Xia, C.; Chen, W.; Wang, X.; Hedhili, M. N.; Wei, N.; Alshareef, H. N., Highly Stable Supercapacitors with Conducting Polymer Core-Shell Electrodes for Energy Storage Applications. *Adv. Energy Mater.* **2015**, *5* (8), 1401805.
11. Agrisuelas, J.; Gabrielli, C.; Garc á-Jare ño, J. J.; Perrot, H.; Sel, O.; Vicente, F., Viscoelastic potential-induced changes in acoustically thin films explored by quartz crystal microbalance with motional resistance monitoring. *Electrochim. Acta* **2015**, *176*, 1454-1463.
12. Mohamoud, M. A.; Hillman, A. R., The effect of anion identity on the viscoelastic properties of polyaniline films during electrochemical film deposition and redox cycling. *Electrochim. Acta* **2007**, *53* (3), 1206-1216.
13. Shpigel, N.; Levi, M. D.; Sigalov, S.; Girshevitz, O.; Aurbach, D.; Daikhin, L.; Jackel, N.; Presser, V., Non-invasive in situ dynamic monitoring of elastic properties of composite battery electrodes by EQCM-D. *Angew. Chem. Int. Ed.* **2015**, *54* (42), 12353-12356.
14. Wang, G.; Zhang, L.; Zhang, J., A review of electrode materials for electrochemical supercapacitors. *Chem. Soc. Rev.* **2012**, *41* (2), 797-828.
15. Zhan, L. Z.; Song, Z. P.; Zhang, J. Y.; Tang, J.; Zhan, H.; Zhou, Y. H.; Zhan, C. M., PEDOT: Cathode active material with high specific capacity in novel electrolyte system. *Electrochim. Acta* **2008**, *53* (28), 8319-8323.
16. Mo, D. Z.; Zhou, W. Q.; Ma, X. M.; Xu, J. K.; Zhu, D. H.; Lu, B. Y., Electrochemical synthesis and capacitance properties of a novel poly(3,4-ethylenedioxythiophene bis-substituted bithiophene) electrode material. *Electrochim. Acta* **2014**, *132*, 67-74.
17. Feng, H. X.; Wang, B.; Tan, L.; Chen, N. L.; Wang, N. X.; Chen, B. Y., Polypyrrole/hexadecylpyridinium chloride-modified graphite oxide composites: Fabrication, characterization, and application in supercapacitors. *J. Power Sources* **2014**, *246*, 621-628.
18. Tang, H.; Wang, J.; Yin, H.; Zhao, H.; Wang, D.; Tang, Z., Growth of polypyrrole ultrathin films on MoS<sub>2</sub> monolayers as high-performance supercapacitor electrodes. *Adv. Mater.* **2015**, *27* (6), 1117-1123.
19. Inzelt, G.; Kertesz, V.; Nyback, A.-S., Electrochemical quartz crystal microbalance study of ion transport accompanying charging-discharging of poly(pyrrole) films. *J. Solid State Electrochem.* **1999**, *3*, 251-257.
20. Wang, L.; Feng, X.; Ren, L.; Piao, Q.; Zhong, J.; Wang, Y.; Li, H.; Chen, Y.; Wang, B., Flexible solid-state supercapacitor based on a metal-organic framework interwoven by electrochemically-deposited PANI. *J. Am. Chem.*

*Soc.* **2015**, *137* (15), 4920-4923.

21. Ambade, R. B.; Ambade, S. B.; Shrestha, N. K.; Nah, Y. C.; Han, S. H.; Lee, W.; Lee, S. H., Polythiophene infiltrated TiO<sub>2</sub> nanotubes as high-performance supercapacitor electrodes. *Chem. Commun.* **2013**, *49* (23), 2308-2310.
22. Snook, G. A.; Kao, P.; Best, A. S., Conducting-polymer-based supercapacitor devices and electrodes. *J. Power Sources* **2011**, *196* (1), 1-12.
23. Zhou, C.; Zhang, Y.; Li, Y.; Liu, J., Construction of high-capacitance 3D CoO@polypyrrole nanowire array electrode for aqueous asymmetric supercapacitor. *Nano Lett.* **2013**, *13* (5), 2078-2085.
24. Escobar-Teran, F.; Arnau, A.; Garcia, J. V.; Jiménez, Y.; Perrot, H.; Sel, O., Gravimetric and dynamic deconvolution of global EQCM response of carbon nanotube based electrodes by Ac-electrogravimetry. *Electrochem. Commun.* **2016**, *70*, 73-77.
25. Griffin, J. M.; Forse, A. C.; Tsai, W. Y.; Taberna, P. L.; Simon, P.; Grey, C. P., In situ NMR and electrochemical quartz crystal microbalance techniques reveal the structure of the electrical double layer in supercapacitors. *Nat. Mater.* **2015**, *14* (8), 812-819.
26. Tsai, W. Y.; Taberna, P. L.; Simon, P., Electrochemical quartz crystal microbalance (EQCM) study of ion dynamics in nanoporous carbons. *Journal of the American Chemical Society* **2014**, *136* (24), 8722-8.
27. Gabrielli, C.; Garcia-Jareño, J. J.; Keddad, M.; Perrot, H.; Vicente, F., Ac-electrogravimetry study of electroactive thin films. II. Application to polypyrrole. *J. Phys. Chem. B* **2002**, *106*, 3192-3201.
28. Kim, L. T. T.; Gabrielli, C.; Pailleret, A.; Perrot, H., Correlation between ion-exchange properties and swelling/shrinking processes in hexasulfonated calix[6]arene doped polypyrrole films: ac-electrogravimetry and electrochemical atomic force microscopy investigations. *Electrochim. Acta* **2011**, *56* (10), 3516-3525.
29. Levi, M. D.; Salitra, G.; Levy, N.; Aurbach, D.; Maier, J., Application of a quartz-crystal microbalance to measure ionic fluxes in microporous carbons for energy storage. *Nat. Mater.* **2009**, *8* (11), 872-875.
30. Simon, P.; Gogotsi, Y., Materials for electrochemical capacitors. *Nat. Mater.* **2008**, *7* (11), 845-854.
31. García-Jareño, J. J.; Gabrielli, C.; Perrot, H., Validation of the mass response of a quartz crystal microbalance coated with Prussian Blue film for ac electrogravimetry. *Electrochem. Commun.* **2000**, *2* (3), 195-200.
32. Hillman, A. R.; Efimov, I.; Skompska, M., Dynamics of regioregular conducting polymer electrodes in response to electrochemical stimuli. *Faraday Discuss.* **2002**, *121*, 423-439.
33. Koehler, S.; Bund, A.; Efimov, I., Shear moduli of anion and cation exchanging polypyrrole films. *Journal of Electroanalytical Chemistry* **2006**, *589* (1), 82-86.
34. Hillman, A. R.; Mohamoud, M. A.; Efimov, I., Time-temperature superposition and the controlling role of solvation in the viscoelastic properties of polyaniline thin films. *Anal. Chem.* **2011**, *83* (14), 5696-707.
35. Ispas, A.; Peipmann, R.; Bund, A.; Efimov, I., On the p-doping of PEDOT layers in various ionic liquids studied by EQCM and acoustic impedance. *Electrochim. Acta* **2009**, *54* (20), 4668-4675.
36. Lyutov, V.; Gruia, V.; Efimov, I.; Bund, A.; Tsakova, V., An acoustic impedance study of PEDOT layers obtained in aqueous solution. *Electrochim. Acta* **2016**, *190*, 285-293.
37. Gabrielli, C.; Garcia-Jareño, J. J.; Perrot, H., Charge compensation process in polypyrrole studied by ac electrogravimetry. *Electrochim. Acta* **2001**, *46* (26), 4095-4103.
38. Hillman, A. R.; Efimov, I.; Skompska, M., Time-temperature superposition for viscoelastic properties of regioregular poly(3-hexylthiophene) films. *J. Am. Chem. Soc.* **2005**, *127* (11), 3817-3824
39. Granstaff, V. E.; Martin, S. J., Characterization of a thickness-shear mode quartz resonator with multiple nonpiezoelectric layers. *J. Appl. Phys.* **1994**, *75* (3), 1319-1329.
40. Sauerbrey, G., The use of a quartz crystal oscillator for weighing thin layers and microweighing applications. *Z. Phys.* **1959**, *155*, 206-222.
41. Camurlu, P., Polypyrrole derivatives for electrochromic applications. *RSC Adv.* **2014**, *4* (99), 55832-55845.
42. Levi, M. D.; Lopez, C.; Vieil, E.; Vorotyntsev, M. A., Influence of ionic size on the mechanism of electrochemical doping of polypyrrole films studied by cyclic voltammetry. *Electrochim. Acta* **1997**, *42* (5), 757-769.
43. Arias, C. R.; Debiemme-Chouvy, C.; Gabrielli, C.; Laberty-Robert, C.; Pailleret, A.; Perrot, H.; Sel, O., New insights into pseudocapacitive charge-storage mechanisms in Li-Birnessite type MnO<sub>2</sub> monitored by fast quartz crystal

microbalance methods. *J. Phys. Chem. C* **2014**, *118* (46), 26551-26559.

44. Sel, O.; To Thi Kim, L.; Debiemme-Chouvy, C.; Gabrielli, C.; Laberty-Robert, C.; Perrot, H., Determination of the diffusion coefficient of protons in Nafion thin films by ac-electrogravimetry. *Langmuir* **2013**, *29* (45), 13655-13660.
45. Levi, M. D.; Sigalov, S.; Aurbach, D.; Daikhin, L., In situ electrochemical quartz crystal admittance methodology for tracking compositional and mechanical changes in porous carbon electrodes. *J. Phys. Chem. C* **2013**, *117* (29), 14876-14889.
46. Christensen, P. A.; Hamnett, A., In situ spectroscopic investigations of the growth, electrochemical cycling and overoxidation of polypyrrole in aqueous solution *Electrochim. Acta* **1991**, *36* (8), 1263-1286.
47. Beck, F.; Braun, P.; Oberst, M., Organic electrochemistry in the solid state-overoxidation of polypyrrole. *Ber. Bunsenges. Phys. Chem.* **1987**, *91*, 967-974.
48. Lu, G.; Li, C.; Shi, G., Polypyrrole micro- and nanowires synthesized by electrochemical polymerization of pyrrole in the aqueous solutions of pyrenesulfonic acid. *Polymer* **2006**, *47* (6), 1778-1784.
49. Wang, J.-G.; Wei, B.; Kang, F., Facile synthesis of hierarchical conducting polypyrrole nanostructures via a reactive template of MnO<sub>2</sub> and their application in supercapacitors. *RSC Adv.* **2014**, *4* (1), 199-202.
50. Chen, Y.; Xu, H.; Wang, S.; Kang, L., Removal of Cr(VI) from water using polypyrrole/attapulgite core-shell nanocomposites: equilibrium, thermodynamics and kinetics. *RSC Adv.* **2014**, *4* (34), 17805-17811.
51. Brédas, J. L.; Street, G. B.; Thémans, B.; André, J. M., Organic polymers based on aromatic rings (polyparaphenylene, polypyrrole, polythiophene): Evolution of the electronic properties as a function of the torsion angle between adjacent rings. *J. Chem. Phys.* **1985**, *83* (3), 1323.
52. Jeon, S. S.; Kim, C.; Ko, J.; Im, S. S., Spherical polypyrrole nanoparticles as a highly efficient counter electrode for dye-sensitized solar cells. *J. Mater. Chem.* **2011**, *21* (22), 8146-8151.
53. GAO, W.; Sel, O.; Perrot, H., Electrochemical and viscoelastic evolution of dodecyl sulfate-doped polypyrrole films during electrochemical cycling. *Electrochim. Acta* **2017**, *233*, 262-273.

## Chapter IV: Tuning charge storage properties of reduced graphene oxides evidenced by in situ gravimetric and viscoelastic explorations

Slightly electrochemically reduced graphene oxide (ERGO) presents an anion preference for charge storage and delivery, while with the progressive removal of oxygen functionalities on its basal planes, cations begin to predominate in charge compensation. This “anion-to-cation” evolution in neutral aqueous media can not only affect the electrochemical charge storage, but also play an important role in electrode’s viscoelasticity. It was demonstrated that oxygen functionalities could modify the interactions between graphene layers and even contribute to pseudocapacitances. However, the role of oxygen functional groups in species transfer and viscoelastic variations still remains poorly understood. Herein, a combined methodology of electrochemical quartz crystal microbalance (EQCM), *ac*-electrogravimetry and electroacoustic impedance measurements was proposed for characterizing the electrochemical and viscoelastic responses of graphene oxides with various degree of electrochemical reduction. With the removal of oxygen containing functional groups, ERGO electrode exhibits (i) a gradually enhanced specific capacitance ( $C_s$ ) with increased flexibility (decreased storage moduli,  $G'$ ); (ii) a dehydration process of cations (i.e. from  $\text{Na}^+\cdot 2\text{H}_2\text{O}$  to  $\text{Na}^+\cdot \text{H}_2\text{O}$ ); and (iii) a potential-dependent “stiffened-softened” behavior. These results open the door for a suitable design of GO-based materials for electrochemical energy storage and shed light on electronic devices where ion-selective behavior plays a key role.

### IV.1. Preamble and Objectives

Owing to high power density and superior cycling performance, supercapacitor (SC) has boosted numerous research efforts in electrochemical energy storage and offered a wide range of potential applications, such as portable electronics, electric vehicles and stand-free power systems<sup>1-6</sup>. The most important component in SC is the electrode material with high surface area and high porosity<sup>7-8</sup>. Among those, carbon-based materials are considered as prospective SC electrode candidates for bulk production<sup>9-10</sup>. Graphene, a  $\text{sp}^2$ -bonded carbon monolayer, has demonstrated itself significantly effective for electrochemical energy storage/delivery due to many appealing features, such as high surface area (theoretically as high as  $2630 \text{ m}^2\cdot\text{g}^{-1}$ ), superior mechanical

properties, excellent electronic conductivity and chemical resilience<sup>2, 10-15</sup>. Reduction of graphene oxide (GO) is widely adopted for the production of graphene because of its low cost, high scalability and competitive yield<sup>16-17</sup>. As a highly defective form of graphene functionalized by enriched oxygen-containing groups, GO may offer higher capacitance than graphene through additional pseudo-capacitive behavior<sup>18-21</sup>. However, the oxygen containing functional groups can also restrain the  $sp^2$  hybridization and thus render the GO less conductive due to degraded  $\pi$ - $\pi$  stacking. From this perspective, the electrochemical charge storage performance of GO is strongly associated with the content of oxygen functional groups on its layers: *i*) high content of oxygen functional groups brings about more pseudocapacitance from reversible redox reactions and improves the wettability of GO electrodes with aqueous solution but results in an inferior conductivity and less electroactive surfaces for electrical double-layer capacitance (EDLC); contrarily, *ii*) low content of oxygen functional groups leads to an enhanced electronic conductivity due to the restoration of the  $\pi$ - $\pi$  network and a higher electroactivity of the surfaces for charge adsorption/desorption, thereby promoting improvements in electrochemical performances of SC. Thus, a direct correlation between the oxygen-containing groups of the GO and the final electrochemical performance of the SCs cannot be disregarded.

Under the consideration that most of the graphenes synthesized through reduction of GO bear some unavoidable extrinsic defects from oxygen-containing groups<sup>16, 22</sup>, a systematic investigation on the electrochemical behavior of GO with different content of oxygen functionalities is highly desirable for well-designed SC electrodes. Additionally, although it has been demonstrated that oxygen containing functional groups could bring about reversible electrochemical reactions, thus contributing to capacitance<sup>18-19</sup>, the mechanism of ionic fluxes during charge-discharge process in GO-based electrodes still remains poorly understood.

Besides superior electrochemical properties, long-term cycling performances are also of importance for an efficient SC electrode. Upon cycling, periodical ion electroadsorption/electrodesorption and/or insertion/extraction are possibly accompanied with solvent flux which lead to repeated species-transfer-induced deformation as well as viscoelastic changes of the GO electrode (stiffened/softened). Such viscoelastic changes which are not completely relaxed at the end of each cycle and tend to gradually accumulate, thereby result in a failure of the mechanical integrity and lead to an eventual cyclability fading. Multiharmonic EQCM with dissipation monitoring (EQCM-D) has been used for the investigation of gravimetric and viscoelastic changes of electrodes during charge storage process by the interpretation of both

frequency ( $\Delta f/n$ ,  $n$  is the overtone order) and resonance width ( $\Delta W/n$ ) changes<sup>23</sup>. Nevertheless, of practical and fundamental importance but scarcely touched is the correlation between electrode viscoelasticity and its electrochemical performance<sup>24-26</sup>.

Electrochemical quartz crystal microbalance (EQCM) and its coupling with electrochemical impedance spectroscopy (the so-called *ac*-electrogravimetry) have proved themselves significantly effective for evaluating the electrochemical behaviors of carbon-based electrodes<sup>27-28</sup>, particularly *in situ* capturing ionic transfer between the electrode and electrolyte. Besides identifying each species participating in the charge compensation process, it can provide a quantitative picture together with the kinetics of transfer of each species, thereby providing a kinetic and gravimetric deconvolution. In addition to the utility of the electrogravimetric methods, the viscoelastic evolutions of the GO electrodes in the process of oxygen-containing groups removal and at different states-of-polarization can be tracked by electroacoustic impedance method<sup>29-31</sup>, from which two important parameters for describing the viscoelasticity of the GO electrodes, i.e., the storage ( $G'$ ) and loss moduli ( $G''$ ) can be estimated.  $G'$  represents the electrode stiffness whereas  $G''$  reflects its viscosity. These parameters can be further utilized to estimate the sensitivity coefficients of the QCM when it is not under gravimetric regime and thus help to differentiate the effect of the mechanical property changes from purely gravimetric responses<sup>29</sup>.

In the current study, ERGO electrodes with different content of oxygen functionalities were prepared and a combined methodology of EQCM, *ac*-electrogravimetry and electroacoustic impedance method was proposed to acquire a deeper insight into (i) the influence of oxygen containing functional groups on the ionic transfer in ERGO electrodes and (ii) the correlation between electrochemical and viscoelastic evolution during the gradual removal of these groups.

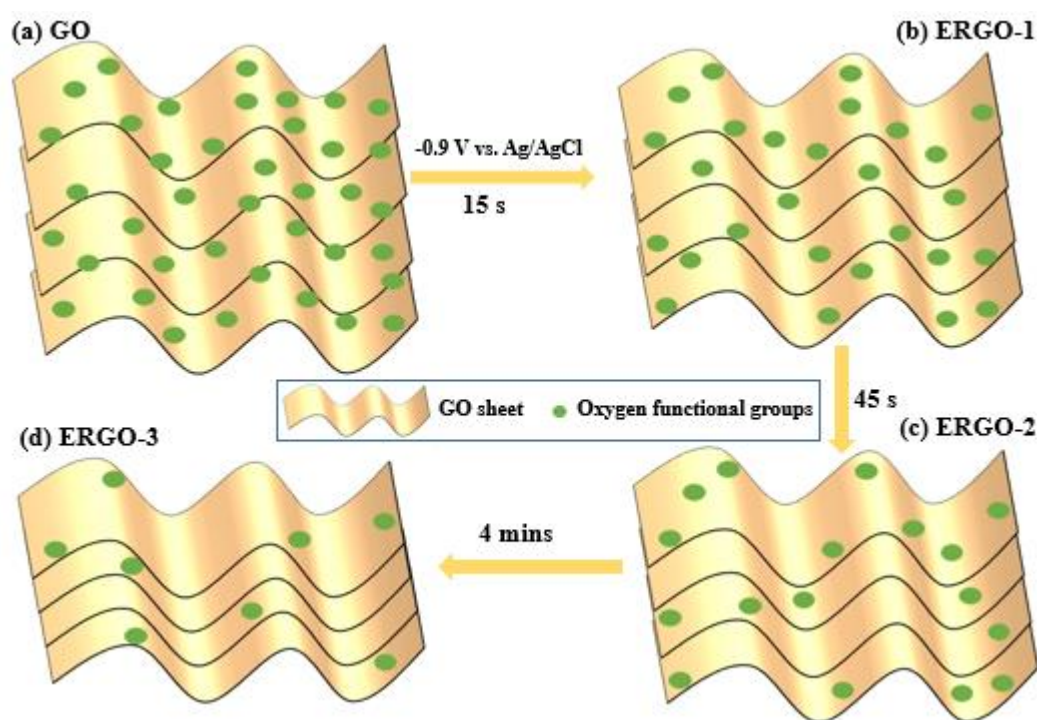
To the best of our knowledge, such a systematic study is unprecedented and is distinguished from the previous works thanks to the non-conventional electrochemical characterization methods employed, which provides the correlation between oxygen containing functional groups and nanostructure of the ERGO layers and their effect on the species (ions or solvent) transfer kinetics, hydration/dehydration of ions and the electrochemical and viscoelastic properties of the electrodes.

## IV.2. Experimental Methods and Theoretical Background

### IV.2.1 Synthesis of ERGO electrodes and structural characterization

GO was synthesized by a modified Hummers method<sup>32</sup>. GO suspension of 1 mg/mL was

prepared from addition of GO powder to bi-distilled water, followed by a consecutive ultrasonication for 5h to get a homogeneous solution. About 40  $\mu\text{L}$  GO suspension were deposited on the gold electrode ( $0.2\text{ cm}^2$ ) of a quartz crystal microbalance resonator (9 MHz-AWS, Valencia, Spain) with the help of a lab-made mask, which ensures the exposure of the gold electrode only. GO film was generated after being dried at  $70\text{ }^\circ\text{C}$  for 1h in an oven. The electrochemical reduction was carried out by a standard three electrode configuration, where GO-coated gold electrode of quartz resonator was used as a working electrode, with a platinum gauze and Ag/AgCl (3 M KCl saturated with AgCl) as a counter and a reference electrode, respectively. The reduced GO films were electrochemically synthesized by chronoamperometry with a Biologic SP-200 potentiostat using EC-Lab software at  $-0.9\text{ V vs. Ag/AgCl}$  in a solution of  $0.5\text{ M NaNO}_3$ . Nitrogen gas was bubbled in the solution prior to the electrochemical reduction and was maintained over the solution until the end of the reduction to ensure a complete saturation in  $\text{NaNO}_3$  solution. The resulting ERGO electrodes were designated as ERGO-1, ERGO-2 and ERGO-3 in accordance with the reduction time of 15 s, 1 min and 5 min, respectively (**Scheme IV.1**).



**Scheme IV.1.** Synthesis process and the expected structural changes for ERGO-1, -2 and -3.

The morphologies of the electrogenerated ERGO electrodes were observed under vacuum conditions using a field emission gun scanning electron microscope (FEG-SEM, Zeiss, Supra 55). The crystallographic structures were determined by X-ray diffraction (XRD), which was performed

at ambient conditions using Phillips PANalytical X'Pert Pro diffractometer with Cu K $\alpha$  radiation ( $\lambda = 1.54184 \text{ \AA}$ ). The electrodes used for XRD were prepared on ITO-coated glass slides and reduced under the same conditions as those on gold electrode of the quartz resonators. X-ray photoelectron spectroscopy analyses were performed using an Omicron Argus X-ray photoelectron spectrometer with monochromatized Al K $\alpha$  excitation (1486.6 eV) with a pass energy of 100 eV and 20 eV for acquisition of the survey and high-resolution spectra, respectively. The emissions of photoelectrons from the sample were analyzed at a take-off angle of 90°. The XPS peak areas were determined after subtraction of a background using Shirley's method. Element peak intensities were corrected by Scofield factors. The experimental data were analyzed using the Avantage software.

### IV.2.2 Electroacoustic impedance measurements

The viscoelastic evolutions of ERGO electrodes were explored by the electroacoustic impedance method to elucidate the relationship between electrochemical and viscoelastic changes of the ERGO electrodes. Electroacoustic impedance measurements were carried out in the potential range between -0.4 V to 0.4 V (at nine different potentials with an interval of 100 mV). An Agilent 4294A impedance analyzer coupled with a lab-made potentiostat (SOTELEM-PGSTAT) was used in order to perform the electroacoustic admittance measurements under polarization. A lab-made software Simad was used for extracting the storage moduli ( $G'$ ) and loss moduli ( $G''$ ) of the ERGO films through fitting the experimental data.  $G'$  is associated with the energy storage capability of the ERGO layers whereas  $G''$  describes the energy dissipation of the electrode due to internal friction and irreversible deformation of ERGO sheets.

The complete theoretical electrical admittance,  $Y_{th}^V(\omega)$ , of the loaded quartz resonator is:

$$Y_{th}^V(\omega) = \frac{1}{Z_{th}^V(\omega)} = G + iB = i \times \omega \times C_p + \frac{1}{Z_m^V(\omega)} \quad (IV.1)$$

where  $G$  is conductance,  $B$  depicts susceptance,  $\omega = 2 \times \pi \times f$ ,  $C_p$  is the parasitic capacitance and  $Z_m^V$  is the motional impedance of the loaded quartz resonator calculated with a viscoelastic model.

The motional impedance,  $Z_m^V$ , can be modelled according to the work of Martin *et al*<sup>33</sup>. If the characteristics of the quartz and of the liquid are considered as constants, the motional electrical impedance,  $Z_m^V$  of the coated resonator is:

$$Z_m^V(\omega) = \frac{h_q^2}{4 \times e_q^2 \times A} \times Z_f \times \frac{Z_s + Z_f \times \tanh(\theta_f \times h_f)}{Z_f + Z_s \times \tanh(\theta_f \times h_f)} \quad (\text{IV.2})$$

where  $h_q$  is the quartz thickness,  $e_q$  is the quartz piezoelectric constant,  $A$  is the active mass area,  $Z_f$  is the acoustic impedance of the film,  $Z_s$  is the acoustic impedance of the liquid,  $\theta_f$  is the complex propagation constant of the film and  $h_f$  is its thickness. Moreover,  $Z_f$  and  $\theta_f$  can be described as:

$$Z_f = \sqrt{\rho_f \times G_f} \quad (\text{IV.3})$$

$$\theta_f = \sqrt{\frac{\rho_f}{G_f}} \quad (\text{IV.4})$$

where  $\rho_f$  is the film density and  $G_f$  is the shear thickness modulus of the film, which can be written as a complex number with a real and imaginary part,  $G_f = G' + jG''$ , where  $j^2 = -1$ .

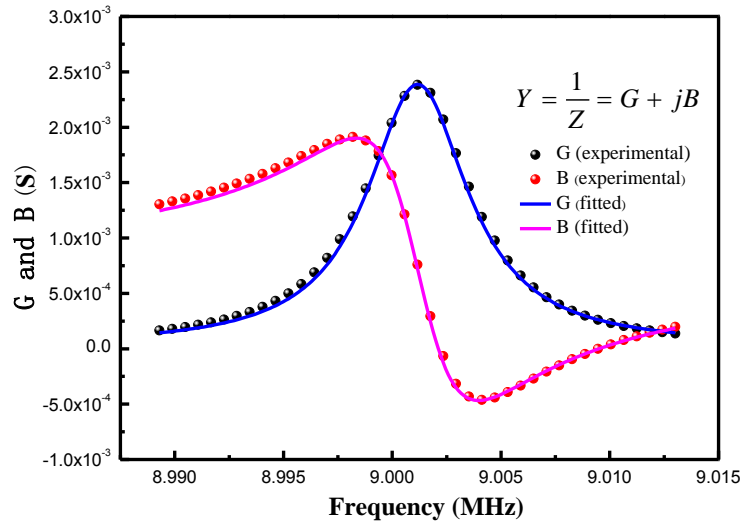


**Figure IV.1.** Electroacoustic admittance measurements: experimental and fitted conductance and susceptance over frequency for ERGO-1 at -0.2 V. Fitting parameters:  $G' = 6.29 \times 10^5 \text{ N.m}^{-2}$ ,  $G'' = 0.84 \times 10^5 \text{ N.m}^{-2}$ ,  $d_f = 146 \text{ nm}$  and  $\rho_f = 2 \text{ g.cm}^{-3}$ .

The acoustic impedance of the solution,  $Z_s$ , is defined as in **Equation IV.3** except that  $G'$  becomes negligible and for a Newtonian liquid,  $G'' = 2\pi f \eta_s$ , where  $f$  is the frequency and  $\eta_s$  the

liquid viscosity. **Figure IV.1** shows an example for the fitting of the experimental response of ERGO-1 at -0.2 V, which takes into consideration four parameters of the film, i.e., film thickness ( $d_f$ ), film density ( $\rho_f$ ),  $G'$  and  $G''$ .

### IV.2.3 Electrogravimetric measurements

The electrogravimetric response of a pristine GO thin film from *ac*-electrogravimetry was too weak to be analyzed due to its poor electronic conductivity. Therefore, it was slightly reduced for 15 s at -0.9 V vs. Ag/AgCl (ERGO-1) with the expectation of maintaining as much oxygen containing functional groups as possible on its sheets, and meanwhile being sufficiently conductive for obtaining a cognitive response in *ac*-electrogravimetry. The electrochemical performances of ERGO electrodes were measured employing a standard three-electrode electrochemical cell which consisted of a ERGO-loaded quartz resonator as the working electrode, Ag/AgCl (3 M KCl saturated with AgCl) as the reference electrode, and platinum gauze as the counter electrode. Electrochemical experiments were carried out at ambient temperature in 1 M NaCl solution as the electrolyte. The potential window for galvanostatic charging-discharging (GCD) tests at different current densities (0.5, 1 and 2 mA·cm<sup>-2</sup>) was confined between -0.5 V and 0.5 V vs. Ag/AgCl, which was applied to cyclic voltammetry measurements as well.

For *ac*-electrogravimetry measurements, a four-channel frequency response analyzer (FRA, Solartron 1254) and a lab-made potentiostat (SOTELEM-PGSTAT) were used. The QCM was performed under dynamic regime, and the modified working electrode was polarized at selected potentials to which a sinusoidal small amplitude potential perturbation (80 mV rms) was superimposed. The frequency range for this potential perturbation was between 63 kHz and 10 mHz. The microbalance frequency shift ( $\Delta f_m$ ) corresponding to the mass change ( $\Delta m$ ) of the modified working electrode was measured simultaneously with the charge response ( $\Delta q$ ) of the electrochemical system. The resulting signals were sent to the four-channel FRA, which allowed the electrochemical impedance ( $\frac{\Delta E}{\Delta I}(\omega)$ ), the electrogravimetric transfer function ( $\frac{\Delta m}{\Delta E}(\omega)$ ) and the charge/potential transfer function ( $\frac{\Delta q}{\Delta E}(\omega)$ ) to be obtained simultaneously at a given potential and frequency modulation,  $f$  (pulsation  $\omega=2\pi f$ ). Various transfer functions such as  $\frac{\Delta E}{\Delta I}(\omega)$ ,  $\frac{\Delta q}{\Delta E}(\omega)$  and  $\frac{\Delta m}{\Delta E}(\omega)$  can be theoretically calculated through the following **Equations IV.5** to **IV.8**<sup>27, 34</sup>.

More details about *ac*-electrogravimetry are given in Chapter II.

$$\frac{\Delta C_i}{\Delta E}(\omega) = \frac{-G_i}{j\omega d_f + K_i} \quad (\text{IV.5})$$

$$\frac{\Delta E}{\Delta I}(\omega) = (j\omega d_f F \sum_i \frac{G_i}{j\omega d_f + K_i})^{-1} \quad (\text{IV.6})$$

$$\frac{\Delta q}{\Delta E}(\omega) = F d_f \sum_i \frac{G_i}{j\omega d_f + K_i} \quad (i: \text{ions}) \quad (\text{IV.7})$$

$$\frac{\Delta m}{\Delta E}(\omega) = -d_f \sum_i M_i \frac{G_i}{j\omega d_f + K_i} \quad (i: \text{ions and non-charged species}) \quad (\text{IV.8})$$

where  $\Delta C_i$  presents concentration variation for each species (ions and free solvent) in ERGO electrodes,  $\omega$  the pulsation,  $d_f$  the film thickness (estimated through QCM measurements),  $M_i$  the atomic weight of involved species,  $K_i$  and  $G_i$  are the partial derivatives of the flux ( $J_i$ ) with respect to the concentration and the potential, respectively.  $K_i$  represents the transfer kinetics of each species whereas  $G_i$  describes the level of difficulty for each species transferred at the electrode/electrolyte interface.

### IV.3. Results and Discussion

#### IV.3.1 Morphology and structure of ERGO electrodes

ERGO thin films with progressively decreased content of oxygen functionalities were electrochemically fabricated as illustrated in **Scheme IV.1**. With increased reduction time, the ERGO sheets gradually lost the oxygen functional groups which was accompanied by a decrease of interspacing between the layers. The morphology of the GO and ERGO electrodes was observed by FEG-SEM as shown in **Figure IV.2**. Both GO and ERGO electrodes displayed a typical wrinkled morphology, which is formed by thin crumpled sheets. Initially, the average GO film thickness was ~160 nm (**Figure IV.2**). Upon subsequent electrochemical reduction, it gradually decreased to ~135 nm for ERGO-1 (**Figure IV.2b**), ~110 nm for ERGO-2 (**Figure IV.2c**) and ~70 nm for ERGO-3 (**Figure IV.2d**), implying a decrease in the interspacing of reduced graphene oxide layers probably due to the removal of oxygen containing functional groups and intercalated water molecules<sup>27</sup>. These measured values can be considered to correspond to the shrunken state of the GO and ERGO films owing to the vacuum condition of the FEG-SEM measurements.

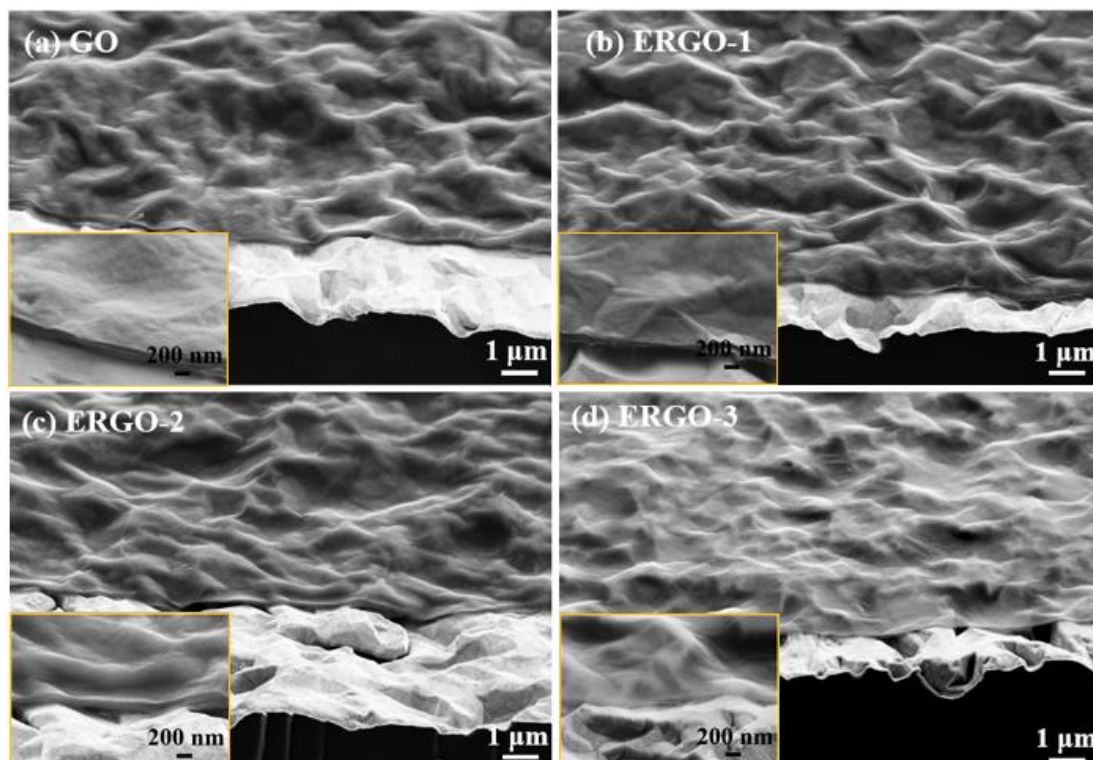


**Figure IV.2.** Morphological observations of graphene oxide film (a) and GO films with different degree of reduction, ERGO-1 to ERGO-3 (b-d). Inset images are higher magnification of each film.

Sauerbrey equation was also employed to calculate the film thickness in air through the relationship between mass change ( $\Delta m$ ) of the ERGO electrode and microbalance frequency shift ( $\Delta f$ ) before and after the electrochemical reduction of the film<sup>35</sup>, i.e.,  $\Delta f = -C_f \times \Delta m$ , where  $C_f$  is the modified sensitivity factor of the quartz crystal resonator ( $C_f = 19.5 \times 10^7$ ,  $18.7 \times 10^7$  and  $\sim 17.8 \times 10^7$  Hz.g<sup>-1</sup>.cm<sup>2</sup> for ERGO-1, -2 and -3, respectively. See details in section IV.3.2). The estimated thickness from Sauerbrey equation is  $\sim 146$ ,  $\sim 122$  and  $\sim 100$  nm for ERGO-1, -2 and -3, respectively. These values were used for the fitting of the electroacoustic and *ac*-electrogravimetric data thereafter. Meanwhile, thanks to the QCM measurements, the mass loss of the GO electrode upon electrochemical reduction process was also estimated with a value of  $\sim 6.8$ ,  $\sim 24.0$  and  $\sim 36.1$  wt% corresponding to ERGO-1, -2 and -3 respectively, which was attributed to the loss of oxygen functionalities and certain amounts of water molecules sandwiched between the layers.

The structural difference of GO electrodes before and after electrochemical reduction was characterized with XRD. **Figure IV.3** shows the XRD patterns of the pristine GO on ITO coated glass slides, revealing a sharp and intense diffraction peak centered at  $2\theta = 11.5^\circ$  (002), corresponding to an interplanar spacing (d-spacing) of 0.77 nm. This value is dependent on the preparation method and the number of water molecules between the layers<sup>36</sup>. After 15 s of

electrochemical reduction, ERGO-1 displayed almost the same reflection peak, confirming that ERGO-1 shared almost the same structural geometry as GO in spite of a measurable thickness decrease observed by FEG-SEM and weight loss by QCM. It may be attributed to the superficial oxygen functional groups on GO layers and water molecules located in the shallow sites between GO layers, which can be easily removed during electrochemical reduction process. However, in the case of ERGO-2, the intensity of the peak (002) drastically faded and a new, broad peak emerged at  $2\theta = 23.5^\circ$  corresponding to a d-spacing of 0.38 nm. The decreased value of d-spacing in ERGO-2 implied that a significant portion of oxygen functional groups had been removed from GO sheets. Moreover, in the pattern of ERGO-3, the peak at  $2\theta = 11.5^\circ$  disappeared and was markedly shifted to  $23.5^\circ$ , indicating that at least a partial reduction of GO was achieved.

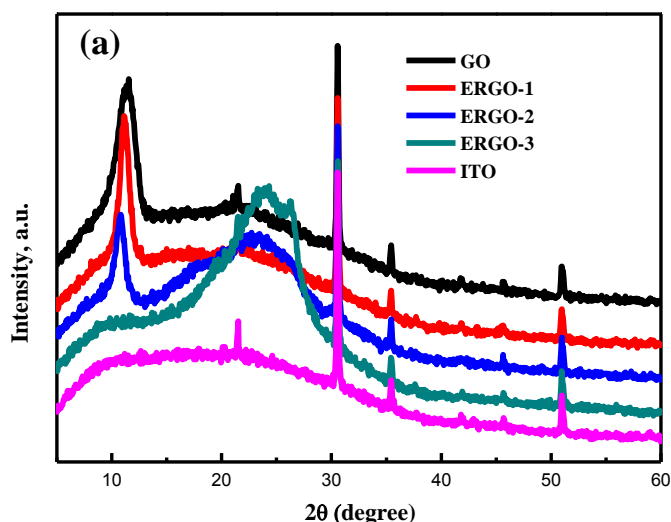


**Figure IV.3.** XRD patterns of pristine GO and GO with various degree of electrochemical reduction.

The reduction degree of GO electrodes is further investigated by XPS. C1s spectrum of GO electrode (**Figure IV.4a**) displays its two main components of C-O (epoxy and hydroxyl,  $\sim 286.9$  eV) and C=C/C-C ( $\sim 284.8$  eV) in aromatic rings, and two minor components i.e., C=O (carbonyl,  $\sim 288.6$  eV) and O-C=O (carboxyl,  $\sim 290.0$  eV) groups<sup>37-40</sup>. After electrochemical reduction for 5 min, all intensities of the oxygen functionalities remarkably decrease (**Figure IV.4b**), especially C-O groups, evidencing that the majority of oxygen functionalities (C-O groups) have been successfully removed. Furthermore, a stronger  $\pi$ - $\pi^*$  shake-up satellite peak around 290.7 eV resumes in ERGO-3, which is a characteristic of aromatic or conjugated systems<sup>41</sup>. **Figure IV.4c** presents the variation of the two major groups (C=C and C-O) as a function of reduction time. It

clearly shows that the main oxygen functional group (C-O) is gradually removed upon electrochemical reduction and ERGO electrode can be sufficiently reduced after 5 min, which is also confirmed by the C/O ratio in **Figure IV.4d**. These results, combined with XRD analysis, indicate the formation of ERGO with different content of oxygen functionalities.

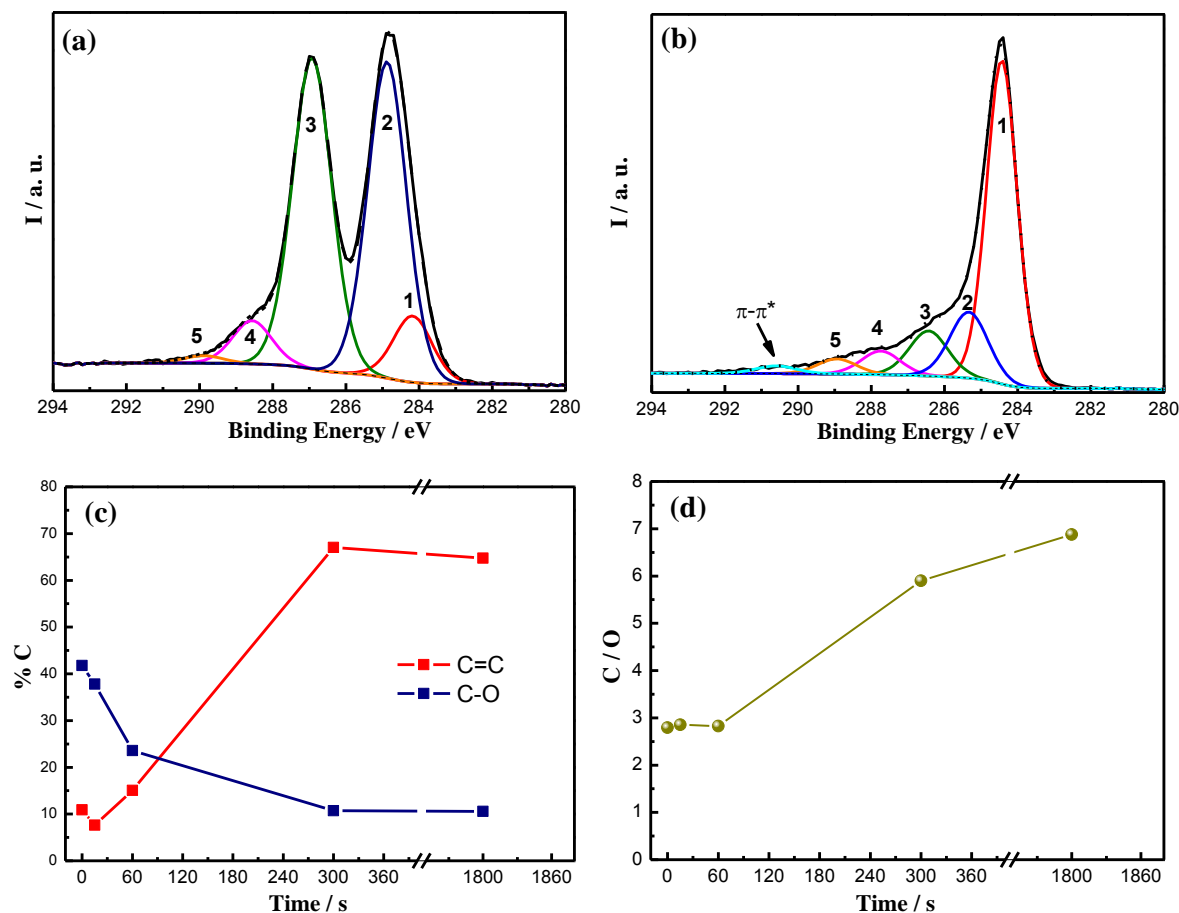


**Figure IV.4.** XPS spectra of GO (a) and ERGO-3 (b), where the curves were fitted considering the following contributions: C=C ( $sp^2$ ; peak 1), C-C ( $sp^3$ ; peak 2), C-O (epoxy and hydroxyl; peak 3), C=O (carbonyl; peak 4), O-C=O (carbonyl; peak 5) and  $\pi-\pi^*$ . The panel (c) presents the relative percentage of C=C and C-O groups and the panel (d) is the C/O ratio from XPS as a function of polarization time. The lines are a guide to eyes.

### IV.3.2 Viscoelasticity of ERGO electrodes and its influence on electrogravimetric performance

Long term mechanical integrity is of significant importance for a high performance SC electrode. However, it is known that the periodical exchange of the species between the electrode and the electrolyte commonly results in the accumulation of unrelaxed structural deformations thus leading to the mechanical failure. Furthermore, it has been demonstrated that the viscoelastic

properties of the deposited film play an essential role in the validity of Sauerbrey equation and can modify the gravimetric response of a quartz resonator<sup>29</sup>. Therefore, when quartz crystal microbalance based methodologies are employed to study the electroadsorption or insertion behavior, special attention should be given to distinguish between the (electro)gravimetric and the (electro)mechanical property changes of the electrodes. Hence, in this study, prior to the electrogravimetric investigations, electroacoustic impedance tests (**Figure IV.1**) were carried out to explore the influence of the progressive removal of oxygen functionalities from ERGO sheets on its viscoelastic evolution, which is described by the storage modulus ( $G'$ ) and the loss modulus ( $G''$ ).

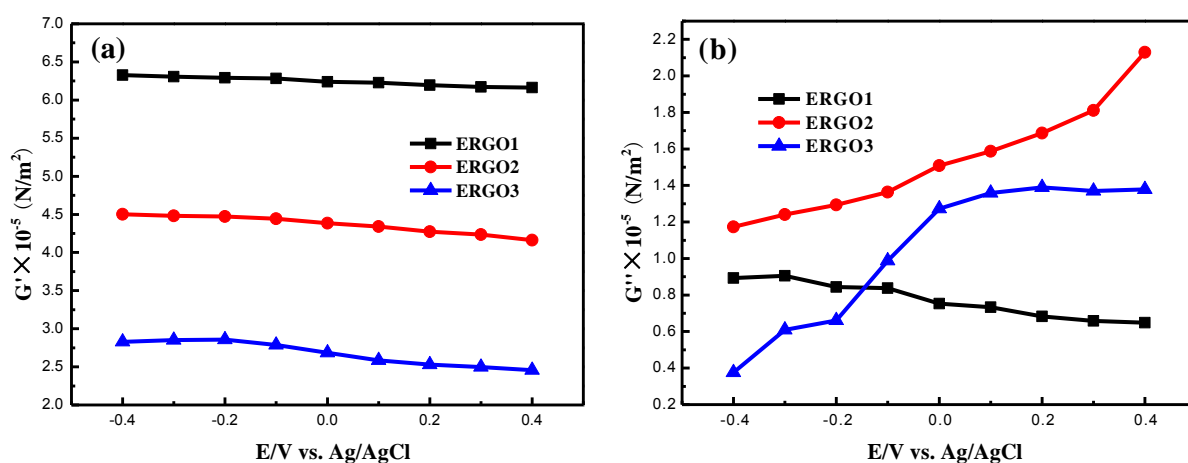


**Figure IV.5.** Evolution of real (a) and imaginary (b) components of complex shear modulus of ERGO electrodes.

As shown in **Figure IV.5a**, ERGO layers exhibit a decrease in the rigidity with progressive removal of oxygen containing functional groups from ERGO-1 to -3. For instance,  $G'$  of the ERGO-1 is reduced by approximately 58% from  $\sim 6.2 \times 10^5 \text{ N}\cdot\text{m}^{-2}$  to  $\sim 2.6 \times 10^5 \text{ N}\cdot\text{m}^{-2}$  for ERGO-3, which are comparable to that of graphene hydrogel<sup>42</sup> and that of a composite  $\text{LiFePO}_4$  electrode used in batteries<sup>43</sup>. By contrast,  $G''$  shows a more complex evolution behavior (**Figure IV.5b**). Specifically,  $G''$  of ERGO-1 remains at lower values at most potentials and decreases gradually from cathodic to anodic potentials (from  $0.89 \times 10^5 \text{ N}\cdot\text{m}^{-2}$  to  $0.65 \times 10^5 \text{ N}\cdot\text{m}^{-2}$ ). However, in the case of ERGO-2 and -3,  $G''$  exhibits an entirely opposite variation tendency with respect to ERGO-1, increasing from  $1.17 \times 10^5 \text{ N}\cdot\text{m}^{-2}$  to  $2.13 \times 10^5 \text{ N}\cdot\text{m}^{-2}$  and  $0.37 \times 10^5 \text{ N}\cdot\text{m}^{-2}$  to  $1.38 \times 10^5 \text{ N}\cdot\text{m}^{-2}$ , respectively.

It has been revealed that the  $G'$  describes the film rigidity (energy storage), whereas  $G''$  is

correlated with film viscosity (energy dissipation)<sup>44</sup>. The decreased  $G'$  and increased  $G''$  from ERGO-1 to -2 reveal that the removal of oxygen containing functional groups and the corresponding restoration of the  $\pi$  network endow the reduced graphene oxide (RGO) layers with less rigidity and more viscosity. It is speculated that strong polar interactions exist between the reduced graphene oxide interlayers mainly from enriched oxygen functionalities in ERGO-1 electrode, resulting in an inferior electrode conductivity and thus poor ions' transfer between electrode/electrolyte interface and transport in electrode bulk. Correspondingly, the friction between the ions and oxygen containing functional groups is greatly weakened and the relative displacement between ERGO layers hardly occurs, through which the energy dissipates during electrochemical process. With the removal of oxygen functionalities from ERGO-1 to -2, such strong polar interactions can be gradually replaced by restored  $\pi$  system, which brings about the exchange of ions in a higher quantity between the electrode and electrolyte. Also, the corresponding deformation of ERGO sheets can be compatible for the accommodation to these increased amount of ions under different states-of-polarization. It in turn enhances energy dissipation in this process by means of *i*) enhanced friction from exchanged species and ERGO layers and *ii*) relative displacement between ERGO layers. Such properties can be presented by high flexibility and high viscosity, i.e., low  $G'$  and high  $G''$ .

In contrast with ERGO-2, ERGO-3 displays a further decreased  $G'$  due to the further removal of hetero-oxygen groups, however, a smaller  $G''$  instead, implying that the graphene oxide sheets with higher degree of reduction become more flexible and less viscous. As a matter of fact, the gradual removal of oxygen containing functional groups (from ERGO2 to ERGO3) results in a further approach of the adjacent layers (the d-spacing of 0.38 nm was achieved in ERGO-3 as shown by XRD, **Figure IV.3**) and leads to the further restoration of its  $\pi$  network with much larger conjugated length as compared to ERGO-2, which may weaken the internal friction between ERGO layers and thus attenuate the dissipation (lower  $G''$ ). Besides, it may facilitate the ionic transfer and thus allow much more species to be accommodated on the electrode during charge storage/delivery. It is speculated that exchanged H<sub>2</sub>O molecules play an essential part in the variation of  $G''$  by means of plasticizing effect<sup>45</sup>. These points will be scrutinized in the discussion part of the *ac*-electrogravimetry data (section **IV.3.4**).

In addition to providing information on the electromechanical behavior, the electroacoustic

studies on the ERGO layers may also permit the exploration of the validity of the gravimetric regime for the further analysis with the QCM and its satellite electrochemical methods. To estimate the influence of viscoelastic variations of ERGO electrode on its electrogravimetric performance, the experimental sensitivity factor of the quartz crystal resonator ( $C_f=16.3 \times 10^7 \text{ Hz.g}^{-1}.\text{cm}^2$  under the hypothesis of a sufficiently rigid electrode<sup>28</sup>) was modified with the consideration of the rheological properties of the electrodes. The calculation was performed by **Equation IV.9** as previously reported<sup>29</sup>. Briefly, the film thickness was maintained constant ( $\sim 146$ ,  $\sim 122$  and  $\sim 100$  nm for ERGO-1, -2 and -3, respectively),  $\rho_f^{\max}$  and  $\rho_f^{\min}$  were confined between  $\pm \rho_f \times 0.5\%$  ( $\rho_f$  was obtained by the fitting procedure). The series frequency,  $f_s^V$ , was calculated at each potential given that  $G'$  and  $G''$  were constant upon a small potential perturbation.

$$C_f^{\text{exp}} = \frac{f_s^V(\rho_f^{\max}, h_f, G_1, G_2) - f_s^V(\rho_f^{\min}, h_f, G_1, G_2)}{(\rho_f^{\max} - \rho_f^{\min}) \times h_f} \quad (\text{IV.9})$$

The resulting modified  $C_f$  values for ERGO-1, -2 and -3 are  $\sim 19.5 \times 10^7$ ,  $\sim 18.7 \times 10^7$  and  $\sim 17.8 \times 10^7 \text{ Hz.g}^{-1}.\text{cm}^2$ , respectively. These modified values will be used in the EQCM (section **IV.3.3**) and for the fitting of the *ac*-electrogravimetric part (section **IV.3.4**).

### **IV.3.3 Cyclic electrogravimetric behavior**

The electrochemical behavior of ERGO electrodes was characterized by galvanostatic charging/discharging (GCD) and cyclic voltammetry (CV). The QCM was coupled with both measurements to track the simultaneous frequency shifts of the ERGO electrodes during cycling, which can be converted into mass responses. Typical galvanostatic charge/discharge curves of three different reduced graphene oxide electrodes obtained at a current density of 0.5, 1 and 2  $\text{mA.s}^{-1}$  are shown in **Figure IV.6a, c** and **e**, while the corresponding mass changes are displayed in **Figure IV.6b, d** and **f**. The charge/discharge curve of the ERGO-3 electrode presents a typical triangle shape with little distortion and much prolonged over the ERGO-1 and -2 electrodes at various current densities, demonstrating that the capacitive behavior plays the major contribution in charge storage and that the specific capacitance of ERGO-3 electrode is significantly higher than that of

ERGO-1 and -2<sup>18</sup>. This reveals that significantly larger surface areas of the ERGO sheets become electroactive and accessible for ions in charge storage/delivery with the progressive removal of oxygen functionalities. Unlike the fairly clear evolution of potential responses, the mass responses of graphene oxides with different degree of reduction display a complex signature. As for ERGO-1, the mass-time response proceeds in a synchronously positive-going pace with potential response, i.e., mass increase during charging and mass decrease during discharging, which is characteristic of anion participation in charge compensation process. By contrast, in the case of ERGO-2 and -3, the mass response (**Figure IV.6d** and **f**) shows a reverse triangular shape, evidencing a transition in the charge storage/delivery process, specifically from anions to cations.

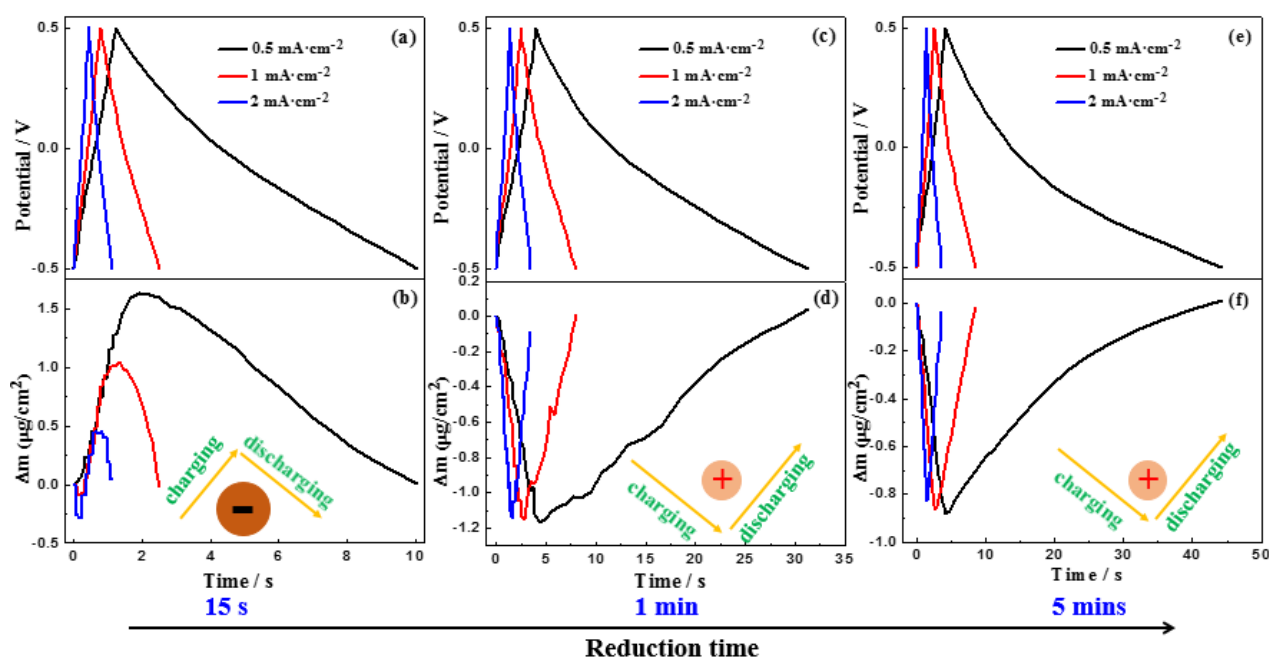


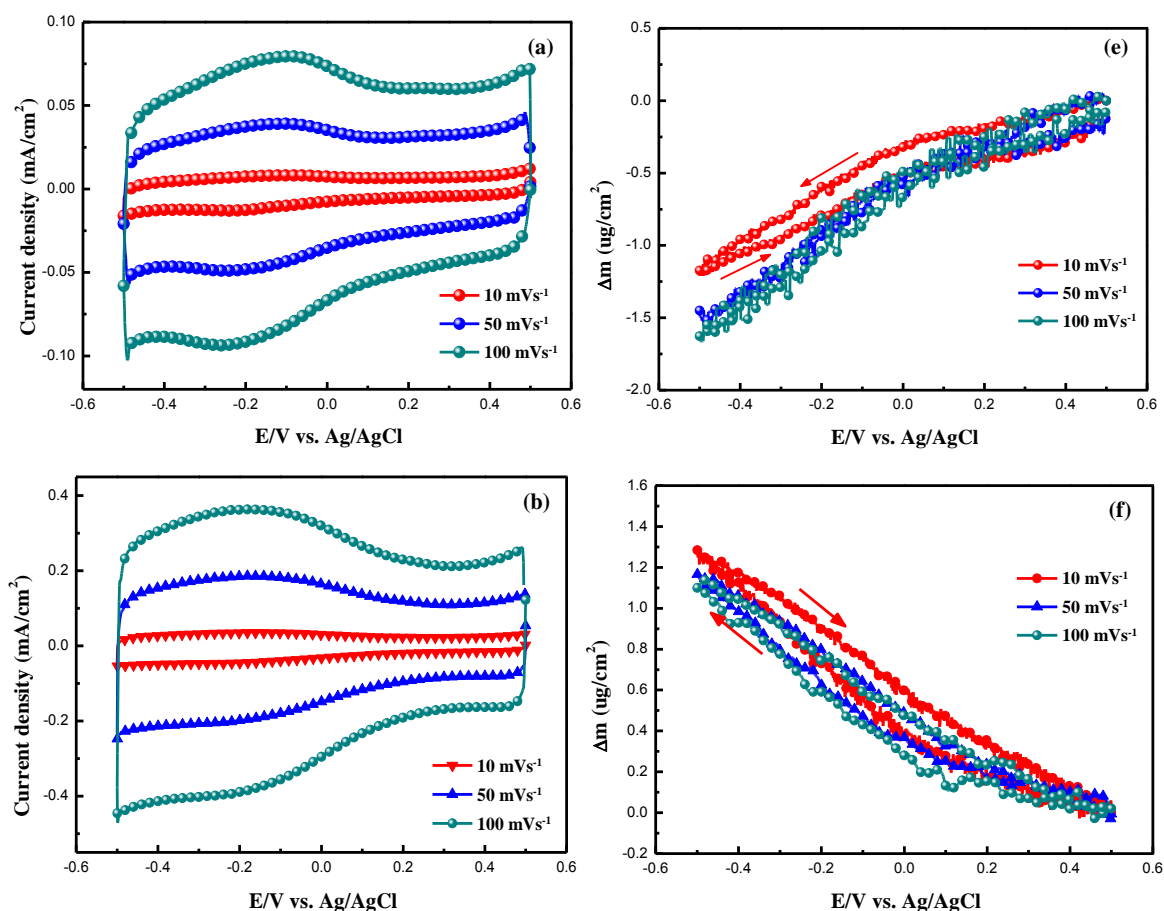
**Figure IV.6.** Galvanostatic charge-discharge of ERGO-1 (a, b), -2 (c, d) and -3 (e, f) at a current density of 0.5, 1 and 2 mA·cm<sup>-2</sup>, respectively.

To confirm this “anion-to-cation” preference of the ERGO electrodes in electrochemical performance upon a progressive removal of oxygen functionalities, the cyclic electrogravimetry (EQCM) measurement was also performed, which tracked the current and the simultaneous mass responses between -0.5 and 0.5 V at various scan rates. **Figure IV.7a-c** shows approximately rectangular shaped CV responses of ERGO electrodes with the slight contribution of broad redox peaks in the potential range of -0.5-0.2 V vs. Ag/AgCl, indicating that the charge storage is mostly from EDLC behavior. The minor deviations of an ideal rectangular response are due to the

additional *pseudo-capacitances*, which stem from the electrochemical reactions of remaining oxygen containing functional groups on ERGO layers at the electrode/electrolyte interface, e.g.,  $>C-OH \Leftrightarrow >C=O+H^++e^-$ <sup>46-47</sup>. In general, the specific capacitance ( $C_s$ ) of the electrode is proportional to its CV area<sup>48</sup>. If the ERGO (1-3) electrodes at  $10 \text{ mV}\cdot\text{s}^{-1}$  are taken as an example (**Figure IV.7d**), an increase in the  $C_s$  values is observed with the progressive removal of oxygen functional groups, as evidenced by the enlarged CV area. The specific capacitance can be calculated based on CV curves using the following equation and listed in **Table IV.1**:

$$C_s = \frac{1}{2mv(E_2 - E_1)} \int_{E_1}^{E_2} I(E)dE \quad (\text{IV.10})$$

where  $m$  is the mass loading of different ERGO electrodes obtained by QCM,  $v$  is the scan rate,  $E_1$  and  $E_2$  are the working voltage, and  $I(E)$  depicts the response in current. The maximum  $C_s$  of  $\sim 160.8 \text{ F}\cdot\text{g}^{-1}$  was obtained at a scan rate of  $10 \text{ mV}\cdot\text{s}^{-1}$  for the ERGO-3 electrode, which exhibits superior conductivity and a very promising charge storage capability<sup>2, 36</sup>.



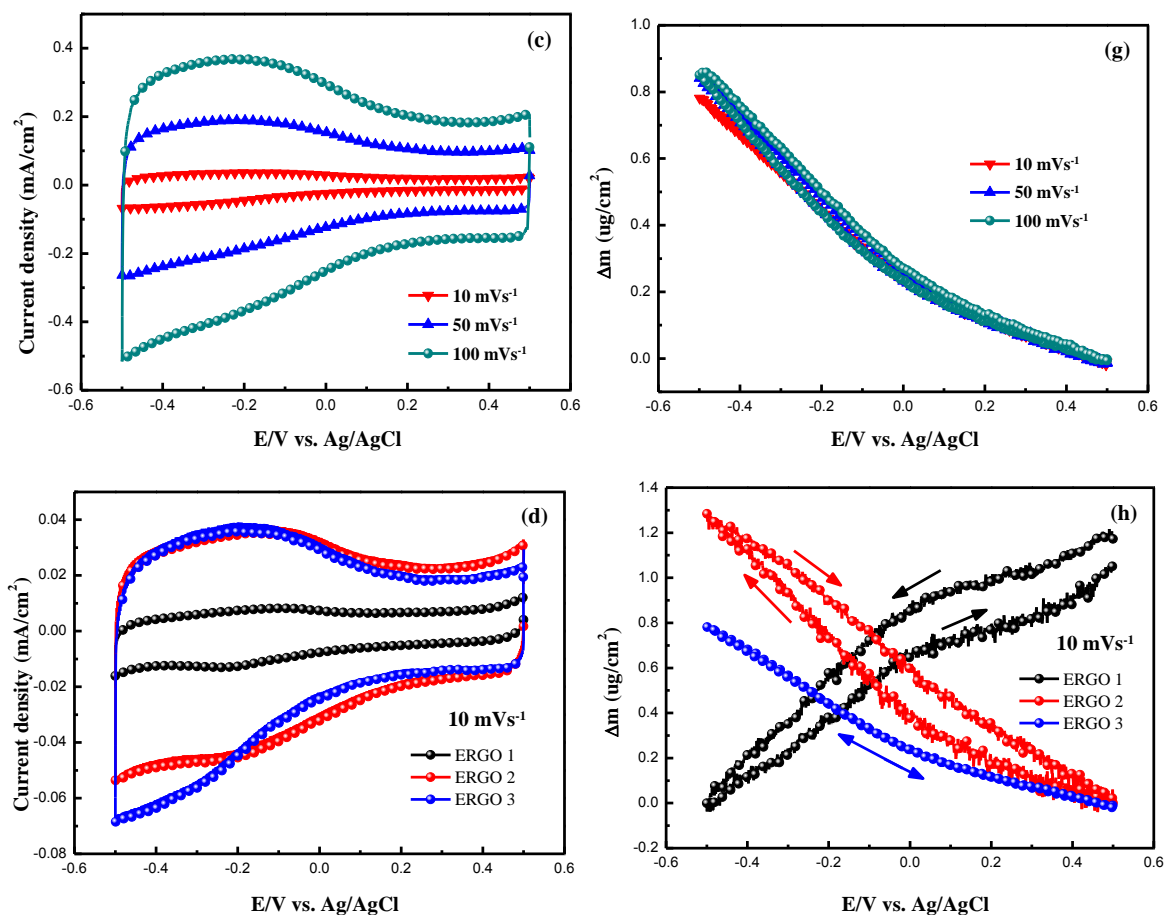


**Figure IV.7.** Cyclic voltammetry (a, b and c), mass change ( $\Delta m$ ) (e, f and g) of ERGO electrodes in 1 M NaCl aqueous solution between -0.5 V and 0.5 V vs. Ag/AgCl at different scan rates. Panels (d) and (h) are CV and mass change of ERGO electrodes obtained at 10  $\text{mV}\cdot\text{s}^{-1}$ .

**Table IV.1.** Specific capacitance ( $\text{F}\cdot\text{g}^{-1}$ ) of ERGO electrodes from CV.

	Scan rate ( $\text{mV}\cdot\text{s}^{-1}$ )		
	10	50	100
ERGO-1	25.7	23.2	22.5
ERGO-2	113.5	110.8	108.7
ERGO-3	160.8	143.1	137.5

Contrary to the fairly unambiguous CV responses, the mass responses of ERGO electrodes exhibit an obvious reversed response upon the electrochemical reduction, as shown in **Figure IV.7e-h**. For slightly-reduced GO electrode (ERGO-1), a mass decrease occurs during cathodic

sweep while mass increase during anodic sweep, which is characteristic of anion participation<sup>34</sup> and in agreement with the observation from GCD measurement (**Figure IV.6b**). For the intermediately-reduced electrode (ERGO-2), the mass response displays an opposite behavior relative to ERGO-1, i.e., mass ingress/egress during cathodic/anodic sweep, respectively. With a further reduction, the same mass change behavior persists for the ERGO-3 electrode, but exhibits less and even negligible hysteresis between the mass response during the cathodic and anodic potential sweep.

Both GCD and CV analysis coupled with the corresponding mass responses suggested that ERGO-1 experiences anion desorption and adsorption during cathodic/anodic sweep, respectively; whereas ERGO-2 and -3 undergo cation adsorption/desorption during cathodic/anodic sweep. In spite of displaying the similar behavior in mass response as ERGO-2 electrode, ERGO-3 shows relatively overlapped mass increase/decrease during the cathodic and anodic sweep without a significant hysteresis, implying a more homogeneous layer structure and composition of the ERGO-3 electrode.

Concerning the aforementioned discussion, anions seem to dominate in charge balance for ERGO-based electrodes with relatively high content of oxygen functionalities while cations' contribution is progressively enhanced with the decrease of oxygen functional groups on its layers. Therefore, it is likely to modify the microstructures of GO-based electrodes by means of tuning the content of oxygen functionalities on its layers, which can affect not only the electrochemical performances but also the nature of the ionic species participating in this process.

However, the GCD and EQCM alone are not qualified to separate each species contribution and to provide their interfacial transfer kinetics since the measurements are done at a certain current density or scan rate<sup>28, 49</sup>. For the deconvolution of the global electrogravimetric response into gravimetric and temporal components, the *ac*-electrogravimetry was suggested as a complementary tool to EQCM. The different scenarios of the charge compensation process for ERGO electrodes in the process of removal of oxygen functional groups are scrutinized.

### IV.3.4 *Ac*-electrogravimetric investigations

To shed light on the subtleties of the charge compensation process observed in cyclic electrogravimetry analysis and to gain insights into the dynamic behavior of each species' transfer at ERGO electrodes interface, *ac*-electrogravimetry measurements were carried out at various states-of-polarization from -0.4 V to 0.4 V with an interval of 100 mV. **Figure IV.8** and **IV.9**

compare the electrochemical impedance,  $\frac{\Delta E}{\Delta I}(\omega)$  and charge/potential transfer function (TF),

$\frac{\Delta q}{\Delta E}(\omega)$  of ERGO electrodes at selective potentials of  $\pm 0.2$  V vs. Ag/AgCl, respectively, which

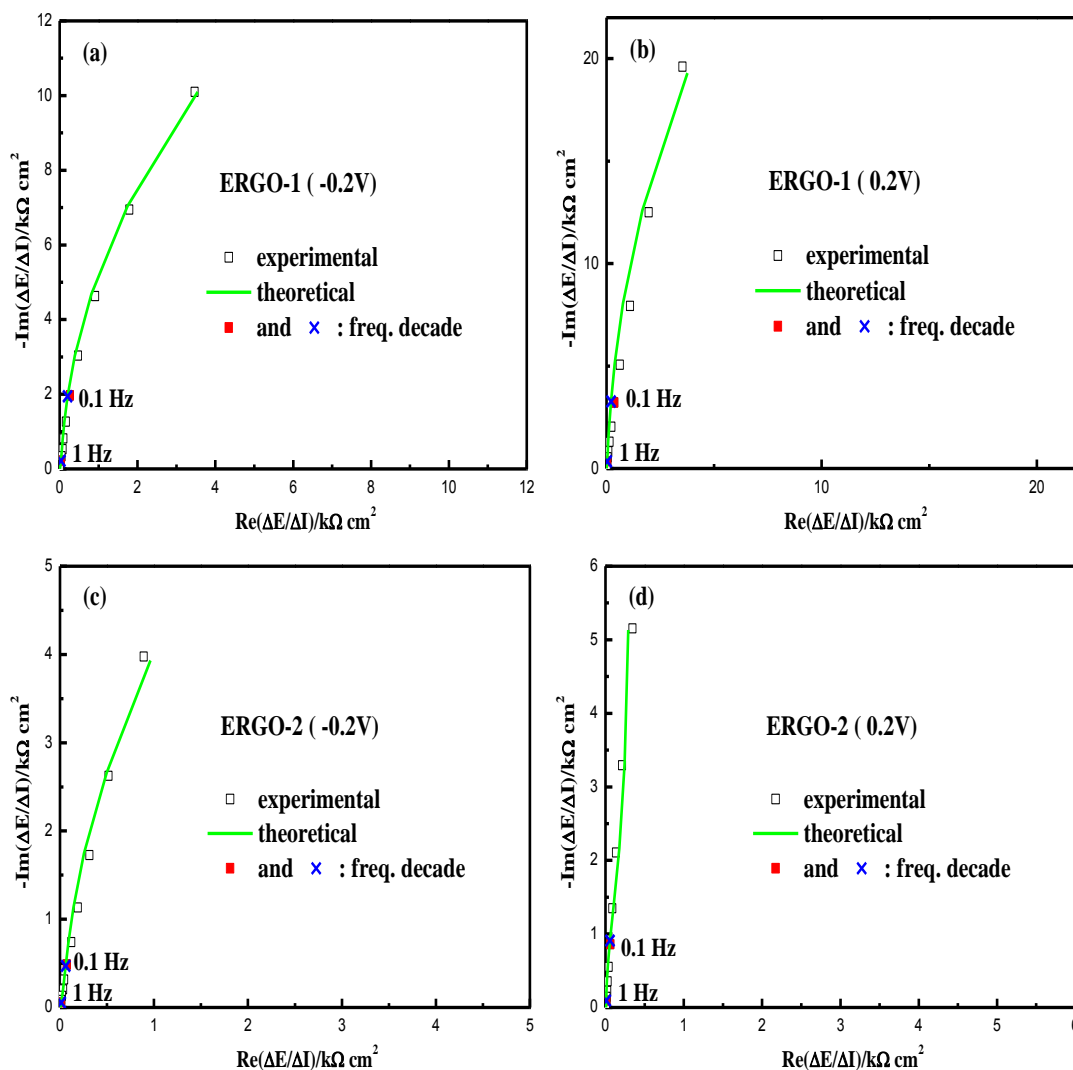
can only reveal the contribution of charged species participating in the charge compensation process.

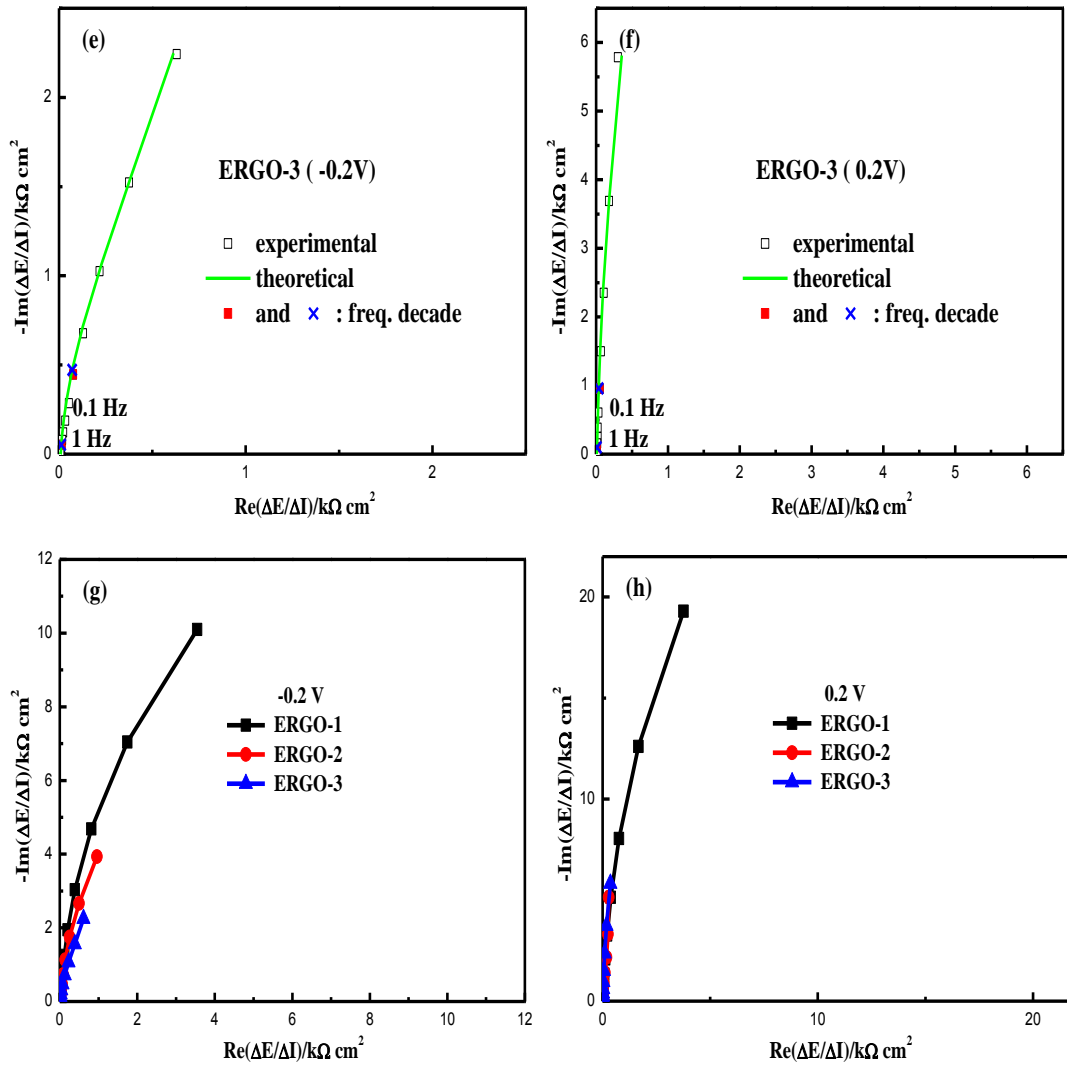
These two potentials were shown herein as representatives of cathodic and anodic states of polarization. The electrochemical impedance,  $\frac{\Delta E}{\Delta I}(\omega)$  (Figure IV.8g and h) at low frequencies

exhibits a slightly distorted straight line implying a multi-ion contribution to charge compensation.

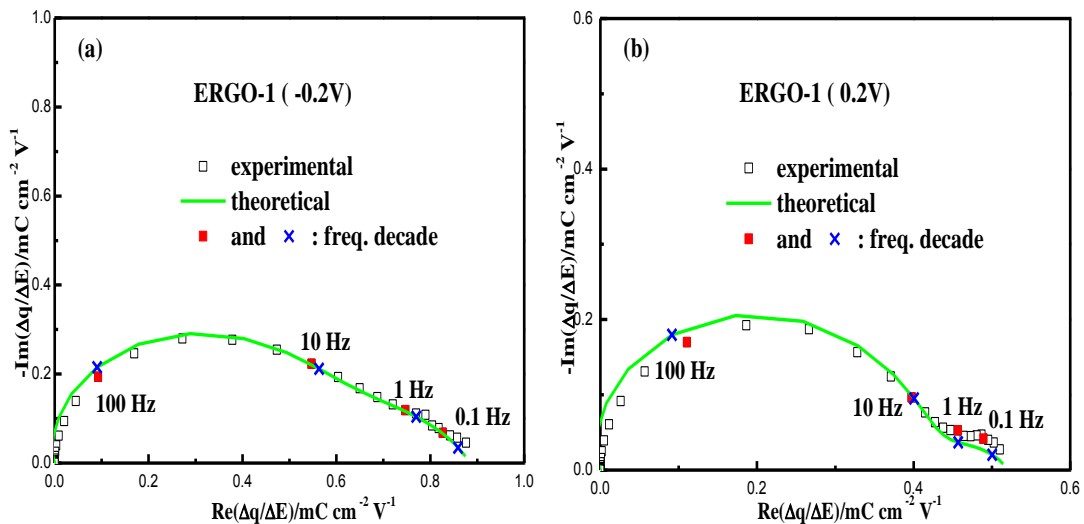
The experimental data of  $\frac{\Delta E}{\Delta I}(\omega)$  and  $\frac{\Delta q}{\Delta E}(\omega)$  were fitted using theoretical functions in

Equations IV.6 and IV.7 and revealed the involvement of three ionic species which resulted in a good agreement between the experimental and the theoretical curves. Two parameters for each ionic species,  $K_i$  and  $G_i$ , could be obtained through this fitting process as listed in Table IV.2.





**Figure IV.8.** Experimental and theoretical  $\frac{\Delta E}{\Delta I}(\omega)$  transfer functions (TFs) for ERGO electrodes. (a), (c) and (e) were measured for ERGO-1, -2 and -3 at -0.2V, while (b), (d) and (f) at 0.2V, respectively. Panels (g) and (h) are theoretical  $\frac{\Delta E}{\Delta I}(\omega)$  TFs of ERGO electrodes at  $\pm 0.2$  V.



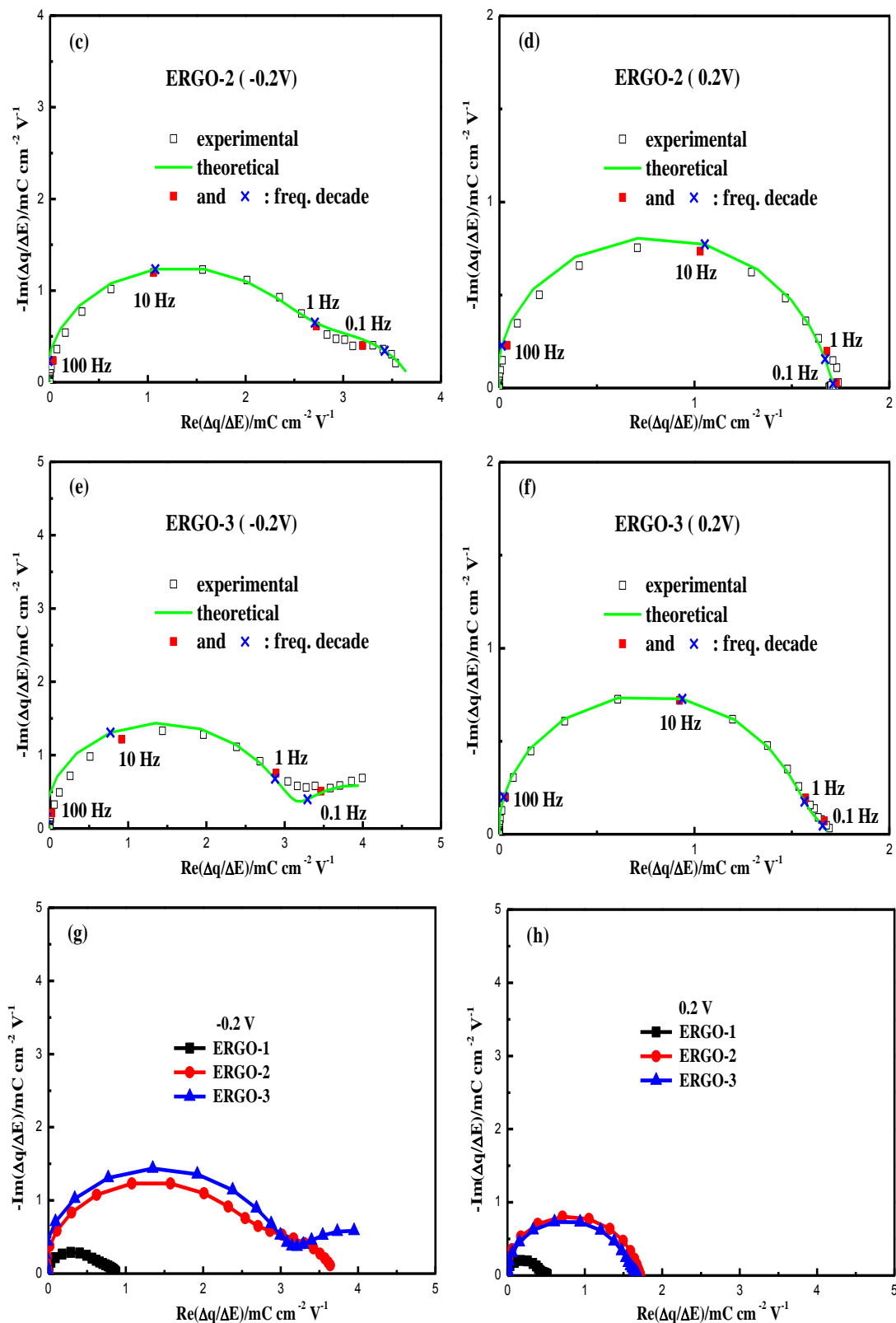


**Figure IV.9.** Experimental and theoretical  $\frac{\Delta q}{\Delta E}(\omega)$  TFs for ERGO electrodes. Panels (a), (c) and (e) are for ERGO-1, -2 and -3 at -0.2 V, while (b), (d) and (f) at 0.2 V, respectively. Panels (g) and (h)

are theoretical  $\frac{\Delta q}{\Delta E}(\omega)$  TFs of ERGO electrodes at  $\pm 0.2$  V.

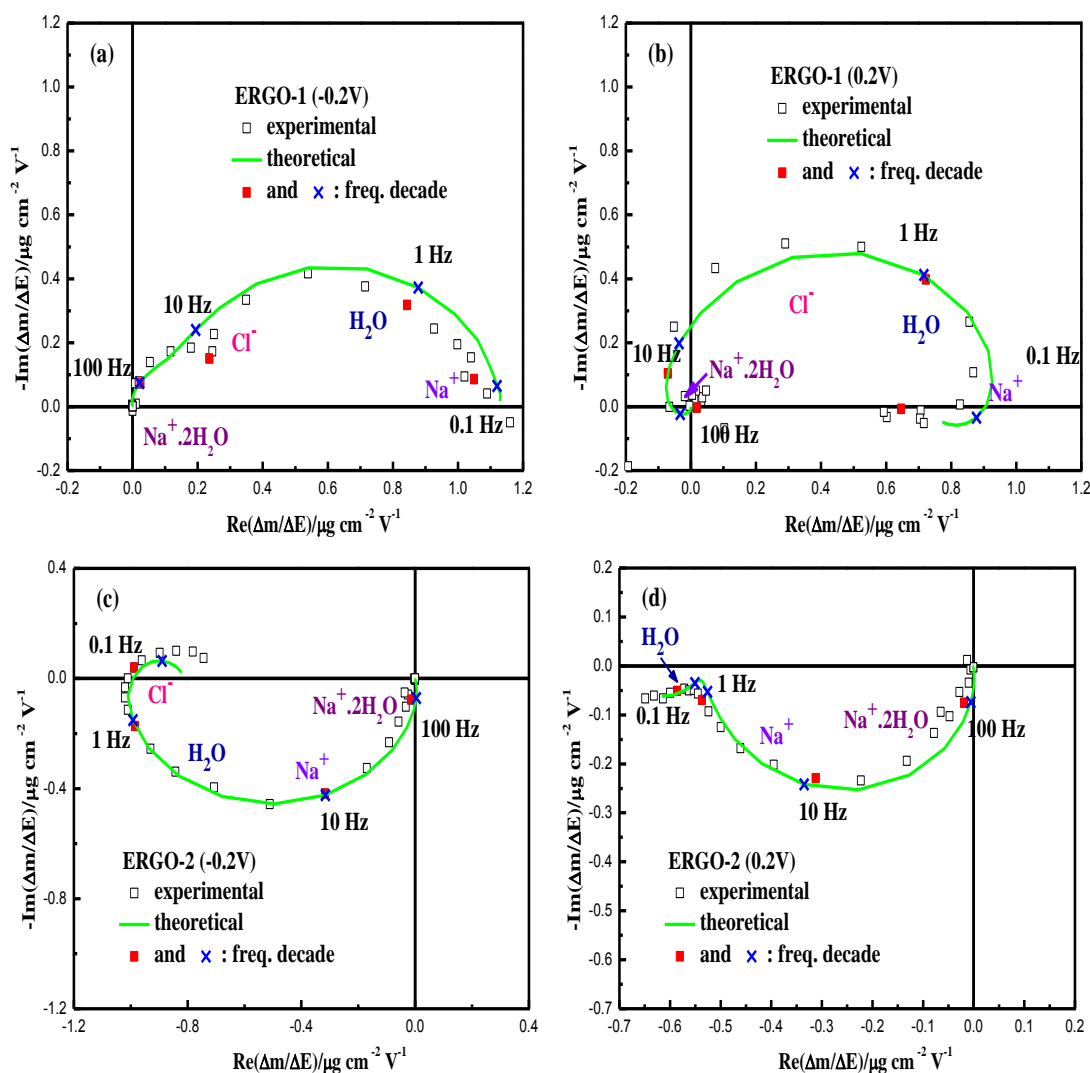
**Table IV.2.** Fitting parameters,  $K_i$  and  $G_i$ , obtained from *ac*-electrogravimetry.

		$K_{c1}$ $\times 10^4$	$G_{c1}$ $\times 10^8$	$K_{c2}$ $\times 10^5$	$G_{c2}$ $\times 10^9$	$K_s$ $\times 10^6$	$G_s$ $\times 10^9$	$K_a$ $\times 10^6$	$G_a$ $\times 10^9$
-0.2 V	ERGO-1	34.75	5.56	7.26	16	299	-1200	2859	-1086
	ERGO-2	15.83	46.7	90.5	1810	151	302	17	-13.74
	ERGO-3	3.77	60.3	28.3	481	189	141	1.63	-2.581
0.2 V	ERGO-1	34.31	54.9	2.86	1.43	106	-475	1935	-309.6
	ERGO-2	20.73	62.2	109.3	1300	1.7	1.27	0	0
	ERGO-3	18.85	79.2	157.1	1890	251	163	19.8	-2.573

Note:  $\text{cm}\cdot\text{s}^{-1}$  and  $\text{mol}\cdot\text{s}^{-1}\cdot\text{cm}^{-2}\cdot\text{V}^{-1}$  are for the units of  $K_i$  and  $G_i$  parameters, respectively. Cation 1 ( $c_1$ ), cation 2 ( $c_2$ ), solvent ( $s$ ) and anion ( $a$ ) in the Table refer to hydrated  $\text{Na}^+$  ( $\text{Na}^+\cdot n\text{H}_2\text{O}$ ,  $n=1$  or  $2$ ),  $\text{Na}^+$ ,  $\text{H}_2\text{O}$  and  $\text{Cl}^-$ .

The  $\frac{\Delta q}{\Delta E}(\omega)$  of the ERGO-1 exhibits a relatively small suppressed loop (or a composition of several loops) at both potentials (**Figure IV.9a and b**), demonstrating the presence of more than one charged species with similar time constant. In the case of ERGO-2, the  $\frac{\Delta q}{\Delta E}(\omega)$  TF is distinguished by an enhancement of the loop diameter. After a further electrochemical reduction, ERGO-3 exhibits even a larger  $\frac{\Delta q}{\Delta E}(\omega)$  TF loop at -0.2 V with an upward tail at low frequency (LF). This suggests that at LF, another species may participate to the process and this species possesses a significantly different time constant to appear as a beginning of a separate loop. However, almost equal diameter of  $\frac{\Delta q}{\Delta E}(\omega)$  loops is observed for ERGO-3 and ERGO-2 at 0.2 V,

illustrating that approximately the same amount of charged species are involved in charge compensation for these two electrodes at this polarized state. Additionally, it can be clearly seen that all ERGO electrodes exhibit a much larger  $\frac{\Delta q}{\Delta E}(\omega)$  loop at -0.2 V relative to 0.2 V, which is consistent with the observation from CV in **Figure IV.7** (much larger area enclosed at cathodic potentials), i.e., higher amount of charges transferred during cathodic potential region (-0.5-0 V) relative to that of the anodic potential region (0-0.5 V).



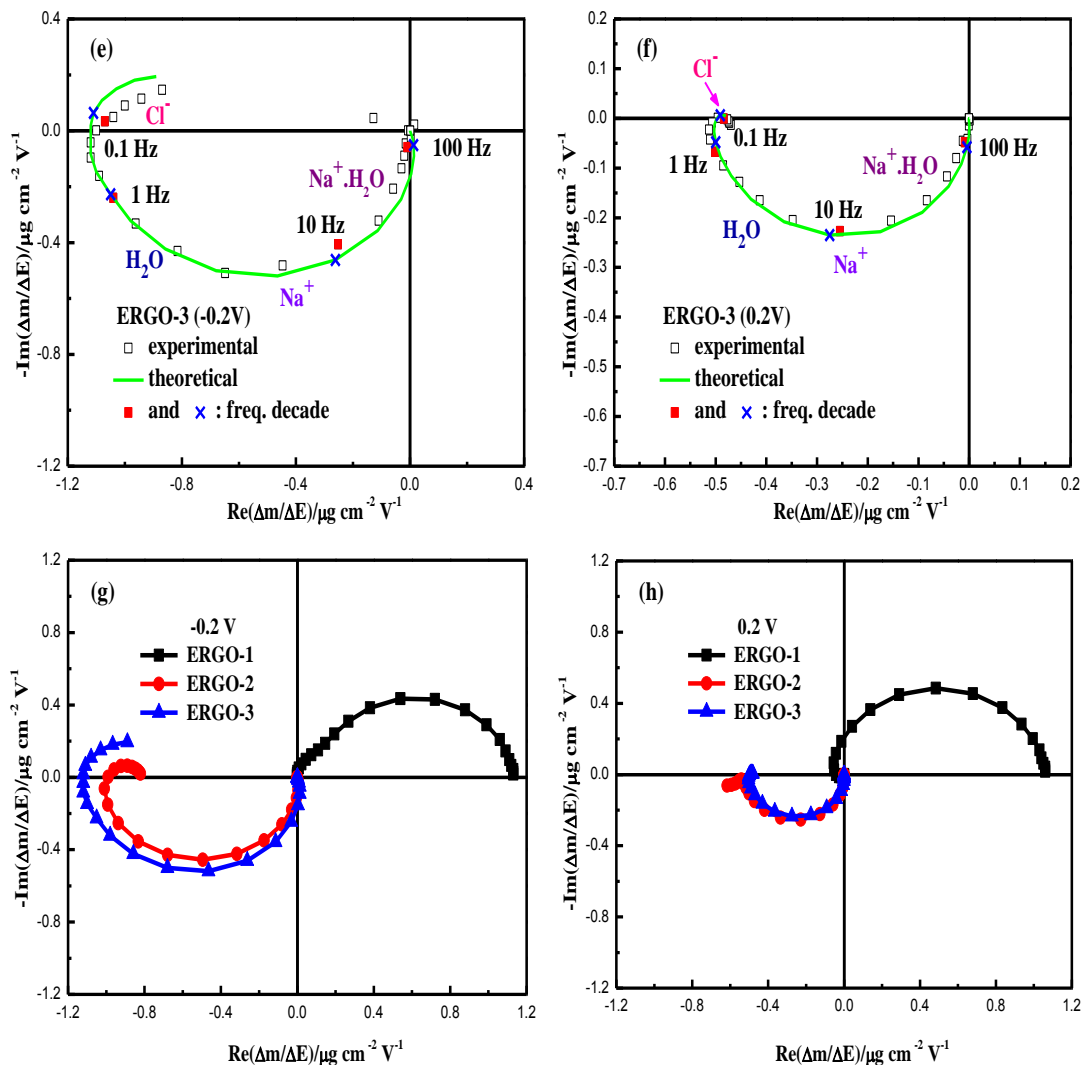


**Figure IV.10.** Evolution of  $\frac{\Delta m}{\Delta E}(\omega)$  TFs with progressive reduction of the ERGO electrodes: (a), (c) and (e) were measured for ERGO-1, -2 and -3 at -0.2V, while (b), (d) and (f) at 0.2V, respectively. Panels (g) and (h) are theoretical  $\frac{\Delta m}{\Delta E}(\omega)$  TFs of ERGO electrodes at  $\pm 0.2$  V.

$\frac{\Delta E}{\Delta I}(\omega)$  and  $\frac{\Delta q}{\Delta E}(\omega)$  TFs provide the contribution of charged species but do not permit their

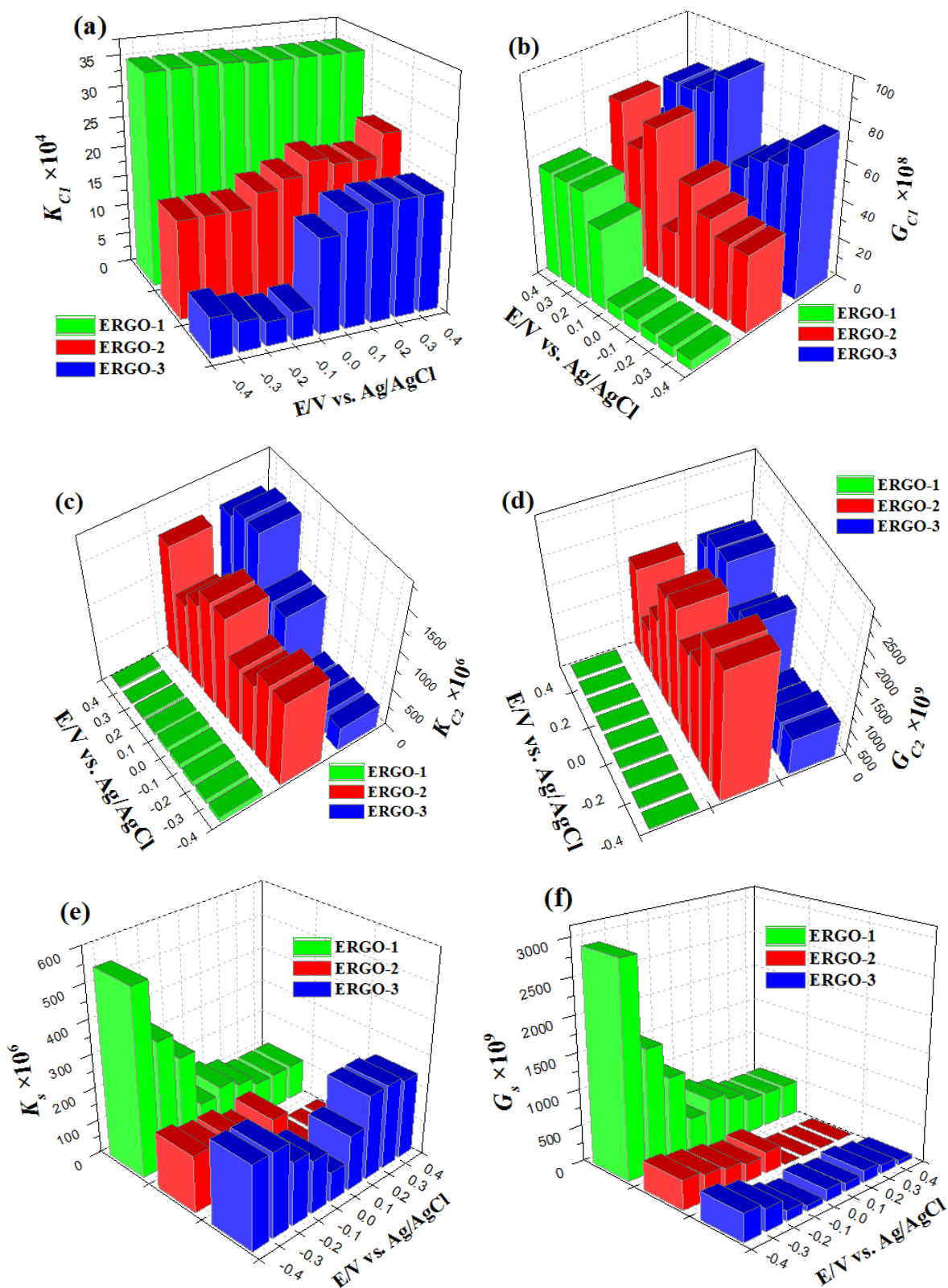
identification. Thus,  $\frac{\Delta m}{\Delta E}(\omega)$  TFs were explored for tracking the flux of both charged and neutral species with their identification as well as for their kinetics of interfacial transfer (**Figure IV.10**).

Two parameters for each ionic species,  $K_i$  and  $G_i$  previously obtained from the  $\frac{\Delta E}{\Delta I}(\omega)$  and

$\frac{\Delta q}{\Delta E}(\omega)$  were used in the fitting process of the  $\frac{\Delta m}{\Delta E}(\omega)$  TF. The additional parameters,  $K_i$  and  $G_i$

for the solvent molecules and the molar mass ( $M_i$ ) of each species were estimated (listed in **Table**

IV.2 at selective potentials of  $\pm 0.2$  V vs. Ag/AgCl). All the parameters for  $K_i$  and  $G_i$  at various potentials in the range of -0.4 V to 0.4 V are summarized in **Figure IV.11**.



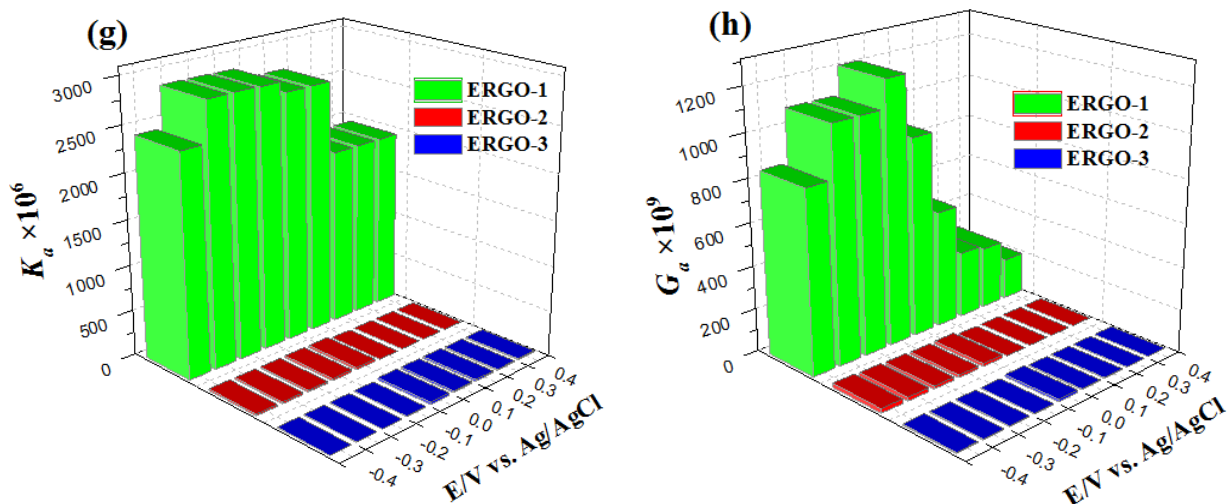


**Figure IV.11.** Fitting parameters in *ac*-electrogravimetry,  $K_i$  and  $G_i$  for each species: (a, b) for cation 1,  $c_1$ ; (c, d) for cation2,  $c_2$ ; (e, f) for solvent,  $s$ ; and (g, f) for anion,  $a$ .

**Figure IV.10** depicts the evolution of  $\frac{\Delta m}{\Delta E}(\omega)$  response of ERGO electrodes at  $\pm 0.2$  V vs. Ag/AgCl with progressive removal of oxygen functionalities. Four different species, i.e., hydrated cations ( $\text{Na}^+ \cdot n\text{H}_2\text{O}$ ,  $n=1$  or  $2$ ), cations ( $\text{Na}^+$ ),  $\text{H}_2\text{O}$  molecules and anions ( $\text{Cl}^-$ ) were identified which resulted in a good agreement between the experimental and the theoretical curves. As shown schematically in **Figure II.8** (Chapter II), the  $\frac{\Delta m}{\Delta E}(\omega)$  response in the first (I) quadrant is characteristic of an anion contribution, while a cation contribution appears in the third (III) quadrant<sup>50</sup>. For ERGO-1, at both potentials, relatively small amount of hydrated cations ( $\text{Na}^+ \cdot 2\text{H}_2\text{O}$ ) were identified at high frequencies (HFs). They were followed by a significant contribution of anions ( $\text{Cl}^-$ ) and  $\text{H}_2\text{O}$  molecules with the same flux direction with anions at high-intermediate and intermediate-low frequencies, respectively. Lastly, cations without hydration shell ( $\text{Na}^+$ ) were observed at very low frequencies. Besides, no significant differences of  $\frac{\Delta m}{\Delta E}(\omega)$  responses were observed between  $-0.2$  V and  $0.2$  V. This illustrates a persistent electrochemical performance of ERGO-1 electrode with anions playing a major part in the charge compensation (**Figure IV.10a** and **b**). On the contrary, the electrogravimetric response of ERGO-2 electrode presents an obvious potential-dependent behavior. Specifically, at  $-0.2$  V, a fairly good agreement between the experimental and theoretical  $\frac{\Delta m}{\Delta E}(\omega)$  data was achieved by considering the contribution of anions ( $\text{Cl}^-$ ) at low frequency (**Figure IV.10c**). However, at  $0.2$  V, this contribution disappeared and replaced by the extension of the contribution from  $\text{H}_2\text{O}$  molecules with the same flux direction as

cations (**Figure IV.10d**). It was observed that the H<sub>2</sub>O molecules in the solvation shell of the Na<sup>+</sup> is gradually removed at anodic potential of 0.3 and 0.4 V, i.e., Na<sup>+</sup>·2H<sub>2</sub>O losing half of its hydration shell to become Na<sup>+</sup>·H<sub>2</sub>O, as shown in **Figure IV.12**.

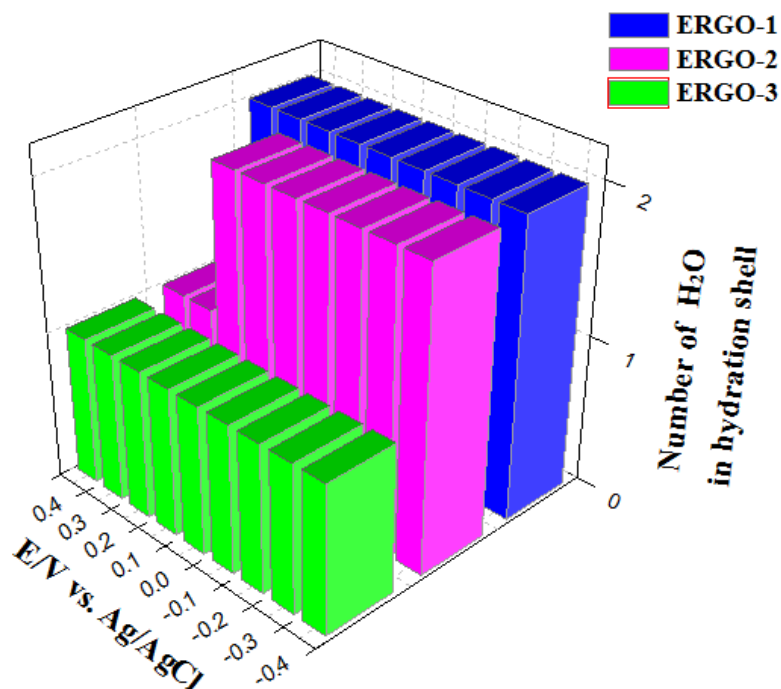


**Figure IV.12.** The evolution of number of H<sub>2</sub>O molecules in cation’s hydration shell at different polarized state from -0.4 to 0.4 V for ERGO electrodes.

ERGO-3 electrode presents one big loop of  $\frac{\Delta m}{\Delta E}(\omega)$  TF in the third (III) quadrant at high and intermediate frequencies, and a small one in the II quadrant at lower frequencies, independently of the applied potential (**Figure IV.10e and f**). It suggests a more homogeneous nanostructure of reduced graphene layers in ERGO-3 electrode with cations as a major charge carrier for charge balance in the potential range studied (-0.4 to 0.4 V). Herein, it is worth mentioning that a drastic decrease of the loop diameter in the III quadrant was observed when the measurement potential was changed from -0.2 V to 0.2 V for ERGO-2 and -3 electrodes, implying a decrease of the cation/free solvent contributions.

It is interesting to mention that hydrated cation (Na<sup>+</sup>·nH<sub>2</sub>O, n=1 or 2) transfers at the electrode/electrolyte interface with a higher kinetics than dehydrated one (Na<sup>+</sup>), as shown in **Figure IV.10**. This can be explained by putting forward the existence of shallow electroactive sites close to the edge of ERGO layers and deep electroactive sites located in the inner of ERGO layers with

higher activation energy for ion adsorption, which has been demonstrated in another 2D material,  $\text{Ti}_3\text{C}_2\text{T}_x$  MXenes<sup>24</sup>. The shallow electroactive sites are quite accessible for hydrated cation adsorption and desorption due to lower activation energy for ion adsorption, leading to high transfer kinetics. However, deep electroactive sites are exclusively approachable for cations only after removing its hydration shell, which requires much more energy and results in lower transfer kinetics of  $\text{Na}^+$ . After removing the oxygen functionalities during electrochemical reduction, the “*d*-spacing” decreased (as shown by XRD patterns in **Figure IV.3**) and it could be speculated that the gap between the layers may close up at the edges from electrolyte side. This can shelter the accessibility for ions especially to shallow electroactive sites, which might cause the dehydration behavior of  $\text{Na}^+ \cdot 2\text{H}_2\text{O}$  to  $\text{Na}^+ \cdot \text{H}_2\text{O}$  from ERGO-1 to -3 electrode (**Figure IV.12**).

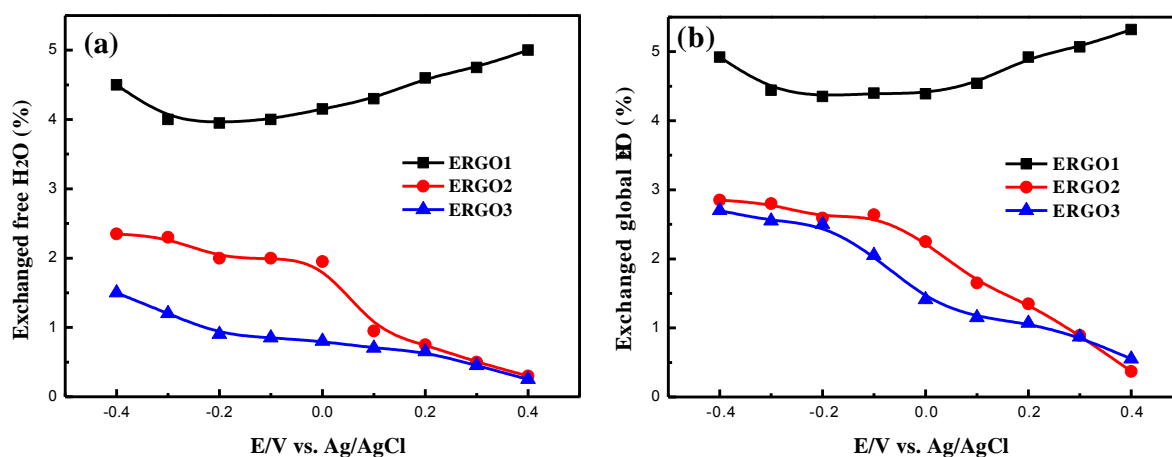


**Figure IV.13.** Exchanged free H<sub>2</sub>O (a) and global H<sub>2</sub>O (b) (calculated by **Equations IV.11** and **IV.12**) participating in charge compensation at each polarized state.

It has been demonstrated that during charge-discharge cycles, the exchange of ions between electrode and electrolyte is often accompanied with free solvent flux to satisfy the dimensional confinement of the electrode materials<sup>30</sup> and the relative displacement of graphene sheets synchronously takes place to meet the geometric requirement of this newly developed structure. Moreover, the solvent exchanged often plays an important role in electrode’s viscoelasticity through plasticizing effect<sup>45</sup>.

The exchanged free H<sub>2</sub>O and global H<sub>2</sub>O participating in charge compensation at each polarized state were calculated by **Equations IV.11** and **IV.12**. Global H<sub>2</sub>O represents the sum of free H<sub>2</sub>O and the H<sub>2</sub>O molecules within the hydration shell of cations. As shown in **Figure IV.13**, the increased H<sub>2</sub>O exchanged between electrode/electrolyte interface in ERGO-1 from cathodic to

anodic potentials (except -0.4 V) brings about progressively stronger plasticizing effect, contributing to the decrease of electrode's viscosity, i.e., lower  $G''$  (**Figure IV.5b**). Contrarily, in ERGO-2 and ERGO-3, less H<sub>2</sub>O exchanged from cathodic to anodic potentials which may account for a higher  $G''$  (**Figure IV.5b**). Briefly, the viscoelasticity of the ERGO electrodes can be tuned through adjusting the content of the hetero-oxygen groups on its layers. More flexibility and less viscosity is expected during the process of removing oxygen functional groups.

$$H_2O(\text{free}) = \left| \frac{-G_{H_2O}}{K_{H_2O}} \right| \quad (\text{IV.11})$$

$$H_2O(\text{global}) = \left| \frac{-G_{H_2O}}{K_{H_2O}} \right| + x \left| \frac{-G_{Na^+ + xH_2O}}{K_{Na^+ + xH_2O}} \right| \quad (\text{IV.12})$$

#### **IV.4. Conclusions**

The ion-selective properties of the reduced graphene oxides have been reported for the very first time through tuning the content of the oxygen containing functional groups on the graphene oxide layers. It was found out that under the experimental conditions of this study, the anions play the major part in the charge balance for ERGO electrode with a high amount of oxygen functionalities. On the contrary, the cation contribution dominates for ERGO electrode with a low content of these groups.

The ERGO electrodes are likely to possess relatively larger gaps between their layers in the cathodic potential range than those in the anodic potential range, permitting a higher amount of species transferred between the electrode and the electrolyte. Besides, for graphene oxide with intermediate reduced state (ERGO-2), this slight decrease in the interlayer distance during a shift from cathodic to anodic potentials leads to the dehydration phenomena of Na<sup>+</sup>·2H<sub>2</sub>O, which may be attributed to the hydrated cations' fading accessibility to shallow electroactive sites near the edge of ERGO layers. With the removal of oxygen functionalities on the ERGO layers which results in the restoration of π-π conjugated system, the ERGO electrodes behave more flexible, leading to an enhanced electrochemical energy storage capability.

The present study exhibited the significance of such an integrated methodology of electroacoustic, EQCM and *ac*-electrogravimetry measurements to be able to probe the viscoelastic and electrochemical evolution of ERGO electrodes with the different content of oxygen functionalities. The viscoelastic parameters obtained from the electroacoustic impedance were

further utilized to estimate the deviation of the sensitivity coefficients of the quartz crystal microbalance when it is not under the gravimetric regime and thus provided the differentiation of the effect of the mechanical property changes from purely gravimetric responses. This combined research methodology can also be employed to obtain insights into the electro(chemical and mechanical) behavior for other 2D materials and might pave the way to understand the charge storage mechanism, facilitating the fabrication of highly efficient SC electrodes with ion-selective properties and superior long-term performance.

### References

1. Miller, J. R.; Simon, P., Electrochemical capacitors for energy management. *Science* **2008**, *321* (5889), 651-652.
2. Stoller, M. D.; Park, S. J.; Zhu, Y. W.; An, J. H.; Ruoff, R. S., Graphene-based ultracapacitors. *Nano Lett.* **2008**, *8* (10), 3498-3502.
3. Gogotsi, Y.; Simon, P., True performance metrics in electrochemical energy storage. *Science* **2011**, *334* (6058), 917-8.
4. Zhu, Y.; Murali, S.; Stoller, M. D.; Ganesh, K. J.; Cai, W.; Ferreira, P. J.; Pirkle, A.; Wallace, R. M.; Cychosz, K. A.; Thommes, M.; Su, D.; Stach, E. A.; Ruoff, R. S., Carbon-based supercapacitors produced by activation of graphene. *Science* **2011**, *332* (6037), 1537-41.
5. Lei, Z.; Christov, N.; Zhao, X. S., Intercalation of mesoporous carbon spheres between reduced graphene oxide sheets for preparing high-rate supercapacitor electrodes. *Energy Environ. Sci.* **2011**, *4* (5), 1866.
6. Li-Feng Chen; Xu-Dong Zhang; Hai-Wei Liang; Mingguang Kong; Qing-Fang Guan; Ping Chen; Zhen-Yu Wu; Yu, S.-H., Synthesis of Nitrogen-Doped Porous Carbon Nanofibers as an Efficient Electrode Material for Supercapacitors. *ASC Nano* **2012**, *6* (8), 7092-7102
7. Largeot, C.; Portet, C.; Chmiola, J.; Taberna, P.-L.; Gogotsi, Y.; Simon, P., Relation between the Ion Size and Pore Size for an Electric Double-Layer Capacitor. *J. Am. Chem. Soc.* **2008**, *130* (9), 2730-2731.
8. Chmiola, J.; Yushin, G.; Gogotsi, Y.; Portet, C.; Simon, P.; Taberna, P. L., Anomalous increase in carbon capacitance at pore sizes less than 1 nanometer. *Science* **2006**, *313* (5794), 1760-1763.
9. Salanne, M.; Rotenberg, B.; Naoi, K.; Kaneko, K.; Taberna, P. L.; Grey, C. P.; Dunn, B.; Simon, P., Efficient storage mechanisms for building better supercapacitors. *Nat. Energy* **2016**, *1* (6), 16070.
10. Zhai, Y.; Dou, Y.; Zhao, D.; Fulvio, P. F.; Mayes, R. T.; Dai, S., Carbon materials for chemical capacitive energy storage. *Adv. Mater.* **2011**, *23* (42), 4828-50.
11. El-Kady, M. F.; Strong, V.; Dubin, S.; Kaner, R. B., Laser scribing of high-performance and flexible graphene-based electrochemical capacitors. *Science* **2012**, *335* (6074), 1326-1330.
12. Wang, M.; Duong le, D.; Mai, N. T.; Kim, S.; Kim, Y.; Seo, H.; Kim, Y. C.; Jang, W.; Lee, Y.; Suhr, J.; Nam, J. D., All-solid-state reduced graphene oxide supercapacitor with large volumetric capacitance and ultralong stability prepared by electrophoretic deposition method. *ACS Appl. Mater. Interfaces* **2015**, *7* (2), 1348-1354.
13. Wang, S.; Liu, N.; Su, J.; Li, L.; Long, F.; Zou, Z.; Jiang, X.; Gao, Y., Highly stretchable and self-healable supercapacitor with reduced graphene oxide based fiber springs. *ACS Nano* **2017**, *11* (2), 2066-2074.
14. Xu, J.; Tan, Z.; Zeng, W.; Chen, G.; Wu, S.; Zhao, Y.; Ni, K.; Tao, Z.; Ikram, M.; Ji, H.; Zhu, Y., A hierarchical carbon derived from sponge-templated activation of graphene oxide for high-performance supercapacitor electrodes. *Adv. Mater.* **2016**, *28* (26), 5222-5228.
15. Yang, X.; Zhu, J.; Qiu, L.; Li, D., Bioinspired effective prevention of restacking in multilayered graphene films: towards the next generation of high-performance supercapacitors. *Adv. Mater.* **2011**, *23* (25), 2833-2838.
16. Raccichini, R.; Varzi, A.; Passerini, S.; Scrosati, B., The role of graphene for electrochemical energy storage. *Nat. Mater.* **2015**, *14* (3), 271-279.
17. X-Y Peng; Liu, X.-X.; Diamond, D.; Lau, K. T., Synthesis of electrochemically-reduced graphene oxide film with controllable size and thickness and its use in supercapacitor. *Carbon* **2011**, *49*, 3488-3496.
18. Xu, B.; Yue, S.; Sui, Z.; Zhang, X.; Hou, S.; Cao, G.; Yang, Y., What is the choice for supercapacitors: graphene or graphene oxide? *Energy Environ. Sci.* **2011**, *4* (8), 2826.
19. Raymundo-Piñero, E.; Cadek, M.; Béguin, F., Tuning Carbon Materials for Supercapacitors by Direct Pyrolysis of Seaweeds. *Adv. Funct. Mater.* **2009**, *19* (7), 1032-1039.
20. Du, Q.; Zheng, M.; Zhang, L.; Wang, Y.; Chen, J.; Xue, L.; Dai, W.; Ji, G.; Cao, J., Preparation of functionalized graphene sheets by a low-temperature thermal exfoliation approach and their electrochemical supercapacitive behaviors. *Electrochim. Acta* **2010**, *55* (12), 3897-3903.
21. Yan, J.; Wang, Q.; Wei, T.; Fan, Z. J., Recent advances in design and fabrication of electrochemical supercapacitors with high energy densities. *Adv. Energy Mater.* **2014**, *4* (4), 1300816.

22. Dreyer, D. R.; Park, S.; Bielawski, C. W.; Ruoff, R. S., The chemistry of graphene oxide. *Chem.Soc.Rev.* **2010**, 39 (1), 228-40.
23. Shpigel, N.; Levi, M. D.; Sigalov, S.; Mathis, T. S.; Gogotsi, Y.; Aurbach, D., Direct assessment of nanoconfined water in 2D  $Ti_3C_2$  electrode interspaces by a surface acoustic technique. *J. Am. Chem. Soc.* **2018**, 140 (28), 8910-8917.
24. Levi, M. D.; Lukatskaya, M. R.; Sigalov, S.; Beidaghi, M.; Shpigel, N.; Daikhin, L.; Aurbach, D.; Barsoum, M. W.; Gogotsi, Y., Solving the capacitive paradox of 2D MXene using electrochemical quartz-crystal admittance and in situ electronic conductance measurements. *Adv. Energy Mater.* **2015**, 5 (1), 1400815.
25. Levi, M. D.; Shpigel, N.; Sigalov, S.; Dargel, V.; Daikhin, L.; Aurbach, D., In situ porous structure characterization of electrodes for energy storage and conversion by EQCM-D: a review. *Electrochim. Acta* **2017**, 232, 271-284.
26. Shpigel, N.; Lukatskaya, M. R.; Sigalov, S.; Ren, C. E.; Nayak, P.; Levi, M. D.; Daikhin, L.; Aurbach, D.; Gogotsi, Y., In situ monitoring of gravimetric and viscoelastic changes in 2D intercalation electrodes. *ACS Energy Lett.* **2017**, 2 (6), 1407-1415.
27. Goubaa, H.; Escobar-Teran, F.; Ressam, I.; Gao, W.; El Kadib, A.; Lucas, I. T.; Raihane, M.; Lahcini, M.; Perrot, H.; Sel, O., Dynamic resolution of ion transfer in electrochemically reduced graphene oxides revealed by electrogravimetric impedance. *J. Phys. Chem. C* **2017**, 121 (17), 9370-9380.
28. Escobar-Teran, F.; Arnau, A.; Garcia, J. V.; Jiménez, Y.; Perrot, H.; Sel, O., Gravimetric and dynamic deconvolution of global EQCM response of carbon nanotube based electrodes by Ac-electrogravimetry. *Electrochem. Commun.* **2016**, 70, 73-77.
29. Garc ía-Jare ño, J. J.; Gabrielli, C.; Perrot, H., Validation of the mass response of a quartz crystal microbalance coated with Prussian Blue film for ac electrogravimetry. *Electrochem. Commun.* **2000**, 2 (3), 195-200.
30. Hillman, A. R.; Efimov, I.; Skompska, M., Dynamics of regioregular conducting polymer electrodes in response to electrochemical stimuli. *Faraday Discuss.* **2002**, 121, 423-439.
31. Koehler, S.; Bund, A.; Efimov, I., Shear moduli of anion and cation exchanging polypyrrole films. *J. Electroanal. Chem.* **2006**, 589 (1), 82-86.
32. Hummers, W. S. J.; Offeman, R. E., Preparation of graphitic oxide. *J. Am. Chem. Soc.* **1958**, 80 (1339).
33. Granstaff, V. E.; Martin, S. J., Characterization of a thickness-shear mode quartz resonator with multiple nonpiezoelectric layers. *J. Appl. Phys.* **1994**, 75 (3), 1319-1329.
34. GAO, W.; Sel, O.; Perrot, H., Electrochemical and viscoelastic evolution of dodecyl sulfate-doped polypyrrole films during electrochemical cycling. *Electrochim. Acta* **2017**, 233, 262-273.
35. Conway, B. E., Electrochemical Supercapacitor: Scientific Fundamentals and Technological Applications. *Kluwer Academic/Plenum Publishers: New York* **1999**.
36. Shao, Y.; Wang, J.; Engelhard, M.; Wang, C.; Lin, Y., Facile and controllable electrochemical reduction of graphene oxide and its applications. *J. Mater. Chem.* **2010**, 20 (4), 743-748.
37. Pei, S.; Zhao, J.; Du, J.; Ren, W.; Cheng, H.-M., Direct reduction of graphene oxide films into highly conductive and flexible graphene films by hydrohalic acids. *Carbon* **2010**, 48 (15), 4466-4474.
38. Shin, H. J.; Kim, K. K.; Benayad, A.; Yoon, S. M.; Park, H. K.; Jung, I. S.; Jin, M. H.; Jeong, H. K.; Kim, J. M.; Choi, J. Y.; Lee, Y. H., Efficient reduction of graphite oxide by sodium borohydride and its effect on electrical conductance. *Adv. Funct. Mater.* **2009**, 19 (12), 1987-1992.
39. Chen, Y.; Zhang, X.; Zhang, D.; Yu, P.; Ma, Y., High performance supercapacitors based on reduced graphene oxide in aqueous and ionic liquid electrolytes. *Carbon* **2011**, 49 (2), 573-580.
40. Debiemme-Chouvy, C.; Thomas, B.; Lucas, I. T.; Tran, T. T. M.; Heintz, J. M.; Veillere, A.; Silvain, J. F., Facile and green reduction of graphene oxide by a reduced polyoxometalate and formation of a nanohybrid. *ChemPlusChem* **2017**, 82 (2), 186-189.
41. Fan, X. B.; Peng, W. C.; Li, Y.; Li, X. Y.; Wang, S. L.; Zhang, G. L.; Zhang, F. B., Deoxygenation of exfoliated graphite oxide under alkaline conditions: a green route to graphene preparation. *Adv. Mater.* **2008**, 20 (23), 4490-4493.
42. Xu, Y. X.; Sheng, K. X.; Li, C.; Shi, G. Q., Self-assembled graphene hydrogel via a one-step hydrothermal process. *ACS Nano* **2010**, 4 (7), 4324-4330.
43. Dargel, V.; Jackel, N.; Shpigel, N.; Sigalov, S.; Levi, M. D.; Daikhin, L.; Presser, V.; Aurbach, D., In situ

multilength-scale tracking of dimensional and viscoelastic changes in composite battery electrodes. *ACS Appl. Mater. Interfaces* **2017**, *9* (33), 27664-27675.

44. Mohamoud, M. A.; Hillman, A. R., The effect of anion identity on the viscoelastic properties of polyaniline films during electrochemical film deposition and redox cycling. *Electrochim. Acta* **2007**, *53* (3), 1206-1216.

45. Hillman, A. R.; Mohamoud, M. A.; Efimov, I., Time-temperature superposition and the controlling role of solvation in the viscoelastic properties of polyaniline thin films. *Anal. Chem.* **2011**, *83* (14), 5696-707.

46. Q. Bao, S. B., C. Li, X. Qi, C. Pan, J. Zang, Z. Lu, Y. Li, D. Tang, S. Zhang and K. Lian, Supercapacitance of solid carbon nanofibers made from ethanol flames. *J. Phys. Chem. C* **2008**, *112* (3612).

47. Zhao, B.; Liu, P.; Jiang, Y.; Pan, D.; Tao, H.; Song, J.; Fang, T.; Xu, W., Supercapacitor performances of thermally reduced graphene oxide. *J. Power Sources* **2012**, *198*, 423-427.

48. Yang, Q.; Bi, R.; Yung, K.-c.; Pecht, M., Electrochemically reduced graphene oxides/nanostructured iron oxides as binder-free electrodes for supercapacitors. *Electrochim. Acta* **2017**, *231*, 125-134.

49. Gabrielli, C.; Garcia-Jareño, J. J.; Perrot, H., Charge compensation process in polypyrrole studied by ac electrogravimetry. *Electrochim. Acta* **2001**, *46* (26), 4095-4103.

50. Gabrielli, C.; Garcia-Jareno, J. J.; Keddah, M.; Perrot, H.; Vicente, F., Ac-electrogravimetry study of electroactive thin films. II. Application to polypyrrole. *J. Phys. Chem. B* **2002**, *106*, 3192-3201.

## Chapter V: Tracking interfacial charge transfer behavior of hydrothermally synthesized ZnO nanostructures via complementary electrogravimetric methods

In this chapter, the mechanism of species fluxes during charge-discharge process in nanostructured ZnO electrode was studied by a combined methodology of electrochemical quartz crystal microbalance (EQCM) and *ac*-electrogravimetry. Under the conditions of this study, anions ( $\text{SO}_4^{2-}$ ) possess the highest kinetics to be transferred at the electrode/electrolyte interface in charge balance while cations (identified as  $\text{Na}^+ \cdot 5\text{H}_2\text{O}$  and  $\text{Na}^+$ ) play the major part as charge carriers. Free  $\text{H}_2\text{O}$  molecules present a sluggish behavior and their interfacial transfer occurs at low scan rate or low frequencies. These findings shed light on the nature of ions and solvent participation in charge balance of hydrothermally synthesized ZnO nanostructures directly grown on the QCM device. The combined methodology proposed herein provides dynamic and gravimetric analysis of interfacial charge transfer and can be extended to investigate other nanostructured metal oxide-based electrodes for energy storage.

### V.1. Preamble and Objectives

Supercapacitors (SCs) are a class of electrochemical energy storage devices well suited to the rapid storage and release of energy<sup>1</sup>. The last four decades have seen a tremendous burgeoning of scientific and industrial interest into the potential applications of SCs, mainly due to their high power density and long cycle life<sup>2-3</sup>. Numerous research efforts have been dedicated to investigating the electrode materials, which play an essential role in optimizing the electrochemical performance of SCs.

Transition metal oxides have been intensively studied as electrode materials due to their fast and reversible redox reactions occurring at or near the electrode surface, which can provide significantly higher capacitances<sup>4-7</sup>. Generally, metal oxides can offer higher energy density than conventional carbon materials and better electrochemical stability than conducting polymers<sup>2</sup>. To date, transitional metal oxides, such as ruthenium oxide ( $\text{RuO}_2$ )<sup>8</sup>, manganese dioxide ( $\text{MnO}_2$ )<sup>9</sup>, zinc oxide ( $\text{ZnO}$ )<sup>10</sup> and nickel oxide ( $\text{NiO}$ )<sup>11</sup> have been intensively studied as electrode materials, which

can offer additional pseudocapacitances during electrochemical performance. Among these candidates, ZnO nanomaterials have been widely used due to its low cost, easy fabrication, morphological diversity and electrochemical activities<sup>12-15</sup>. ZnO nanomaterials can be solely deposited on the substrate<sup>10</sup> or composited with other metal oxides<sup>14</sup>, conducting polymers<sup>16</sup> and carbon-based materials<sup>17</sup> to serve as energy storage electrodes. However, of great fundamental importance but almost barely touched is the mechanism of ionic/non-ionic fluxes during charge-discharge process in ZnO-based electrodes, which plays an essential role in the design of supercapacitor electrodes with high efficiency.

Electrochemical quartz-crystal microbalance (EQCM) has gained wide applicability to evaluate the electrochemical behaviour of electrodes<sup>18-22</sup>, particularly *in situ* capturing of the global transfer of the species at the electrode/electrolyte interface. Mass and charge variations measured simultaneously during the electrode cycling allow the derivation of the global mass per mole of electrons (MPE) that is exchanged between the electrode and the electrolyte according to the

equation:  $MPE = F \frac{\Delta m}{\Delta q}(\omega)$ , where  $F$  is the Faraday number,  $\Delta m$  and  $\Delta q$  are the mass and charge

variations, respectively. If only one species is exchanged, then the MPE corresponds to its molar mass. In the cases where multiple ion transfer occurs, using Faraday's law to interpret classical EQCM data reaches its limitations. To discriminate between the involved species, Donnan-type electrical double layer models were incorporated into the gravimetric EQCM equations<sup>23</sup>. Additionally, it has been demonstrated that coupling the QCM with electrochemical impedance spectroscopy (the so-called *ac*-electrogravimetry) contributes to disentangle the subtleties of global charge compensation process involving multiple species, offering a quantitative picture of each participant with their transfer kinetics and identifying them by their molar masses.

Under a fixed potential with a small sinusoidal perturbation, frequency dependant mass and charge variations are obtained and used to generate both the classical EIS transfer function (TF),  $\frac{\Delta E}{\Delta I}(\omega)$  and the mass/potential TF,  $\frac{\Delta m}{\Delta E}(\omega)$ . These TFs are then fitted with an appropriate model to obtain detailed identification of the species involved in the charge transfer mechanism, along with the kinetics and the relative concentrations associated with each species<sup>24</sup>.

In the chapter, this non-classical but emerging methodology in the energy storage domain<sup>25-27</sup> is adopted to characterize the electrochemical energy storage behaviour of ZnO-based electrodes and elucidate the subtleties in transfer of species during charge balance. To the best of our knowledge,

this is the first time that ZnO is grown on QCM devices for energy storage purposes and investigated by the classical EQCM and its complementary counterpart *ac*-electrogravimetry for understanding its charge storage mechanism. Electroacoustic study has not been conducted assuming that the ZnO structures are rigid.

## V.2. Experimental Methods and Theoretical Background

### V.2.1. Electrode preparation and characterization

A precursor solution was prepared with 0.02 M zinc nitrate hexahydrate and 0.02 M hexamethylenetetramine (HMTA). A quartz resonator (9 MHz-AWS, Valencia, Spain) was immersed in the solution, which was transferred to a Teflon-lined stainless steel autoclave and maintained at 120 °C for 12 h. After the hydrothermal process, ZnO nanostructures generated on the resonators were rinsed several times with deionized water.

EQCM and *ac*-electrogravimetry measurements were performed in 0.25 M Na<sub>2</sub>SO<sub>4</sub> under nitrogen atmosphere. ZnO nanostructures grown on the quartz resonator were used as the working electrode, with Ag/AgCl (3 M KCl saturated with AgCl) and platinum gauze as the reference and counter electrode, respectively. The potential window for EQCM was confined between 0 V and 0.6 V *vs.* Ag/AgCl in cyclic voltammetry (CV) and 0 V and 0.8 V *vs.* Ag/AgCl in galvanostatic charge/discharge (GCD). A lab-made QCM device (Miller oscillator) was used to measure frequency shift ( $\Delta f$ ) of the quartz crystals. The mass change ( $\Delta m$ ) of ZnO electrode on the quartz crystals during electrochemical process can be estimated by the microbalance frequency shift ( $\Delta f$ ) through Sauerbrey equation<sup>28</sup>, i.e.,  $\Delta f = -C_f \times \Delta m$ , where  $C_f$  is the experimental sensitivity factor of the quartz crystal resonator ( $C_f = 16.3 \times 10^7 \text{ Hz} \cdot \text{g}^{-1} \cdot \text{cm}^2$ )<sup>25</sup>.

For *ac*-electrogravimetry measurements, a four-channel frequency response analyzer (FRA, Solartron 1254) and a lab-made potentiostat (SOTELEM-PGSTAT) were used. The QCM was performed under dynamic regime, and the modified working electrode was polarized at selected potentials to which a sinusoidal small amplitude potential perturbation was superimposed. The frequency range was between 63 KHz and 10 mHz. The mass change,  $\Delta m$  of the working electrode was measured simultaneously with the *ac* response,  $\Delta I$  of the electrochemical system. Frequency/voltage converter is the key component of the *ac*-electrogravimetry set-up which translates the QCM frequency response ( $\Delta f$ ) to a continuous voltage change ( $\Delta V_f$ ) with the aim of obtaining a transfer function (TF) *via* a frequency response analyzer (FRA) (which cannot directly

analyze the frequency response). Finally, the resulting signals  $\frac{\Delta V_f}{\Delta V}(\omega)$  and  $\frac{\Delta V}{\Delta I}(\omega)$  were sent to a four-channel FRA, which led to the electrogravimetric TF ( $\frac{\Delta m}{\Delta E}(\omega)$ ) and the electrical TF ( $\frac{\Delta E}{\Delta I}(\omega)$ ) to be obtained simultaneously at a given potential and frequency modulation,  $f$  (pulsation  $\omega=2\pi f$ ). More details about *ac*-electrogravimetry are given in Chapter II.

### V.2.2. Theoretical considerations for *ac*-electrogravimetry

Under the effect of a sinusoidal potential perturbation with low amplitude,  $\Delta E$ , imposed to the electrode/film/electrolyte system, sinusoidal fluctuations of concentration,  $\Delta C_i$  are observed. The theoretical TFs are calculated through the following equations<sup>26, 31</sup>:

$$\frac{\Delta C_i}{\Delta E}(\omega) = \frac{-G_i}{j\omega d_f + K_i} \quad (i: \text{ions and non-charged species}) \quad (\text{V.1})$$

$$\frac{\Delta E}{\Delta I}(\omega) = \frac{1}{j\omega F d_f \sum_i \frac{G_i}{j\omega d_f + K_i}} \quad (i: \text{ions}) \quad (\text{V.2})$$

$$\frac{\Delta q}{\Delta E}(\omega) = F d_f \sum_i \frac{G_i}{j\omega d_f + K_i} \quad (i: \text{ions}) \quad (\text{V.3})$$

$$\frac{\Delta m}{\Delta E}(\omega) = -d_f \sum_i M_i \frac{G_i}{j\omega d_f + K_i} \quad (i: \text{ions and non-charged species}) \quad (\text{V.4})$$

where  $\Delta C_i$  presents concentration variation for each species,  $\omega$  is the pulsation,  $d_f$  is the film thickness,  $M_i$  depicts the molar mass of involved species,  $K_i$  and  $G_i$  are the partial derivatives of the flux ( $J_i$ ) with respect to the concentration and the potential, respectively.  $K_i$  represents the transfer kinetics of each species while  $G_i$  is the reciprocal of the transfer resistance ( $R_{t_i}=1/FG_i$ ), exhibiting the ease or difficulty in the species transfer at the film/electrolyte interface.

The theoretical expressions (**Equations V.2-4**) were used to fit the experimental responses of the electrochemical impedance,  $\frac{\Delta E}{\Delta I}(\omega)$ , the charge/potential TF,  $\frac{\Delta q}{\Delta E}(\omega)$  and the electrogravimetric TF,  $\frac{\Delta m}{\Delta E}(\omega)$ , which provided the key parameters ( $M_i$ ,  $K_i$ ,  $G_i$  and  $R_{t_i}$ ) related to each species (where  $i$  can be a cation, an anion or solvent) to be extracted.

### V.3. Results and Discussion

The synthesis of the nanostructures was performed directly on the quartz resonators by hydrothermal method. As shown in **Figure V.1a**, ZnO nanostructures are densely grown on the quartz resonator, formed by flower-like bundles of individual nanorods with a diameter of  $\sim 300$ - $800$  nm and length of  $\sim 2$ - $7$   $\mu\text{m}$ . The discrete ZnO nanorods may facilitate the exposure to the electrolyte and thus offer a large surface area for the electrochemical processes. XRD patterns are recorded (**Figure V.1b**) and the peaks present between  $32^\circ$  and  $69^\circ$  demonstrate that the synthesized ZnO nanorods exhibit the crystalline nature of wurtzite hexagonal structure, which is in good agreement with standard ZnO peaks (JCPDS 36-1451)<sup>29-30</sup>.

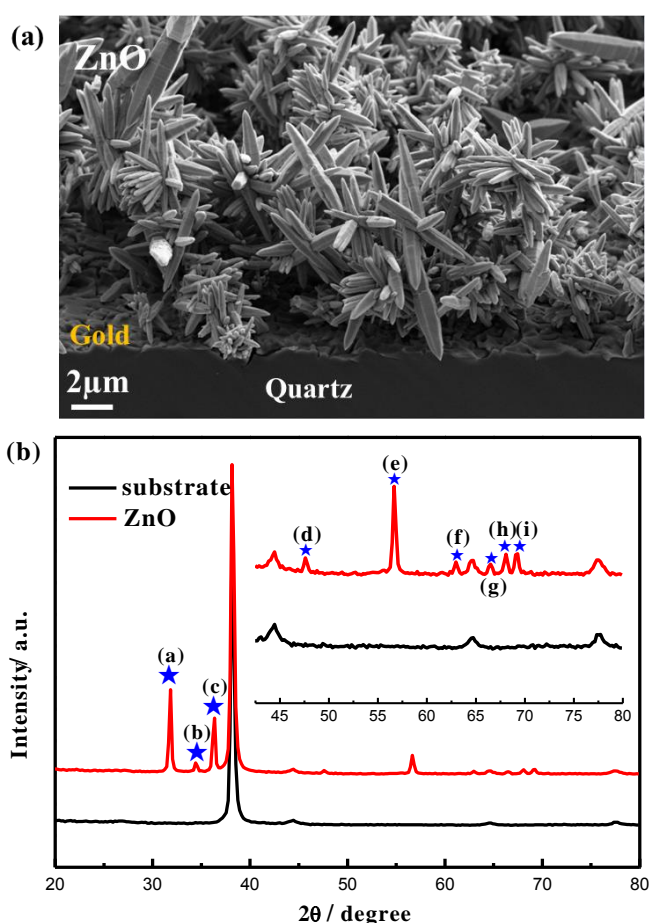


**Figure V.1.** (a) FEG-SEM image and (b) XRD spectra of ZnO nanostructures hydrothermally synthesized on the gold electrode of the quartz resonator. The peaks centered at  $2\theta = 32^\circ, 34^\circ, 36^\circ, 47^\circ, 56^\circ, 63^\circ, 66^\circ, 68^\circ$  and  $69^\circ$  correspond to the lattice planes (100), (002), (101), (102), (110), (103), (200), (112) and (201), respectively. The inset in (b) is the magnification of the spectra between  $2\theta = 42.5^\circ$  and  $80^\circ$ .

### V.3.1. Cyclic Electrogravimetry (EQCM) and QCM-coupled GCD:

The electrochemical performance of ZnO nanorods was characterized by cyclic voltammetry (CV) and galvanostatic charge-discharge (GCD) techniques. The QCM was coupled with both measurements to track the simultaneous frequency shifts of the ZnO-based electrode during cycling, which can be converted into mass responses through Sauerbrey equation<sup>28</sup>. **Figure V.2a** exhibits approximately rectangular CV curves, with a cathodic peak around 0.1 V and an anodic peak around 0.2 V. This electrochemical behaviour due to the dominant capacitive response in the CV curve can be attributed to an electroadsorption process of Na<sup>+</sup> ions occurring at different electroactive sites of the ZnO electrode:



However, this simplified scheme does not take into account of (i) the ion solvation effect, (ii) the possible presence of more than one ionic species which may participate in the charge compensation process and affect the charge/discharge rates, and (iii) the influence of free electrolyte molecules that can interact, indirectly, with the electrodes.

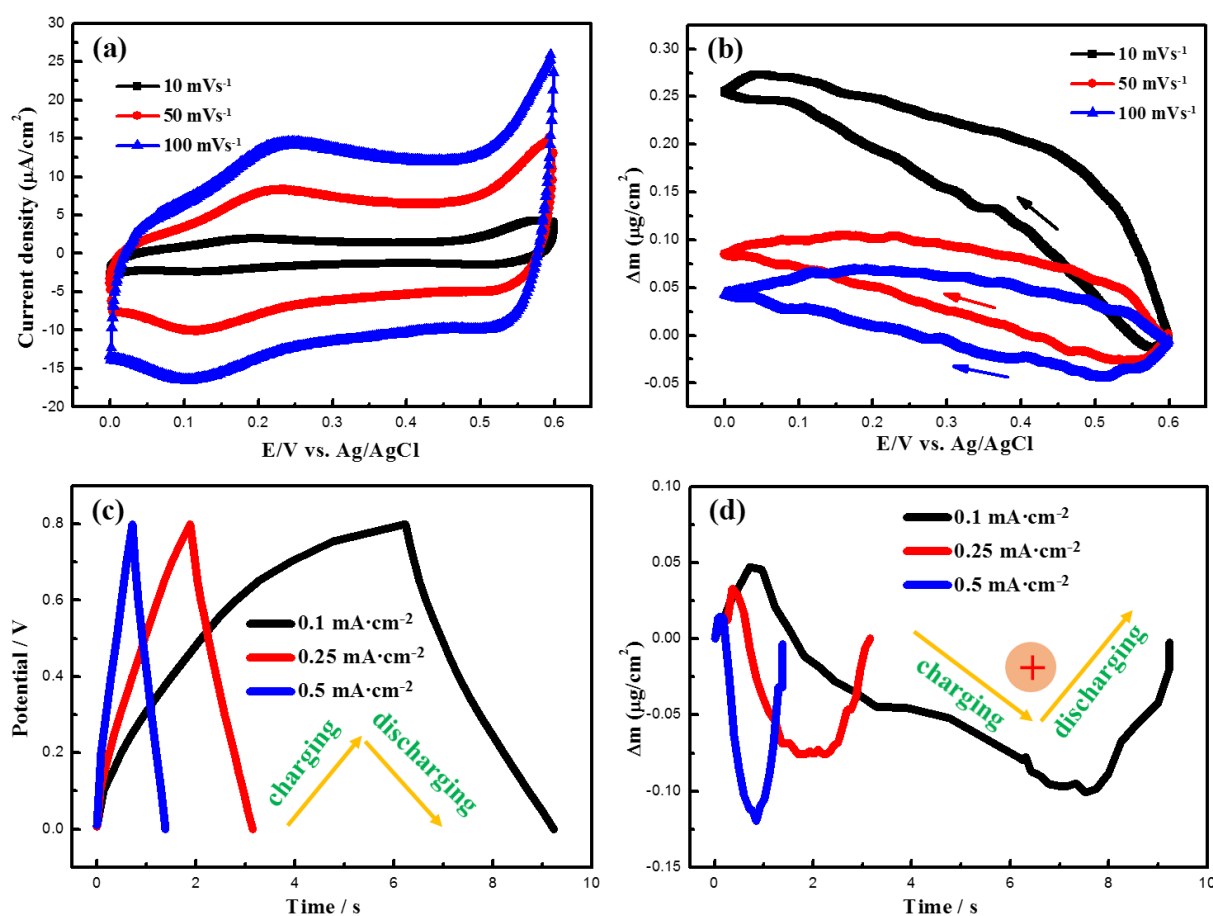


**Figure V.2.** Cyclic voltammetry (a) and galvanostatic charge/discharge (c) measurements of ZnO

electrode on the gold electrode of the quartz resonator with the corresponding mass variations of the electrode (b and d) measured in 0.25 M Na<sub>2</sub>SO<sub>4</sub>.

Utilizing the simultaneous QCM measurements permits the corresponding mass responses ( $\Delta m$ - $E$ ) to be obtained during CV scans (**Figure V.2b**). Mass response mainly presents ingress/egress during cathodic/anodic sweep, which is indicative of cation participation in charge compensation process<sup>31</sup>. GCD curves were measured to further evaluate the electrochemical performance of ZnO-based electrode. The corresponding mass-time response proceeds in an inverse pace with potential-time response, i.e., mass decrease during charging and mass increase during discharging, which indicates that the cation plays a major role in charge balance.

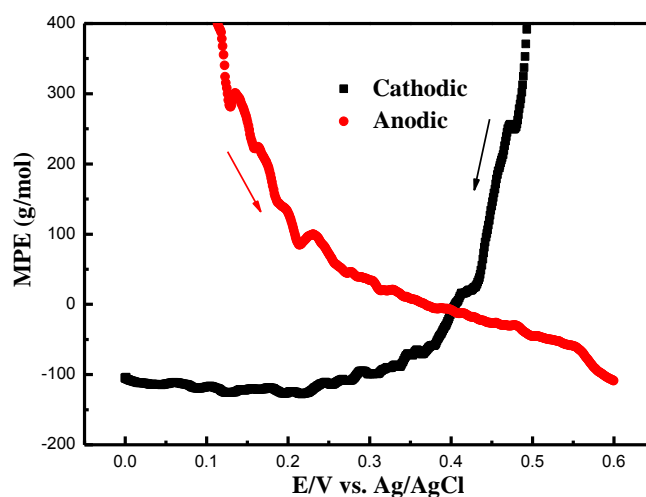


**Figure V.3.** MPE calculated from CV curve during a cathodic and an anodic sweep at a scan rate of 50 mV/s.

To obtain indications on the nature of the transferred species, the  $MPE = F\Delta m / \Delta q$  was calculated from the EQCM data (**Figure V.3**). If only one species is exchanged, then the MPE corresponds to its molar mass. Positive and negative values of the MPE correspond to a major contribution to the energy storage mechanism by anions and cations, respectively. Here, we obtain a MPE of  $\sim -100$  g $\cdot$ mol<sup>-1</sup> below 0.3 V and  $\sim -50$  g $\cdot$ mol<sup>-1</sup> above 0.4 V for the cathodic sweep and anodic sweep, respectively. The lower value for the cathodic sweep suggests that the cations are hydrated and/or accompanied by free solvent molecules. This value increases during the anodic sweep ( $\sim -50$  g $\cdot$ mol<sup>-1</sup>), indicating that multiple species are exchanged and interfacial behaviour is complex.

QCM-coupled CV and GCD measurements are performed at a certain scan rate or current density, therefore they require either the incorporation of Donnan-type models into the gravimetric

EQCM equations<sup>23</sup> or complementary methods to elucidate if there is a multiple species contribution to the charge compensation process<sup>32</sup>. To get a deeper insight into the charge compensation behaviour occurring in the ZnO-based electrode, from both gravimetric and kinetic point of view, the *ac*-electrogravimetry was suggested. The different scenarios of the charge compensation process for ZnO-based electrodes are scrutinized by this coupled method emerging in the field of energy storage<sup>25, 27</sup>.

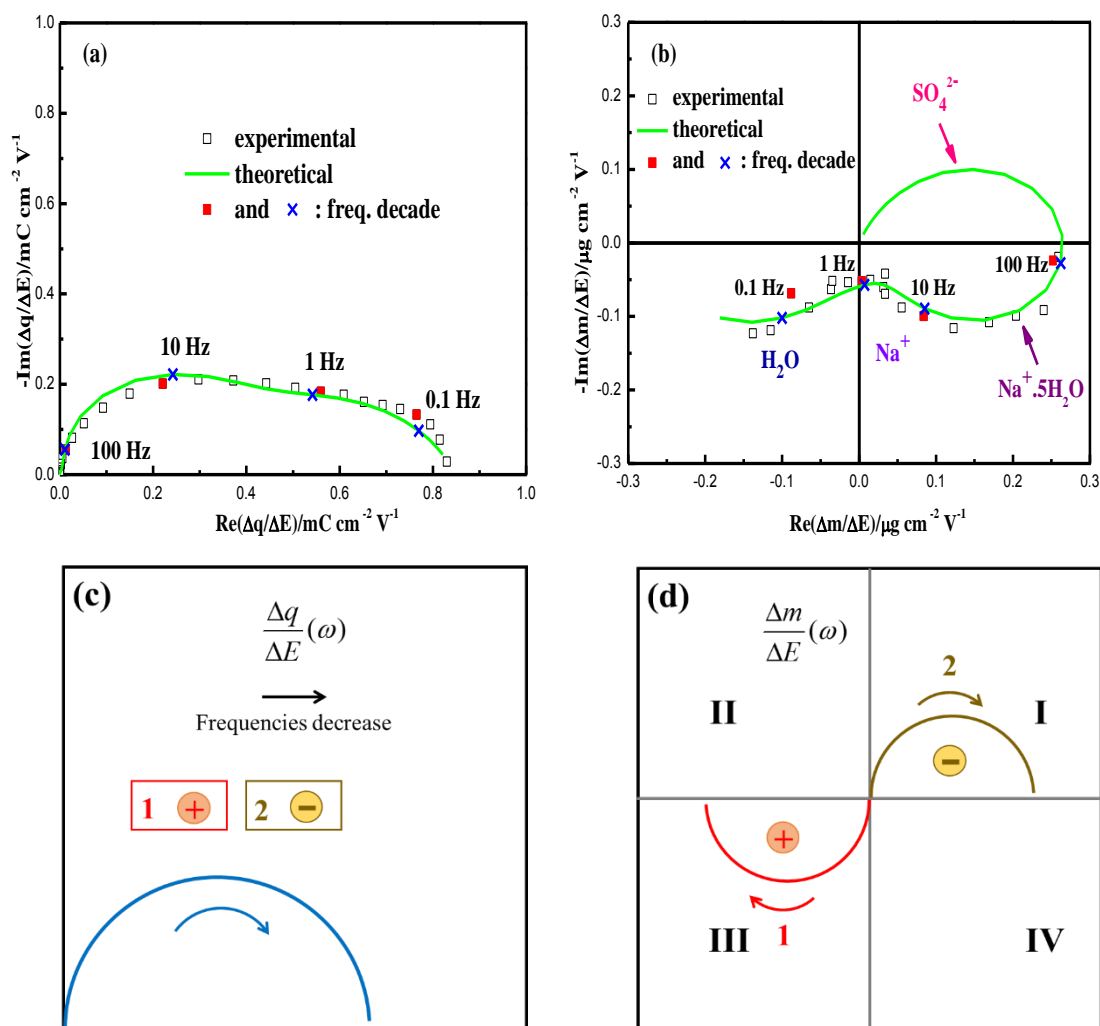


**Figure V.4.**  $\frac{\Delta q}{\Delta E}(\omega)$  (a) and  $\frac{\Delta m}{\Delta E}(\omega)$  (b) Transfer Functions (TFs) at 0.3V vs. Ag/AgCl.

Schematic representation of the TFs for  $\frac{\Delta q}{\Delta E}(\omega)$  (c) and  $\frac{\Delta m}{\Delta E}(\omega)$  (d). The following parameters

were used in the fitting of the experimental data:  $K_i$  (kinetics of transfer, in  $\text{cm}\cdot\text{s}^{-1}$ ),  $G_i$  (the inverse of the transfer resistance, in  $\text{mol}\cdot\text{s}^{-1}\cdot\text{cm}^{-2}\cdot\text{V}^{-1}$ ):  $K_{C1}$ : 0.0088,  $G_{C1}$ :  $2.375 \times 10^{-7}$ ;  $K_{C2}$ :  $2.199 \times 10^{-4}$ ,  $G_{C2}$ :  $9.456 \times 10^{-9}$ ;  $K_s$ :  $3.77 \times 10^{-5}$ ,  $G_s$ :  $4.524 \times 10^9$ ;  $K_a$ : 0.06,  $G_a$ :  $-2.149 \times 10^{-6}$ .  $C_1$ :  $\text{Na}^+\cdot 5\text{H}_2\text{O}$  (113

$\text{g}\cdot\text{mol}^{-1}$ ),  $\text{C}_2$ :  $\text{Na}^+$  ( $23 \text{ g}\cdot\text{mol}^{-1}$ ),  $\text{S}$ :  $\text{H}_2\text{O}$  ( $18 \text{ g}\cdot\text{mol}^{-1}$ ) and  $\text{A}$ :  $\text{SO}_4^{2-}$  ( $96 \text{ g}\cdot\text{mol}^{-1}$ ).

### V.3.2. QCM-coupled to Electrochemical Impedance Spectroscopy (*Ac*-electrogravimetry)

*Ac*-electrogravimetry measurements were performed in the same potential range used for CV measurements, at various states-of-polarization from 0 V to 0.6V vs. Ag/AgCl with an interval of 100 mV. **Figure V.4a** and **b** present  $\frac{\Delta q}{\Delta E}(\omega)$  (calculated from the electrochemical impedance,

theoretical part in **Equations V.2** and **V.3**) and  $\frac{\Delta m}{\Delta E}(\omega)$  TFs at 0.3V, where the experimental data

were fitted using theoretical functions in **Equations V.3** and **V.4**. It is important to note that for the

$\frac{\Delta m}{\Delta E}(\omega)$  TF, the experimental data were not visualized at high frequency region in **Figure V.4b**

beyond  $\sim 100$  Hz due to the instrumental limitations, i.e., the validity region of the frequency-voltage convertor is  $\sim 100$  Hz to  $\sim 1$  mHz. This may indicate that there is a fast species contributing to the charge storage but cannot be detected by *ac*-electrogravimetry with the current frequency-voltage convertor. Theoretically, anions and cations share the same response behaviour in

$\frac{\Delta q}{\Delta E}(\omega)$  TF, but anions characteristically appear in the quadrant I (Cartesian system) in

$\frac{\Delta m}{\Delta E}(\omega)$  while cations locate in the quadrant III, as shown in **Figure V.4c** and **d**. Therefore, in the

present work, the mass response at high frequency emerging in the quadrant I can originate from either anions or free  $\text{H}_2\text{O}$  molecules with the same transfer direction as anions<sup>24</sup>. Herein, four species based on different kinetics, i.e., anions ( $\text{SO}_4^{2-}$ ), hydrated cations ( $\text{Na}^+\cdot 5\text{H}_2\text{O}$ ), cations ( $\text{Na}^+$ ) and  $\text{H}_2\text{O}$  molecules were proposed which led to a good agreement between the experimental and the theoretical functions in terms of both the shape and the frequencies (**Figure V.4**). It is highlighted that the identification of the species can be achieved thanks to the electrogravimetric TF

( $\frac{\Delta m}{\Delta E}(\omega)$ ) which involves the molar mass ( $M_i$ ) of the species involved in the charge compensations

(**Equation V.4**).

Then, the *ac*-electrogravimetry data obtained at various states-of-polarization from 0 V to 0.6V vs. Ag/AgCl were analysed and it was observed that the presence of several species persists. This finding is further supported by comparing the *ac*-electrogravimetry data with that of EQCM (see the

section: V.3.3. Comparison of the EQCM and Ac-electrogravimetry mass responses).

The transfer kinetics of each species,  $K_i$ , are summarized in **Figure V.5a**.  $\text{SO}_4^{2-}$  anions exhibit the highest kinetics of transfer at the electrode/electrolyte interface in the charge compensation process, followed by hydrated cations ( $\text{Na}^+\cdot 5\text{H}_2\text{O}$ ) and dehydrated cations ( $\text{Na}^+$ ), and  $\text{H}_2\text{O}$  molecules present the lowest kinetics, i.e.,  $K(\text{SO}_4^{2-}) > K(\text{Na}^+\cdot 5\text{H}_2\text{O}) > K(\text{Na}^+) > K(\text{H}_2\text{O})$ . It is in good agreement with the inverse order of their transfer resistances:  $R_t(\text{SO}_4^{2-}) < R_t(\text{Na}^+\cdot 5\text{H}_2\text{O}) < R_t(\text{Na}^+) < R_t(\text{H}_2\text{O})$ , as depicted in **Figure V.5b**. The contribution of various species to electrochemical reactions with different kinetics of transfer has already been observed in the earlier work of Hillman *et al.* on nickel hydroxide thin films by combining probe beam deflection (PBD) technique and EQCM<sup>33-35</sup>, and also in our recent work on SWCNT based electrodes<sup>25</sup>.

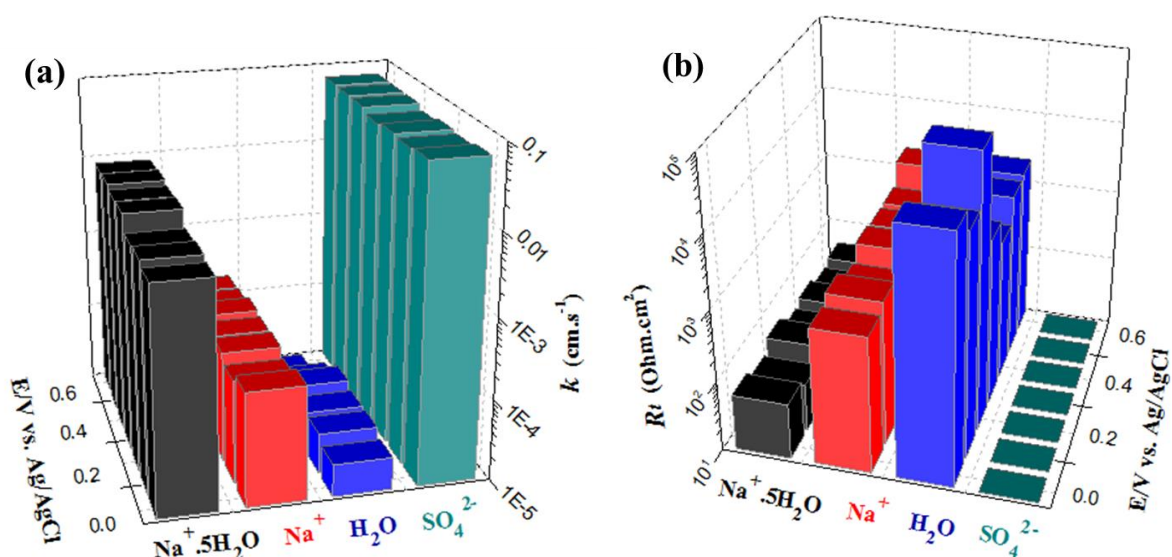


**Figure V.5.** Transfer kinetics,  $K_i$  ( $\text{cm}\cdot\text{s}^{-1}$ ) (a) and corresponding transfer resistances,  $R_{ti}$  ( $\Omega\cdot\text{cm}^2$ ) (b) for each species participating in charge balance.

The charge storage mechanism of another transitional metal oxide,  $\text{MnO}_2$ , has been widely investigated, and it was proposed that the charge could be stored by either i) the surface adsorption of alkali metal cations ( $\text{C}^+$ )<sup>36</sup> or ii) the intercalation of both protons ( $\text{H}^+$ ) and alkali metal cations ( $\text{C}^+$ )<sup>37-38</sup> in the electrolyte. However, direct analogy of the charge storage mechanism proposed for the other metal oxides may not be applicable to  $\text{ZnO}$ . In the present work,  $\text{SO}_4^{2-}$  and  $\text{Na}^+\cdot 5\text{H}_2\text{O}$  present a quick response upon potential perturbation, which is presumably ascribed to their fast electroadsorption behaviour. Dehydrated  $\text{Na}^+$  is also considered to be electroadsorbed but in the  $\text{ZnO}$  bulk, onto the less accessible sites, due to a relatively slow transfer kinetics (**Figure V.6**).

Furthermore, free H<sub>2</sub>O molecule exhibits a sluggish behaviour and participates in charge balance at lowest frequencies. It is supposed to be electrodragged by Na<sup>+</sup>,<sup>25</sup> as evidenced by the same flux direction of H<sub>2</sub>O and Na<sup>+</sup>.

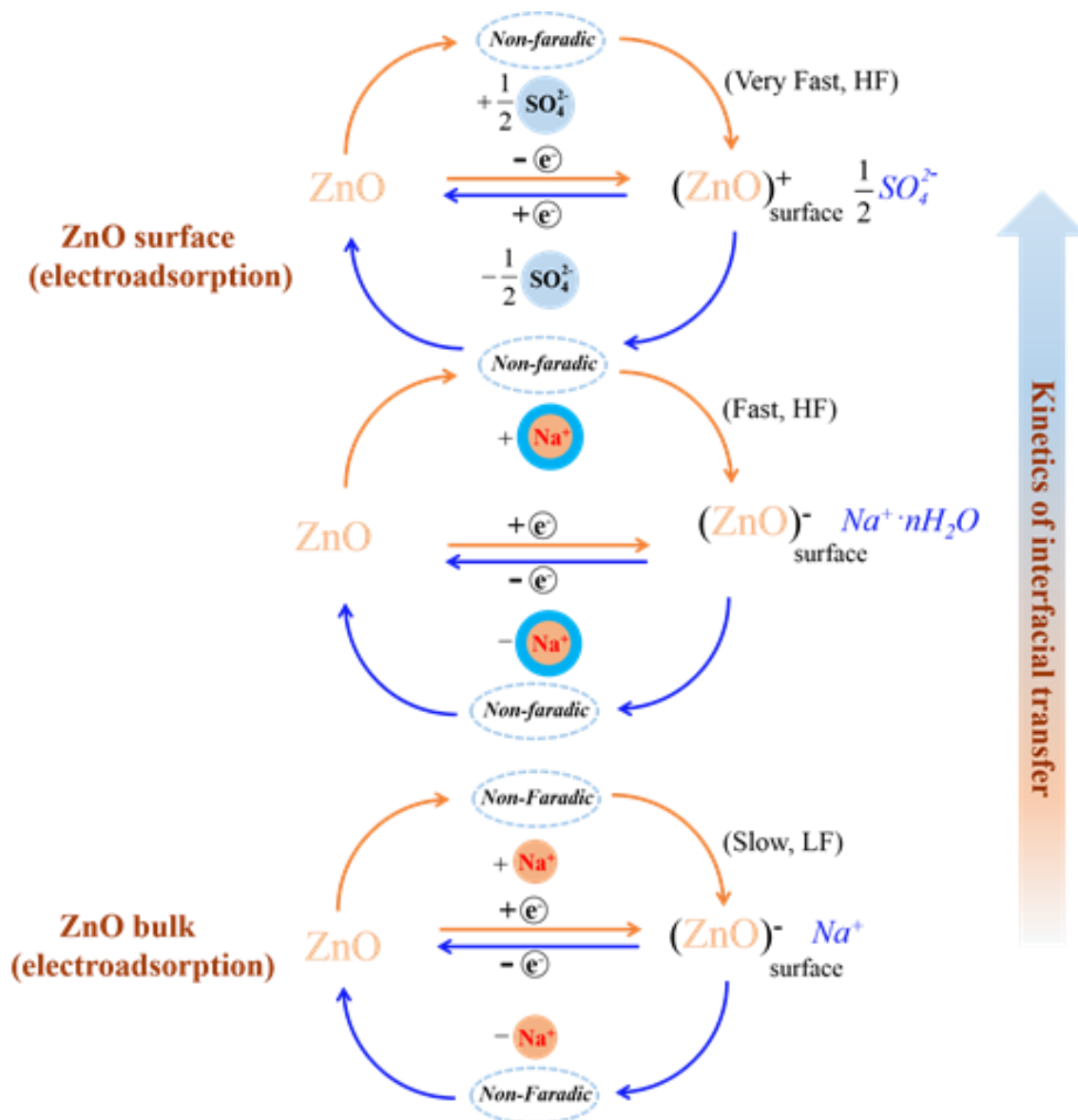


**Figure V.6.** A schematic presentation of ions participating in the charge balance, where cations with blue shell (1<sup>st</sup> step) represent the hydrated cation, i.e., Na<sup>+</sup>·nH<sub>2</sub>O (n=5).

Actually, it is speculated that there exist at least two different electroactive sites for charge storage in synthesized ZnO nanostructures. The first is on the surface of ZnO, where the charge storage occurs (under the conditions of this study) either by the electroadsorption and electrodesorption of SO<sub>4</sub><sup>2-</sup> and Na<sup>+</sup>·5H<sub>2</sub>O, respectively (**Figure V.6**). After the surficial electroactive sites are saturated with SO<sub>4</sub><sup>2-</sup> and Na<sup>+</sup>·5H<sub>2</sub>O by a fast electroadsorption behaviour, contributing to

the responses at high frequency (HF) in *ac*-electrogravimetry (**Figure V.4b**), the second electroactive sites in the bulk of ZnO may begin to come into use. Dehydrated Na<sup>+</sup>·5H<sub>2</sub>O (i.e., Na<sup>+</sup>) may electrodrag free H<sub>2</sub>O molecules into/out of ZnO bulk and, consequently, bring about a response from free H<sub>2</sub>O molecules at lowest frequency (LF) in *ac*-electrogravimetry (**Figure V.4b**).

### V.3.3. Comparison of the EQCM and *Ac*-electrogravimerty mass responses

In order to validate our hypothesis involving multi-species contribution to the charge storage and also to confirm the presence of the anionic species appearing at the HF region (see theoretical curve in **Figure V.4b**), a methodology benefiting from the complementarity of the EQCM and *ac*-electrogravimetry is developed as follows<sup>25</sup>: From *ac*-electrogravimetry, the relative concentration changes of each species ( $\Delta C_i$ ) with respect to the potential variation can be estimated by using **Equation V.5**; specifically, the estimation of the relative concentration change with respect to the individual species ( $C_i - C_0$ ) can be obtained after integration of **Equation V.5**:

$$\frac{\Delta C_i}{\Delta E}(\omega) = \frac{-G_i}{K_i} \quad (\omega \rightarrow 0) \quad (\text{V.5})$$

The concentration variation of individual species ( $C_i - C_0$ ) obtained from *ac*-electrogravimetry is shown in **Figure V.7a**. These ( $C_i - C_0$ ) values are transformed into corresponding mass variations of each species (**Figure V.7b**). Subsequently, the total mass change (total  $\Delta m$  from *ac*-electrogravimetry in **Figure V.7c**) is reconstructed by the addition of individual mass contribution from all species concerned in *ac*-electrogravimetry. A good agreement between the total mass change from *ac*-electrogravimetry and the EQCM response obtained at 10 mV/s emerges. It is further highlighted that *ac*-electrogravimetry results are obtained from individual measurements at stationary potentials and the reconstructed mass response is in good agreement with the EQCM data from cyclic voltammetry at the lowest scan rate measured. This is highly significant since it evidences that the *ac*-electrogravimetry result in **Figure V.7b** is indeed a deconvolution of the global EQCM mass response into distinct contributions.

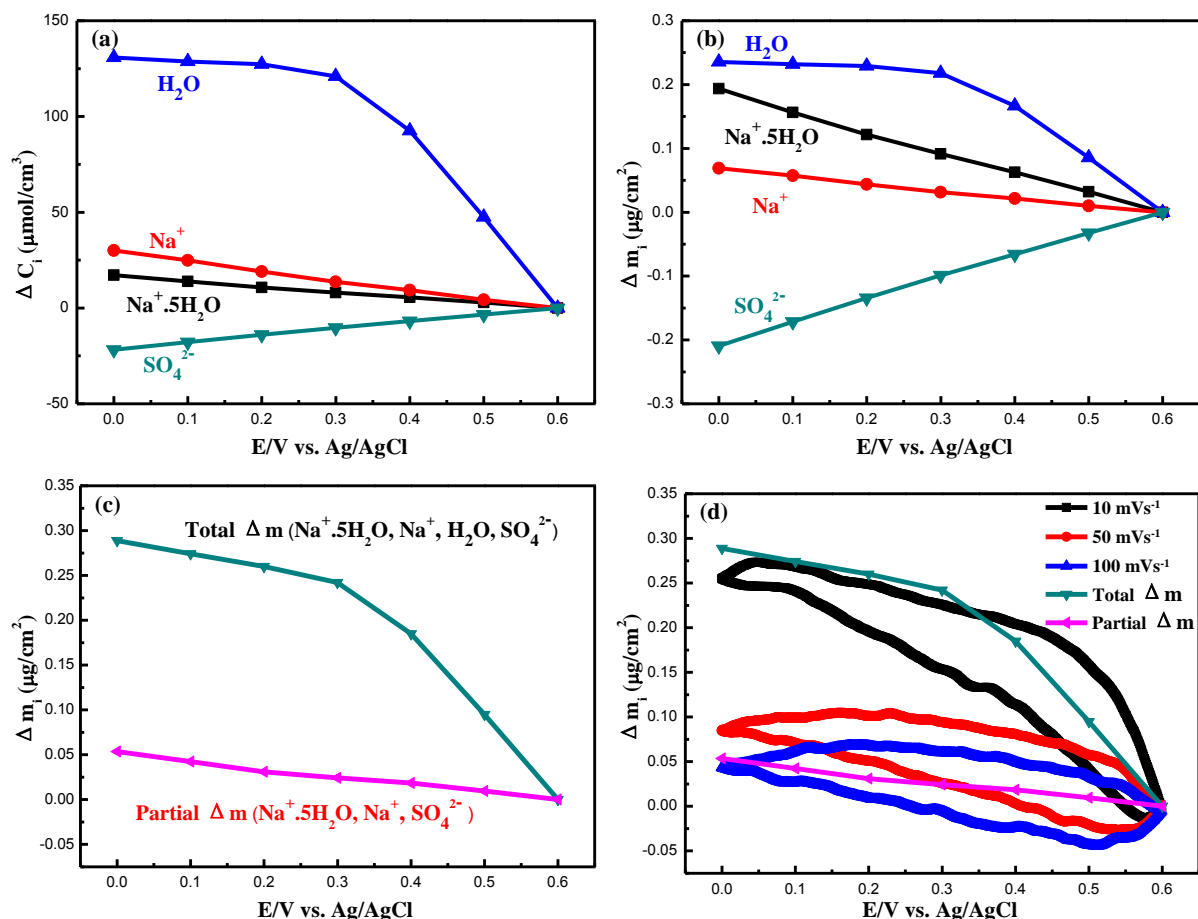


**Figure V.7.** Relative concentration change (a) and the corresponding mass change (b) of each species as a function of potential; mass variation (total and partial  $\Delta m$ ) reconstructed from *ac*-electrogravimetry (c) and the comparison of mass variation between *ac*-electrogravimetry and EQCM (d).

Furthermore, to explain the scan rate dependent mass response in **Figure V.7d**, the following is considered based on the *ac*-electrogravimetry findings: free  $\text{H}_2\text{O}$  molecules display the lowest transfer kinetics in charge balance (the slowest species), therefore, a partial mass change (partial  $\Delta m$  in **Figure V.7c**) can be obtained with the removal of the mass contributions from free  $\text{H}_2\text{O}$  molecules. This presents the mass response at high, intermediate and intermediate-low frequencies. Then, a close agreement between the partial  $\Delta m$  from *ac*-electrogravimetry and EQCM response at a high scan rate (100  $\text{mV/s}$ ) (**Figure V.7d**) can also be achieved. This implies that all of these 4 species detected by *ac*-electrogravimetry including the free  $\text{H}_2\text{O}$  molecules can be transferred at the electrode/electrolyte interface at low scan rate (10  $\text{mV/s}$ ). However, it hardly occurs for  $\text{H}_2\text{O}$  to be transferred at the electrode/electrolyte interface at a higher scan rate (100  $\text{mV/s}$ ). These comparisons present further evidence for the fitting hypothesis of the *ac*-electrogravimetry data that

the missing responses at HF are from anion contributions. It is evident that if the contribution of the anions is neglected, a good agreement between the EQCM and *ac*-electrogravimetry would not be achieved (**Figure V.7**). These results highlight the complementarity of the EQCM and *ac*-electrogravimetry, the limitations of either of which can be compensated by the other to unveil the subtleties of the charge storage mechanisms.

### V.4. Conclusions

The complementary combination of EQCM and *ac*-electrogravimetry was proposed herein to study the charge storage mechanism of hydrothermally synthesized ZnO nanostructures. EQCM provides a global mass response from cations in charge storage/delivery process, while *ac*-electrogravimetry offers a gravimetric and dynamic picture on the subtleties during this process: four different species ( $\text{SO}_4^{2-}$ ,  $\text{Na}^+ \cdot 5\text{H}_2\text{O}$ ,  $\text{Na}^+$ , and  $\text{H}_2\text{O}$ ) were detected to participate in charge balance with different kinetics to transfer the electrode/electrolyte interface. This study further emphasizes the complementarity of the EQCM and *ac*-electrogravimetry where certain instrumental limitations that challenge the detection of fast ion dynamics can be overcome by exploiting the two methods. This combined methodology can be extended to investigate the charge storage mechanism and species fluxes in other nanostructured electrodes, facilitating the design of optimized SC electrodes.

### References

1. Conway, B. E., *Electrochemical Supercapacitors: Scientific Fundamentals and Technological Applications* Kluwer Academic/Plenum, New York **1999**.
2. Wang, G.; Zhang, L.; Zhang, J., A review of electrode materials for electrochemical supercapacitors. *Chem. Soc. Rev.* **2012**, *41* (2), 797-828.
3. Miller, J. R.; Simon, P., Electrochemical capacitors for energy management. *Science* **2008**, *321* (5889), 651-652.
4. Cottineau, T.; Toupin, M.; Delahaye, T.; Brousse, T.; Bélanger, D., Nanostructured transition metal oxides for aqueous hybrid electrochemical supercapacitors. *Appl. Phys. A* **2006**, *82* (4), 599-606.
5. Simon, P.; Gogotsi, Y., Materials for electrochemical capacitors. *Nat. Mater.* **2008**, *7* (11), 845-854.
6. Augustyn, V.; Simon, P.; Dunn, B., Pseudocapacitive oxide materials for high-rate electrochemical energy storage. *Energy Environ. Sci.* **2014**, *7* (5), 1597.
7. Brezesinski, T.; Wang, J.; Polleux, J.; Dunn, B.; Tolbert, S. H., Templated nanocrystal-based porous TiO<sub>2</sub> films for next-generation electrochemical capacitors. *J. Am. Chem. Soc.* **2009**, *131* (5), 1802-1809.
8. Shen, J. F.; Li, T.; Huang, W. S.; Long, Y.; Li, N.; Ye, M. X., One-pot polyelectrolyte assisted hydrothermal synthesis of RuO<sub>2</sub>-reduced graphene oxide nanocomposite. *Electrochim. Acta* **2013**, *95*, 155-161.
9. Long, X.; Zeng, Z. G.; Guo, E. J.; Shi, X. B.; Zhou, H. J.; Wang, X. H., Facile fabrication of all-solid-state flexible interdigitated MnO<sub>2</sub> supercapacitor via in-situ catalytic solution route. *J. Power Sources* **2016**, *325*, 264-272.
10. Bae, J.; Song, M. K.; Park, Y. J.; Kim, J. M.; Liu, M.; Wang, Z. L., Fiber supercapacitors made of nanowire-fiber hybrid structures for wearable/flexible energy storage. *Angew. Chem. Int. Ed.* **2011**, *50* (7), 1683-1687.
11. Wang, D.-W.; Li, F.; Cheng, H.-M., Hierarchical porous nickel oxide and carbon as electrode materials for asymmetric supercapacitor. *J. Power Sources* **2008**, *185* (2), 1563-1568.
12. Sankapal, B. R.; Gajare, H. B.; Karade, S. S.; Salunkhe, R. R.; Dubal, D. P., Zinc oxide encapsulated carbon nanotube thin films for energy storage applications. *Electrochim. Acta* **2016**, *192*, 377-384.
13. Yang, P.; Xiao, X.; Li, Y.; Ding, Y.; Qiang, P.; Tan, X.; Mai, W.; Lin, Z.; Wu, W.; Li, T.; Jin, H.; Liu, P.; Zhou, J.; Wong, C. P.; Wang, Z. L., Hydrogenated ZnO core-shell nanocables for flexible supercapacitors and self-powered systems. *ACS Nano* **2013**, *7* (3), 2617-2626.
14. He, Y. B.; Li, G. R.; Wang, Z. L.; Su, C. Y.; Tong, Y. X., Single-crystal ZnO nanorod/amorphous and nanoporous metal oxide shell composites: Controllable electrochemical synthesis and enhanced supercapacitor performances. *Energy Environ. Sci.* **2011**, *4* (4), 1288-1292.
15. Illy, B. N.; Ingham, B.; Toney, M. F.; Nandhakumar, I.; Ryan, M. P., Understanding the selective etching of electrodeposited ZnO nanorods. *Langmuir : the ACS journal of surfaces and colloids* **2014**, *30* (46), 14079-14085.
16. Pruna, A.; Shao, Q.; Kamruzzaman, M.; Zapien, J. A.; Ruotolo, A., Enhanced electrochemical performance of ZnO nanorod core/polypyrrole shell arrays by graphene oxide. *Electrochim. Acta* **2016**, *187*, 517-524.
17. Chen, Y. L.; Hu, Z. A.; Chang, Y. Q.; Wang, H. W.; Zhang, Z. Y.; Yang, Y. Y.; Wu, H. Y., Zinc oxide/reduced graphene oxide composites and electrochemical capacitance enhanced by homogeneous incorporation of reduced graphene oxide sheets in zinc oxide matrix. *J. Phys. Chem. C* **2011**, *115* (5), 2563-2571.
18. Hillman, A. R.; Efimov, I.; Skompska, M., Dynamics of regioregular conducting polymer electrodes in response to electrochemical stimuli. *Faraday Discuss.* **2002**, *121*, 423-439.
19. Levi, M. D.; Daikhin, L.; Aurbach, D.; Presser, V., Quartz crystal microbalance with dissipation monitoring (EQCM-D) for in-situ studies of electrodes for supercapacitors and batteries: A mini-review. *Electrochem. Commun.* **2016**, *67*, 16-21.
20. Bruckenstein, S.; Brzezinska, K.; Hillman, A. R., EQCM studies of polypyrrole films. 1. Exposure to aqueous sodium tosylate solutions under thermodynamically permselective conditions. *Electrochim. Acta* **2000**, *45*, 3801-3811.
21. Levi, M. D.; Salitra, G.; Levy, N.; Aurbach, D.; Maier, J., Application of a quartz-crystal microbalance to measure ionic fluxes in microporous carbons for energy storage. *Nat. Mater.* **2009**, *8* (11), 872-875.
22. Lin, Z.; Taberna, P.-L.; Simon, P., Advanced analytical techniques to characterize materials for electrochemical capacitors. *Curr. Opin. Electrochem.* **2018**, *9*, 18-25.

23. Shpigel, N.; Levi, M. D.; Sigalov, S.; Aurbach, D.; Daikhin, L.; Presser, V., Novel in situ multiharmonic EQCM-D approach to characterize complex carbon pore architectures for capacitive deionization of brackish water. *J. Phys. Condens. Matter* **2016**, *28* (11), 114001.
24. Gabrielli, C.; Garcia-Jareño, J. J.; Keddad, M.; Perrot, H.; Vicente, F., Ac-electrogravimetry study of electroactive thin films. II. Application to polypyrrole. *J. Phys. Chem. B* **2002**, *106*, 3192-3201.
25. Escobar-Teran, F.; Arnau, A.; Garcia, J. V.; Jiménez, Y.; Perrot, H.; Sel, O., Gravimetric and dynamic deconvolution of global EQCM response of carbon nanotube based electrodes by Ac-electrogravimetry. *Electrochem. Commun.* **2016**, *70*, 73-77.
26. Goubaa, H.; Escobar-Teran, F.; Ressam, I.; Gao, W.; El Kadib, A.; Lucas, I. T.; Raihane, M.; Lahcini, M.; Perrot, H.; Sel, O., Dynamic resolution of ion transfer in electrochemically reduced graphene oxides revealed by electrogravimetric impedance. *J. Phys. Chem. C* **2017**, *121* (17), 9370-9380.
27. Arias, C. R.; Debiemme-Chouvy, C.; Gabrielli, C.; Laberty-Robert, C.; Pailleret, A.; Perrot, H.; Sel, O., New insights into pseudocapacitive charge-storage mechanisms in Li-Birnessite type MnO<sub>2</sub> monitored by fast quartz crystal microbalance methods. *J. Phys. Chem. C* **2014**, *118* (46), 26551-26559.
28. Sauerbrey, G., Use of quartz vibrator for weighing thin films on a microbalance. *Z. Phys.* **1959**, *155*, 206-210.
29. Dong, X.; Cao, Y.; Wang, J.; Chan-Park, M. B.; Wang, L.; Huang, W.; Chen, P., Hybrid structure of zinc oxide nanorods and three dimensional graphene foam for supercapacitor and electrochemical sensor applications. *RSC Adv.* **2012**, *2* (10), 4364.
30. Wang, J.; Gao, Z.; Li, Z. S.; Wang, B.; Yan, Y. X.; Liu, Q.; Mann, T.; Zhang, M. L.; Jiang, Z. H., Green synthesis of graphene nanosheets/ZnO composites and electrochemical properties. *J. Solid State Chem.* **2011**, *184* (6), 1421-1427.
31. GAO, W.; Sel, O.; Perrot, H., Electrochemical and viscoelastic evolution of dodecyl sulfate-doped polypyrrole films during electrochemical cycling. *Electrochim. Acta* **2017**, *233*, 262-273.
32. Gabrielli, C.; Garcia-Jareño, J. J.; Perrot, H., Charge compensation process in polypyrrole studied by ac electrogravimetry. *Electrochim. Acta* **2001**, *46* (26), 4095-4103.
33. French, H. M.; Henderson, M. J.; Hillman, A. R.; Vieil, E., Temporal resolution of ion and solvent transfers at nickel hydroxide films exposed to LiOH. *Solid State Ionics* **2002**, *150*, 27-37.
34. French, H. M.; Henderson, M. J.; Hillman, A. R.; Vieil, E., Ion and solvent transfer discrimination at a nickel hydroxide film exposed to LiOH by combined electrochemical quartz crystal microbalance (EQCM) and probe beam deflection (PBD) techniques. *J. Electroanal. Chem.* **2001**, *500*, 192-207.
35. Gonsalves, M.; Hillman, A. R., Effect of time scale on redox-driven ion and solvent transfers at nickel hydroxide films in aqueous lithium hydroxide solutions. *J. Electroanal. Chem.* **1998**, *454*, 183-202.
36. Lee, H. Y.; Goodenough, J. B., Supercapacitor behavior with KCl electrolyte. *J. Solid State Chem.* **1999**, *144*, 220-223.
37. Pang, S. C.; Anderson, M. A.; Chapman, T. W., Novel electrode materials for thin-film ultracapacitors: Comparison of electrochemical properties of sol-gel-derived and electrodeposited manganese dioxide. *J. Electrochem. Soc.* **2000**, *147* (2), 444-450.
38. Toupin, M.; Brousse, T.; Belanger, D., Charge storage mechanism of MnO<sub>2</sub> electrode used in aqueous electrochemical capacitor. *Chem. Mater.* **2004**, *16* (16), 3184-3190.

## **Chapter VI: Reduced graphene oxide-sheltered ZnO nanostructures showing enhanced electrochemical performance revealed by an in situ electrogravimetric study**

This chapter presents the synthesis and characterization of vertically aligned ZnO nanostructures sheltered by electrochemically reduced graphene oxide (ERGO), i.e., ZnO@ERGO, which are directly generated on quartz resonators of microbalance sensors. The vertical orientation of the ZnO nanorods are distinct from the random orientation of the ZnO structures studied in Chapter V and achieved by a two-step synthesis method involving an electrochemically grown seed layer and a subsequent hydrothermal growth. Furthermore, the deposited ERGO thin layer turned out to be highly effective to enhance the electrochemical performances of vertically oriented ZnO nanorods as supercapacitor electrodes. The charge storage mechanism of ZnO@ERGO electrodes with this unique architecture was firstly studied by classical electrochemical quartz crystal microbalance (EQCM), showing a global cation-exchange behavior in Na<sub>2</sub>SO<sub>4</sub> electrolyte. A complementary technique, *ac*-electrogravimetry, was then used to deconvolute the EQCM response into individual contributions from Na<sup>+</sup>·H<sub>2</sub>O, SO<sub>4</sub><sup>2-</sup> and H<sub>2</sub>O molecules, offering a quantitative picture of each participant in the charge balance process with their transfer kinetics.

### **VI.1. Preamble and Objectives**

One dimensional (1D) ZnO nanostructures have been widely studied as supercapacitor (SC) electrodes since they cannot only provide short diffusion path for ions and but also serve as efficient mechanical support for other electroactive materials<sup>1-4</sup>. However, the inferior electrical conductivity of ZnO remains a major obstacle and limits rate capability for high power performance, thus hindering its wide applications in energy storage<sup>5</sup>. The hybridization of carbon materials with ZnO offers the benefits of both the electrical double layer (EDL) capacitance of the carbon materials with large specific surface area (SSA) and the faradaic contribution of the ZnO, thereby optimizing the electrochemical performance of the ZnO-based SCs<sup>6</sup>. Among carbon materials, graphene has spurred significant interest in electrochemical energy storage due to its high SSA, superior electronic conductivity and chemical resilience<sup>7-9</sup>. Therefore, an integration of 1D ZnO

nanostructures and graphene seems to be promising for electrode materials. Though SCs employing ZnO and graphene composites have been extensively investigated, the ionic flux into the electrode, which plays a fundamental role in practical use, has not yet been studied by an in situ approach.

EQCM has developed into a powerful in situ technique to measure ionic fluxes in different electrochemical systems<sup>10-13</sup>, in which not only the current response ( $\Delta I$ ) but also the in situ capturing of global gravimetric change ( $\Delta m$ ) at the electrode/electrolyte interface is tracked during an electrochemical process. Insights into the ionic flux are anticipated through evaluating the average mass per mole of electrons ( $MPE$ ) exchanged between the electrode and the electrolyte<sup>14-16</sup>. To further explore the transfer dynamics and exact identity of each participant during electrochemical process, a non-conventional complementary technique, *ac*-electrogravimetry, was proposed. A kinetic and gravimetric deconvolution of the EQCM response has been attained by coupling electrochemical impedance spectroscopy (EIS) with a fast QCM, which generates both the classical EIS transfer function (TF),  $\frac{\Delta E}{\Delta I}(\omega)$  and the mass/potential TF,  $\frac{\Delta m}{\Delta E}(\omega)$ . Then, these TFs are fitted with an appropriate model to scrutinize the identity of the species involved in the charge transfer mechanism, along with the kinetics and the relative concentration changes associated with each species<sup>17-19</sup>.

Herein, a thin ERGO sheltering incorporated onto 1D ZnO nanorods (ZnO@ERGO) was prepared as the electrode, showing an advancement in the synthesis of novel nanostructured electrode materials for supercapacitors. The electrochemical processes involved in the ZnO@ERGO electrode were investigated by a complementary methodology comprising EQCM and *ac*-electrogravimetry. Electroacoustic study has not been conducted assuming that the ZnO structures are rigid and the ERGO constituted of only a few layers, can be considered acoustically thin enough.

## V.2. Experimental Methods and Theoretical Background

### VI.2.1. Synthesis of ZnO seed layer

As schematically shown in **Figure VI.1a**, a ZnO seed layer was firstly electrodeposited on the surface of a gold coated quartz resonator (9 MHz-AWS, Valencia, Spain) under polarization at -1.0 V vs. Ag/AgCl (3 M KCl saturated with AgCl) for 15 s in a solution of 5 mM Zn(NO<sub>3</sub>)<sub>2</sub>·6H<sub>2</sub>O (98%, Sigma-Aldrich) and 0.1 M KCl, which is held at 80 °C.

### VI.2.2. Synthesis of ZnO nanostructures

The vertically aligned ZnO nanostructures were synthesized by a hydrothermal process (**Figure VI.1a**). A precursor solution was prepared with 0.01 M  $\text{Zn}(\text{NO}_3)_2 \cdot 6\text{H}_2\text{O}$  and 0.01 M hexamethylenetetramine (HMTA; 99%, Sigma-Aldrich) and then, transferred to a Teflon-lined stainless steel autoclave. The ZnO-seeded quartz resonator was immersed into the precursor solution. After that, the autoclave was maintained at 120 °C for 4 h and then, cooled down to room temperature naturally. After the hydrothermal growth, ZnO nanostructures generated on the resonator were rinsed several times with bi-distilled water.

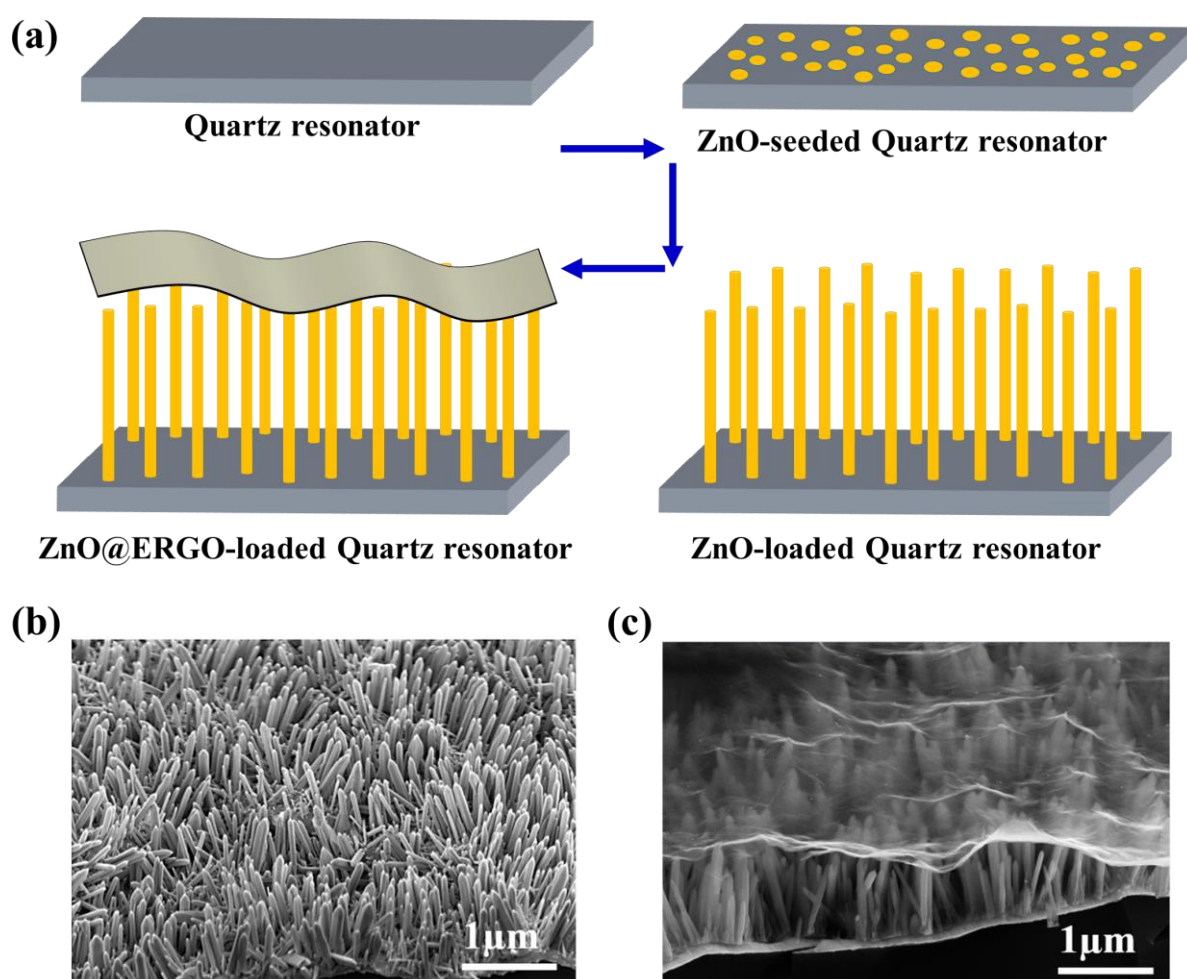


**Figure VI.1.** Schematic representation of synthetic process for ZnO@ERGO composites (a) and FEG-SEM images of ZnO nanostructures (b) and ZnO@ERGO composites (c) synthesized on the gold electrode of the quartz resonator.

### VI.2.3. Preparation procedures for ZnO@ERGO electrode

GO was synthesized via a modified Hummers method<sup>20</sup>. GO suspension of 1 mg/mL was

prepared by adding GO powder into bi-distilled water followed by 5 h of sonication. Then ~ 10  $\mu\text{L}$  of the GO suspension was deposited on the ZnO-loaded gold electrode ( $0.2\text{ cm}^2$ ) of the quartz resonator by a lab-made mask, which ensures the only exposure of the gold electrode. After dried at  $70\text{ }^\circ\text{C}$  in an oven for 30 min, GO thin film deposited on ZnO nanostructures (ZnO@GO) was generated. Subsequently, GO film was electrochemically reduced using the same three electrode configuration as described for the electrodeposition of ZnO seed layer. The reduction of the GO film deposited on the ZnO (ZnO@ERGO) was realized by chronoamperometry with a Biologic SP-200 potentiostat using EC-Lab software at  $-0.9\text{ V vs. Ag/AgCl}$  for 10 min in a solution of  $0.5\text{ M NaNO}_3$ . Nitrogen gas was bubbled in the solution prior to the electrochemical reduction and was maintained over the solution until the end of the reduction to ensure a complete saturation in  $\text{NaNO}_3$  solution.

### VI.2.4. Morphological observation of the electrode

The morphologies of the electrogenerated ZnO- and ZnO@ERGO-loaded electrodes were observed under vacuum conditions using a field emission gun scanning electron microscope (FEG-SEM, Zeiss, Supra 55).

### VI.2.5. Complementary electrogravimetric characterizations (EQCM and ac-electrogravimetry)

EQCM tests were conducted by coupling cyclic voltammetry (CV) and galvanostatic charge/discharge (GCD) with QCM to track the simultaneous microbalance frequency changes of the electrode during cycling. Both EQCM and *ac*-electrogravimetry measurements were performed in  $0.25\text{ M Na}_2\text{SO}_4$  under nitrogen atmosphere, where a ZnO- or ZnO@ERGO-loaded quartz resonator was used as the working electrode, Ag/AgCl (3 M KCl saturated with AgCl) as the reference electrode and a platinum grid as the counter electrode. The potential window for EQCM was confined between  $-0.6\text{ V}$  and  $0.6\text{ V vs. Ag/AgCl}$ . The mass change ( $\Delta m$ ) of the electrode during electrochemical process can be estimated by the microbalance frequency change ( $\Delta f$ ) through Sauerbrey equation<sup>21</sup>, i.e.,  $\Delta f = -C_f \times \Delta m$ , where  $C_f$  is the experimental sensitivity factor of the quartz crystal resonator ( $C_f = 16.3 \times 10^7\text{ Hz.g}^{-1}.\text{cm}^2$ )<sup>18</sup>.

*Ac*-electrogravimetry measurements were performed in dynamic regime, where the frequency range was between 63 KHz and 10 mHz (for details, see Ref.<sup>17, 19</sup>). Two important experimental TFs,

$\frac{\Delta q}{\Delta E}(\omega)$  and  $\frac{\Delta m}{\Delta E}(\omega)$  can be obtained simultaneously and fitted through the following

theoretical expressions at a given potential and frequency modulation,  $f$  (pulsation  $\omega=2\pi f$ )<sup>22</sup>.

$$\frac{\Delta C_i}{\Delta E}(\omega) = \frac{-G_i}{j\omega d_f + K_i} \quad (\text{VI.1})$$

$$\frac{\Delta q}{\Delta E}(\omega) = Fd_f \sum_i \frac{G_i}{j\omega d_f + K_i} \quad (i: \text{ions}) \quad (\text{VI.2})$$

$$\frac{\Delta m}{\Delta E}(\omega) = -d_f \sum_i M_i \frac{G_i}{j\omega d_f + K_i} \quad (i: \text{ions and non-charged species}) \quad (\text{VI.3})$$

$$\frac{\Delta C_i}{\Delta E}(\omega) = \frac{-G_i}{K_i} \quad (\text{if } \omega \rightarrow 0) \quad (\text{VI.4})$$

where  $\Delta C_i$  presents concentration variation for each species in the film,  $\omega$  is the pulsation,  $d_f$  is the film thickness,  $F$  is the Faraday constant,  $M_i$  depicts the molar mass of involved species,  $K_i$  and  $G_i$  are the partial derivatives of the ionic/free solvent flux ( $J_i$ ) with respect to the concentration and the potential, respectively.  $K_i$  represents the transfer kinetics of each species while  $G_i$  is the reciprocal of the transfer resistance ( $Rt_i = \frac{1}{FG_i}$ ), exhibiting the ease or difficulty in the species transfer at the film/electrolyte interface (more details about *ac*-electrogravimetry are given in Chapter II).

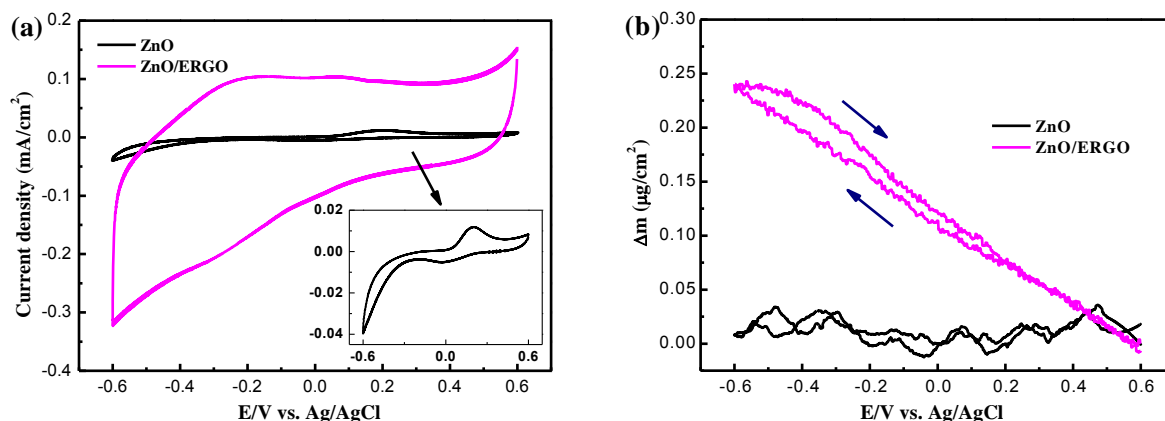
### VI.3. Results and Discussion

The synthesis of ZnO@ERGO nanocomposite is schematically illustrated in **Figure VI.1a**, which was performed on the surface of quartz resonator for the first time. **Figure VI.1b** and **c** show the morphologies of ZnO nanostructures, exhibiting vertically aligned individual nanorods with a length of ~800 nm. A transparent thin ERGO layer on the top of ZnO nanostructures is clearly observed in **Figure VI.1c**. This unique architecture is anticipated to provide the benefits of both EDL capacitance of the ERGO layers and faradaic reaction of the ZnO. Additionally, both the upper and lower surfaces of ERGO layer are accessible to electrolyte, offering a higher SSA for the electrochemical processes.

**Figure VI.2a** displays the CV curves of vertically aligned ZnO nanostructures and ZnO@ERGO composites. Their simultaneous mass responses converted from the frequency changes of QCM are shown in **Figure VI.2b**. It is noted that the current responses of the vertically

aligned and randomly oriented ZnO nanostructures (See **Figure V.2** in Chapter V) are in the same order of magnitude. The modest current response of the both ZnO nanostructures, probably due to the inferior conductivity is envisaged to be improved with a composite approach. A current surge is observed after a thin ERGO layer incorporated onto the vertically aligned ZnO nanostructures. Thereafter, the electrochemical/electrogravimetric behaviors of vertically aligned ZnO and ZnO@ERGO composites are discussed in a comparative manner.

The deviation of rectangular shape of typical EDL is ascribed to pseudocapacitive behaviors of ZnO nanorods<sup>6</sup> and the residual oxygen functionalities on ERGO nanosheets<sup>23</sup>. Unlike the negligible mass variation of ZnO nanostructures (**Figure VI.2b**), the ZnO@ERGO composites present a mass ingress around  $0.25 \mu\text{g}\cdot\text{cm}^{-2}$  during cathodic scan and highly reversible egress during anodic scan, implying a cation-exchange behavior at the electrode surface. GCD measurements were performed to further explore the electrochemical properties of ZnO- and ZnO@ERGO-loaded electrodes (**Figure VI.2c** and **d**). The non-linear charge/discharge curves of both electrodes further evidence their pseudocapacitive behaviors, which are different from the triangular shape of pure EDL device<sup>23</sup>. Apparently,  $E-t$  curves of ZnO@ERGO-loaded electrode (**Figure VI.2d**, the upper panel) is substantially prolonged over that of ZnO-loaded electrode (**Figure VI.2c**, the upper panel) at each current density, showing markedly improved electrochemical performance. Furthermore, the  $m-t$  response of ZnO@ERGO-loaded electrode (**Figure VI.2d**, the down panel) proceeds in an inversely-proportional pace with respect to potential-time response, i.e., mass decrease during charging and increase during discharging, indicative of cation participation in charge balance. Interestingly, almost the same amount of mass is exchanged ( $0.26 \mu\text{g}\cdot\text{cm}^{-2}$ ) at different current densities during a charge/discharge process compared to that in a CV cycle, demonstrating the highly reversible charge storage behavior.



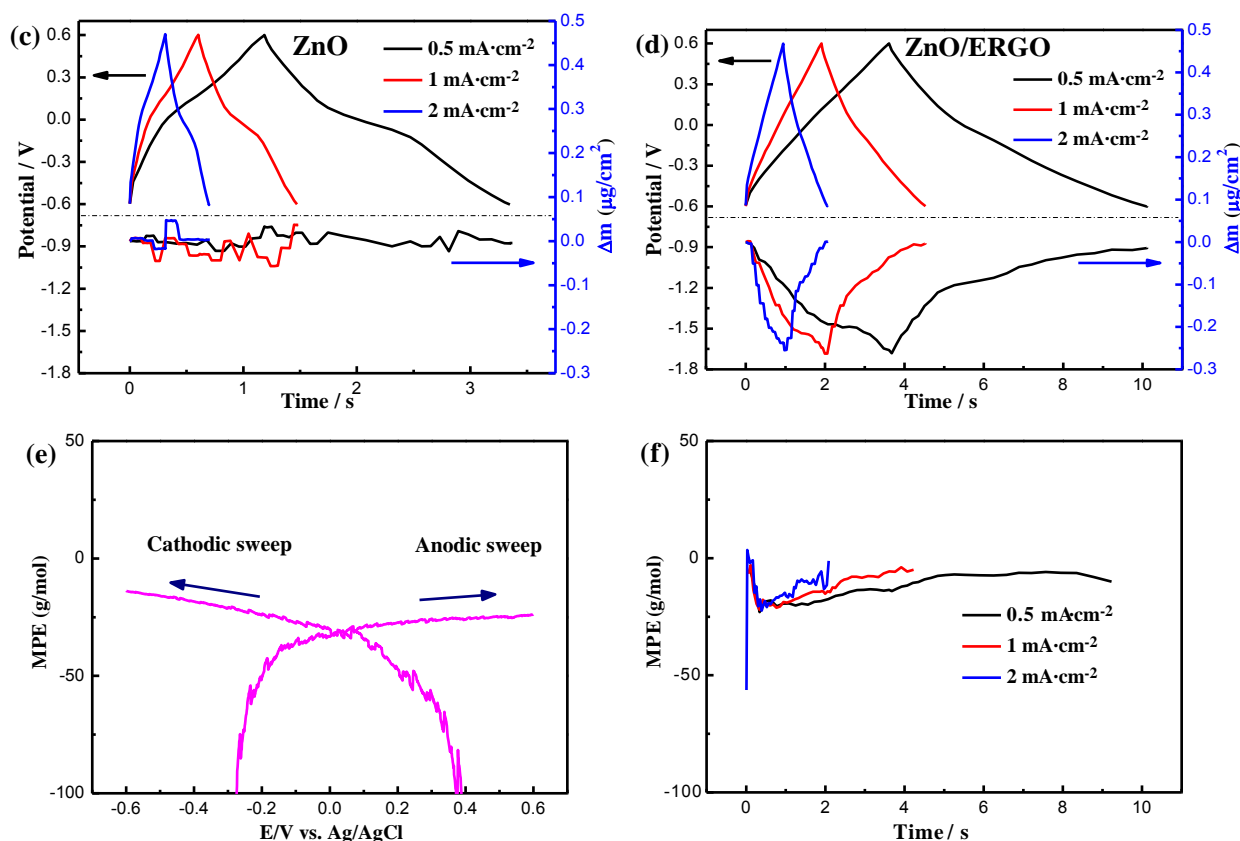


**Figure VI.2.** CV curves at  $100 \text{ mV}\cdot\text{s}^{-1}$  (a, b) and GCD curves at 0.5, 1 and  $2 \text{ mA}\cdot\text{cm}^{-2}$  (c, d) in  $0.25 \text{ M Na}_2\text{SO}_4$  solution; (e) and (f) are the corresponding *MPE* of ZnO@ERGO-loaded electrode calculated from a CV and GCD cycle, respectively.

The  $MPE = F\Delta m/\Delta q$  calculated from the EQCM data can provide indications of the nature of transferred species during cycling. If only one species is involved in the charge storage process, the value of *MPE* would be its molar mass. The cation and anion contributions lead to the negative and positive signs of *MPE* values, respectively<sup>22</sup>. **Figure VI.2e** and **f** compare the *MPE* of species involved in a CV and GCD cycle, presenting a value ranging from  $-25$  to  $-15 \text{ g}\cdot\text{mol}^{-1}$ , respectively. From these two values,  $\text{Na}^+$ , with a *MPE* of  $-23 \text{ g}\cdot\text{mol}^{-1}$ , seems to be the main charge carrier during electrochemical processes, but this deviation between the experimental and theoretical *MPE* values merits special analysis. The potential-dependent and time-dependent behaviors of *MPE* value in CV and GCD demonstrate a multi-species transfer and complex interfacial behavior, which, however, cannot be interpreted by conventional EQCM analysis based on Faraday's law. In such cases, sophisticated models, i.e., Donnan-type electrical double layer were applied to identify various species intervening in the charge compensation<sup>16</sup>. Yet, the analysis in transfer kinetics of involved species still remains challenging since the measurements are performed at a certain scan rate (in CV)

or current density (in GCD). Hence, from both gravimetric and kinetic point of view, the *ac*-electrogravimetry was alternatively suggested to get a deeper insight into the charge compensation behavior occurring in the ZnO@ERGO electrode.

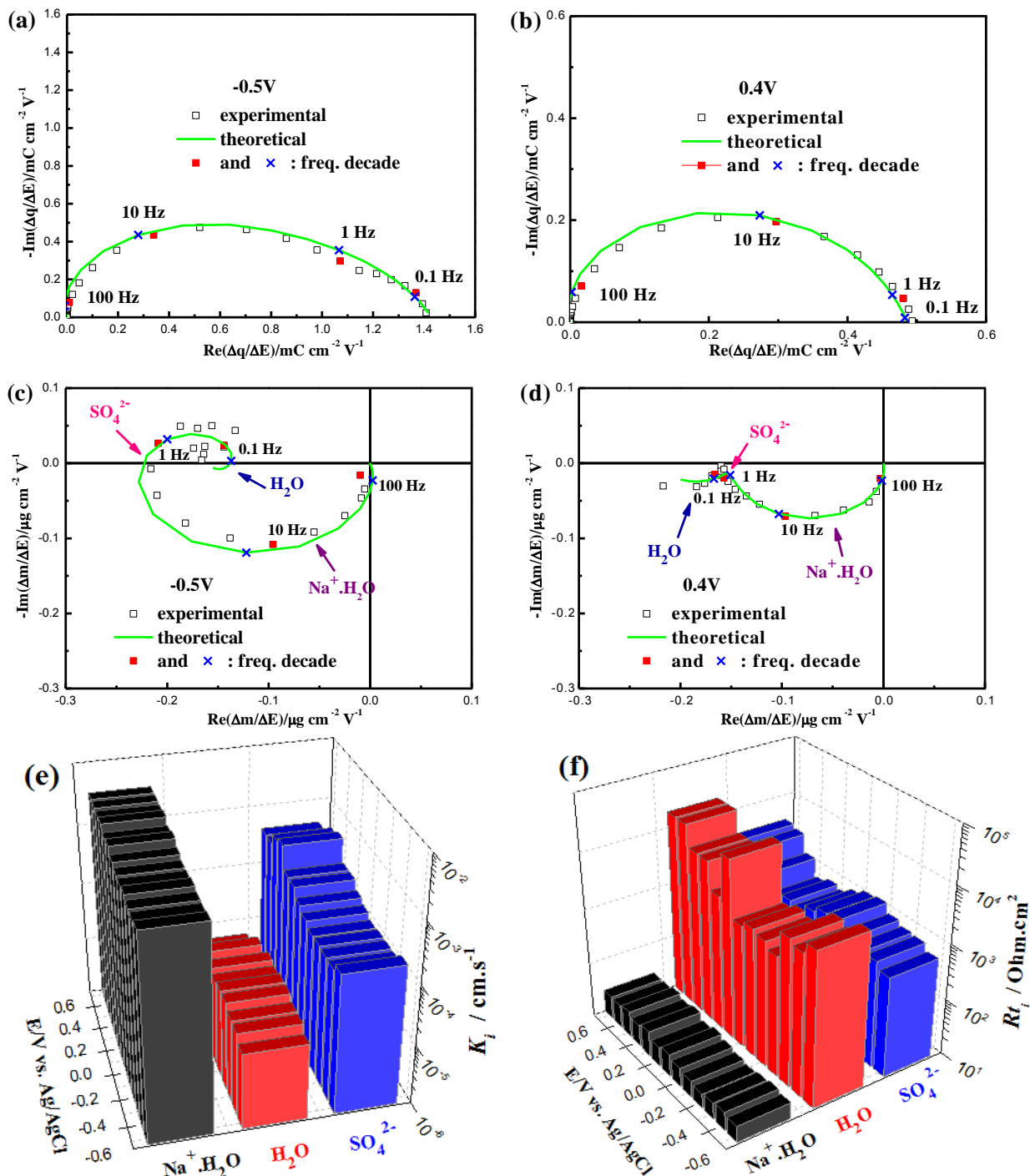


**Figure VI.3.**  $\frac{\Delta q}{\Delta E}(\omega)$  (a and b) and  $\frac{\Delta m}{\Delta E}(\omega)$  (c and d) transfer functions at -0.5V and 0.4V vs. Ag/AgCl. Transfer kinetics,  $K_i$  ( $\text{cm}\cdot\text{s}^{-1}$ ) (e) and transfer resistances,  $R_{t_i}$  ( $\Omega\cdot\text{cm}^2$ ) (f) for each species

participating in charge balance.

*Ac*-electrogravimetry measurements were conducted at various states-of-polarization from -0.6 V to 0.6 V vs. Ag/AgCl with an interval of 100 mV. This range corresponds exactly to that used in the EQCM measurements. Compared to  $\frac{\Delta q}{\Delta E}(\omega)$  TF, only considering the ionic species transfer, the  $\frac{\Delta m}{\Delta E}(\omega)$  TF also takes the free solvent contribution into account. The experimental data were fitted using theoretical functions in **Equations VI.2** and **VI.3**, where a configuration involving the transfer of hydrated cations ( $\text{Na}^+\cdot\text{H}_2\text{O}$ ), anions ( $\text{SO}_4^{2-}$ ) and free  $\text{H}_2\text{O}$  molecules is proposed at all potentials to achieve a good agreement for both  $\frac{\Delta q}{\Delta E}(\omega)$  and  $\frac{\Delta m}{\Delta E}(\omega)$  TFs, between experimental and theoretical data. **Figure VI.3a-d** display the  $\frac{\Delta q}{\Delta E}(\omega)$  and  $\frac{\Delta m}{\Delta E}(\omega)$  TFs at selective potentials of 0.4 V and -0.5 V vs. Ag/AgCl (one in the cathodic and another in the anodic part). At both potentials,  $\text{Na}^+\cdot\text{H}_2\text{O}$  cations were identified at high frequencies (HFs), followed by the transfer of  $\text{SO}_4^{2-}$ . Lastly,  $\text{H}_2\text{O}$  molecules were exchanged at low frequencies (LFs), exhibiting the opposite flux direction to anions. The transfer kinetics ( $K_i$ ) and resistances ( $R_{ti}$ ) for each species estimated at all potentials are summarized in **Figure VI.3e** and **f**.  $\text{Na}^+\cdot\text{H}_2\text{O}$  persists in presenting a higher transfer kinetics than its anionic counterpart ( $\text{SO}_4^{2-}$ ) transferred in charge balance. The transfer of the hydrated cationic species and the hydration number found here is in line with the cosmotropic-type behavior of  $\text{Na}^+$  as described in the work of Levi and co-workers<sup>24-25</sup>.  $\text{H}_2\text{O}$  molecules are exchanged at the lowest kinetics rate, which is ascribed to their highest transfer resistance, i.e.,  $R_t(\text{H}_2\text{O}) > R_t(\text{SO}_4^{2-}) > R_t(\text{Na}^+\cdot\text{H}_2\text{O})$ . According to the aforementioned discussion, it is speculated that the insertion of  $\text{SO}_4^{2-}$  anions could push out the water molecules trapped between ERGO layers due to the volume-exclusion effect and hence, result in the response from free  $\text{H}_2\text{O}$  molecules at LFs, which is also verified by other ions with a low charge-per-size ratio<sup>24-25</sup>.

To further shed light on the multi-species contribution to the charge storage in ZnO@ERGO electrode, an approach benefiting from the complementarity of the EQCM and *ac*-electrogravimetry is proposed. Specifically, the relative concentration changes for each species (**Figure VI.4a**) can be estimated by integration of **Equation VI.4**, which can be transformed into corresponding mass variations (**Figure VI.4b**). Then, the gravimetric reconstruction is obtained by the addition of

individual mass contributions from all species concerned in *ac*-electrogravimetry (Figure VI.4c). A good agreement between  $\Delta m_{(\text{global})}$  measured with EQCM and reconstructed  $\Delta m$  from *ac*-electrogravimetry is achieved (Figure VI.4d). It evidences the complementarity of the EQCM and *ac*-electrogravimetry: the former can provide a global response of species transfer, which can be deconvoluted into individual contribution of each species together with their dynamics of transfer by the latter.

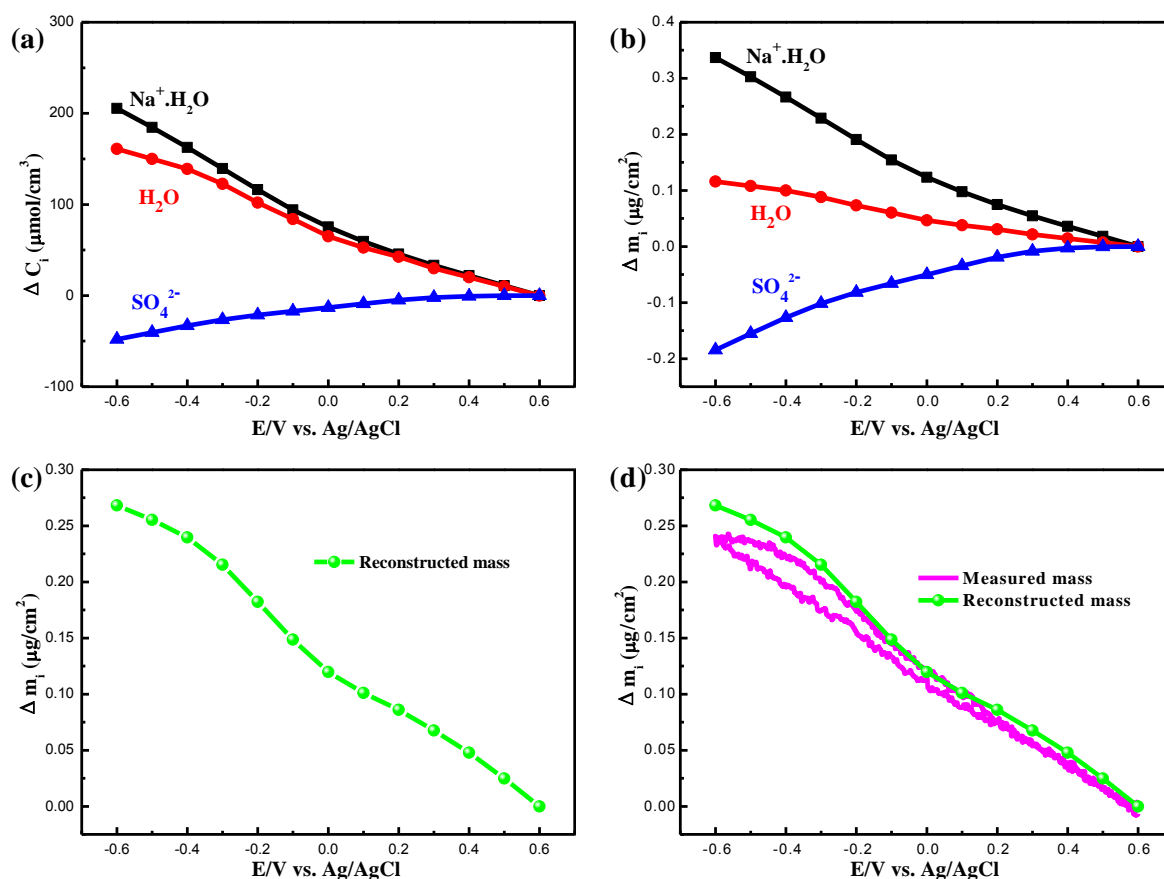


**Figure VI.4.** Relative concentration change (a) and the corresponding mass change (b) of each species as a function of potential; mass variation reconstructed from *ac*-electrogravimetry (c) and the comparison of mass variations obtained from EQCM and *ac*-electrogravimetry (d).

## VI.4. Conclusions

The ZnO@ERGO nanocomposites were successfully synthesized on the gold coated quartz resonators. A thin ERGO sheltering onto ZnO nanostructures noticeably enhanced the electrochemical performance of the pristine ZnO electrode. The charge storage mechanism of the ZnO@ERGO supercapacitor electrode was scrutinized via complementary electrogravimetric

## **Chapter VI: Metal oxide/Carbon based composite electrodes - an electrogravimetric study**

---

methods, EQCM and *ac*-electrogravimetry. The nanocomposite exhibits a global cation-exchange behavior for energy storage according to EQCM, which is actually resulted from the addition of a multi-species contribution revealed by *ac*-electrogravimetry. Compared with its anionic counterpart ( $\text{SO}_4^{2-}$ ),  $\text{Na}^+\cdot\text{H}_2\text{O}$  with a higher transfer kinetics plays a major role in charge storage.

### References

1. Bae, J.; Song, M. K.; Park, Y. J.; Kim, J. M.; Liu, M.; Wang, Z. L., Fiber supercapacitors made of nanowire-fiber hybrid structures for wearable/flexible energy storage. *Angew. Chem. Int. Ed.* **2011**, *50* (7), 1683-1687.
2. He, Y. B.; Li, G. R.; Wang, Z. L.; Su, C. Y.; Tong, Y. X., Single-crystal ZnO nanorod/amorphous and nanoporous metal oxide shell composites: Controllable electrochemical synthesis and enhanced supercapacitor performances. *Energy Environ. Sci.* **2011**, *4* (4), 1288-1292.
3. Yang, P.; Xiao, X.; Li, Y.; Ding, Y.; Qiang, P.; Tan, X.; Mai, W.; Lin, Z.; Wu, W.; Li, T.; Jin, H.; Liu, P.; Zhou, J.; Wong, C. P.; Wang, Z. L., Hydrogenated ZnO core-shell nanocables for flexible supercapacitors and self-powered systems. *ACS Nano* **2013**, *7* (3), 2617-2626.
4. Pruna, A.; Shao, Q.; Kamruzzaman, M.; Zapien, J. A.; Ruotolo, A., Enhanced electrochemical performance of ZnO nanorod core/polypyrrole shell arrays by graphene oxide. *Electrochim. Acta* **2016**, *187*, 517-524.
5. Li, Z.; Liu, P.; Yun, G.; Shi, K.; Lv, X.; Li, K.; Xing, J.; Yang, B., 3D (Three-dimensional) sandwich-structured of ZnO (zinc oxide)/rGO (reduced graphene oxide)/ZnO for high performance supercapacitors. *Energy* **2014**, *69*, 266-271.
6. Chen, Y. L.; Hu, Z. A.; Chang, Y. Q.; Wang, H. W.; Zhang, Z. Y.; Yang, Y. Y.; Wu, H. Y., Zinc oxide/reduced graphene oxide composites and electrochemical capacitance enhanced by homogeneous incorporation of reduced graphene oxide sheets in zinc oxide matrix. *J. Phys. Chem. C* **2011**, *115* (5), 2563-2571.
7. Stoller, M. D.; Park, S. J.; Zhu, Y. W.; An, J. H.; Ruoff, R. S., Graphene-based ultracapacitors. *Nano Lett.* **2008**, *8* (10), 3498-3502.
8. El-Kady, M. F.; Strong, V.; Dubin, S.; Kaner, R. B., Laser scribing of high-performance and flexible graphene-based electrochemical capacitors. *Science* **2012**, *335* (6074), 1326-1330.
9. Wang, S.; Liu, N.; Su, J.; Li, L.; Long, F.; Zou, Z.; Jiang, X.; Gao, Y., Highly stretchable and self-healable supercapacitor with reduced graphene oxide based fiber springs. *ACS Nano* **2017**, *11* (2), 2066-2074.
10. Gabrielli, C.; Garcia-Jareño, J. J.; Perrot, H., Charge compensation process in polypyrrole studied by ac electrogravimetry. *Electrochim. Acta* **2001**, *46* (26), 4095-4103.
11. Hillman, A. R.; Efimov, I.; Skompska, M., Dynamics of regioregular conducting polymer electrodes in response to electrochemical stimuli. *Faraday Discuss.* **2002**, *121*, 423-439.
12. Levi, M. D.; Salitra, G.; Levy, N.; Aurbach, D.; Maier, J., Application of a quartz-crystal microbalance to measure ionic fluxes in microporous carbons for energy storage. *Nat. Mater.* **2009**, *8* (11), 872-875.
13. Tsai, W. Y.; Taberna, P. L.; Simon, P., Electrochemical quartz crystal microbalance (EQCM) study of ion dynamics in nanoporous carbons. *J. Am. Chem. Soc.* **2014**, *136* (24), 8722-8728.
14. Arias, C. R.; Debiemme-Chouvy, C.; Gabrielli, C.; Laberty-Robert, C.; Pailleret, A.; Perrot, H.; Sel, O., New insights into pseudocapacitive charge-storage mechanisms in Li-Birnessite type MnO<sub>2</sub> monitored by fast quartz crystal microbalance methods. *J. Phys. Chem. C* **2014**, *118* (46), 26551-26559.
15. L   T.; Aradilla, D.; Bidan, G.; Billon, F.; Delaunay, M.; G  rard, J. M.; Perrot, H.; Sel, O., Unveiling the ionic exchange mechanisms in vertically-oriented graphene nanosheet supercapacitor electrodes with electrochemical quartz crystal microbalance and ac-electrogravimetry. *Electrochem. Commun.* **2018**, *93*, 5-9.
16. Shpigel, N.; Levi, M. D.; Sigalov, S.; Aurbach, D.; Daikhin, L.; Presser, V., Novel in situ multiharmonic EQCM-D approach to characterize complex carbon pore architectures for capacitive deionization of brackish water. *J. Phys. Condens. Matter* **2016**, *28* (11), 114001.
17. Gabrielli, C.; Garcia-Jareno, J. J.; Keddad, M.; Perrot, H.; Vicente, F., Ac-electrogravimetry study of electroactive thin films. II. Application to polypyrrole. *J. Phys. Chem. B* **2002**, *106*, 3192-3201.
18. Escobar-Teran, F.; Arnau, A.; Garcia, J. V.; Jim  nez, Y.; Perrot, H.; Sel, O., Gravimetric and dynamic deconvolution of global EQCM response of carbon nanotube based electrodes by Ac-electrogravimetry. *Electrochem. Commun.* **2016**, *70*, 73-77.
19. Goubaa, H.; Escobar-Teran, F.; Ressam, I.; Gao, W.; El Kadib, A.; Lucas, I. T.; Raihane, M.; Lahcini, M.; Perrot, H.; Sel, O., Dynamic resolution of ion transfer in electrochemically reduced graphene oxides revealed by electrogravimetric impedance. *J. Phys. Chem. C* **2017**, *121* (17), 9370-9380.

## Chapter VI: Metal oxide/Carbon based composite electrodes - an electrogravimetric study

---

20. Hummers, W. S. J.; Offeman, R. E., Preparation of graphitic oxide. *J. Am. Chem. Soc.* **1958**, *80* (1339).
21. Sauerbrey, G., Use of quartz vibrator for weighing thin films on a microbalance. *Z. Phys.* **1959**, *155*, 206-210.
22. GAO, W.; Sel, O.; Perrot, H., Electrochemical and viscoelastic evolution of dodecyl sulfate-doped polypyrrole films during electrochemical cycling. *Electrochim. Acta* **2017**, *233*, 262-273.
23. Xu, B.; Yue, S.; Sui, Z.; Zhang, X.; Hou, S.; Cao, G.; Yang, Y., What is the choice for supercapacitors: graphene or graphene oxide? *Energy Environ. Sci.* **2011**, *4* (8), 2826.
24. Shpigel, N.; Levi, M. D.; Sigalov, S.; Mathis, T. S.; Gogotsi, Y.; Aurbach, D., Direct assessment of nanoconfined water in 2D  $\text{Ti}_3\text{C}_2$  electrode interspaces by a surface acoustic technique. *J. Am. Chem. Soc.* **2018**, *140* (28), 8910-8917.
25. Levi, M. D.; Sigalov, S.; Salitra, G.; Elazari, R.; Aurbach, D., Assessing the solvation numbers of electrolytic ions confined in carbon nanopores under dynamic charging conditions. *J. Phys. Chem. Lett.* **2011**, *2* (2), 120-4.

## General Conclusions

The individual conclusions on each aspect carried out in this thesis are given in the conclusion section at the end of preceding chapters. Here, conclusions that have been generalized based on this thesis are highlighted as below:

### ***Complementarity of the electrogravimetric and electroacoustic methods***

Combining EQCM and *ac*-electrogravimetry is demonstrated as a powerful in situ methodology to analyze species' transfer behavior in different electrochemical systems which is of particular interest for energy storage, as discussed from Chapter III to VI. EQCM provides a global species-transfer response during electrochemical process, while its complementary counterpart, i.e., *ac*-electrogravimetry, offers a quantitative picture of each participant in charge balance with their transfer kinetics. The systems studied in Chapters V and VI constitute examples further highlighting the complementarity between EQCM and *ac*-electrogravimetry, the limitations of either of which can be compensated by the other to unveil the subtleties of the charge storage mechanisms. It is also the first time where a parallel and comparative study is done systematically by using the two approaches for each system considered. Additionally, the electrode's viscoelastic properties can be tracked through the electroacoustic impedance measurements, as described in Chapters III and IV. Therefore, the use of this combined methodology involving EQCM, *ac*-electrogravimetry and electroacoustic impedance measurements paves the way to understand the charge storage mechanism and the relationship between electrode's electrochemical and mechanical properties, facilitating the fabrication of highly efficient SC electrodes with superior cyclability. Overall, the beneficial aspects of the QCM and its satellite electrochemical/electroacoustic methods are consolidated during this thesis by extending them to characterize sophisticated materials in terms of composition and morphology: they are achieved by adapting the materials synthesis methods to be realized directly on QCM resonators.

### ***Ion-selective behavior of electrode materials in charge storage***

Ionic flux into electrode materials plays a fundamental role in energy storage systems like

supercapacitors. Obvious ion-selective behaviors in charge storage were observed in PPy- and ERGO-based electrodes, as discussed in Chapters III and IV. Specifically, for fresh and slightly cycled PPy-based electrodes, cations are mainly exchanged at the electrode/electrolyte interface for charge balance while anions turn out to be the major charge carrier for aged electrodes. As for ERGO-based electrode with a high amount of oxygen functionalities, anions play a major role for the charge compensation, which, however, is replaced by cations with the progressive removal of oxygen functionalities on its layers related to an electrochemical reduction reaction. Especially, the work on ERGO thin films is an example showing that ion-exchange behavior can be tuned by a careful modification of the surface functional properties which was monitored by electrogravimetric methods.

### ***Desolvation of hydrated cations***

It was demonstrated that the hydrated cations were capable of participating in the charge storage after a (partial) desolvation. In PPy-based electrodes, the hydrated cations ( $\text{Na}^+ \cdot 2\text{H}_2\text{O}$ ) gradually remove their hydration shell for charge compensation at  $-0.6 \text{ V vs. SCE}$  during film aging process in NaCl media, as discussed in Chapter III. This effect is also correlated to an increase of the PPy-film rigidity which prevents the large solvated cations from entering the material. In a similar manner, the removal of oxygen functionalities on ERGO layers leads to a dehydration process of exchanged cations (i.e., from  $\text{Na}^+ \cdot 2\text{H}_2\text{O}$  to  $\text{Na}^+ \cdot \text{H}_2\text{O}$ ), which also exhibits potential-dependent behavior for ERGO-2 electrode as discussed in Chapter IV.

### ***The indirect role of free H<sub>2</sub>O in charge storage***

Although the ionic flux is essential in charge balance, the accompanied exchange of free H<sub>2</sub>O still plays a non-negligible role, which is revealed in PPy-, ERGO-, ZnO- and ZnO@ERGO-based electrodes (discussed in Chapters III, IV, V and VI, respectively). For PPy-based electrode, a higher amount of H<sub>2</sub>O insertion at more cathodic potential leads to a swollen state of the electrode, facilitating the transfer of bigger ions, such as  $\text{Na}^+ \cdot 2\text{H}_2\text{O}$  and  $\text{DS}^-$  as discussed in Chapter III; for ERGO-based electrode, the H<sub>2</sub>O exchanged often plays an important role in electrode's viscoelasticity through plasticizing effect (discussed in Chapter IV); free H<sub>2</sub>O presents a sluggish transfer behavior in both ZnO- and ZnO@ERGO-based electrodes (discussed in Chapter V and VI, respectively), which is believed to be electrodragged by ions or caused by the dimensional

confinement of the electrode.

### ***Viscoelastic effects on charge storage***

Viscoelastic changes of electrodes caused by periodical ion electroadsorption/electrodesorption and/or insertion/extraction play an important role in charge storage. As discussed in Chapter III, the charge storage capability of PPy-based electrode is gradually faded due to the increasing rigidity of the PPy film, which prohibits not only the ions' transfer between electrode/electrolyte interface but also the transport in PPy bulk; in ERGO-based electrode, oxygen functionalities could modify the interactions between graphene layers. The electrode viscoelastic and electrochemical performances can be tuned through adjusting the content of the hetero-oxygen groups on its layers: increased flexibility of the electrode allows for a higher amount of ions exchanged, leading to an enhancement of specific capacitance.

## Résumé de la Thèse en Français

### Études électrochimiques et électromécaniques d'électrodes nanostructurées pour supercondensateurs

Les supercondensateurs (SCs) sont une classe de dispositifs de stockage d'énergie électrochimique bien adaptés au stockage et à la libération rapide de cette énergie. L'étude du flux d'espèces à l'interface d'électrodes/électrolyte est un point essentiel pour améliorer les performances de ces supercondensateurs. Cette thèse explore de manière très approfondie, et avec une combinaison d'outils originaux, le transfert d'espèces dans les mécanismes de stockage de charge au sein de matériaux d'électrodes de supercondensateurs couramment utilisés, comme les polymères conducteurs, les matériaux carbonés ou les oxydes de métaux de transition. De plus, l'évolution mécanique de certaines électrodes ont également été étudiées afin de mettre en lumière la corrélation entre les évolutions électrochimiques et viscoélastiques de ces films à l'origine des SCs.

Dans cette thèse, des films de polypyrrole dopés au dodécylsulfate de sodium (PPy-DS), des films d'oxyde de graphène réduit électrochimiquement (ERGO) et des films nanostructurés de ZnO ont été synthétisés comme représentatifs des électrodes conductrices à base de polymère, de carbone et d'oxyde métallique, respectivement. Pour atteindre l'objectif de recherche mentionné ci-dessus, une méthodologie combinée impliquant la microbalance à quartz électrochimique (EQCM), l'électrogravimétrie à courant alternatif (*ac*-électrogravimétrie) et les mesures d'impédance électroacoustique a été adoptée. Plus précisément, l'EQCM est utilisé pour une visualisation *in situ* du transfert global des espèces à l'interface électrode/électrolyte, alors que son homologue l'*ac*-électrogravimétrie contribue à décrire les subtilités du processus global de compensation de charge impliquant plusieurs espèces. Elle offre une image quantitative de chaque participant avec leur cinétique de transfert et une identification par leurs masses molaires. Par conséquent, le couplage de l'EQCM avec l'*ac*-électrogravimétrie fournit un puissant outil pour dévoiler les subtilités des mécanismes de stockage de charge au sein de l'électrode pendant le processus électrochimique. De plus, l'évolution viscoélastique de ces films peut être suivie grâce aux mesures

d'impédance électroacoustique. Par conséquent, l'utilisation de cette méthodologie combinée ouvre la voie à la compréhension du mécanisme de stockage de charge et de la relation entre les propriétés électrochimiques et mécaniques des électrodes, facilitant la fabrication d'électrodes SC hautement efficaces avec une éventuelle cyclabilité supérieure.

En ce qui concerne les électrodes à base de polymères, le défi le plus important est la stabilité lors de cycles successifs. En conséquence, après avoir présenté l'état de l'art sur SCs dans le chapitre I et les méthodes expérimentales générales dans le chapitre II, le chapitre III décrit la corrélation entre les variations électrochimiques et viscoélastiques d'un film de PPy-DS pendant des cycles successifs. Les phénomènes d'adsorption ionique et les changements viscoélastiques des films d'ERGO avec différents teneurs en oxygène sont présentés dans le chapitre IV. Les comportements de transfert de charge interfacial du ZnO et de son composite ZnO/ERGO sont examinés dans les chapitres V et VI, où la bonne complémentarité entre l'EQCM et l'*ac*-électrogravimétrie est mise en évidence. Enfin, la conclusion générale de la présente thèse est présentée dans le chapitre VII.

## Chapitre I

Le chapitre I présente tout d'abord les principes fondamentaux d'un supercondensateur, puis, les défis qui se présentent pour faire des dispositifs efficaces et enfin, les applications possibles. En général, un supercondensateur est constitué de deux électrodes en contact avec un électrolyte isolé électriquement par un séparateur. Pendant le processus de charge, les charges peuvent être stockées et séparées à travers les deux interfaces électrode/électrolyte, ce qui fournira de l'énergie électrique pour le circuit externe lors de la décharge, comme illustré **Figure 1**.

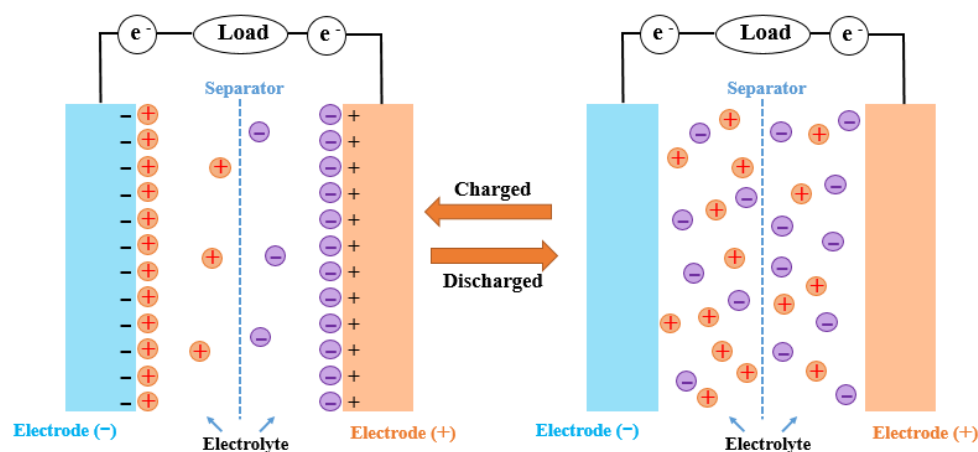


**Figure 1.** Illustration schématique d'un SC à l'état chargé et déchargé

Selon le mécanisme de stockage de charge, les supercondensateurs peuvent être classés selon deux types: les condensateurs électriques à double couche (EDLC), qui stockent les charges par adsorption électrostatique des ions à l'interface électrode/électrolyte, sont généralement basés sur des matériaux à base de carbone; les pseudocondensateurs, dont l'énergie est stockée par des réactions redox rapides et réversibles entre l'électrolyte et les espèces électroactives à la surface de l'électrode à des potentiels caractéristiques, sont généralement basés sur des oxydes de métaux de transition et des polymères conducteurs. Dans ce dernier cas, les phénomènes d'électroadsorption sont toujours actifs.

Les supercondensateurs se caractérisent par une puissance élevée, une excellente cyclabilité et une charge rapide avec peu d'entretien. Ils possèdent une densité de puissance beaucoup plus élevée que les batteries et une densité d'énergie beaucoup plus importante que les condensateurs conventionnels. L'application des SCs s'est étendue à l'électronique portable (comme les appareils photo numérique et les téléphones portables), aux véhicules électriques, aux véhicules hybrides électriques, aux outils électriques, aux techniques laser à impulsions, aux alimentations stabilisées et au stockage de l'énergie générée par les cellules solaires. Bien qu'ils présentent de nombreux avantages, les SCs doivent encore faire face à certains défis, comme une faible densité énergétique ( $\sim 5 \text{ Wh kg}^{-1}$ ) par rapport aux batteries ( $> 50 \text{ Wh kg}^{-1}$ ) et un taux d'autodécharge élevé.

Trois grandes catégories de matériaux d'électrodes électroactives pour fabriquer des SCs sont disponibles: les matériaux à base de carbone, de polymères conducteurs ou d'oxydes de métaux de transition. Ils seront examinés en détail avec les nouvelles tendances dans le développement des électrodes pour les SCs: avantages/désavantages et performances seront étudiés. Les matériaux à base de carbone sont largement utilisés comme matériaux d'électrode EDLC, car ils présentent une conductivité, une porosité et une stabilité électrochimique excellente; les polymères conducteurs sont considérés comme ayant un potentiel séduisant dans les applications SCs en raison de leur capacité de charge élevée, leur faible coût (par rapport aux oxydes métalliques), leur respect de l'environnement, leur conductivité élevée dans un état dopé et leur large fenêtre de potentiel; les oxydes métalliques des métaux de transition ont été intensivement étudiés comme matériaux d'électrode en raison de leurs réactions redox rapides et réversibles, avec une densité énergétique plus élevée par rapport aux matériaux à base de carbone conventionnels ainsi qu'une meilleure stabilité électrochimique que les polymères conducteurs.

Les outils d'évaluation des performances des matériaux d'électrodes SCs sont également passés en revue dans cette partie. La voltampérométrie cyclique (CV), la charge/décharge galvanostatique (GCD) et la spectroscopie d'impédance électrochimique (EIS) sont les techniques les plus couramment utilisées pour évaluer les propriétés électrochimiques des SCs. De plus, une méthode non conventionnelle de caractérisation électrochimique, la microbalance électrique à quartz (EQCM) et l'électrogravimétrie en courant alternatif (*ac*-électrogravimétrie) ont été utilisées conjointement pour étudier les performances électrochimiques des SCs. Considérant que les propriétés mécaniques sont également importantes pour une électrode SCs efficace, une méthode d'étude de ces propriétés, via des mesures électroacoustique, a également été discutée. Enfin, les objectifs et les grandes lignes de la thèse sont présentés à la fin de ce chapitre.

### Chapitre II

Le chapitre 2 présente tout d'abord les techniques de caractérisation des matériaux utilisés dans cette thèse: spectroscopie infrarouge à transformée de Fourier (FTIR), spectroscopie ultraviolet-visible (UV-vis), microscopie électronique à balayage (MEB), diffraction des rayons X (XRD), spectroscopie photoélectronique à rayons X (XPS). Ensuite, les caractérisations électrochimiques et électrogravimétriques sont présentées : la microbalance électrochimique à quartz (EQCM) et l'électrogravimétrie en courant alternatif (*ac*-électrogravimétrie). Des mesures d'impédance électroacoustique sont aussi décrites afin de caractériser la mécanique des films pour SCs.

### Chapitre III

Le chapitre 3 étudie la corrélation entre les propriétés électrochimiques et viscoélastiques d'un film électrogénéré de polypyrrole dopé au dodécylsulfate de sodium (PPy-DS) pendant le cyclage électrochimique. Cette étude a été menée en combinant des caractérisations EQCM, *ac*-électrogravimétriques et électroacoustiques. La procédure expérimentale est illustrée schématiquement **Figure 2**.

L'électrode PPy-DS évolue au cours des cyclages successifs dans un électrolyte aqueux de type NaCl et présente: (i) une transition sélective ionique évidente des cations aux anions dans le processus de compensation de charge (**Figure 3**) ; (ii) une performance globale électrochimique

inférieure accompagnée d'une rigidité accrue lors des cyclages successifs (**Figure 4**); et (iii) une capacité d'échange ionique diminuée à l'interface film/électrolyte. Les électrodes en polymère conducteur PPy-DS présentent un intérêt pour le stockage de l'énergie et la relation entre les propriétés électrochimiques et viscoélastiques pendant le cycle électrochimique est essentielle pour assurer les performances de ces dispositifs. Dans cette perspective, l'*ac*-électrogravimétrie combinée à des mesures électroacoustiques peut être suggérée comme méthode pour sonder de façon synchrone et profonde l'évolution électrochimique et mécanique de ces films. Cela constitue une méthode expérimentale nouvelle pour étudier le mécanisme de vieillissement des électrodes conductrices à base de polymère.

Enfin, un mécanisme de l'évolution structurale de l'électrode PPy-DS pendant les cycles est proposé comme le montre la **Figure 5**. Cela permet de rigidifier le film PPy-DS de deux façons: le balayage anodique et des cyclages successifs du film. Les deux phénomènes peuvent limiter le transfert des Na<sup>+</sup> hydratés. À la fin des cycles électrochimique, le film ne connaît plus guère de changement de volume, ce qui s'accompagne d'une diminution de la performance électrochimique.

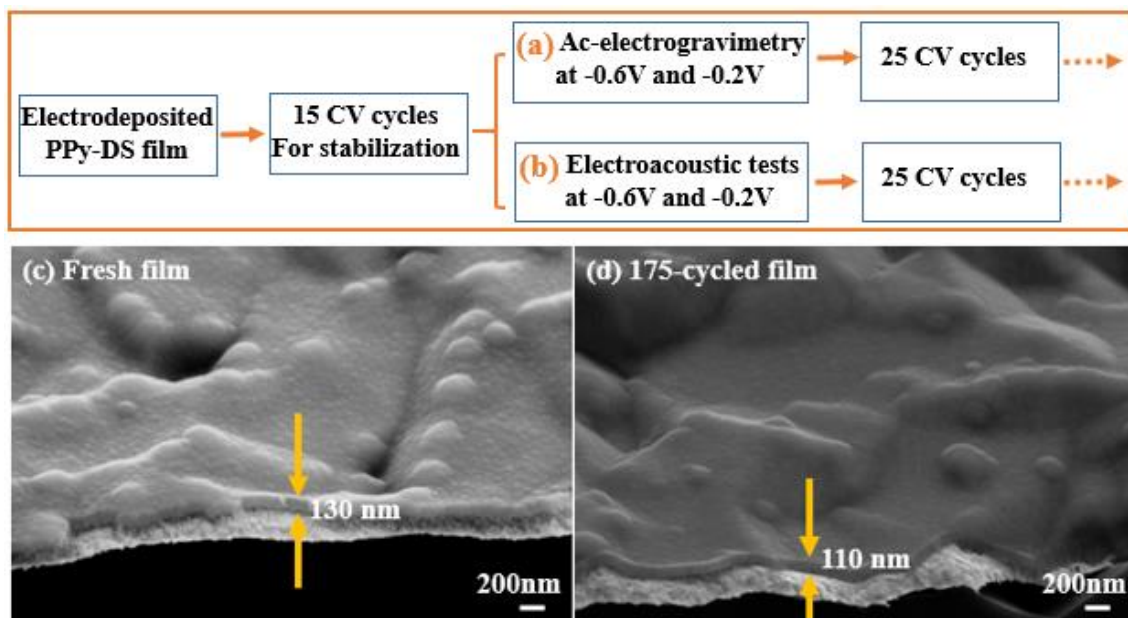


**Figure 2.** Illustration des procédures de mesure pour (a) l'*ac*-électrogravimétrie et (b) l'impédance électroacoustique pendant le cyclage électrochimique du film; (c) et (d) sont les observations morphologiques du film PPy-DS frais et après 175 cycles par le FEG-SEM, respectivement.

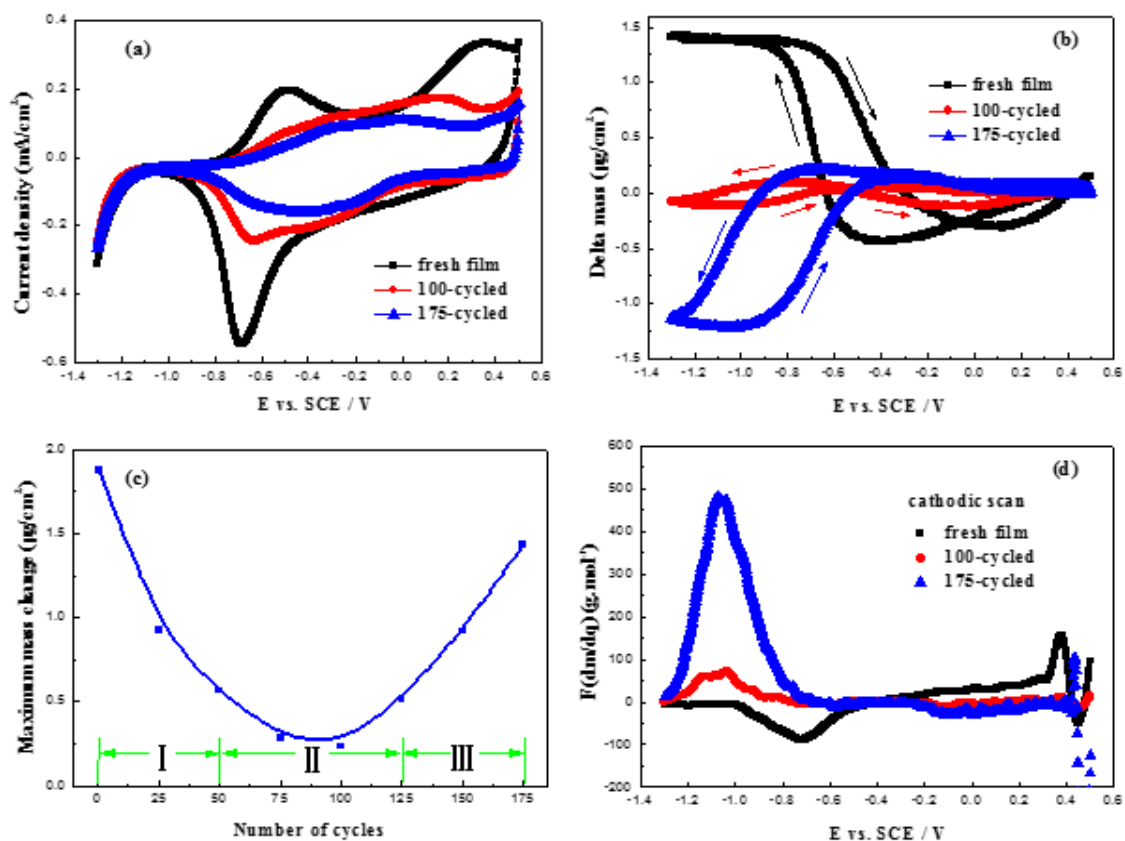


**Figure 3.** Voltampérométrie cyclique (a), variation de masse ( $\Delta m$ ) (b), variation de masse maximale (c) et fonction  $F(dm/dq)$  calculée à partir de la branche de réduction (d) du film PPy-DS dans une solution aqueuse de NaCl 0,25 M entre -1,3 V et 0,5 V vs ECS à une vitesse de balayage de 50  $mV \cdot s^{-1}$ .

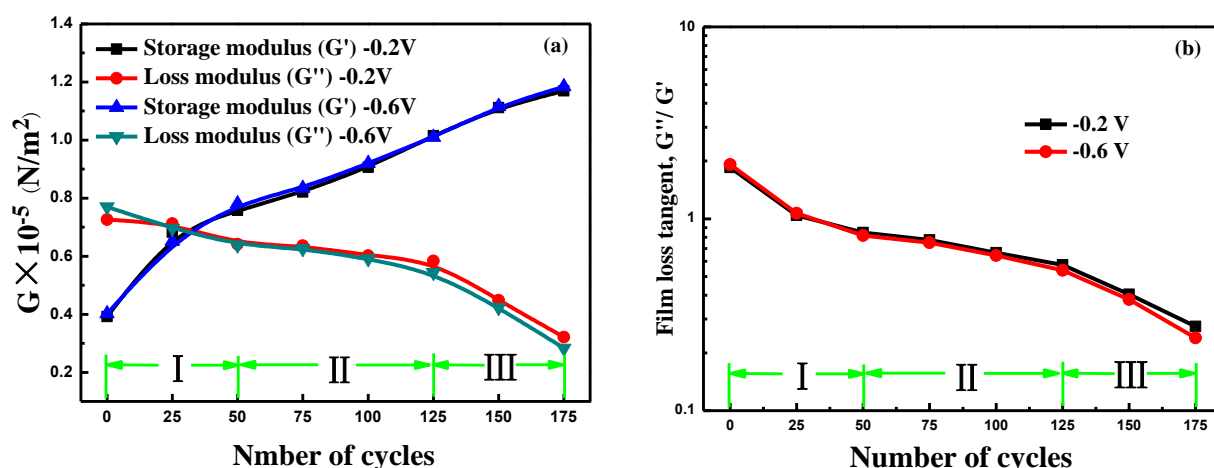


**Figure 4.** (a) Évolution des composantes réelles et imaginaires du module de cisaillement complexe et (b) évolution de la tangente du coefficient de perte du film entre -0,2V et -0,6V lors des cycles successifs.

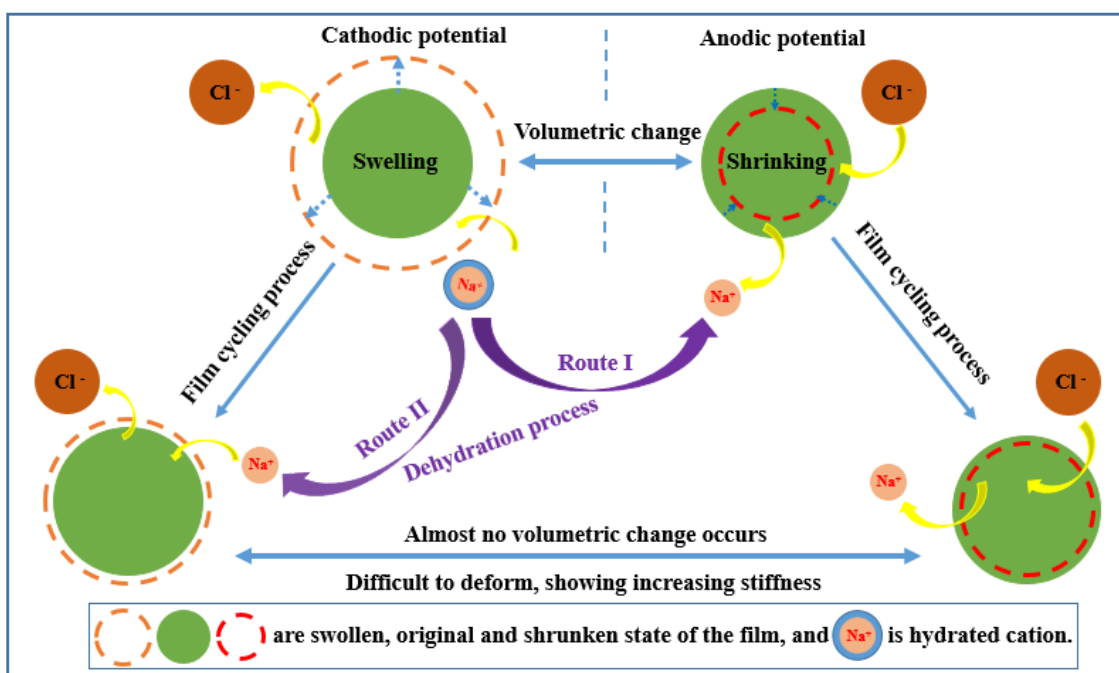


**Figure 5.** Schéma de l'évolution structurale de l'électrode PPy-DS pendant le cyclage du film, sans tenir compte de l'échange des molécules d'eau libre.

## Chapitre IV

Le chapitre 4 montre que l'oxyde de graphène légèrement réduit électrochimiquement (ERGO) présente une préférence anionique pour le stockage de charges, tandis qu'avec l'élimination progressive des fonctionnalités de l'oxygène sur ses plans basaux, les cations commencent à prédominer dans la compensation de charge (**Figure 6**). Cette évolution "anion-cation" en milieu aqueux neutre peut non seulement affecter le stockage de charge électrochimique, mais aussi jouer un rôle important dans les propriétés mécaniques de l'électrode (**Figure 7**). Il a été démontré que les fonctions oxygène pouvaient modifier les interactions entre les couches de graphène et même contribuer au comportement pseudocapacitif des films. Cependant, le rôle des groupes fonctionnels à base d'oxygène dans le transfert d'espèces et les variations viscoélastiques restent encore mal compris. Une méthodologie combinée de microbalance électrochimique à quartz (EQCM), d'*ac*-électrogravimétrie et de mesures d'impédance électroacoustique a été proposée pour caractériser les réponses électrochimiques et viscoélastiques des oxydes de graphène avec différents degrés de réduction électrochimique. Au cours de l'élimination des groupes fonctionnels contenant de l'oxygène, l'électrode d'ERGO présente: (i) une capacité spécifique progressivement améliorée

avec une flexibilité accrue (coefficient de rigidité  $G'$ , diminué); (ii) un processus de déshydratation des cations avec passage de  $\text{Na}^+ \cdot 2\text{H}_2\text{O}$  à  $\text{Na}^+ \cdot \text{H}_2\text{O}$  (**Figure 8**). Ces résultats ouvrent la porte à une mise au point appropriée de matériaux à base de GO pour le stockage d'énergie électrochimique où le comportement sélectif des ions joue un rôle primordial.

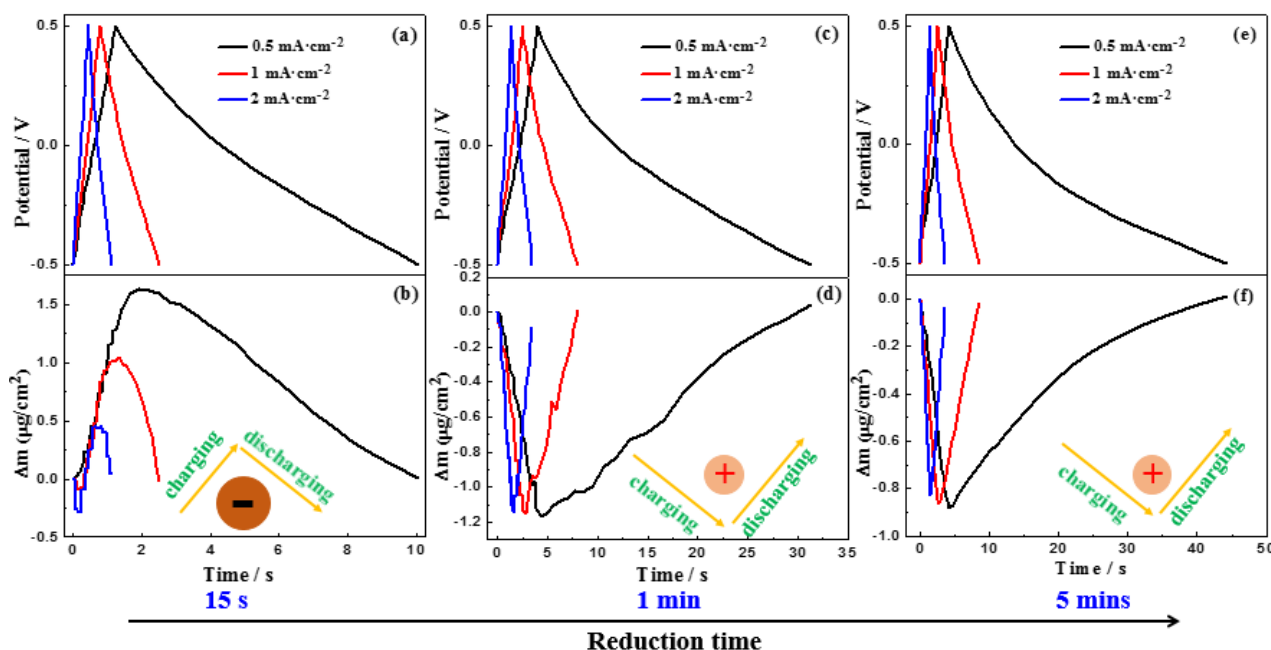


**Figure 6.** Charge-décharge galvanostatique de différents films ERGO-1 (a, b), -2 (c, d) et -3 (e, f) à une densité de courant de 0,5, 1 et 2 mA·cm<sup>-2</sup>, respectivement.

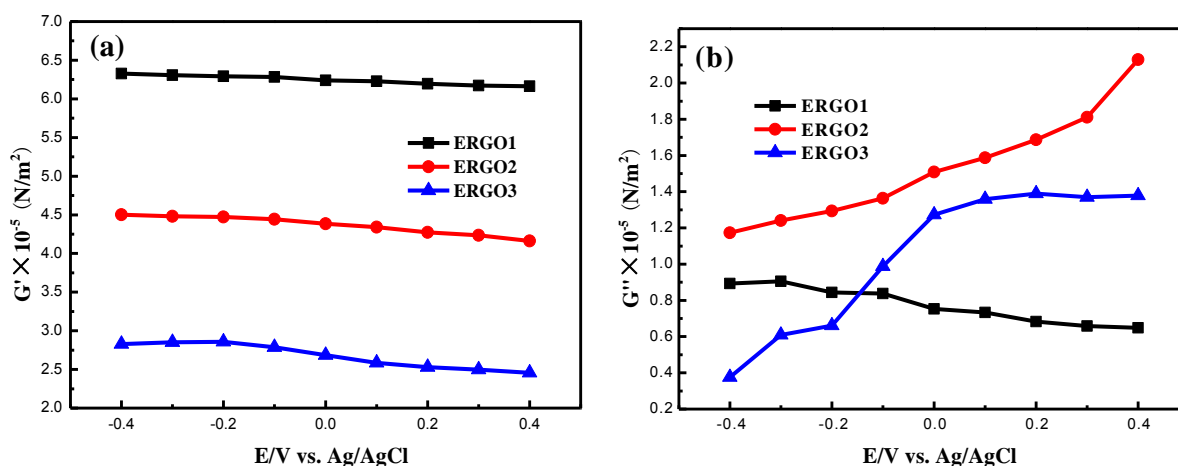


**Figure 7.** Évolution de (a) composantes réelles et (b) imaginaires du module de cisaillement complexe des électrodes d'ERGO.

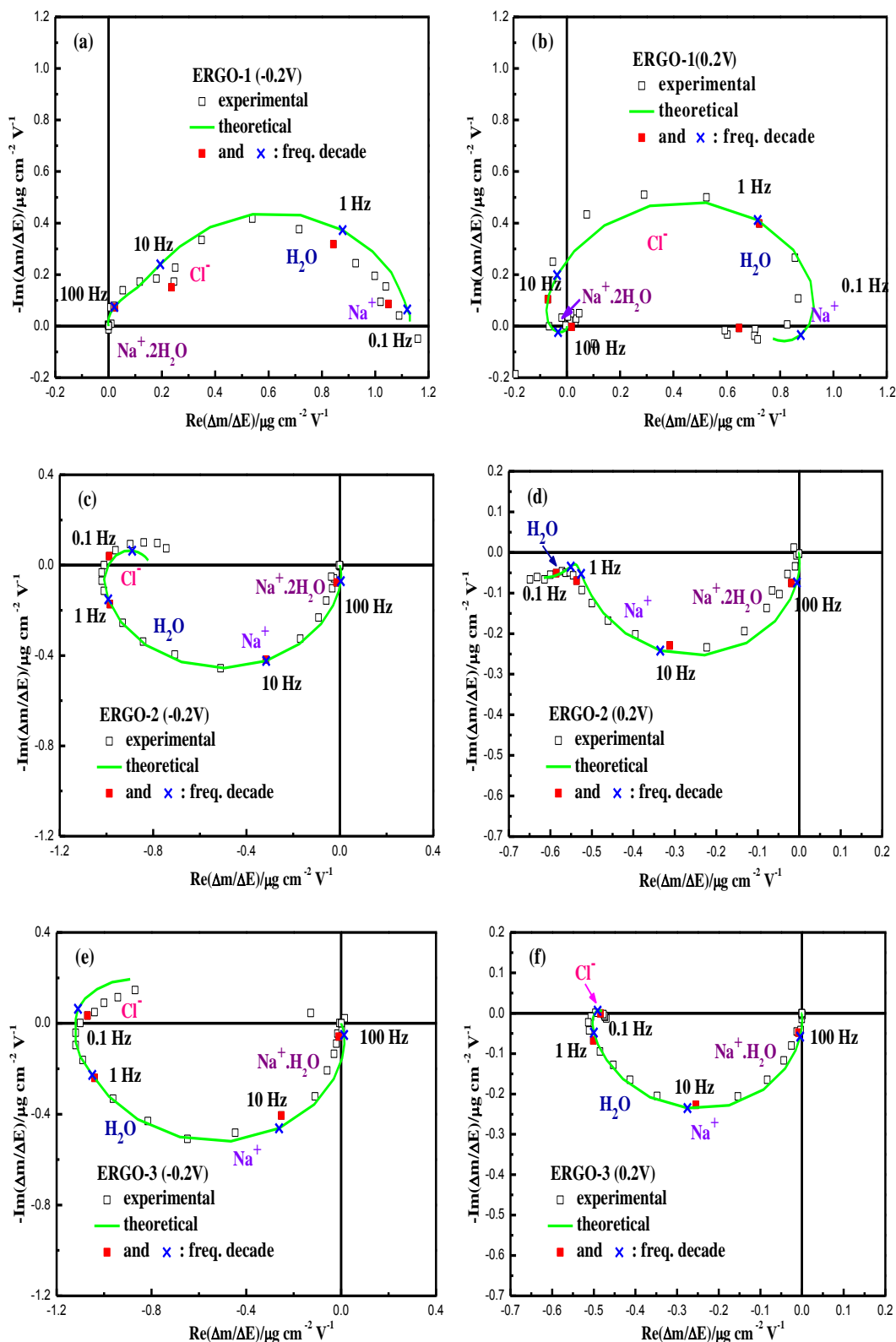


**Figure 8.** Évolution de la fonction de transfert de  $\Delta m/\Delta E(\omega)$  avec réduction progressive des électrodes ERGO: (a), (c) et (e) ont été mesurés pour ERGO-1, -2 et -3 à -0,2 V, tandis que (b), (d) et (f) à 0,2 V.

## Chapitre V

Le chapitre 5 explore le mécanisme des flux d'espèces pendant le processus de charge-décharge d'une électrode de ZnO nanostructurée synthétisée hydrothermiquement (**Figure 9**) par une méthodologie combinée de microbalance électrochimique à quartz (EQCM) et d'*ac*-électrogravimétrie. Dans les conditions de notre étude, les anions ( $\text{SO}_4^{2-}$ ) possèdent la cinétique de transfert la plus élevée à l'interface électrode/électrolyte tandis que les cations (identifiés comme  $\text{Na}^+ \cdot 5\text{H}_2\text{O}$  and  $\text{Na}^+$ ) jouent le rôle principal en tant que porteurs de charge avec une cinétique de transfert plus lente (**Figure 10**). Les molécules de  $\text{H}_2\text{O}$  libre présentent un comportement l'éthargique et leur transfert interfacial se produit à basse fréquence. Ces résultats mettent en lumière la nature des ions et la participation du solvant dans l'équilibre des charges au sein des nanostructures de ZnO directement sur le dispositif QCM. De plus, ce chapitre met l'accent sur la complémentarité de l'EQCM et de l'*ac*-électrogravimétrie (**Figure 11**), où certaines limitations instrumentales qui mettent en cause la détection de la dynamique des ions rapides peuvent être surmontées en exploitant les deux méthodes. La méthodologie combinée proposée ici fournit une analyse dynamique et gravimétrique du transfert de charges interfaciales et peut être étendue à l'étude d'autres électrodes nanostructurées à base d'oxyde métallique pour le stockage d'énergie.

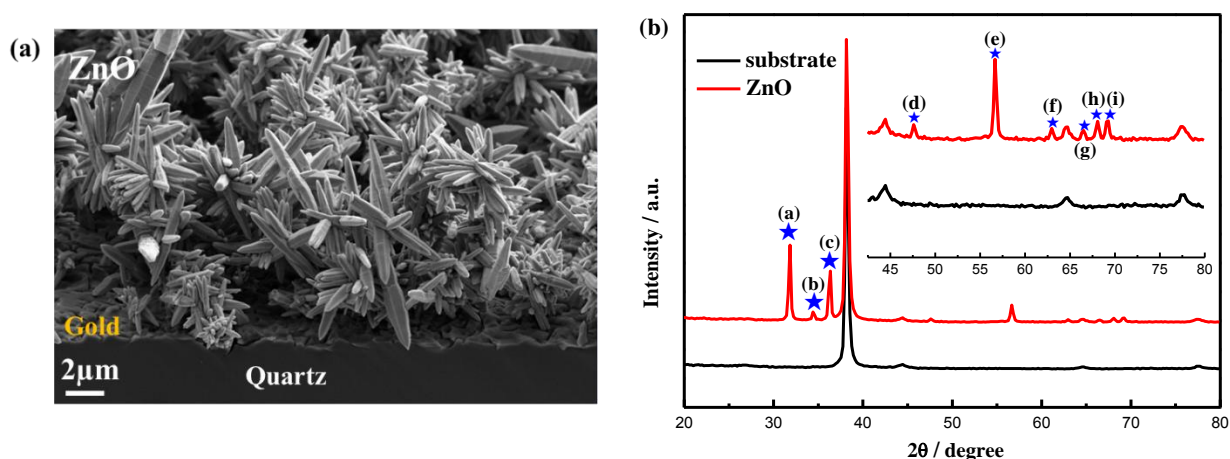


**Figure 9.** (a) Image FEG-SEM et (b) spectres XRD de nanostructures ZnO synthétisées hydrothermiquement sur l'électrode en or du résonateur à quartz. Les pics centrés à  $2\theta = 32^\circ, 34^\circ, 36^\circ, 47^\circ, 56^\circ, 63^\circ, 66^\circ, 68^\circ$  et  $69^\circ$  correspondent aux plans (100), (002), (101), (102), (110), (103), (200), (112) et (201), respectivement. L'incrustation en (b) est le grossissement pour  $2\theta$  entre  $42,5^\circ$  et  $80^\circ$ .

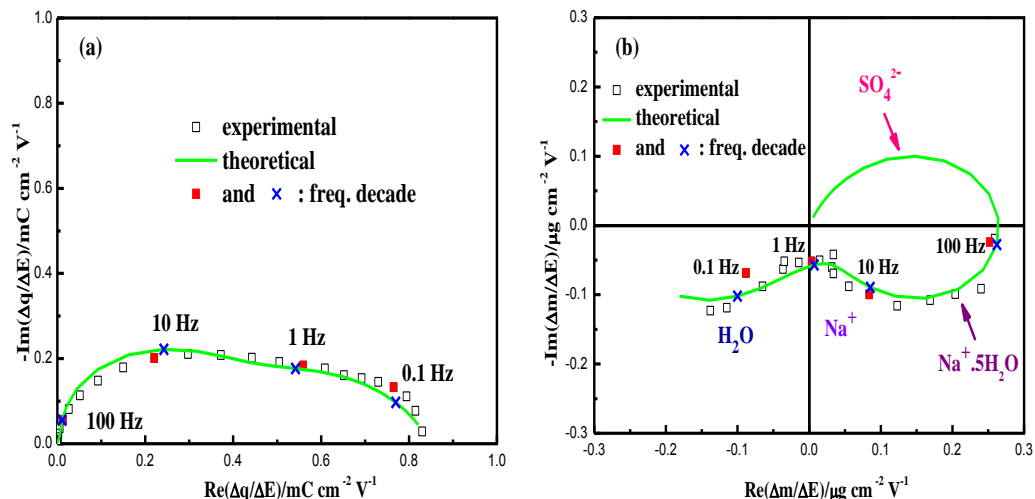


Figure 10.  $\frac{\Delta q}{\Delta E}(\omega)$  (a) et  $\frac{\Delta m}{\Delta E}(\omega)$  (b) fonctions de transfert à 0,3V vs Ag/AgCl dans une solution de  $\text{Na}_2\text{SO}_4$  0,25 M.

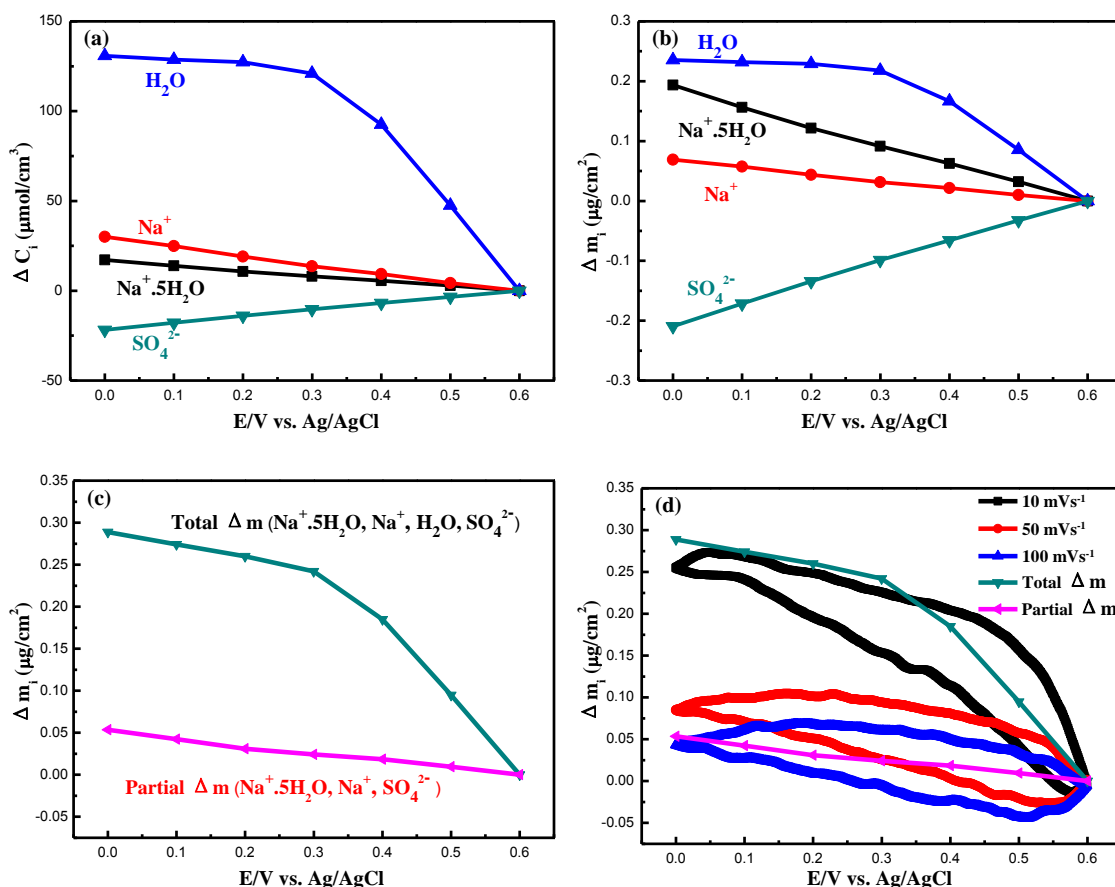
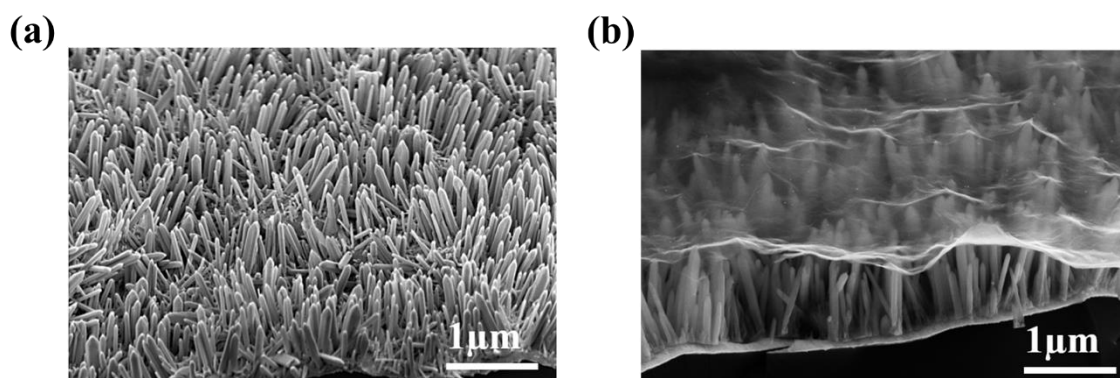


Figure 11. Changement de la concentration relative (a) et changement de masse correspondant (b) de chaque espèce en fonction du potentiel; variation de masse (Total et Partiel  $\Delta m$ ) reconstruite à partir de l'ac-électrogravimétrie (c) et comparaison de la variation de masse entre

l'*ac*-électrogravimétrie et l'EQCM (d).

## Chapitre VI

Le chapitre 6 porte sur la synthèse et la caractérisation de nanotiges de ZnO alignés verticalement et recouvertes par un film d'oxyde de graphène réduit électrochimiquement (ERGO). Une structure ZnO@ERGO ainsi générée directement sur les résonateurs à quartz (**Figure 12**). La couche mince d'ERGO déposée s'est avérée très efficace pour améliorer les performances électrochimiques des nanocomposites ZnO@ERGO en tant qu'électrodes de SCs (**Figure 13**). Le mécanisme de stockage de charge des électrodes ZnO@ERGO a d'abord été étudié par microbalance à quartz électrochimique (EQCM). Cela montre un comportement global d'échange cationique dans l'électrolyte Na<sub>2</sub>SO<sub>4</sub>. Une technique complémentaire, l'*ac*-électrogravimétrie, a ensuite été utilisée pour déconvoluer la réponse de l'EQCM. La contribution individuelle de différentes espèces Na<sup>+</sup>·H<sub>2</sub>O, SO<sub>4</sub><sup>2-</sup> et H<sub>2</sub>O a été mise en évidence avec des cinétiques de transfert différentes (**Figure 14**).



**Figure 12.** Images FEG-SEM des nanostructures ZnO (a) et des composites ZnO@ERGO (b) synthétisés sur l'électrode d'or du résonateur à quartz.

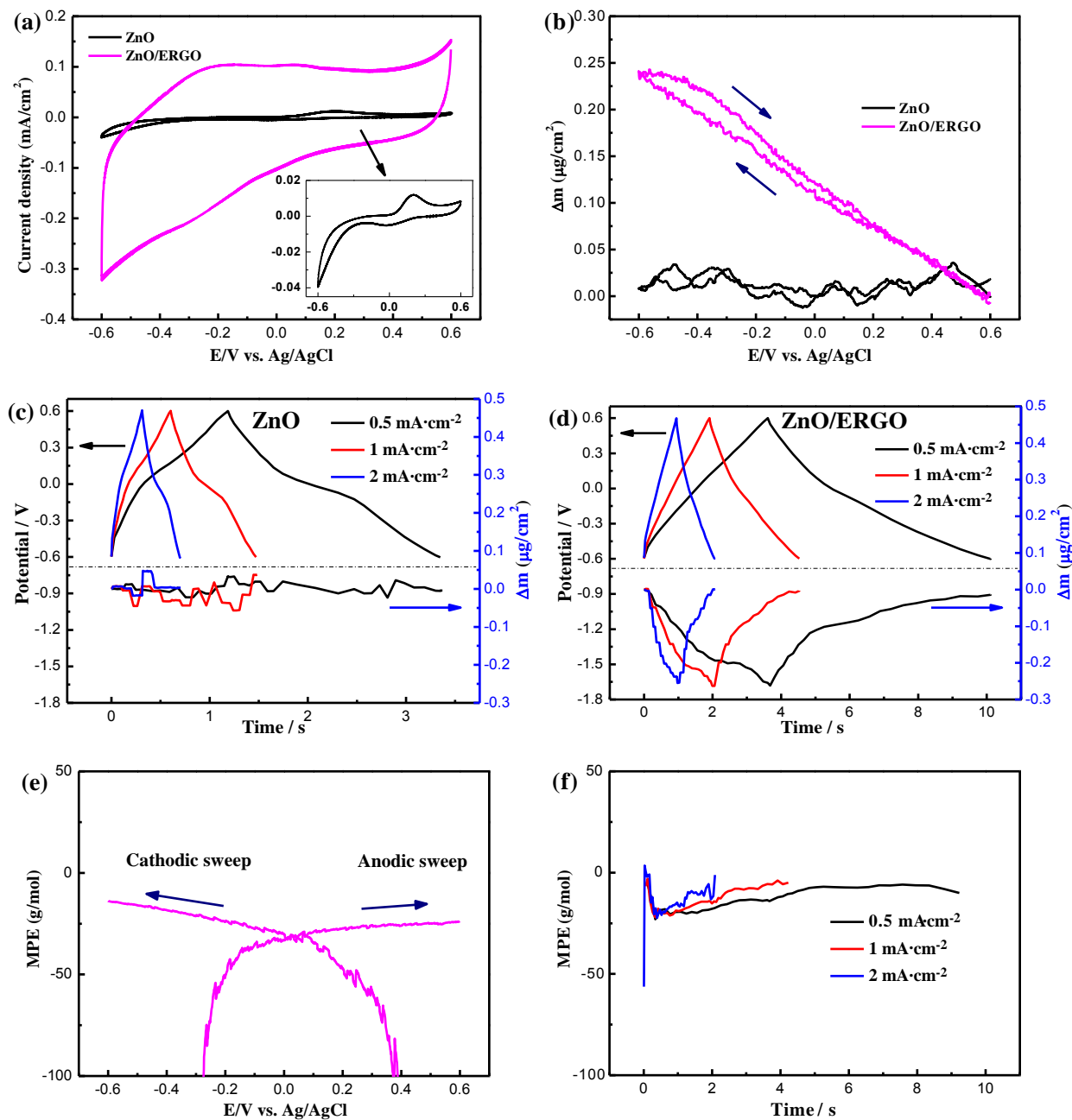


**Figure 13.** Courbes d'électrogravimétries à 100 mV/s (a, b) et courbes GCD à différentes densités de courant (c, d) dans une solution de Na<sub>2</sub>SO<sub>4</sub> 0,25 M ; (e) et (f) sont la masse correspondante par mole d'électrons de l'électrode chargée ZnO@ERGO calculée à partir d'un cycle CV et GCD, respectivement.

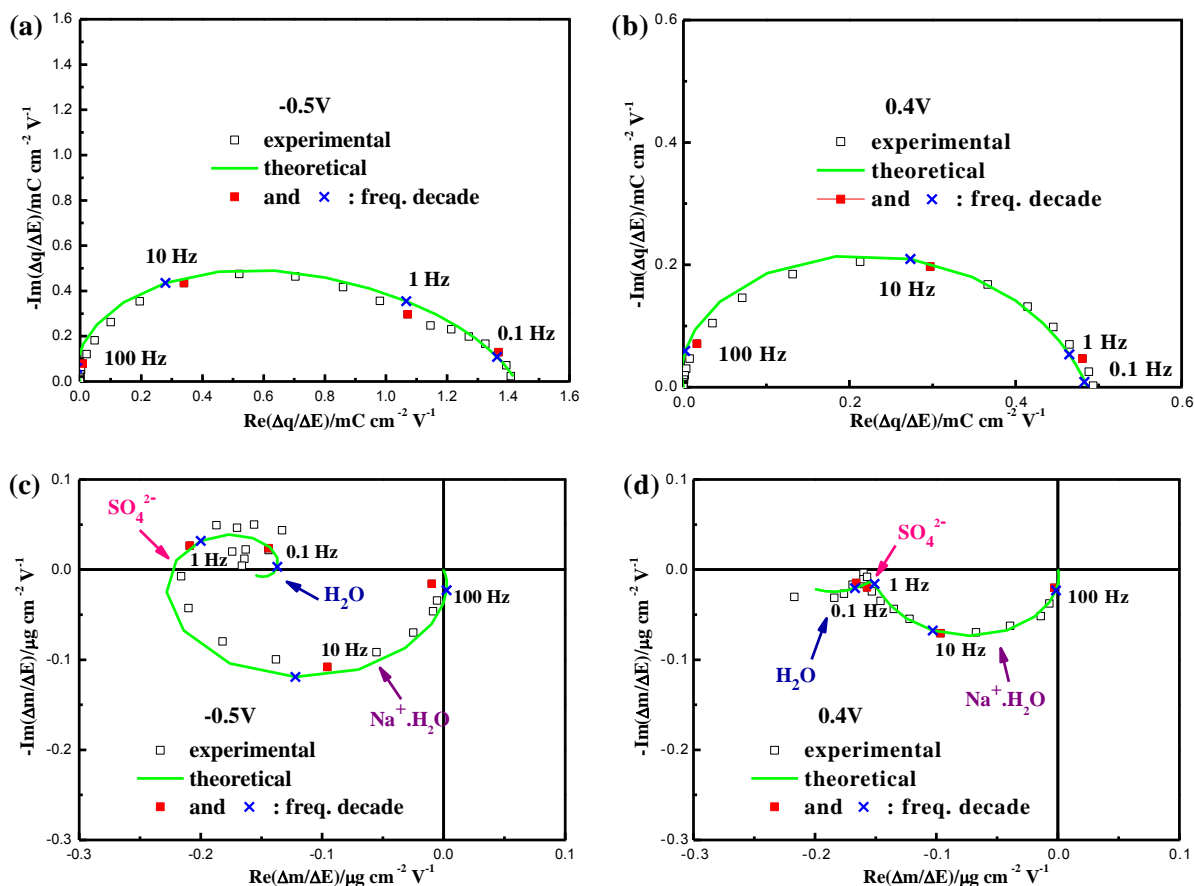


**Figure 14.**  $\frac{\Delta q}{\Delta E}(\omega)$  (a et b) et  $\frac{\Delta m}{\Delta E}(\omega)$  (c et d) fonctions de transfert à -0,5V et 0,4V vs Ag/AgCl dans une solution de  $\text{Na}_2\text{SO}_4$  0,25 M.

### Conclusion Générale

Certaines conclusions basées sur la thèse sont généralisées dans ce chapitre.

#### 1. Comportements sélectifs d'ions au sein de matériaux utilisables pour le stockage de charges

Le flux ionique dans les matériaux d'électrodes joue un rôle fondamental dans le stockage de charges au sein des supercondensateurs. Un comportement sélectif ionique évident dans le stockage de charge a été observé dans les électrodes à base de PPy et d'ERGO, tel que discuté dans les chapitres III et IV. En particulier, pour les électrodes fraîches et peu cyclées à base de PPy, les cations sont principalement échangés à l'interface électrode/électrolyte tandis que les anions s'avèrent être le principal support de charges pour les électrodes de PPy vieillissantes; pour les électrodes d'ERGO à haute teneur en oxygène, les anions jouent un rôle majeur pour le stockage de charge, qui, cependant, sont remplacés par des cations avec élimination progressive des fonctionnalités à base d'oxygène dans ces films d'ERGO.

### 2. Désolvation de cations hydratés

Les cations hydratés sont capables de participer au stockage de charge avec une désolvation (partielle) de leur coquille de solvation. Dans l'électrode à base de PPy, les cations hydratés ( $\text{Na}\cdot 2\text{H}_2\text{O}$ ) perdent progressivement la coquille de solvation pour la compensation de charge à -0,6 V vs ECS pendant le processus de vieillissement du film, comme discuté au chapitre III; l'élimination des fonctionnalités à base d'oxygène dans les couches d'ERGO conduit à un processus de déshydratation des cations, passage de  $\text{Na}^+\cdot 2\text{H}_2\text{O}$  à  $\text{Na}^+\cdot \text{H}_2\text{O}$ , comme discuté au chapitre IV.

### 3. Rôle de l'eau libre dans le stockage de charge

Bien que le flux ionique soit essentiel à l'équilibre des charges, cet échange est souvent accompagné d'un flux de  $\text{H}_2\text{O}$  libre qui joue un rôle non négligeable. Ce phénomène a été observé dans le cas des électrodes à base de PPy, ERGO, ZnO et ZnO@ERGO examinés dans les chapitres III, IV, V et VI, respectivement. Pour les électrodes à base de PPy, une grande quantité de  $\text{H}_2\text{O}$  est déterminée pour les potentiels les plus cathodiques ce qui conduit à un état gonflé du film; Cela facilite le transfert d'ions plus gros, tels que  $\text{Na}^+\cdot 2\text{H}_2\text{O}$  et  $\text{DS}^-$  (voir chapitre III); pour les électrodes à base d'ERGO, le  $\text{H}_2\text{O}$  échangé joue souvent un rôle important dans la viscoélasticité de l'électrode par un effet plastifiant (voir chapitre IV); l'eau libre présente un comportement de transfert lent pour les électrodes à base de ZnO et ZnO@ERGO comme discuté dans les chapitres V et VI, respectivement. Ce mouvement d'eau résulte d'un effet d'entraînement de la part des ions ou d'un effet d'exclusion.

### 4. Effets viscoélastiques sur le stockage de charge

Les variations viscoélastiques des électrodes causées par l'electrodesorption/ electrodesorption ionique et/ou l'insertion/extraction jouent un rôle important dans le stockage de charge. Comme indiqué dans le chapitre III, la capacité de stockage de charge des électrodes à base de PPy s'estompe progressivement en raison de la rigidité croissante des chaînes PPy, ce qui interdit non seulement le transfert d'ions à l'interface électrode/ électrolyte mais aussi le transport au sein du PPy. Dans le chapitre IV, la flexibilité accrue de l'électrode d'ERGO permet d'échanger une plus grande quantité d'ions, ce qui conduit à une amélioration de la capacité spécifique.